

Does Richard Feynman Dream of Electric Sheep? Topics
on Quantum Field Theory, Quantum Computing, and
Computer Science

Thesis by
Junyu Liu

In Partial Fulfillment of the Requirements for the
Degree of
Doctor of Philosophy

The logo for the California Institute of Technology (Caltech), featuring the word "Caltech" in a bold, orange, sans-serif font.

CALIFORNIA INSTITUTE OF TECHNOLOGY
Pasadena, California

2021
Defended May, 3, 2021

© 2021

Junyu Liu

ORCID: 0000-0003-1669-8039

All rights reserved except where otherwise noted

ACKNOWLEDGEMENTS

Caltech is really an amazing school with an excellent academic environment. I am very lucky to have been here to receive so many educational opportunities, collaborations, and friendships. As a starting point of my professional career, I am trying to be a theoretical physicist, a dream I have had from childhood. It has also provided me an excellent platform to interact with great minds not only inside the campus, but also the whole high energy physics and quantum information science community. These important five years are treasures in my whole life.

Firstly, I wish to thank my advisors. I am lucky enough to be advised by three great scientists at the same time, Clifford Cheung, John Preskill, and David Simmons-Duffin, (listed in the alphabetical order). They are great academic advisors, encouraging me to solve important scientific problems, and giving me infinite suggestions about science and careers during my hard time.

Cliff is really a hero. I will remember infinite discussions we had on the fourth floor of Downs-Lauritsen, or under the beautiful sunshine of Pasadena. For me, Cliff is a great mentor, teacher, and friend both in my academic and personal life. From him, I learned how to dive into interesting science deeply and think about important problems, and also be active on exploring different scientific areas and their intersections. I believe those exceptional insights and profound knowledge will benefit me throughout my life.

For me, John is one of the most outstanding wise men of our time, and it has been my great honor to interact and work with him. When I was looking for research opportunities as a young graduate student, John brought a fascinating world, quantum information science, to me. What I have learned the most from him is to consider the long-term impact when choosing a research topic. As a great mentor, John is very considerate and full of patience, of which I will have a lasting memory.

David is a legend in theoretical physics. Working with David is a fantastic experience. When I ask David questions, he can remember almost everything and write a crystal-clear explanation on the blackboard, including complicated series of conformal block expansions. At the same time, David is also an excellent friend, and I am very thankful for his tolerance of my jokes, the outstanding organization of the bootstrap collaboration, and the Caltech conformal group.

To continue, I wish to thank other collaborators during my graduate school: Ning Bao, Alexander Buser, Shai Chester, Jordan Cotler, Hrant Gharibyan, Masanori Hanada, Masazumi Honda, Nicholas Hunter-Jones, Per Kraus, Walter Landry, Aitor Lewkowycz, Tianlin Li, Yue-Zhou Li, Don Marolf, David Meltzer, Ashley Milsted, Eric Perlmutter, David Poland, Grant Remmen, Vladimir Rosenhaus, Eva Silverstein, Ning Su, Jinzhao Sun, Gonzolo Torroba, Alessandro Vichi, Guifre Vidal, Yuan Xin, Beni Yoshida, Xiao Yuan, Qi Zhao, Yehao Zhou, and You Zhou. Working with all of you has given me excellent and unforgettable memories!

I also wish to thank many other physics or STEM colleagues for your discussions and friendships: Soner Albayrak, Victor Albert, Mustafa Amin, Guy-Gur Ari, Nima Arkani-Hamed, Yimu Bao, Yoni Bentov, David Berenstein, Dominic Berry, Fernando Brandão, Charles Cao, Marcela Carena, Sean Carroll, Xie Chen, Gong Cheng, Andrew Childs, Soonwon Choi, Clay Cordova, William Cottrell, Elizabeth Crosson, Bartek Czech, Alex Dalzell, Maria Derda, Xi Dong, Rajeev Erramilli, Bradley Filippone, Liam Fitzpatrick, Weibo Fu, Andras Gilyen, Victor Gorbenko, Yingfei Gu, Charles Hadfield, Nicole Yunger Halpern, Connor Hann, Daniel Harlow, Jim Hartle, Tom Hartman, Patrick Hayden, Hong-Ye Hu, Yangrui Hu, Robert Huang, Alexander Jahn, Liang Jiang, Zhang Jiang, Denis Karateev, Kohtaro Kato, Emanuel Katz, Isaac Kim, Alexei Kitaev, Natalie Klco, Murat Kologlu, Shota Komatsu, Grisha Korchemsky, Petr Kravchuk, Richard Kueng, Henry Lamm, Adam Levine, Zhijin Li, Ying-Ying Li, Shu Lin, Ying-Hsuan Lin, Hong Liu, Jiahui Liu, Peter Love, Andreas Ludwig, Matilde Marcolli, Antonio Mezzacapo, Spiros Michalakis, Alexey Milekhin, Ryan Mishmash, Evgeny Mozgunov, Sepehr Nezami, Hiroshi Ooguri, Sam Pallister, Julio Parra-Martinez, Fernando Pastawski, Geoffrey Penington, Xiao-Liang Qi, Daniel Ranard, Sam Roberts, Junchen Rong, Slava Rychkov, Subir Sachdev, Burak Şahinoğlu, Prashant Saraswat, Martin Savage, Steve Shenker, Gary Shiu, Ashmeet Singh, Ronak Soni, Jon Sorce, Douglas Stanford, Leo Stein, Alexandre Streicher, Yuan Su, Jia-Rui Sun, Chong Sun, Brian Swingle, Eugene Tang, Aron Wall, Tian Wang, Wanchun Wei, Mark Wilde, Mark Wise, Zhong-Zhi Xianyu, Dan Xie, Hao-Lan Xu, Xi Yin, Yi-Zhuang You, Ellis Ye Yuan, Pengfei Zhang, Shangnan Zhou, and Sisi Zhou.

Furthermore, I wish to thank so many wonderful places I'd had the chance to visit: Stanford (thanks Xiao-Liang Qi and Eva Silverstein for hosting), UCSB/KITP (thanks Don Marolf for hosting), UCSD (thanks Yi-Zhuang You for hosting), UC Berkeley (thanks Soonwon Choi for hosting), Fermilab, University of Chicago,

University of Colorado Boulder, Princeton, IAS, Harvard, MIT, ···, partially with the help of the Simons collaborations on "It from Qubit" and "the Nonperturbative Bootstrap", QOALAS collaboration, and the MURI collaboration on "Quantum Codes, Tensor Networks, and Quantum Spacetime." I also wish to thank the IAS summer school, TASI summer school, PsiQuantum Corporation for their study and internship opportunities in Summer 2018, 2019, and 2020 respectively.

I wish to thank all my friends during my graduate school, especially Wen-Loong Ma for his efficiency on eating, Honglie Ning for his driving skill, Burak Şahinoğlu and Eugene Tang for some dark secrets about clubs, Weibo Fu, Masanori Hanada, Zhe Jia, Xiang Li, David Meltzer, Ashley Milsted and Yehao Zhou for their long-lasting friendship and help, Xinyue Dai, Nicole Jinglin Gao for her paintings, and Rui Niu, Linrui Xiong for her arts. Moreover, I wish to thank all my IQIM friends, quantum information friends, Downs-Lauritsen fourth floor friends, high energy friends, physics friends, and other friends during my graduate study. I also wish to thank my friends who interact with me in the Los Angeles local organizations, including Animals, Anime, Cats, Film, Hanfu, and Rave.

Thank you, Carol Silberstein, for your hard work in the Downs-Lauritsen fourth floor; Mika Walton and Marcia Brown, for your hard work on my student fairs; and Laura Kim, Daniel Yoder, for your hard work about international students like me. Thank you Ryan Patterson for being my committee chair and making me suggestions about cyberpunk.

I wish to thank the University of Science and Technology of China, the Hong Kong University of Science and Technology, Nanjing University, McGill University and my undergraduate mentors, especially Robert Brandenberger, Yi-Fu Cai, Gang Chen, Henry Tye, and Yi Wang, who educated me as an undergraduate student and brought me to the path of graduate study.

Finally, I wish to thank my cat Pafu for her lovely face. I wish to thank my father An Liu my mother Li Ren and my grandmother Suqiong Zeng for their infinite amount of financial and emotional support.

ABSTRACT

In this thesis, we mainly discuss three topics in theoretical physics: a proof of the weak gravity conjecture, a basic statement in the string theory landscape using the black hole entropy, solving the critical $O(3)$ model using the conformal bootstrap method involving semidefinite programming, and numerical simulation of the false vacuum decay using tensor network methods. Those topics cover different approaches to deep understanding of quantum field theories using concepts and methods of information theory, and computer science with classical and quantum computations.

PUBLISHED CONTENT AND CONTRIBUTIONS

This thesis contains the following three scientific publications.

C. Cheung, **J. Liu**, and G. N. Remmen (**alphabetical order**), *Proof of the Weak Gravity Conjecture from Black Hole Entropy*, JHEP **10**, 004, (2018), arXiv:1801.08546 [hep-th].

J. Liu participated in the conception of the project and the writing of the manuscript, deriving a general formula between the extremal condition and Wald entropy and applying the symbolic algebra on generalization to higher dimensions, and the writing of the manuscript.

S. M. Chester, W. Landry, **J. Liu**, D. Poland, D. Simmons-Duffin, N. Su, and A. Vichi (**alphabetical order**), *Bootstrapping Heisenberg Magnets and their Cubic Instability*, Phys. Rev. D **104**, 105013, Editors' Suggestion, (2021), arxiv:2011.14647 [hep-th].

J. Liu participated in the conception of the project, the writing of the manuscript, and the organization of the collaboration, applying and strengthening the island and the OPE scan algorithm of the conformal $O(3)$ model, applying the symbolic algebra to deriving crossing equations with symmetries, and searching for the critical gap with dynamical algorithms.

A. Milsted, **J. Liu**, J. Preskill, and G. Vidal, *Collisions of false-vacuum bubble walls in a quantum spin chain*, PRX Quantum **3**, 020316, (2022), arXiv:2012.07243 [quant-ph].

J. Liu participated in the conception of the project, including numerical simulations on the dynamical evolution and entanglement/energy flux determination of the kink scattering process using software, as well as the writing of the manuscript.

TABLE OF CONTENTS

Acknowledgements	iii
Abstract	vi
Published Content and Contributions	vii
Table of Contents	vii
List of Illustrations	xi
List of Tables	xxi
Chapter I: Introduction: aspects of "cyberpunkian" quantum field theory . . .	1
1.1 Space opera and Cyberpunk	1
1.2 Quantum field theory	5
1.3 Simulating quantum field theory using quantum devices	9
1.4 Conformal field theory and large-scale optimization	12
1.5 The theoretical landscape and data science	16
1.6 Some comments	20
Some physics	20
Black hole thought experiment and quantum information science	20
It from qubit and the non-perturbative bootstrap	21
Church-Turing Thesis in 2021	23
CS-inspired physics and physics-inspired CS	24
Theoretical considerations	24
Benchmarking quantum devices using fundamental physics	25
High energy physics in the low energy lab	26
Towards the future	27
Waiting for quantum technology	27
Fundamental science using oracles	28
Companies, colliders	31
Chapter II: Proof of the Weak Gravity Conjecture from Black Hole Entropy . . .	33
2.1 Introduction	33
2.2 Proof of $\Delta S > 0$	38
Assumptions	38
Positivity Argument	39
Explicit Example	43
Unitarity and Monotonicity	44
2.3 Classical vs. Quantum	45
Leading Contributions	45
Region of Interest	46
2.4 Black Hole Spacetime	47
Unperturbed Solution	48
Perturbed Solution	49

2.5	Calculation of Entropy	50
	Wald Entropy Formula	50
	Interaction Contribution	51
	Horizon Contribution	51
2.6	New Positivity Bounds	53
	General Bounds	53
	Examples and Consistency Checks	54
	The Weak Gravity Conjecture	56
	Entropy, Area, and Extremality	58
2.7	Discussion and Conclusions	59
Chapter III: Bootstrapping Heisenberg Magnets and their Cubic Instability . .		61
3.1	Introduction	61
	Theoretical approaches to the 3d $O(3)$ model	63
	$O(N)$ vs. multi-critical models	65
	Field theory results	67
	Monte Carlo results	69
	The conformal bootstrap	69
	Structure of this work	70
3.2	The $O(3)$ model	70
	Crossing equations	70
	Ward identities	73
3.3	The tiptop algorithm	73
	Software and algorithm	74
	Exploring the current gap	75
	Rescaling	75
	Adaptively meshing the box	77
	Jumping to a larger gap	78
3.4	Results	79
	Dimension bounds with OPE scans	79
	Central charges and $\lambda_{\phi\phi_s}$	82
	Upper bound on Δ_{t_4}	83
3.5	Future directions	84
Chapter IV: Collisions of false-vacuum bubble walls in a quantum spin chain		88
4.1	Selecting a spin chain	92
4.2	Methods	93
	Constructing bubble states	93
	Time evolution	98
	Particle detection	99
4.3	Results	100
	Kink dynamics	100
	Bubble dynamics	101
	The Ising model	102
	Near the Tri-Critical Ising point	104
	Entropy and computational cost	107
4.4	Discussion	109

Bibliography	113
Appendix A: Appendices of Chapter 2	134
A.1 Generalization to Arbitrary Dimension	134
Black Hole Spacetime	134
Calculation of Entropy	135
New Positivity Bounds	137
A.2 Field Redefinition Invariance	138
Appendix B: Appendices of Chapter 3	140
B.1 Code availability	140
B.2 Software setup and parameters	140
B.3 Tensor structures	140
B.4 Computed points	145
Appendix C: Appendices of Chapter 4	149
C.1 Infinite MPS	149
Nonuniform windows	149
C.2 Finding the true and false vacua	150
Finding the true vacuum	150
Finding the false vacuum	150
Finding an iMPS for the false vacuum	152
C.3 MPS quasiparticle states	152
Optimizing the excitation tensor B	154
Broken symmetry and kinks	154
Wavepackets	157
Localized states and Bloch-state parameter redundancy	159
Two-particle states	160
C.4 Particle detection via quasiparticle basis states	164
Checking consistency in the projected wavefunction	165
Fourier analysis	166
Efficient computation of the quasiparticle Fourier analysis	167
Other sources of error	168
C.5 Evolving through time	169
C.6 Comparison with quench approaches	172
C.7 Velocity and Bloch oscillations	175
Single-kink evolution	175
Bubble evolution	175
C.8 Zero longitudinal field	179
C.9 Entanglement generated by an elastic collision	181
Appendix D: Other publications	185

LIST OF ILLUSTRATIONS

<i>Number</i>	<i>Page</i>
1.1 A remarkable prediction from the lattice gauge theory community. Some light hadrons have been predicted using lattice QCD. This is from Figure 3 of [1].	8
1.2 An artist's creation of the quantum simulation projects of kink scattering [2, 3]. The depiction of characters is based entirely on their images in reality. From left to right: Burak Şahinoğlu, Ashley Mislited, Junyu Liu, John Preskill, and Guifre Vidal. Other ingredients include cosmic bubbles (physical objects that are similar to kinks), a spacecraft, a cat (Schrödinger's cat), and the Bell state. The figure is credited to Jinglin Nicole Gao. Figures shown in the screen utilize the figures in our scientific paper [3].	13
1.3 An artist's creation about the superfluid helium conformal bootstrap project [4] and [5]. The depiction of characters is based entirely on their images in reality. From left to right: Shai Chester, David Meltzer, Junyu Liu, Walter Landry, Alessandro Vichi, David Poland, David Simmons-Duffin, and Ning Su. Other ingredients include islands (a theoretical physics terminology referring to the isolated region in the theoretical space using the bootstrap method), a spacecraft (referring to the Space Shuttle Columbia experiment), a diagram as stars in the sky (referring to the conformal block expansion, the basics of the bootstrap equation in the conformal field theory). The figure is credited to Jinglin Nicole Gao.	16
1.4 An illustration of the string theory landscape and the swampland. This is from Figure 1 of [6].	19
1.5 An imaginary plot might be made by future cyberpunkian physicists, especially high energy phenomenologists. This kind of plot includes the required computational resource needed for observations and existing computational resources provided by companies. As far as I know, no such plot existed until June 2021, which put together experimental organizations and quantum companies. I am conjecturing here that this type of plot will appear in the future.	32

2.1	Black holes of maximal charge shown as a function of mass m and charge-to-mass ratio q/m . Higher-dimension operators induce corrections to the extremality condition. If these corrections are positive, then the WGC is automatically satisfied (upper solid curve) since large black holes are unstable to decay to smaller ones. If these corrections are negative (lower solid curve), then the WGC mandates additional light, superextremal particles to avoid an infinite number of stable extremal black hole remnants.	36
2.2	Constraints on higher-dimension operator coefficients derived from black hole entropy. The shaded regions are excluded, with the gradations corresponding to incremental values of $\xi \in (0, 1/2)$. The left and right panels correspond to $d_3 > 0$ and $d_3 < 0$, respectively. In either case, $d_0 < 0$ is forbidden so $d_0 > 0$ and the WGC is automatically satisfied.	54
3.1	The max coordinates Δ_{\max} for a collection of feasible, infeasible, and in-progress points.	75
3.2	Different types of feasible points. Only the points feasible at $\Delta_{\text{gap}} = \Delta_{\text{previous}}$ are used for rescaling.	75
3.3	Points from Figure 3.1 after rescaling.	77
3.4	Points from Figure 3.3 with an adapted mesh. Points that are feasible at $\Delta_{\text{gap}} < \Delta_{\text{feasible}}$ have been removed. The blue spiral indicates an empty candidate cell. The other empty cells are not diagonal from a feasible cell, so they are not considered.	77
3.5	The $\Lambda = 43$ conformal bootstrap dimension island (black) compared with the Monte Carlo results [7, 8] (green).	80
3.6	Comparison between the conformal bootstrap islands at $\Lambda = 19, 27, 35, 43$ projected to the $\{\Delta_\phi, \Delta_s\}$, $\{\Delta_\phi, \Delta_t\}$, and $\{\Delta_s, \Delta_t\}$ planes and the Monte Carlo results of [7, 8].	81

- 3.7 Two-dimensional projection of the results of the `tiptop` search at $\Lambda = 35$. The x coordinate is related to the three scalar dimensions via (B.8). Projections in y and z look similar. We have superimposed a convex hull encompassing the allowed points on top, obscuring some of the disallowed points. We can see the behaviour of the `tiptop` algorithm, exploring the island at one Δ_{t_4} before jumping to a larger Δ_{t_4} . The jumps become progressively smaller, indicating convergence. We computed 16 points simultaneously, and this calculation took several months during which the `tiptop` algorithm was being developed. So the points reflect occasional crashes and small inefficiencies in the set of computed points. 84
- 3.8 Three-dimensional islands of allowed points at different Δ_{t_4} at $\Lambda = 35$, demonstrating how the islands shrink as we approach the maximum Δ_{t_4} . The x , y , and z coordinates are related to the three scalar dimensions via (B.8). The values for Δ_{t_4} , from the largest region to smallest, are 2.989, 2.99025, and 2.9905, with smaller values including all allowed points at larger values. 85
- 4.1 Cartoon showing the collapse of a false-vacuum bubble in a spin chain. The magnetization $\langle Z \rangle$ is positive in the true vacuum, but negative in the false vacuum. A bubble-wall collision is a scattering process, which may be (a) free (no interaction), (b) elastic (no particle production), or (c) inelastic (particle production). Note that in free and elastic scattering of topological particles the left (right) particle always remains a kink (antikink). 90
- 4.2 Evolution of the excess energy density e (relative to vacuum), as a fraction of total excess energy E , in a spin chain for two initial states: (a) created by applying a spatially smeared string operator to the vacuum and (b) constructed from MPS tensors to contain kink and antikink quasiparticle wavepackets. In (a) meson pairs are produced immediately at the string edges, whereas in (b) there is no particle production until the initial kink and antikink collide. The dynamics are restricted to a window of ~ 1000 sites, leading to boundary effects in (a). For more details, see App. C.6. 92

- 4.3 Partial phase diagrams of the extended Ising chain [9, 10], both without and with a small longitudinal field h that breaks the \mathbb{Z}_2 symmetry. At $h = 0, g = 1$ there is a continuous (symmetry-breaking) phase transition described by the Ising CFT for $\lambda \lesssim 0.428$, and by the Tri-Critical Ising (TCI) CFT at $\lambda \approx 0.428$. By studying the spin chain near to these transitions ($g \rightarrow 1, h \rightarrow 0$), we can access emergent, relativistic quantum field theories with confined kinks [11, 12]. Points (i), (ii), and (iii) correspond to the data shown in the figures below. 94
- 4.4 Diagram illustrating the various types of states, and their spin profiles, relevant for simulations. For example, our initial states are *wavepackets* constructed from kink-antikink pairs (a type of excited meson). The product states listed are eigenstates of H when $g = 0, \lambda = 0$. Away from this regime, we use MPS to accurately capture fluctuations in the vacua and excited states. 96
- 4.5 Spin expectation values and relative energy density e/E for (i) the Ising model ($\lambda = 0, g = 0.8, h = 0.007$) and (ii) the generalized Ising model nearer to the Tricritical Ising CFT fixed point (TCI) ($\lambda = 0.41, g = 0.98, h = 0.001$). For (i), the initial wavepackets have $\sigma = 25$ and are 248.5 sites apart ($E/m_\mu = 3.72$). For (ii), $\sigma = 40$ with separation 287.4 ($E/m_\mu = 2.62$). The MPS bond dimensions are $D = 10$ and $D = 18$ for the vacua of (i) and (ii), respectively. During the simulation the dimensions are restricted to $D \leq 128$ and the integration step size is $\delta t = 0.05$ 102
- 4.6 Portion of state (by probability) outside of the MPS bubble subspace $\kappa\bar{\kappa}^{(0,0)}$ for simulations (i) and (ii) of Fig. 4.5. Here we fully account for momentum dependence of the basis states $|\kappa\bar{\kappa}_{j,k}\rangle$ via a Fourier analysis and count only contributions with $k - j \geq 60$ (see App. C.4). For Ising (i), the small probability after the first collision of $t \approx 90$ indicates elastic scattering of kinks, in stark contrast with the TCI case (ii), where the probability remains high after the first collision at $t \approx 150$. In (i), the growth of the post-collision probability with subsequent collisions is consistent with increasingly inaccurate representation of accumulating entanglement (due to the limit imposed on the MPS bond dimension D), as well with delocalization of the wavepackets, since contributions from kink-antikink pairs with small separation $k - j$ are not counted. 103

- 4.7 Dispersion relations (numerical, using MPS) of kinks κ and mesons μ for $\lambda = 0.41$, $g = 0.98$. For mesons, energies are shown with and without a weak longitudinal field. Individual kinks do not have a finite energy for $h > 0$. Threshold energies for pair production are shown (computed assuming $h = 0$ for kinks and $h = 0.001$ for mesons), as is the energy (labelled Ψ) of the simulation shown in Fig. 4.5 for parameter-set (ii). 104
- 4.8 Spin expectation values for simulation (ii) of Fig. 4.5 at time $t = 270$ (bond dimension $D \leq 128$) after projection into selected quasiparticle subspaces and normalization. The amount of wavefunction captured by each (approximately orthogonal) subspace is given as a probability P (see App. C.4). Included subspaces are $\mu\mu$, a pair of mesons of lowest energy, and $\kappa\bar{\kappa}^{(a,b)}$, a bubble made of a kink of type a and an antikink of type b (where 0 is the lowest-energy kink quasiparticle, and 1 is the next highest – see Fig. 4.7). 105
- 4.9 Entanglement entropy (base 2) for cuts (left-right bipartitions) of the spin chain as a function of time for the simulations (i) and (ii) of Fig. 4.5. Convergence with the bond dimension D slows as time goes on. For example, in (i) the max. cut entropy at $D \leq 128$ is very likely not converged after $t \approx 400$ 107
- 4.10 Peak maximum cut entropy during the first collision as a function of energy (ii) close to ($\lambda = 0.41$, $g = 0.98$, $h = 0.001$) and (iii) further from the TCI point ($\lambda = 0.3$, $g = 0.9$, $h = 0.0069$), with the energy controlled by the initial kink separation. The meson mass m_μ in lattice units is 0.43 for (ii) vs. 0.97 for (iii), while the vacuum correlation length ξ is 3.6 sites for (ii) and 1.8 sites for (iii), both indicating that (ii) is closer to criticality. The initial wavepacket width is $\sigma = 40$ for (ii) and $\sigma = 19$ for (iii). The kink velocity (lattice units) at the start of the first entropy jump (see Fig. 4.9) is also shown. Decreasing velocity with energy indicates the onset of Bloch oscillations. 108
- B.1 The convex hulls of the allowed points in the affine space (B.8) at derivative orders $\Lambda = 19, 27, 35, 43$. The red and black data points are the allowed points at derivative orders $\Lambda = 35, 43$ 146

- C.1 Error made ($1 - \langle \phi_j(B) | \phi_j(B(p)) \rangle$) in ignoring the momentum dependence of the tensor B used to construct MPS quasiparticle states, for both kink and meson excitations, for the Hamiltonian parameters used in simulations (i) and (ii) of the main text. The momentum-eigenstate freedom on $B(p)$ is fixed so that $\langle \phi_j(B) | \phi_k(B') \rangle = \delta_{jk}$. . . 155
- C.2 Estimated error (1 - infidelity per site) on momentum eigenstates $|\phi(B, p)\rangle$ for kink quasiparticles, due to the choice of orthogonality conditions on B used to achieve $\langle \phi_j(B) | \phi_k(B) \rangle = \delta_{jk}$. Here we compare the left and right orthogonality conditions, (C.14) and (C.16).158
- C.3 Spin expectation values of a kink position MPS $|\kappa_j\rangle$ for (i) the Ising model and (ii) close to the Tri-Critical-Ising (TCI) point. The bond dimension is $D = 8$ for the Ising data, and $D = 18$ for the TCI data. We plot the spins for various ways of fixing the momentum-eigenstate freedom: the left and right orthogonal conditions, (C.14) or (C.16), and the reflection-symmetric conditions (C.26), beginning from a B tensor optimized using either the left or right conditions (since this makes a small *physical* difference to the result – see App. C.3). . . . 161
- C.4 Single-kink wavepacket energy as a function of the width σ , for the \mathbb{Z}_2 -symmetric Ising model $g = 0.8, \lambda = 0, h = 0$ (in the SSB phase). We plot the energy (relative to the energy of the kink-quasiparticle momentum eigenstate) for two different ways of fixing the momentum-eigenstate freedom on the B tensors used to construct the wavepacket state: an orthogonal choice $\langle \kappa_j | \kappa_k \rangle = \delta_{jk}$ (left and right conditions are equivalent when $h = 0$) and the reflection-symmetrized choice (C.26). In both cases the MPS tensors used to construct the state are tuned to the wavepacket momentum $p = 0$. . . 162

- C.5 Portion of a single-kink wavepacket state outside of the single-kink subspace $\kappa^{(0)}$ as a function of the wavepacket width σ , for the \mathbb{Z}_2 -broken Ising model $g = 0.8$, $\lambda = 0$, $h = 0.007$. We plot the error for two different ways of fixing the momentum-eigenstate freedom on the B tensors used to construct the wavepacket: the left orthogonal choice $\langle \kappa_j | \kappa_k \rangle = \delta_{jk}$ and the reflection-symmetrized choice (with B *optimized* using the left orthogonal conditions). In both cases the MPS tensors used to construct the state are tuned to the wavepacket momentum, which is $p = 0$. The projection into the $\kappa^{(0)}$ subspace uses B tensors optimized using the left orthogonal conditions and fully accounts for momentum dependence via a Fourier analysis. . . . 163
- C.6 Portion of the evolved bubble wavefunction outside of the kink-antikink "sector" for simulation (i) of Fig. 4.5 ($\lambda = 0$, $g = 0.8$, $h = 0.007$) at time $t = 150$, as a function of the minimum separation $d_{\min} := \min(k - j)$ permitted in the two-quasiparticles basis states $|\kappa\bar{\kappa}_{j,k}^{(0,0)}\rangle$. Probabilities are computed via a Fourier analysis, taking into account the momentum-dependence of the basis states. The basis error due to interaction effects is estimated using (C.31). . . . 169
- C.7 Quasiparticle "sector" projection probabilities for simulation (ii) of Fig. 4.5 ($\lambda = 0.41$, $g = 0.98$, $h = 0.001$) at time $t = 270$, as a function of the minimum separation $d_{\min} := \min(k - j)$ permitted in the two-quasiparticles basis states $|\cdot\cdot_{j,k}\rangle$. Probabilities are computed via a Fourier analysis, taking into account the momentum-dependence of the basis states. The basis error due to interaction effects is estimated using (C.31). . . . 170
- C.8 Evolution of the energy expectation value and MPS truncation error for simulation (ii) of the main text. We compare different maximum bond dimensions D as well as different RK4 time-step sizes δt (for $D \leq 64$), observing that the effects of the time step are most noticeable in the energy drift, whereas the bond-dimension most obviously affects the truncation error at around the time of the first collision ($t \approx 150$). The $D \leq 128$ simulation is initialized from $D \leq 64$, $\delta t = 0.05$ at $t = 90$. The uptick in the energy drift at $t \approx 480$ is due to unconfined wavepackets hitting the boundaries of the simulation window. . . . 173

- C.9 Schmidt spectra for the maximum-entropy cut before and after the first collision in simulation (ii) of the main text. The bond dimension is 128. 174
- C.10 Evolution of spin and energy density expectation values and the cut entropy for parameter set (ii) of the main text ($\lambda = 0.41$, $g = 0.98$, $h = 0.001$), with three different initial states. State (a) is prepared by acting on the vacuum with a string operator $\prod_{j=x_L}^{x_R-1} X_j$, which flips the spins to form a bubble-like state with energy $E/m_\mu = 8.69$. State (b) is similar to (a), but with the ends of the string smeared out using Gaussian packets of width $\sigma = 40$, reducing the energy to $E/m_\mu = 4.02$. State (c) is the initial state discussed in the main text with $E/m_\mu = 2.62$, using quasiparticle wavepackets for the kinks and the false vacuum for the middle region. The evolution parameters are the same in all cases: The maximum bond dimension is 64 and the RK4 step size is 0.05. In (a), dramatic errors in the simulation occur at $t \approx 150$, indicating the difficulty of simulating these dynamics versus (b) and (c). In both (a) and (b), ballistic energy-spread emanating from the initial kinks indicates that they have complex quasiparticle content, resulting in immediate inelastic scattering. In contrast, the tuned quasiparticle kinks of (c) do not produce appreciable ballistic spread until the bubble walls have collided. 176
- C.11 Evolution of the energy expectation value and MPS truncation error for the simulations of Fig. C.10. Energy drift ($|1 - E(t)/E(0)|$) indicates deviation from unitary evolution and results from restriction to a maximum bond dimension of 64 as well as from numerical integration errors (RK4 step size 0.05). Truncation error (estimated as the maximum over cuts of the smallest Schmidt coefficient) results from the limited bond dimension and increases as entanglement is produced. 177
- C.12 Evolution of spin expectation values $\langle Z \rangle$ for a single kink in the \mathbb{Z}_2 -broken Ising model, with parameters $\lambda = 0$, $g = 0.4$, $h = 0.01$. The vacuum bond dimension is $D = 6$, allowed to evolve to a maximum $D \leq 32$. The RK4 time-step size was $\delta t = 0.01$ 178

- C.13 Evolution of the position and momentum expectation values of the wavefunction of Fig. C.12 after projection onto the single-kink position basis states $|\kappa_j\rangle$. For the Hamiltonian parameters in question (see Fig. C.12), the momentum dependence of the basis states is negligible, and could be ignored for the projection. 178
- C.14 Evolution of the kink velocity for the single-kink simulation of Fig. C.12. Here, the velocity is computed from the projection of the wavefunction into the $|\kappa_j\rangle$ position basis in two different ways: from finite-differences of the position expectation value and from the momentum expectation value, via the numerical dispersion relation $E(p)$. That there is a good match shows that the kink-quasiparticle ansatz successfully captures the confined quasiparticles present in the \mathbb{Z}_2 -broken Ising model. 179
- C.15 Momentum of the kink in simulation (i) of the main text (Ising), computed from the projected wavefunction in the $\kappa\bar{\kappa}^{(0,0)}$ basis. The bond dimension is 128. Since the $\kappa\bar{\kappa}^{(0,0)}$ basis does not accurately capture the state when the kink is very close to the antikink, this data is not complete during the collision ($t \approx 90$). The error bars indicate the standard deviation of the momentum distribution. 180
- C.16 Kink and antikink wavepacket velocity for the Ising model, simulation (i) of the main text, computed as the finite difference of the interpolated position of the 0-intercept of $\langle Z_j \rangle$. The bond dimension is 128. Note that the data is only likely to be accurate up to $t \approx 500$, as suggested by Fig. 4.9. The onset of the first collision is indicated by the dotted line, which is the time at which the maximum cut entropy begins to grow rapidly. 180

- C.17 Kink and antikink wavepacket velocity for simulation (ii), computed as the finite difference of the interpolated position of the 0-intercept of $\langle Z_j \rangle$. The bond dimension is 128. The interpretation of the 0-intercept as the position breaks down both during and, to some extent, after the collision: During the collision, the zero intercept disappears altogether as the kink and antikink merge and all spin expectation values are > 0 . After the collision, there are in this case (see Fig. 4.8) at least two different bubble "branches" of the wavefunction, both contributing to the spin expectation values. The onset of the first collision is indicated by the dotted line, which is the time at which the maximum cut entropy begins to grow rapidly. 181
- C.18 Cut entropy for kink-antikink collisions, in the absence of a longitudinal field, with initial kink momentum p and antikink momentum $-p$, for three different values of p . The Hamiltonian parameters are $g = 0.9$, $\lambda = 0.3$, $h = 0$, and the wavepacket width is $\sigma = 19.0$. The vacuum bond dimension is $D = 14$, with a limit $D \leq 64$ imposed during evolution. The integration time-step size was $\delta t = 0.05$ 182

LIST OF TABLES

<i>Number</i>	<i>Page</i>
3.1 Comparison of conformal bootstrap (CB) results with previous determinations from Monte Carlo (MC) simulations. We denote the leading rank-0, rank-1, rank-2, and rank-4 scalars by s, ϕ, t, t_4 , respectively. Bold uncertainties correspond to rigorous intervals from bootstrap bounds. Uncertainties marked with a * indicate that the value is estimated non-rigorously by sampling points.	63
3.2 Comparison of field theory results using various techniques: fixed-dimensional expansion in three dimensions ($d = 3$ exp), epsilon expansion (ε -exp) and high temperature expansion (HT). We denote the leading rank-0, rank-1, rank-2, and rank-4 scalars by s, ϕ, t, t_4 , respectively. Another estimate of Δ_t in the fixed-dimensional expansion can be found in [13] in terms of the crossover exponents $\phi_T = Y_2\nu$, with $Y_2 = 3 - \Delta_t$. We do not report it here because the errors depend on the value of ν used.	67
3.3 Four-point function configurations that give independent crossing equations under equating their s - and t -channels, along with whether even or odd spins ℓ^\pm appear for each irrep in each channel, and the number of crossing equations that each configuration yields.	72
B.1 Parameters used for the computations of the conformal bootstrap islands in section 3.4. The sets S_Λ are defined in (B.1).	141
B.2 Parameters used for the optimization computations in section 3.4. The set S_{35} is defined in (B.1).	141
B.3 Allowed points in the $\Lambda = 43$ island.	147
B.4 Disallowed points computed at $\Lambda = 43$	148
B.5 Allowed points in the $\Lambda = 43$ island used to obtain bounds on $\lambda_{\phi\phi_s}$, C_T , and C_J , along with the gaps above Δ_T and Δ_J that were assumed.	148

Chapter 1

INTRODUCTION: ASPECTS OF "CYBERPUNKIAN" QUANTUM FIELD THEORY

1.1 Space opera and Cyberpunk

Maybe a good way to start this thesis is through science fiction. Generically, there are many ways to classify science fiction stories¹. One example is through the contents. If a science fiction story is mainly talking about interstellar wars, outer-space civilizations, and spacetime traveling, it is usually called "space opera". If a science fiction story is mainly talking about the relationships among digital technologies, robots, and humans, it is called "cyberpunk"^{2,3}.

As one of the most important subgenres, space opera has a longer history. Currently, some people believe that it originally appeared in some American magazines in the 1920s. After people understand much better about our universe during and after the wars, space operas have been significantly developed, especially around the Cold War. On the other hand, cyberpunkian stories are relatively new. They have been widely created and discussed after people realize the potential of digital technologies, computer science, and the Internet. If I am allowed to choose two representatives for those two subgenres, I wish to choose the film series *Star Wars* by George Lucas for space opera, and the novel *Do Androids Dream of Electric Sheep?* by Philip Dick for cyberpunk⁴.

Science, a systematic and fundamental understanding of the nature, and science fiction, a fantastic imagination of how science and technology could change human society in the future, might be closely related to the development of human society itself. I firstly start to understand this when I read the lecture notes, *Nature and the Greeks* and *Science and Humanism* by Erwin Schrödinger [14], who partially expresses similar feelings from my understanding. During the Cold War, with the

¹The classification is in the non-academic sense. For a long time, science fiction novels are not recognized in the mainstream of literature.

²There are some other topics, for instance, Steampunk. Another more common way to classify science fiction is through *hard* or *soft* science fiction, referring to roughly speaking if the story is more scientific or more literary.

³Sometimes, cyberpunk describes an icy future world ruled by technology with a flavor of dystopia. However, we hope to use a broader definition of cyberpunk, that in the possible future, humanity will coexist in harmony with high technology.

⁴The film version of it, directed by Ridley Scott in 1982, is the celebrated *Blade Runner*.

fierce competition between the United States and the Soviet Union, mankind made tremendous progress in the field of science and technology. The possible nuclear war promoted great development of nuclear physics. Related basic sciences, such as particle physics and collider physics, made great strides. We have established the Standard Model of particle physics. At the same time, humans are trying to develop space science in response to possible space races. During this time, the understanding of general relativity and black hole physics are also significantly improved. People discovered the laws of black hole thermodynamics and the existence of Hawking radiation. Later, the thirst for unified theory prompted people to construct string theory. In the field of science fiction, people create a variety of space operas, acclaiming their own fantasy about the future. In those fantasy stories, people conquered the stars, battles broke out on the back of the moon, and restaurants were opened at the end of the universe. The dolphins left the earth and told humans, bye, thank you for your fish⁵. I don't know if all those stories are really logically connected, but in practice, they happened at a similar time.

However, after the end of the Cold War, human history has undergone some changes. If you ask college students today what kind of STEM majors earn the most income, I believe a considerable number of people will answer, computer science or electronic engineering (see [15]). With the development of Internet technology, the world is increasingly developing towards the predictions of cyberpunk novels. In 2021 today, the extensive application of statistical learning theory, optimization theory, and machine learning technology can make computer face recognition possible. People indulge in the new capital world built by Facebook, Youtube, Amazon, and Tiktok. Some people are beginning to worry about whether widely used information technology will affect people's privacy and freedom within certain limits (see [16]).

At a similar time, physics associated with computers has been fully developed. Technically, computer programs have revolutionized the research methods of a large number of physicists. If the *Mathematica* program has a particularly serious problem at some point, I believe that a considerable number of high-energy theoretical physics papers will go wrong. With regard to the direction of computational physics, some physicists still use lattice gauge theory to accurately calculate the phenomena of strongly coupled physics, as suggested by Wilson, Feynman, and many other people. Physics related to strong correlation and complexity, such as condensed matter physics, cold atom physics, etc., has made great progress. At present, quite

⁵This is from *Hitchhiker's Guide to the Galaxy* by Douglas Adams.

a lot of this type of research is motivated by so-called quantum computing. This is a possible next-generation computing technology that utilizes the fundamental principles of quantum mechanics. Conceptually, computing technology is as inseparable as physics, because the principles of physics stipulate the limits of computing technology occurring in this world. In recent years, people have also tried to discuss the application of information theory towards physics itself, such as quantum simulation and black hole information, to be discussed later. In the world of science fiction stories, from the ancient *Blade Runner* to the recent *Ready Player One*, cyberpunkian masterpieces are constantly emerging, and gradually constitute one of the most important subgenres in the field of science fiction.

As a graduate student in physics rather than a sociologist, I can only state some of the facts I have observed, and I cannot assert the logical connection between social development, science fiction genre, and physics research. At the same time, as a theoretical physicist, my job is to try to understand the laws of nature and the universe. A natural question is, what can the emerging information technology bring to the development of current theoretical physics? How to use the huge power of computer science, statistical science, and complexity science based on academic, industrial and capital interaction, to promote the development of basic physics, and create a new science belonging to our cyberpunkian era?

Here, I wish to propose a research direction I am currently working on. I call it *Cyberpunkian Quantum Field Theory*⁶.

I am a big fan of quantum field theory itself, which for me, and for many other people, is synonymous with fundamental physics. Quantum field theory, as a basic paradigm, could describe almost everything that appears in physics books: particle scattering, gravity, black hole (at long distance), string theory, condensed-matter, and the early universe. If physicists finally get to know the Theory of Everything, I believe a significant portion of it is based on quantum field theory. For me, quantum field theory is like a space opera. It describes a large number of unsolved secrets of the universe we live in. In quantum field theory, or in basic physics, you can see planets collide, particles scatter, and see the formation of black holes and the origin of the universe. In the world of theoretical physics, there are a lot of unknown parts waiting for us to explore.

⁶I am following one of my school sisters, Nicole Yunger Halpern, who used to be one of the core members in John Preskill's quantum information group. She created a word, *Quantum Steampunk*, for the field called *quantum thermodynamics* she contributed [17].

When I use the term *cyberpunk*, I want to distinguish it from common vocabulary, the so-called *computational physics*. Beyond traditional terminology, I hope to emphasize that cyberpunk quantum field theory can be based on the following two aspects. First, cyberpunkian science prefers to use information theory and technology that are cutting-edge and even under development, for instance, machine learning, optimization problems, applied mathematics and statistics, and quantum computing. Secondly, I hope that cyberpunkian physics is not only practical, but also theoretically helpful to physics itself, or even vice versa. Just as superstring theory expert Edward Witten does for the mathematical community, we could also use physics theory to guide possible computer science discoveries.

In the following discussion, I hope to describe the possible prospects of this science. Of course, technically, these stories are already happening. The Large Hadron Collider (LHC) operating in Europe is constantly using machine learning algorithms to process data on particle collisions. Dark matter detection satellites operating in the sky will also cooperate with companies in industry to deal with scientific issues of interest (see for instance [18]). However, as a theoretical physicist, I hope that in the future, people will be able to do more in-depth research on theoretical physics issues related to cutting-edge information technology. At least, I think this forms part of physical science in our generation.

In the following discussion, I will use the following three simple examples to demonstrate that cyberpunkian quantum field theory may become an important and effective science. It includes quantum simulation of quantum field theory, large-scale optimization of conformal field theory, and discussion of the relationship between quantum field theory landscape and big data science. I will also do a simple non-technical discussion of quantum field theory, and a simple outlook on this related issue, including black hole thought experiment and quantum information science, *It from qubit* and *the non-perturbative bootstrap*, Church-Turing Thesis, Computer Science(CS)-inspired physics and physics-inspired CS, possible future of classical and quantum technology, and finally, companies and colliders.

As a science fiction lover, I often think about such problems. What will the science I do look like in two hundred or one thousand years? Will it still be meaningful? From scholasticism to modern science, we take nearly three hundred years. The popularity of the internet is what happened in the past three decades. What will the world look like in two thousand years? Will the banking industry be completely changed by quantum computing? Will humans make a collider as big as the Milky

Way? Will the military use Higgs particles as weapons?

Writing this thesis, in a sense, is to express my sincere respect for some great scientists. Lev Landau, Enrico Fermi, Richard Feynman, Steven Weinberg, Ken Wilson, Chen-Ning Yang, Steven Hawking, Edward Witten, Alexander Zamolodchikov, etc., and nowadays in our quantum era, Alexei Kitaev and John Preskill. They established the deepest human understanding of the universe during those prosperous years, and defines the science of our time. I think that the current status of physics has given me some opportunities for fledgling young people. To me, traditional physicists are like hackers. They discovered the secrets of this world through various means. Cyberpunkian physicists seem to try to build a completely new, Turing-complete world. For me, they are all important sciences. Maybe one day, when people can find a variety of new particles on the collider, reach the boundary of the black hole horizon, or freely edit topological quantum qubits, some of them will think that, what we are doing currently, are treasures.

1.2 Quantum field theory

In order to discuss cyberpunkian quantum field theory, I will first introduce what quantum field theory is. Here I will provide a non-technical introduction to quantum field theory.

So what is quantum field theory? A possible generic description is that it is a quantum formulation of continuum physics in the spacetime. Consider that we have complicated interactions among some atoms and molecules placed discretely in the spacetime. There are physical laws governing the forces, for instance, the Van der Waals force. However, if we feel it is too complicated to keep track of interactions of all particles, we could zoom out and ask what the *emergent* description is when we are looking at a length scale that is much larger than the lattice spacing. Sometimes we are able to arrive at a beautiful emergent description, for instance, if those molecules form a liquid, which is called hydrodynamics. In this case, hydrodynamics is a *field theory*. When the full procedure is treated quantumly, for instance, if we are considering some interacting quantum harmonic oscillators, the description is called quantum field theory, where we are assuming that there are an infinite number of quantum harmonic oscillators located in a continuum spacetime.

A deep interpretation between the lattice model and the quantum field theory description is given by Ken Wilson, and the above process is called renormalization. People find that the renormalization process occurs in almost all phenomena in

our nature: statistical physics, string theory, gravity, particle scattering, etc.. In a sense, all physical theories should look like quantum field theory in a certain limit. Quantum field theory is, in fact, one of the deepest understandings human beings have obtained about our nature.

There are many possible quantum field theories that describe different phenomena in our world. One basic method of classifying quantum field theories is based on the strength of couplings: weakly-coupled quantum field theory, strongly-coupled quantum field theory, and somewhere in the middle. Non-technically speaking, strongly-coupled theory means that interactions among different local degrees of freedom in the spacetime are strong. Imagine that we are starting from a free theory, which means no interaction. The theory could be described easily by quantum harmonic oscillators located on each site. Then we start to turn on the interaction in some way, where those small harmonic oscillators start to couple with each other or with itself in some non-trivial ways. When the extra coupling we have added is small enough, we could use perturbation theory to solve the system, given the fact that we already know the free theory data pretty well. When the coupling is strong, the usual perturbation theory breaks down, and it is not very easy to describe such physics in the continuum spacetime description. Now let us imagine that we turn on the coupling towards some extremely strong regime, then something funny will happen. For instance, the perturbation on one side of the system could quickly propagate towards the other side. This is somewhat similar to the *critical point* of a phase transition, where the system is changing from one phase, for instance, the solid state, towards the other phase, for instance, the liquid state. For a second-order phase transition, where non-technically speaking, some physical variables transform continuously around the critical point, one could use strongly-coupled quantum field theory to describe it. Generically, it is called *conformal field theory*.

The above procedure during increasing interactions, could be described by the theory of *renormalization group*. For a weakly-coupled theory, we have some generic frameworks to describe it based on perturbative expansions. We have some physical interpretations for terms appearing in the expansion, which is called the *Feynman diagram*. For a generic theory where the coupling is strong enough, it is usually very hard to describe if the theory is very general. Some physicists invent smart ways to solve the theory in some special cases. For instance, when the theory has conformal symmetry, which is roughly speaking, scale invariance besides the usual spacetime Lorentz symmetry, we could use the symmetry, and

some other internal constraints to partially, or even completely, solve the theory [19]. One could try some other similar strategies when the theory is integrable, namely, when it contains infinite number of conserved charges [20]. When the theory is supersymmetric, sometimes one could do perturbative expansions easier because in this case the Feynman diagrams might have some cancellations and maybe one could use it to solve part of non-perturbative physics. Some other methods, for instance, the duality between weakly-coupled gravitational theories and strongly-coupled quantum field theories without gravity, which is called *holography* or the AdS/CFT (Anti-de Sitter Space/Conformal Field Theory) correspondence (we will mention it later) [21], might shed light on solving strongly-coupled quantum field theories. All of them are still active research directions in theoretical physics.

However, people still don't have a very good understanding of strongly-coupled quantum field theory in general. For instance, the strongly coupled regime of quantum chromodynamics(QCD) is still not clearly understood, even if we have the above theoretical methods at hand. One could measure several properties of strongly-coupled QCD in some low energy colliders, and it is extremely hard to predict some bound states using theoretical calculations from quantum field theories. The Yang-Mills existence and mass gap problem defined as one of the Millennium Prize Problems is also about field theories beyond the weakly-coupled regime, and it is still an open problem even without a very precise mathematical definition. The high-temperature superconductivity phenomenon might also admit a low energy effective field theory description around the critical point of their phase diagrams, but it is still far from a very concise formulation and a reasonable prediction. I probably could list many problems of this type, involving theoretical understandings and phenomenological predictions of quantum field theories. All of them are closely related to the universe we live in, and all of them seem challenging. Maybe for some people, it is fair to say that we still don't understand quantum field theories, although it is already at least half a century after its birth.

Another particularly important example is string theory, which is a candidate for a consistent theory that could describe everything appearing in this world, from quantum black holes, big bang physics, to subatomic, atomic, and molecular physics. String theory itself could be formulated in a quantum field theory manner. In particular, quantum black holes could also be understood as a specific strongly-coupled quantum field theory phenomenon. If we address the weakly-coupled limit, one could compute graviton exchange in a semiclassical fashion of quantum field

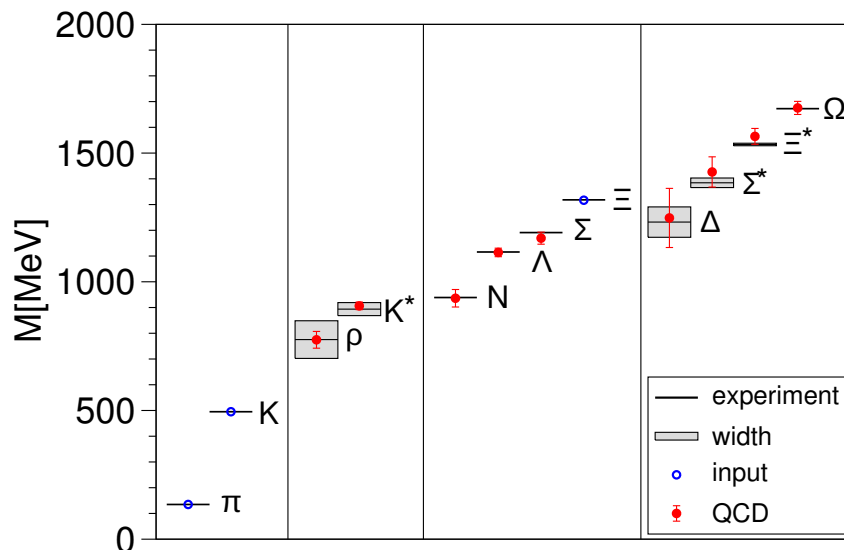


Figure 1.1: A remarkable prediction from the lattice gauge theory community. Some light hadrons have been predicted using lattice QCD. This is from Figure 3 of [1].

theory in the curved spacetime, which is called gravitational waves.

Okay, so some people may say that if pure theoretical methods fail, why we don't try numerics? This is a very fair statement, and yes, we have already tried. Ken Wilson and other people suggest that maybe we could solve strongly-coupled quantum field theories by making a lattice regularization. That is, trying to discretize your space in a lattice. One could try to solve the theory in the lattice, and take some reasonable limits towards the continuum. For gauge theories used in particle physics, this subject is usually called the *lattice gauge theory*.

Nowadays, the idea about regularizing field theories in a lattice has made significant progress. In Figure 1.1, where I am quoting Figure 3 of [1], people could match some experimental observations about the light hadron spectrum with QCD by a first-principle calculation. It agrees very well! This type of agreement could not only show powerful predictability of quantum field theories but also show the fact that nature is a good computer!

However, despite its glorious success, there are several fundamental limitations to the current algorithms. The main problem is that, in principle, quantum field theory contains an infinite large Hilbert space on each site located in the spacetime. This demands a huge amount of computational resources! Here, I am claiming that, in order to solve more important problems, we have to be smarter: the numerical

challenge we face on simulating and predicting quantum field theories forces us to use the most cutting-edge methods from information technology, while some novel, fundamental understanding of quantum field theories and fundamental physics themselves will come from computer science, classical or quantum. This is the place where cyberpunkian physicists should go.

In the following discussions, I will mainly describe three cyberpunkian research directions I have worked on: simulating quantum field theories using quantum devices, conformal field theory and large-scale optimization, and string theory versus data science. Later, I will discuss some general comments about fundamental physics and information technology.

1.3 Simulating quantum field theory using quantum devices

Going back to the story of lattice gauge theory, here I am pointing out some difficulties in solving quantum field theories by putting them in a lattice only with a classical computer and brute force methods.

The first problem is the computational power. Lattice quantum field theory has a very large Hilbert space. In principle, we have a continuum number of sites located in the spacetime, while each site has an infinite Hilbert space dimension. By truncating the local Hilbert space and choosing a cutoff for lattice spacing, we are able to solve the theory in a finite, but large, Hilbert space dimension, with proper treatment of an extrapolation of numerical results towards the continuum. This is a very high computational cost. Firstly, it is extremely hard to do it naively using the way of exact diagonalization, namely, diagonalize a large Hamiltonian directly. Secondly, one could try to measure some correlation functions using random algorithms, for instance, some versions of Monte Carlo methods. This is usually cheaper than exact diagonalization, but it is still hard to operate due to a large number of sites and a large number of configurations to sample. The second problem is the sign problem. For fermionic theories, when we compute some predictions using Monte Carlo method by doing some samplings of path integrals, we will often encounter oscillating amplitudes, making the result hard to converge. Those problems have challenged the current lattice gauge theory community for a long time, and people find that it is extremely hard to make predictions, for instance, for real-time physics.

Thus, in order to solve quantum field theory in general, especially for strongly-coupled theory in a lattice, one might consider some potential future computational devices. One could imagine that the computation could be done in a quantum

computer, which could simulate physical process of quantum field theory itself. I find that many quantum computing people like to quote what Richard Feynman said in his paper [22], and I am happy to quote it again:

... trying to find a computer simulation of physics, seem to me to be an excellent program to follow out... and if you want to make a simulation of nature, you'd better make it quantum mechanical, and by golly it's a wonderful problem, because it doesn't look so easy.

Richard Feynman is, at least partially, a particle theorist. In fact, as indicated from his paper [22], it seems that one of the earliest motivations for quantum computing is to simulate quantum field theories. (See a review article given by John Preskill [23].)

Nowadays, in 2021, quantum computing becomes one of the most exciting scientific areas, receiving significant attention from academia, industry, government, and the whole society. John Preskill [24] announced that nowadays we are living in a quantum era which is called NISQ (Noisy Intermediate-Scale Quantum), where a quantum computer with 50-100 qubits may be able to perform tasks that exceed the capabilities of today's classical digital computers, but the noise of quantum gates will limit the size of quantum circuits that can be reliably executed. In fact, Google already claims that they have achieved quantum supremacy, that is, quantum computers can accomplish tasks that classical computers cannot [25]. For simulating quantum field theories themselves, quantum computing methods could provide certain advantages against two main problems I have mentioned before for simulating quantum field theory in a classical computer. Firstly, quantum computing is proceeded by quantum states made by qubits, and unitary evolution made by unitary operators acting on the Hilbert space. Roughly speaking, the space it contains, is naturally, exponentially large than classical computation. Secondly, quantum computing is able to solve the sign problem naturally [26], which might potentially remove the sign problem difficulty appearing in the fermionic quantum Monte Carlo simulation.

One early remarkable quantum algorithm to simulate quantum field theories is called the Jordan-Lee-Preskill algorithm (see the original papers [27, 28], and a series of related papers [29, 30]). This type of algorithm contains state preparation, time evolution, and measurement of some specific quantum field theory tasks happening at strong coupling. One could also associate the above algorithm into some certain

complexity classes [30]. This algorithm, especially the time evolution of the quantum field theory Hamiltonian, is shown to be polynomial in system size, sharpening the potential quantum advantage for simulating quantum field theories in quantum computers.

In the above framework, simulating quantum field theories could be generally regarded as simulating some specific Hamiltonians. Thus, it is natural to utilize methods from general Hamiltonian simulations developed by the quantum algorithm community. When simulating a quantum Hamiltonian, one could roughly classify quantum simulation algorithms in the following three types: digital, analog, and variational quantum simulation. The above Jordan-Lee-Preskill algorithm is a typical algorithm for digital simulation, where we assume a possible universal quantum computer when we are constructing the algorithm. For analog simulation, the algorithm is developed by constructing an actual Hamiltonian in the cold-atomic lab, for instance, the Hamiltonian made by Rydberg atoms. Variational algorithms are somehow in the middle: it will make use of variational methods, only covering a subset of the whole Hilbert space. Variational algorithms might be constructed in a hybrid quantum-classical way, which is made suitable for near-term quantum devices. All of them are potentially useful for simulating quantum field theories.

When constructing quantum simulation algorithms or actually doing simulations in a quantum computer or in the lab, classical simulation might play an important and specific role. Firstly, quantum-classical hybrid algorithms are widely used. Especially in the near-term, quantum algorithms are only helpful to speed up calculations in certain steps in a whole classical algorithm. Those classical pieces may not be replaceable. Secondly, classical algorithms might be helpful to find limitations of classical computations, and understand conceptually and technically where quantum algorithms might play a role. Here I wish to mention specifically two types of algorithms: matrix product state (MPS) algorithms and semidefinite programming (SDP) algorithms. Of course, both of those algorithms have very wide applications that are even beyond the scope of physics. MPS algorithms are helpful for identifying some low energy states of quantum many-body systems in the 1+1 dimension, which could have emergent field theory behaviors around critical points. SDP algorithms are basics of convex programming that are widely used in operations research and optimization, which are also basic algorithms for solving higher-dimensional conformal field theories numerically (we will describe this in more detail in the next section). Both of them are important classical algorithms. It

is important to understand their advantages and limitations comparing to quantum computation, where quantum field theories are perfect playgrounds to test them.

I also wish to mention here part of my own contributions. With one of my advisors, John Preskill, I have been exploring quantum simulation of domain wall scattering in 1+1 dimensional quantum field theories. Domain walls, or kinks, in the 1+1 dimensional scalar field theories, are the simplest examples of topological defects. They are like walls splitting two different field configurations in the theory. The existence of domain walls is closely related to vacuum decay in cosmology, sharpening its relevance to the real world. Historically, there are many authors who studied kinks in quantum field theories at weak or strong coupling (for instance, [31, 32]), but strongly-coupled kinks are extremely hard to solve at strong-coupling for non-integrable, 1+1 dimensional quantum field theories. In the work with John Preskill and Burak Şahinoğlu, we are trying to construct theoretical algorithms to simulate scattering process of kinks, while in the work with Ashley Milsted, John Preskill and Guifre Vidal, we are trying to study analog models in spin chains and simulate the kink scattering process in the MPS approximation [2, 3]. (see Figure 1.2 for an artistic illustration. The work [3] is presented in Chapter 4 of the thesis)

Simulating quantum field theories are generically helpful for studying quantum field theories appearing in the formal high energy theory community, for instance, theories with supersymmetry, in higher dimensions or containing gravitational sectors. One possible ambitious goal might be studying large- N supersymmetric gauge theory and trying to verify Maldacena's conjecture about the AdS/CFT correspondence [21]. It might also be helpful for studying high energy phenomenology, experiments or observations, for instance, solving QCD in the strongly-coupled regime. Those studies might also benefit the community of quantum algorithms, which will provide novel, clear tasks, cool applications, and good targets for benchmarks. Finally, it might be helpful for conceptual understanding of quantum simulation in our physical world, namely, the Church-Turing Thesis. We will discuss those issues later.

1.4 Conformal field theory and large-scale optimization

In this section, we will move to another topic that is more related to classical computation instead of quantum. That is, conformal bootstrap and its relation to large-scale optimization.

We discuss before the concept conformal field theory, which appears in some statistical models as a low energy effective description around the second-order phase



Figure 1.2: An artist's creation of the quantum simulation projects of kink scattering [2, 3]. The depiction of characters is based entirely on their images in reality. From left to right: Burak Şahinoğlu, Ashley Misltd, Junyu Liu, John Preskill, and Guifre Vidal. Other ingredients include cosmic bubbles (physical objects that are similar to kinks), a spacecraft, a cat (Schrödinger's cat), and the Bell state. The figure is credited to Jinglin Nicole Gao. Figures shown in the screen utilize the figures in our scientific paper [3].

transition. Around the critical point of some statistical models, partially because of the scale invariance, the spacetime symmetry of the theory has been extended from the usual rotational or Lorentzian symmetry towards a larger symmetry: conformal symmetry⁷. Such a theory might be a little counter-intuitive: one could make a transformation from the far infinity to the origin of the coordinate system, and the action of the theory is still invariant. Thus, conformal field theories are used to describe violent behaviors around the critical point, which experiences a drastic change between different two phases. The behavior is *universal*, which means that multiple microscopic models might correspond to the same conformal field theory. The low energy spectra of conformal field theories will provide some universal numbers that are measurable in the statistical system, which are called critical exponents. Thus, multiple microscopic models might share the same critical exponents. One standard example is that the phase transition of the boiling water shares the same

⁷Although there are still some technical differences between scale invariance and conformal invariance.

universality class with the 3d Ising model, a model made by physicists to describe the dynamics of magnets. Because of universality, conformal field theory is a very generic concept that could be applied in many places that admit second-order phase transitions. Moreover, conformal field theory technologies are directly applicable to string theories, since the worldsheet theory of string theories is conformally invariant.

Non-trivial conformal field theories are typical strongly-coupled quantum field theories, making them very hard to solve. However, conformal invariance strongly constrains the behaviors of the theory. For instance, some correlation functions are directly constrained as some specific forms. Some people believe that conformal field theories, and some other strongly-coupled field theories, are fragile in the following sense. These theories are like precise gears: as long as few conditions are input, the strong limitation of conformal symmetry will isolate or even uniquely determine these theories. This philosophy of understanding quantum field theory is called bootstrap, a possible way of understanding strong coupling without really quantize those theories from classical actions.

The bootstrap philosophy in particle physics is studied widely in some certain time scales around the last century (for instance, [33, 34]), but quickly decays with many open problems unsolved, replaced by related studies about QCD. However, recently, the idea of bootstrap in field theories has returned to be a hot topic in the high energy physics community, since we become more cyberpunkian. People notice that one could solve bootstrap equations, the consistency equations appearing in strongly-coupled quantum field theories, by optimization technics. For instance, bootstrap equations in conformal field theories are identities where a sum over contributions from different sectors of the theory is equal to zero, which looks like a hyperplane in some higher dimensional Euclidean spaces. Roughly speaking, the hyperplane could be located by finding some other optimal hyperplanes cutting the space towards small pieces, while the methods for finding optimal planes are standard in optimization and operations research: the semidefinite programming (SDP). The modern technologies of computer science allow people to work on optimization problems numerically at large scale, making numerical bootstrap possible (see a summary by [19, 35]). In fact, conformal bootstrap holds the world record for solving the most digests of the Holy Grail problem in statistical physics: determining the critical exponents for the 3d Ising model [36]. Considering the fact that the 3d Ising model shares the same critical exponents with the boiling water, and that water is

the basic substance of life, we can even use those bootstrap results about the critical exponents to communicate with outer space: If an extraterrestrial life responds to the critical exponents we sent about boiling water, we might think that the alien has a high level of civilization because they can use conformal field theory and large-scale optimization to accurately calculate the critical exponents. Furthermore, numerical bootstrap using large-scale optimization inspires a flow of theoretical research about conformal field theory (see, for instance, [37]), which are helpful for other parts of theoretical physics like string theory.

The study of the conformal bootstrap is also helpful for experiments since quantities like critical exponents are universal and measurable in principle. Historically, there is an interesting experiment happening at the Space Shuttle Columbia measuring the critical exponents of superfluid helium phase transition. The experiment is claimed to be the most accurate measurement of critical exponents in human history up to now⁸. However, the experimental results from the measurement are inconsistent with the theoretical Monte Carlo simulation by 8σ . Recently, a collaboration in the conformal bootstrap community, including me, successfully verifies the theoretical result and significantly improves the accuracy of Monte Carlo simulation. Although the explanation of the inconsistency between theory and experiment is still unknown, this work shows that the conformal bootstrap method is useful for predicting important real-world physics. (See the papers [4] and [5], and an artistic description of the collaboration 1.3.) In fact, further investigations by us in [38] show that the three-dimensional Heisenberg magnets are unstable against cubic anisotropy by investigating the conformal $O(3)$ model, and we expect that there is an ocean of real-world problems where the conformal bootstrap method is able to solve (the work [38] is presented in Chapter 3 of the thesis).

Of course, solving conformal field theories using the bootstrap philosophy is closely related to cyberpunkian physics, where large-scale optimization method associated with hardcore cluster computation plays a crucial role. Nowadays, conformal bootstrap becomes one of the most important mainstream in the area of theoretical physics, which has wide potential applications among string theory, condensed matter physics, and particle physics. In the algorithm level, Simons Foundation launches a collaboration, *the non-perturbative bootstrap*, to support our research, and we have a professional soft engineer, Walter Landry, helping us make the best software for solving SDPs for our physical purpose. Although we believe that we

⁸The measurement is happening in a space shuttle because the measurement involves the heat capacity at constant pressure, which requires a zero-gravity environment to mitigate the error.



Figure 1.3: An artist’s creation about the superfluid helium conformal bootstrap project [4] and [5]. The depiction of characters is based entirely on their images in reality. From left to right: Shai Chester, David Meltzer, Junyu Liu, Walter Landry, Alessandro Vichi, David Poland, David Simmons-Duffin, and Ning Su. Other ingredients include islands (a theoretical physics terminology referring to the isolated region in the theoretical space using the bootstrap method), a spacecraft (referring to the Space Shuttle Columbia experiment), a diagram as stars in the sky (referring to the conformal block expansion, the basics of the bootstrap equation in the conformal field theory). The figure is credited to Jinglin Nicole Gao.

are currently using the most cutting-edge optimization results from the operations research community [39], the current algorithms still have an opportunity for potential significant improvement. We also wish to mention that SDP is an extremely useful algorithm that admits a large quantum speedup. Thus, conformal bootstrap might potentially provide clear physical applications for the quantum SDP solver, and will be helpful for benchmarking quantum algorithms and devices [40].

1.5 The theoretical landscape and data science

In this section, I wish to comment on the landscape of quantum field theories and its relation to data science.

Quantum field theory (or the whole fundamental theoretical physics), at least for many people, including me, is an extremely difficult subject. Theorists have constructed a large number of quantum field theories, which describe some general phenomena in this world or a certain universe. Some theories live in high dimen-

sions or some highly-curved spacetime that humans cannot easily understand. The various counter-intuitive phenomena appearing in the strongly-coupled theory make it more difficult for physicists to control. Some quantum field theories cannot even be precisely defined mathematically. Moreover, quantum field theory can have many parameters and many possible descriptions, which may lead to the same or different predictions. I think, at least for me, many problems cannot be thoroughly studied in my whole life. If I am supposed to give a name for the space of quantum field theories, I will call it the *landscape*, a common term used by high energy physicists.

Another difficulty of quantum field theory lies in its experimental difficulty. Probably the best way to verify quantum field theory in the subatomic world is various high-energy physics experiments, especially collider experiments. Experimental results from colliders could verify or expand predictions from some quantum field theories by colliding subatomic particles at some certain energies. This is an extremely complicated process. From the various nuclear resonance states of the low energy collider to the hadron jet on the hadron collider, physics involved in those processes is very difficult to calculate and measure. This often requires a huge amount of engineering and the efforts of countless researchers to achieve.

Perhaps physicists should thank themselves for being in this cyberpunk era. The famous hadron collider, LHC, generates a lot of data every day. A considerable part of the data will be processed by professional data scientists or particle physicists. Therefore, big data science is an important means of contemporary particle physics research. For example, machine learning is becoming an important means of processing experimental data of particle physics. In terms of phenomenological theories that are closer to experimental observations, data science has also gradually become an important way to explore the predictions brought by different effective field theories and Wilson parameters, or to simulate experimental data to reconstruct particle resonance states. I here cite two related works on experiment and phenomenology [41, 42]. Interested readers can easily find more works on the Internet.

Here, I prefer to discuss a story that is mainly about formal high energy theory. Perhaps the most sophisticated networks of quantum field theories are constructed by string theorists. String theory itself could also be understood as a paradigm adapting numerous quantum field theory descriptions. One way to quantify the complexity of string theory is to count its vacua. In some simplest quantum mechanical models, we are familiar with, for instance, hydrogen atoms with Coulomb's force, the degeneracy

of the vacuum states is usually very few. However, there is potentially a very large amount of vacuum degeneracy in string theory. There are so many choices of microscopic theory, compactification manifold, bundle or brane configuration, flux, etc. Some people believe that the total number of string theory vacua might be finite, and the estimate is usually huge numbers, for instance, 10^{500} (see some early papers, [43–45]).

The gigantic possible choices of string theory vacua seem leading to many different possibilities of physical predictions, for instance, different realizations of effective field theories at low energies, and different possibilities of constants appearing in our universe, for instance, the mass of the electron. The physical interpretation of the string theory landscape and its possible relationship with some *illegal theories* which could not correspond to any realizations of quantum gravity, are still open problems. People call those the collection of illegal theories the *swampland*.

The study of string theory landscape and the swampland is a very difficult subject, partially due to the complexity of string theory itself. If we assume that string theory is the Theory of Everything, can it lead to a consistent description of our world and our energy scales, for instance, the standard model? If so, how is it located in the string theory landscape?

Currently, many people are very interested in the so-called *swampland program*. This is a research direction that is aiming to possible interpretations of the boundary between the landscape and the swampland (which is called the *swampland criterion*). In fact, the space of the swampland is also very large and nontrivial. There are many low energy effective actions that may not be allowed by any formulations of string theories, and it is very important to understand why. Currently, people formulate a large web of conjectures and statements about the landscape and swampland and try to test them by explicit examples, physical or mathematical proofs. (see Figure 1.4). One of the most important statements among so many swampland conjectures is called the *weak gravity conjecture*. The statement is that for theories in the landscape allowing gauge symmetry, they have to allow quantum states that are sufficiently charged. Roughly speaking, that is to say, gravity is always weak compared to the electromagnetic force. This could serve as a swampland criterion. In the work [46], with Clifford Cheung and Grant Remmen, we prove this statement for a very generic setup of gravitational theories containing charges. We show that the weak gravity conjecture naturally follows from the saddle point analysis of black hole solutions in the gravitational path integral, which could be partially understood as

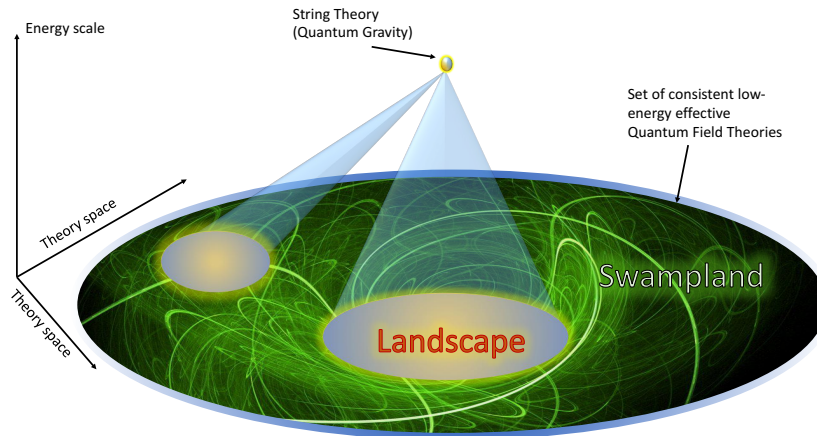


Figure 1.4: An illustration of the string theory landscape and the swampland. This is from Figure 1 of [6].

an infrared consistency requirement of the low energy effective description of string theory (The work [46] is presented in Chapter 2 of the thesis).

Despite some partial theoretical success, the landscape is still extremely hard to study. Even if we could formulate conjectures, it is very hard to test them among 10^{500} different vacua. In fact, this huge number is larger than the number of atoms in the whole visible universe. So can we finally study them towards the bottom, and finally find a successful explanation of our universe?

My personal view is that maybe currently some of us could also stick on pure theoretical research, but eventually, maybe we have to rely on cyberpunkian technologies to find the final answer. The data space is too large, but in an optimistic point of view, I think using data science like technics about machine learning, it is not hopeless to find the answer accurately. Let me give an example of Go. We could roughly count its complexity as the following: notice that the standard Go board has 361 points, so we could have an estimate of possible methods for placing black and white stones as $361! \sim 10^{678}$, which is also a very large number. However, machine learning algorithms could still handle Go right now, and we all remember the famous event in 2016, where the computer program AlphaGo beats the best human player Lee Sedol. Maybe one day, we could use machines to resolve all puzzles in quantum field theory and string theory. One could regard all theoretical efforts we have made now as training data, and currently, we are still mostly trying to produce valuable training data. Eventually, we might need a machine to resolve the puzzle of our universe. I think maybe machines are good at questions of the following type: Can

we predict the probability of obtaining a Standard Model gauge group at low energy inside the string landscape?

In fact, there are already some works about machine learning and string theory. Some of the early comments about string theory landscape and computational complexity are made by Michael Douglas, one of the founders of the concept *string theory landscape* (see [47–49]). I used to think about a related problem if one could use neural networks to predict random inflationary potentials induced by string landscape in the early universe cosmology when I was an undergrad student in 2014, and write a paper in 2017 [50]. Nowadays, some string theorists and data scientists are now actively initialization collaborations and obtain good results to explore the string theory landscape using cyberpunkian tools (see for instance [51–53]). I feel that it will be great where people might potentially gain great insight inside the landscape from those fancy machines.

1.6 Some comments

Finally, we will arrive at some comments about physics and computer science.

Some physics

Black hole thought experiment and quantum information science

There is a particularly interesting direction appearing recently addressing the connection between quantum black holes, spacetime and quantum information science in the high energy physics community. Here, we will review some recent developments in this direction, and address its connection with cyberpunkian quantum field theory.

After Hawking discovered the area law formula and information paradox of black holes [54, 55], understanding quantum information content in the quantum black hole and its radiation process becomes a Holy Grail of theoretical physicists. Partially based on the observation of Hawking, the work of Juan Maldacena in 1997 [21] and other related works formulate a greater picture that connects a higher-dimensional quantum gravitational theory and a lower-dimensional quantum field theory living in the boundary of the spacetime. This proposal, which we call *holography* or AdS/CFT, has some explicit realizations in string theory and becomes a compelling paradigm for a theory of quantum gravity. In 2006, Ryu and Takayanagi proposed a formula that connects quantum entanglement in the boundary theory towards the extremal surface in the quantum gravitational system [56]. Further connections

include the following: the nature of the Ryu-Takayanagi formula could be understood in the language of quantum error correction [57]; quantum black holes could quickly scramble the information and recovery of black hole information from the Hawking radiation could be interpreted from the quantum Shannon theory [58]; the quantum complexity of quantum states could be understood from the gravitational action or spacetime volume in some circumstances [59]; and many other amazing discoveries.

Recent activities in the theoretical physics community about the connection between quantum information theory and quantum spacetime has a slogan, *It from qubit* [60]. There is a productive collaboration named by this slogan, funded by Simons Foundation, focusing on leading research along this direction. The philosophy behind this seems to imply that all realities in this world, including spacetime, matter, and energy, are inextricably linked to quantum information. In my opinion, this can also be regarded as part of cyberpunkian quantum field theory. After all, a considerable part of this picture needs to be explained by some weakly-coupled or strongly-coupled quantum field theories. In this process, first of all, quantum information theory, or computer science in general, play a heuristic role in the study of quantum gravity. Second, information loss is not only a quantum information process but also a physics process, so describing this process requires the organic cooperation of computer scientists and physicists. Finally, physics, in turn, inspires some results of quantum information, such as guiding the establishment of some new properties of quantum error correction codes.

There are many works currently in this field are completely about black holes. However, if we are tired a little bit about black holes, we could consider quantum cosmology, another interesting and possibly observable resource of quantum gravity. Recently, there is a new version of holography beyond the usual asymptotic AdS boundary condition, which is called $T\bar{T}$ holography (see [61, 62]) where I help established, that is potentially useful for the theoretical study of de Sitter space and quantum simulation of quantum cosmology (see [63–65]).

It from qubit and the non-perturbative bootstrap

At the same time, I would like to mention again another Simons Collaboration project that is going on almost simultaneously, *the non-perturbative bootstrap* [66]. The research I mentioned earlier about the relationship between conformal field theory and large-scale optimization is one of the most important components of this cooperative program. Up to now, this plan also includes some other parts, such as

S-matrix bootstrap, Hamiltonian truncation, and some other supersymmetric and string theory research. Some of them also use large-scale optimization methods. Their common purpose is probably to use the bootstrap method to solve a large number of non-perturbative quantum field theory related problems.

In my Ph.D. research career, I am very lucky to join these two great research projects at the same time. One of my Ph.D. advisors, John Preskill, is the leader of *it from qubit* collaboration. My other doctoral advisor, David Simmons-Duffin, is one of the main forces of *the non-perturbative bootstrap*. Their profound wisdom and research style deeply influenced me. I realize that I am in a lucky *middle position* and had the opportunity to learn the core content of these two sciences.

Obviously, these two plans are complementary. For example, conformal field theory is actually the boundary theory of quantum gravity, so conformal bootstrap is likely to be a concrete realization of some black hole information problems. In a sense, the cyberpunk quantum field theory I studied can be regarded as a cross between these two sciences. It is somewhat different from the two, but it can also complement each other and form part of a larger picture of theoretical physics and computer science.

For example, a considerable part of the research on *it from qubit* is based on toy models of quantum circuits, but I hope to generalize them as hard-core field theory stories. Unlike the problem of formal theory that *it from qubit* mainly focuses on, I also hope that we can discuss some problems that are closer to real experiments or observations, such as particle phenomenology, cosmology, and statistical physics. Furthermore, I do not want to use only quantum information tools, but more general computer science, such as data mining and machine learning. These can be regarded as the differences between *it from qubit* and cyberpunkian quantum field theory.

On the other hand, my main research direction and *the non-perturbative bootstrap* have the following differences. First of all, researchers of the non-perturbative bootstrap tend to use the field theory method, but I also hope to combine the field theory method with the lattice-based method and make them complementary. On the other hand, *the non-perturbative bootstrap* tends to use more theoretical research methods, but I also hope to extend these issues to experimental simulations, such as experiments on quantum devices based on cold atom physics, or demonstrations of some thought experiments in conformal field theories, like conformal collider physics, in the lab. Finally, at present, the non-perturbative bootstrap technology mainly adopts classical computing, but I also tend to extend them to the field of quantum computing, and moreover, push the algorithms used in the cutting-edge

quantum field theory research towards the industry level.

Church-Turing Thesis in 2021

In addition, I hope to discuss a more *metaphysical* issue that has emerged in recent years in the physics community, namely, the research on the Church-Turing Thesis.

A thesis is not a theorem, it is just a proposal or a conjecture. In other words, it may be right or wrong. The Church-Turing thesis is an argument about the Turing machine's ability to interpret the world. We will use the original words by Susskind in his recent paper [67]

Thesis 1. *Any computation that can be done by a physical system can be done by a Turing machine.*

The Church-Turing thesis is believed to be correct. However, the thesis itself does not really address anything about the efficiency of the computation. When we are addressing the efficiency of the Turing machine, we sometimes say that the thesis is *extended*. In fact, we have the following *quantum-Extended Church Turing* thesis.

Thesis 2. *Any calculation that cannot be done efficiently by a quantum Turing machine (or quantum circuit), cannot be done efficiently by any physical system consistent with the laws of physics.*

When we are addressing the complexity or efficiency of our computation in a quantum circuit, the above thesis is highly informal and needs to be formalized. For instance, the efficiency, which means the number of basic operations in the quantum circuits, seems to be dependent on the choice of the time coordinate, and thus inconsistent naively with special or general relativity. In fact, there are constructions in the general relativity, where we call the Malament-Hogarth spacetime, such that the halting problem could even be solved [68] (See a related discussion by [69] about computability and summation over topologies in the gravitational path integral). Secondly, there are confusions about holographic duality and quantum Church-Turing Thesis: It seems that measuring entanglement entropies is hard, but measuring area of the extremal surface is easy; It seems that measuring computational complexity for quantum states is hard, but measuring volume or action in the gravitational theory is easy. But based on holographic correspondence, entropies and areas are connected, as complexities and volumes are also connected. So what is the magic? Is it because the holographic mapping itself is computationally hard,

or it is a violation of the quantum-extended Church-Turing Thesis? The situation becomes more intriguing when the gravitational system involves a black hole, and the answers towards this question are still not completely known [67, 70–72].

Here, I wish to add two comments about the current status of research along the line of Church-Turing Thesis.

- Some aspects of the study of the quantum-extended Church-Turing thesis could be addressed concretely using quantum field theories, at least in some latticed versions. This type of research will involve concretely about designing algorithms for a given setup of quantum field theory and prove the statement about computational complexity. We regard this as part of our cyberpunkian quantum field theory program.
- The above discussion about AdS/CFT shows that understanding the complexity of duality maps themselves might be important. Duality is usually understood as a reformulation of one theory to the other theory, one Lagrangian to the other Lagrangian, one state to the other state. It might be interesting to discuss the complexity of AdS/CFT, and also, other dualities established among several quantum field theories and string theories [73], which are actually, hot topics in the frontier of theoretical physics that have profound applications in particle physics and condensed-matter systems [74]. For instance, one could ask, what is the complexity of S or T duality in some specific setups? The *complexity web* of duality webs among the landscape of field theories might play an important role in understanding Church-Turing Thesis.

CS-inspired physics and physics-inspired CS

Theoretical considerations

As we discussed before, many examples in this article show that concepts and results from computer science are helpful for the development of physics in recent years. This could happen in a purely theoretical or conceptual level. Here we wish to discuss another possibility, where physics goes backward to inspire interesting progress in computer science. We call it *physics-inspired computer science*.

There are several typical examples recently happening, based on the development of the connection between quantum information theory and quantum gravity. For instance, the original proof of the strong subadditivity of von Neumann entropy is

very technical [75, 76], but the holographic version of the proof based on AdS/CFT is highly intuitive and simplified [77]. Moreover, the linear growth of complexity in some setups of local random circuits proved recently in [78, 79] is partially inspired by Susskind based on the wormhole growth in AdS/CFT [80]. There is also a work about relationships between black hole microstates and large violations of additivity conjecture, one of the most important problems in quantum information theory [81].

Of course, other aspects of theoretical computer science are also possible to be inspired by physics. A particularly interesting discussion recently is about a possible connection between renormalization group theory and machine learning [82]. In some formulations, some people believe that the optimization and learning process in the parameters of the neural network could be understood as renormalization. Maybe one could derive some renormalization group flow equation for those parameters. One might even consider discussing phase transitions in the neural networks. If it is a second-order phase transition, conformal field theory might be helpful in predicting phenomena happening in the network. There are some impressive works done by Google recently, about generically using quantum field theory and tensor network technics for machine learning problems (see for instance [83]).

Benchmarking quantum devices using fundamental physics

Currently, we are still in a very early stage towards the great plan where quantum devices are able to provide impressive computational powers against classical computation or find some other remarkable applications in our ordinary life. Currently, quantum devices are still in the lab where people have to deal with the mitigation of noise and errors. It is important to find some clear targets where people have some universal, useful standards to show their computational capability of quantum devices. Here I am providing a possibility where fundamental physics should be helpful for benchmarking quantum devices.

Fundamental physics in general, or quantum field theory in a more specific sense, have many unsolved and important problems. For instance, as introduced before, strongly-coupled quantum field theories are very hard to solve. If one could simulate some non-perturbative physics using quantum devices, which is far beyond the limitation of classical computation, it could clearly show the capacity of the devices. This is not only following the original intuition of Richard Feynman about quantum computation, but also practical for the current development of quantum hardware.

Let me give a more precise example, e.g., evaluation of critical exponents in some

critical systems admitting a second-order phase transition and an emergent conformal field theory. For some complicated systems where the critical exponents are not analytically solved, the critical exponents are only known to some digits. Those numbers are universal, namely, independent of, for instance, metrology, or the unit we use. The error bars of those critical exponents could be clear targets for benchmarking quantum devices. This could clearly be a win-win situation for both fundamental physics and quantum industry since it will not only be helpful for devices themselves, but also for exploring something unknown about our nature. This potentially requires fruitful collaborations between physicists, computer scientists, and engineers.

High energy physics in the low energy lab

There is another aspect of the above story, where some quantum simulation tasks might be more motivated to explore physics itself. This could be understood partly as a mostly non-commercial application of quantum computing in the NISQ era. Since a large part of me is a high energy physicist, I will be mostly appreciated if we could explore high energy physics problems using quantum devices. I wish to call this as *high energy physics in the low energy lab*.

Simulating high energy physics in the cold-atomic or condensed-matter labs might already have a long history. For instance, topological condensed-matter physicists could nowadays measure topological invariants directly in their labs. It has its own interests, of course, to measure topological phenomena in the statistical-mechanical systems. On the other hand, it will be no hurt to understand those experiments alternatively as simulators of emergent topological quantum field theories, originally designed for applications in string theory.

Aside from simulating quantum field theories, which we have discussed before, people have rising interests recently for simulating quantum gravity toy models. For example, people discuss recently *quantum gravity in the lab* to simulate some thought experiments using their quantum devices [84]. I am not sure if those simulations will be able to simulate physics that is beyond the current capability of classical computations nowadays, but I believe that future simulation will tell us much more fruitful knowledge that is far beyond what we currently know. Moreover, at least, simulating high energy physics in the low energy lab, is helpful for demonstration of principles, that we are able to simulate some exotic physical phenomena and bring those experiments from high energy physics itself to more general physicists. For

instance, a particularly interesting example I have in mind is the so-called *conformal collider physics* largely due to the work of Hofman and Maldacena [85]. This experiment considers particle colliders established on the celestial sphere of conformal field theories, which is closely related to the black hole information paradox [86], and the electron-electron collider in particle physics [87, 88]. One could actually consider simulating this experiment in the critical cold-atomic or condensed-matter systems in the lab and compare it with theory, to show that quantum devices are able to simulate novel strongly-coupled emergent field theory dynamics. Another side of the story is to detect some experimental or phenomenological problems in high energy physics that might be answered using cold-atomic, condensed-matter, or quantum information technology, where I believe are, in rapid development (see a list of this type of projects announced by Fermilab [89]).

Towards the future

Waiting for quantum technology

Although many theoretical, numerical, simulation and experimental works have been done about our quantum devices, a fault-tolerant, universal quantum computer until May, 2021, has not appeared on the earth. Although many people believe that finally human will have such a computer at some point in the future, it is not super clear when precisely the day will come.

For some people, it is a little confusing why people need to do so much theoretical research by assuming a currently imaginary machine with quantum computational power. However, my personal view about this question is that science is always looking at the future. For instance, for detecting gravitational waves, we have waited nearly one hundred years, from pure theoretical constructions towards practical detections. For particle colliders, people propose some possibility of new particles, and particle physicists are still trying to detect them at least for half a century. The future attributes of science and technology could probably also be described by cyberpunk.

The modern development of science and technology is always associated with risk. If there is no risk and everything is definite, it may not be good science. If we are allowed to have a bet for detecting gravitational waves or detecting new particles, it is natural that some people will bet a useful quantum computer will appear at some point or even in the near future, and I am sure that for some people it is a pretty safe bet compared to other physics and technology challenges. During the development,

there are many byproducts that we have mentioned above, which could be regarded as rewards towards the final achievement of quantum computing.

Fundamental science using oracles

Here we wish to discuss a word, *oracle*, to emphasize a possible future where more cyberpunkian technologies have been used for scientific research.

The word "oracle" usually means that there is an existence which could provide some wise suggestions or reasonable predictions of the future, inspired by the gods. Related concepts are widely existing from ancient history, for instance, the Oracle of Delphi in ancient Greece. Nowadays, some computer scientists use the word "oracle" in the complexity theory, usually means a black box function in an algorithm. However, here we wish to use this word for something more general: in modern research, many aspects of our work have to rely on oracles made by information technologies.

In a very general sense, our personal computers and mobile phones could be understood as oracles: most of us don't understand how those machines are running, and we are still using them without that much verifications. For physicists, mathematicians, their books, and well-established results published in, for instance, *Annals of mathematics*, could be regarded as oracles, since usually, physicists don't want to prove them, but instead directly use them when needed. For some theoretical physicists, if they don't want to study in detail about some aspects of string theory, but they are willing to use the results, they could cite Edward Witten's paper and use the result by the trust without checking. In this sense, Edward Witten's word is an oracle (just like what I am doing now [73]). For high energy theoretical physicists, the software *Mathematica* is one of the most common oracles. Because of this oracle, theoretical physicists don't need to check how to play with Taylor expansions of some special functions or computing the Riemann tensor for a given metric by hand [90]. This hugely speeds up our modern development of theoretical physics⁹.

Here, I am claiming that future information technology might significantly change the way we are doing research even further, towards somewhere beyond our imagination. Maybe at some point, we don't need to actually write any papers, and all operations are somehow collaboratively appearing in some universal, well-established framework on the internet, speeded-up by artificial intelligence and quantum com-

⁹However, there are still some theoretical physicists who claim that they are Luddites [91] and don't wish to use *Mathematica*. Some of them are also doing great jobs on hardcore computations.

puting. Maybe we don't need to provide any technical details of any works while machines will help us figure it out, and humans are just able to provide some generic views. Anyway, I think some aspects of those stories might happen someday, even during my life. These imaginings mean that we need more and more oracles.

Aside from the way we are practically doing science, oracles also often appear in the scientific contents itself. For instance, the existence of the 3d Ising bootstrap island for mixed operators is still mysterious. People don't have enough theoretical understanding of it. The way we obtain it is from complicated crossing equations and large-scale optimization, which could be regarded as oracles. What is the final answer to the critical exponents of the 3d Ising model? If we think about this problem in terms of crossing equations, the answer is obtained by the consistency of four-point correlation functions with mixing operators. If we transform it into semidefinite programming, it will be obtained from some super complicated crossing equations. If it turns out that the answer could be represented by some numbers where human beings are familiar with, it might be a very deep fact about the transcendental nature of hypergeometric functions, or representation theories about the conformal group. Maybe there is a Ramanujan-type formula hidden there, which might be indicated by oracles of large-scale optimization, or maybe machine learning [92].

Talking about Ramanujan, I think there are some better examples in mathematics instead of physics. In fact, the story of Srinivasa Ramanujan himself is highly related to the original meaning of oracles. During the time Ramanujan lived in the last century, he did not have a complete education in mathematics, but he could still discover a large set of amazing formulas about special functions and prime numbers. Many of them were highly intriguing but not proved, inspiring many potential discoveries from algebraic geometry to number theory¹⁰. So how was he able to find those magic formulas? He said, "An equation for me has no meaning unless it expresses a thought of God". It seems that he was crediting his formulas to his family goddess Namagiri Thayar, although some people believe that it was from intuitions behind thinking about math for a long time. Of course, Ramanujan is pretty unique in history, and I am not sure if it is wise enough to choose some beliefs in order to make some scientific discoveries, but I am saying that some future information technology will bring people solid, incomprehensible predictions, serving as oracles. In fact, people already start to do this. There is a machine learning project made by Google called the *Ramanujan Machine*,

¹⁰If you don't know his story, you could look at the movie *The Man Who Knew Infinity* [93].

which is trying to discover some conjectural identities about special constants and continued fractions [94]. Based on their website [95], they are already able to generate conjectures by neural networks, and some of them seem not yet proved by professional mathematicians.

Besides discovering new conjectures, one of the first steps is probably to try to verify the known proof. About this, I wish to quote some recent activities by a well-established number theorist, Kevin Buzzard (see, for instance, this article [96]). According to him, there is no person on earth who could completely understand all details of Fermat's Last Theorem: the proof is so complicated, and people have to use many known results by trusting the original author, and all those details lead to a huge amount of literature. Nowadays, many aspects of mathematics, for instance, arithmetic algebraic geometry, Langlands program, or closer to physics, symplectic geometry, become extremely technical, and there is usually a very limited number of persons who could understand details of the proof. Thus, maybe it is necessary to try to verify some proofs based on machine, just in the aspects of logical consistency, since unlike modern physics allowing some degrees of fuzzy logic, mathematical proofs only allow two consequences: correct or wrong.

Kevin Buzzard is working on gathering fundings and establish codes to verify known mathematical proofs, and some concepts of new mathematics, for instance, perfectoids introduced by Peter Scholze, could be realized by codes. Maybe this is a promising direction that is helpful for future mathematics, although young people in this field have to prove themselves by proving theorems. In physics, parts of theoretical physics directions are more rigorous in the mathematical sense, especially some aspects of quantum field theory or quantum information science, since the basic rule is more or less well-established. In other parts, for instance, quantum gravity, people have to make conjectural guess since the building blocks are not completely developed. Maybe for the former, it makes sense to do some verifications also. And in the long-term future, when people really discover a theory of everything, people could put all physics and mathematics axioms and theorems in a computer, to make solid predictions in our cyberpunkian future.

The current progress of number theory often tells us how limited people know about some simple concepts like prime numbers or rational numbers. For instance, about the Diophantine equation, the celebrated Birch-Swinnerton-Dyer (BSD) conjecture, one of the Millennium Prize Problems, could tell us something about the structures of solutions for the cubic equations (not proven). Problems in more general cases,

higher degrees, more variables, are extremely hard to answer, while some of them are approaching some deepest sides of modern mathematics, where it is relatively easy to formulate a question that no one on the earth could solve. I would feel that maybe many of those problems are too hard for human brains, and in the future, we have to rely on oracles made by cyberpunkian technologies.

Companies, colliders

Here, we wish to comment on the relations between cyberpunkian quantum field theory and phenomenology. In many parts of this article, I am talking about some formal research, which seems to be not that related to real observations and experiments. However, it is not true. As we mentioned before, strongly-coupled quantum field theories are everywhere: people need to use strongly-coupled QCD to predict meson spectra and real-time dynamics happening in some colliders. In the condensed-matter system and statistical physics, predictions from strongly-coupled field theory are helpful to study strong-correlated systems, and they are directly measurable as quantum materials. In the sky, models with dark matter and dark energy might need strongly-coupled field theories to understand, cosmic phase transitions happening in the early universe might also be an exotic strongly-coupled field theory phenomena. Black hole physics is directly related to observations from event horizon telescope and LIGO (Laser Interferometer Gravitational-Wave Observatory) experiments about gravitational waves. I feel that all of them might need potential computational speedup or formal understanding from information theory. In a sense, they are all cyberpunkian physics!

It might be interesting to comment on some modern aspects of relations between academia and industry. Traditionally, some people studying fundamental physics might feel that pure potential physical breakthroughs may not be related to any commercial companies. However, I feel that in our quantum era, it might be common that academia and industry will have more communications.

Many companies, for instance, Google, Amazon, Microsoft, IBM, etc., have the ambition nowadays to make useful quantum computers for potential commercial purposes. Scientific academia, as part of public service sometimes funded by the government and donation, is aiming at providing high-quality research about our nature. In our quantum era, people start to communicate with each side frequently. We often see examples where quantum information scientists switch back and forth between two sides, and make great progress for both. There are several quantum

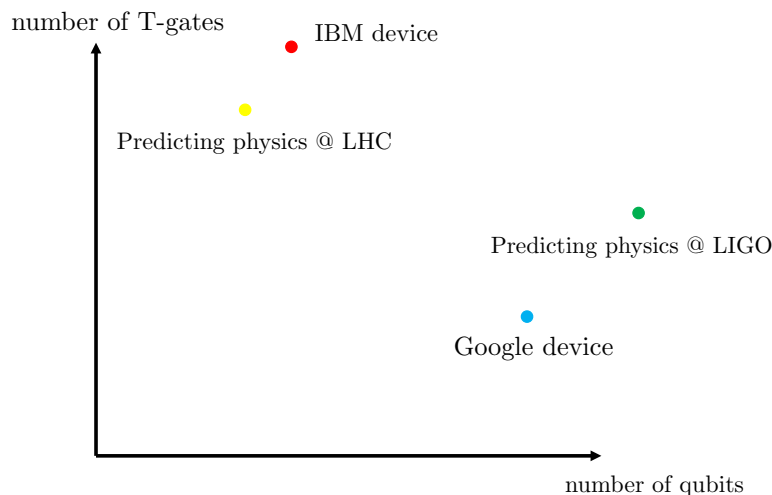


Figure 1.5: An imaginary plot might be made by future cyberpunkian physicists, especially high energy phenomenologists. This kind of plot includes the required computational resource needed for observations and existing computational resources provided by companies. As far as I know, no such plot existed until June 2021, which put together experimental organizations and quantum companies. I am conjecturing here that this type of plot will appear in the future.

centers from commercial companies established around the university campus, for instance, Microsoft Station Q at Santa Barbara, and the new Amazon quantum center at Pasadena. One remarkable work done recently about simulating quantum gravity in the lab is also such a great collaboration between company and university [84]. For me, it is exciting to imagine that Google is starting to probe properties of traversable wormholes.

It is exciting to see that both government and private industrial communities are willing to help establish some exciting new areas relating to fundamental physics and information technology. Previously, I am impressed by some high energy physics research collecting data from completely different experimental organizations and comparing them with each other. For instance, the electroweak phase transition happening in the early universe, might need observational and experimental data both from the ground (colliders) and the sky (gravitational wave detectors), and the data analysis might be made in the same plot (see, for instance, Figure 2 of [97]). I am imagining that one day, people will make plots which mention companies like Google and IBM, experimental organizations like LHC and LIGO in the same place (See Figure 1.5). I hope that the day may not be too far off.

PROOF OF THE WEAK GRAVITY CONJECTURE FROM BLACK HOLE ENTROPY

This chapter is based on C. Cheung, **J. Liu**, and G. N. Remmen ([alphabetical order](#)), *Proof of the Weak Gravity Conjecture from Black Hole Entropy*, JHEP **10**, 004, (2018), arXiv:1801.08546 [hep-th].

Abstract: We prove that higher-dimension operators contribute positively to the entropy of a thermodynamically stable black hole at fixed mass and charge. Our results apply whenever the dominant corrections originate at tree level from quantum field theoretic dynamics. More generally, positivity of the entropy shift is equivalent to a certain inequality relating the free energies of black holes. These entropy inequalities mandate new positivity bounds on the coefficients of higher-dimension operators. One of these conditions implies that the charge- to-mass ratio of an extremal black hole asymptotes to unity from above for increasing mass. Consequently, large extremal black holes are unstable to decay to smaller extremal black holes and the weak gravity conjecture is automatically satisfied. Our findings generalize to arbitrary spacetime dimension and to the case of multiple gauge fields. The assumptions of this proof are valid across a range of scenarios, including string theory constructions with a dilaton stabilized below the string scale.

2.1 Introduction

In this paper we argue that black hole thermodynamics implies new constraints on the coefficients of higher-dimension operators. Our results are based on a certain universal property of entropy. In particular, consider a system \mathcal{T} prepared in a macrostate whose microstate degeneracy is quantified by entropy S . Now let us define the system $\tilde{\mathcal{T}}$ to be a restriction of \mathcal{T} in which a handful of degrees of freedom have been frozen to a fixed configuration. If $\tilde{\mathcal{T}}$ is prepared in the same macrostate as \mathcal{T} , then the corresponding entropy \tilde{S} will be less than S because the microstate degeneracy is diminished. Thus, we find that

$$S = \tilde{S} + \Delta S, \tag{2.1}$$

where the entropy shift ΔS is strictly positive.

A similar logic applies to black hole entropy. Consider the low-energy effective field theory of photons and gravitons in general spacetime dimension D , defined at a scale far below the mass gap. The effective Lagrangian is

$$\mathcal{L} = \tilde{\mathcal{L}} + \Delta\mathcal{L}, \quad (2.2)$$

where the first term describes pure Einstein-Maxwell theory,¹

$$\tilde{\mathcal{L}} = \frac{1}{2\kappa^2}R - \frac{1}{4}F_{\mu\nu}F^{\mu\nu}, \quad (2.3)$$

and the second term encodes corrections from higher-dimension operators,

$$\begin{aligned} \Delta\mathcal{L} = & c_1R^2 + c_2R_{\mu\nu}R^{\mu\nu} + c_3R_{\mu\nu\rho\sigma}R^{\mu\nu\rho\sigma} \\ & + c_4RF_{\mu\nu}F^{\mu\nu} + c_5R_{\mu\nu}F^{\mu\rho}F^\nu{}_\rho + c_6R_{\mu\nu\rho\sigma}F^{\mu\nu}F^{\rho\sigma} \\ & + c_7F_{\mu\nu}F^{\mu\nu}F_{\rho\sigma}F^{\rho\sigma} + c_8F_{\mu\nu}F^{\nu\rho}F_{\rho\sigma}F^{\sigma\mu}. \end{aligned} \quad (2.4)$$

Without loss of generality, we have dropped all terms involving $\nabla_\rho F_{\mu\nu}$, which are equivalent via the Bianchi identities to terms already accounted for or terms involving $\nabla_\mu F^{\mu\nu}$ [98], which vanish in the absence of charged matter sources, which we assume throughout.

For our analysis, we study a large black hole of fixed mass m and charge q as measured in natural units at spatial infinity. In the presence of higher-dimension operators, the metric is

$$g_{\mu\nu} = \tilde{g}_{\mu\nu} + \Delta g_{\mu\nu}. \quad (2.5)$$

Unless otherwise stated, all variables with tildes like $\tilde{g}_{\mu\nu}$ will denote quantities corresponding to a Reissner-Nordström black hole of the same mass and charge in pure Einstein-Maxwell theory, while variables with deltas like $\Delta g_{\mu\nu}$ will denote the leading corrections from higher-dimension operators, which are linear in the coefficients c_i .

It is straightforward to compute the black hole entropy using the Wald formula [99],²

$$S = -2\pi \int_\Sigma \frac{\delta\mathcal{L}}{\delta R_{\mu\nu\rho\sigma}} \epsilon_{\mu\nu}\epsilon_{\rho\sigma}, \quad (2.6)$$

where the integration region Σ is the horizon and $\epsilon_{\mu\nu}$ is the binormal to the horizon, normalized so that $\epsilon_{\mu\nu}\epsilon^{\mu\nu} = -2$. A large portion of our technical analysis will be

¹Throughout, we work in units where $\kappa^2 = 8\pi G$, metric signature $(-, +, \dots, +)$, and sign conventions $R_{\mu\nu} = R^\rho{}_{\mu\rho\nu}$ and $R^\mu{}_{\nu\rho\sigma} = \partial_\rho\Gamma^\mu{}_{\nu\sigma} - \partial_\sigma\Gamma^\mu{}_{\nu\rho} + \Gamma^\mu{}_{\rho\alpha}\Gamma^\alpha{}_{\nu\sigma} - \Gamma^\mu{}_{\sigma\alpha}\Gamma^\alpha{}_{\nu\rho}$.

²A general formula for entanglement entropy has also been proposed [100], but this reduces to the Wald formula for the static Killing horizons relevant to our analysis.

the explicit evaluation of Eq. (2.6) at fixed q and m . The entropy shift ΔS is then defined according to Eq. (2.1), where

$$\tilde{S} = \frac{\tilde{A}}{4G} = \frac{2\pi\tilde{A}}{\kappa^2} \quad (2.7)$$

is the Bekenstein-Hawking entropy [101, 102]. Deviations from Eq. (2.7) arise from higher-dimension operator corrections to the Lagrangian, $\mathcal{L} = \tilde{\mathcal{L}} + \Delta\mathcal{L}$, and the area of horizon, $A = \tilde{A} + \Delta A$.

Using standard thermodynamic identities we show that corrections to the Bekenstein-Hawking entropy of a black hole at fixed mass and charge satisfy

$$\Delta S > 0 \quad (2.8)$$

whenever the free energy of the black hole is less than that of a Reissner-Nordström black hole at the same temperature,

$$F(\beta) < \tilde{F}(\beta). \quad (2.9)$$

Using Euclidean path integral methods we then prove Eq. (2.9) for *i*) a thermodynamically stable black hole in *ii*) a theory in which the dominant contributions to higher-dimension operators are generated at tree level by massive quantum fields. The underlying logic of our proof mirrors the parable of \mathcal{T} and $\tilde{\mathcal{T}}$ discussed previously. In particular, $\tilde{\mathcal{L}}$ is obtained directly from the ultraviolet completion of \mathcal{L} by placing a restriction on massive field fluctuations in the Euclidean path integral. The difference between S and \tilde{S} then quantifies the entropy contributions from these modes.

Condition *i*) holds for positive specific heat [103], excluding from consideration the Schwarzschild black hole but permitting Reissner-Nordström black holes over a range of charge-to-mass ratios, $q/m > \sqrt{2D-5}/(D-2)$. Condition *ii*) arises naturally in a number of physically-motivated contexts such as string theory, which typically predicts the existence of gravitationally-coupled scalars like the dilaton. If supersymmetry breaking occurs below the string scale, then these states are well described by quantum field theory and can be integrated out at tree level to generate the higher-dimension operators in Eq. (2.4). Note that condition *ii*) is perfectly consistent with additional corrections entering at loop level or from intrinsically stringy dynamics, provided these contributions are parametrically smaller than the tree-level component.

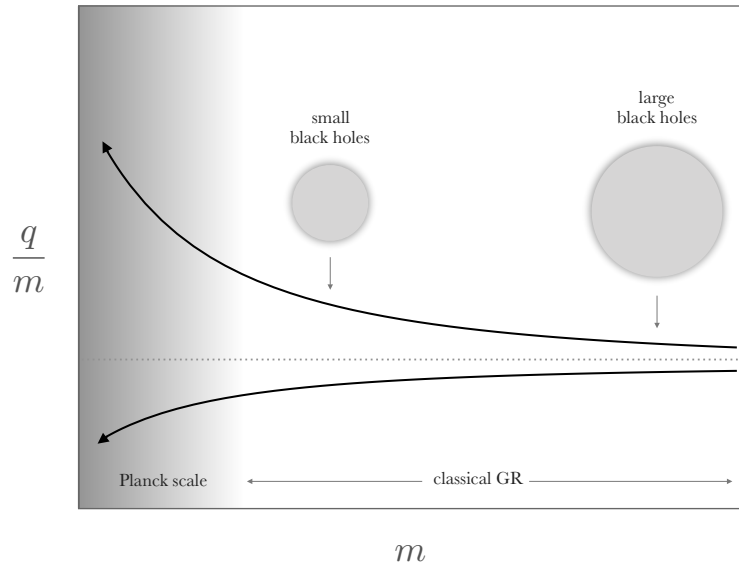


Figure 2.1: Black holes of maximal charge shown as a function of mass m and charge-to-mass ratio q/m . Higher-dimension operators induce corrections to the extremality condition. If these corrections are positive, then the WGC is automatically satisfied (upper solid curve) since large black holes are unstable to decay to smaller ones. If these corrections are negative (lower solid curve), then the WGC mandates additional light, superextremal particles to avoid an infinite number of stable extremal black hole remnants.

While we have only proven the free energy condition in Eq. (2.9) under certain assumptions, its connection to positivity of the entropy shift in Eq. (2.8) is robust and completely general. Furthermore, a trivial corollary to Eq. (2.8) is a positivity condition on the differential entropy generated at each mass threshold encountered while flowing to the infrared.

Remarkably, classical entropy corrections dominate over quantum contributions over a broad range of black hole masses still within the regime of validity of the effective field theory. Within this window, our proof of Eq. (2.8) applies. Since the shift in entropy depends on the coefficients of higher-dimension operators, we derive a new class of positivity bounds on the effective field theory. This produces a one-parameter family of constraints on the corresponding coefficients c_i labeled by the charge-to-mass ratio of the black hole from which the bound was derived. Although these conditions are derived from a very particular black hole construction, the resulting positivity bounds constrain the coefficients c_i in general and are independent of the background.

For the case of highly charged black holes, we obtain a positivity condition on a very specific combination of higher-dimension operator coefficients. Remarkably, it is this exact combination of parameters that also enters into the higher-dimension operator correction to the extremality condition for black holes. In particular, we find that the charge-to-mass ratio for an exactly extremal black hole satisfies

$$\frac{q}{m} - 1 \propto \Delta S, \quad (2.10)$$

where the right-hand side is positive by Eq. (2.8). Since higher-dimension operators decouple at long distances, the charge-to-mass ratio asymptotes to unity *from above* as we consider larger and larger extremal black holes. Thus, from charge and energy conservation, it is always possible for an extremal black hole to decay to smaller extremal black holes of marginally higher charge-to-mass ratio, as shown in Fig. 2.1. Notably, the existence of such states is precisely mandated by the weak gravity conjecture (WGC), which asserts that an Abelian gauge theory consistently coupled to gravity must contain a state whose charge exceeds its mass in Planck units [104], so

$$\frac{q}{m} > 1. \quad (2.11)$$

The motivation for the WGC is to forbid the existence of an infinite number of stable states not protected by symmetry. The main result of this paper is that this bound is automatically satisfied by small black holes. Though mysterious at first glance, the connection between entropy and extremality in Eq. (2.10) actually follows immediately from the near-horizon properties of the metric for a charged black hole. As we will show, this connection enables us to straightforwardly extend all of our arguments to the multi-charge generalization of the WGC [105] in arbitrary dimension D .

The WGC is satisfied in numerous concrete examples and is strongly motivated by folk theorems forbidding exact global symmetries that arise in the vanishing-charge limit. Moreover, the WGC is a celebrated avatar of the so-called swampland program [104, 106–108], whose ultimate aim is to systematically delineate regions in effective field theory space consistent with quantum gravitational ultraviolet completion.

Strictly speaking, a bona fide swampland condition distinguishes between low-energy effective field theories that from an infrared standpoint are otherwise entirely consistent. From this perspective it is unclear whether a theory that fails the WGC is in the swampland or *merely pathological* in a sense that can be diagnosed purely from low-energy considerations. For this reason, a related effort has sought to

exclude regions of the low-energy parameter space using infrared consistency, e.g., constraints from causality, unitarity, and analyticity of scattering amplitudes [108–112]. While the WGC has previously eluded a formal general proof, the present work demonstrates that it is mathematically equivalent to a certain well-motivated—and in many circumstances provable—property of black hole entropy.

The remainder of this paper is organized as follows. In Sec. 2.2 we prove, given certain assumptions, that corrections to the Bekenstein-Hawking entropy are positive. Afterwards, in Sec. 2.3 we discuss how various contributions to the black hole entropy arise and estimate their relative size. In order to constrain the coefficients of higher-dimension operators, we restrict to black holes within a certain mass range. Next, in Sec. 2.4 we present the perturbative solution for a charged black hole in the presence of higher-dimension operators. We then compute the black hole entropy in Sec. 2.5 and translate the positivity condition on entropy into a new class of bounds on higher-dimension operator coefficients in Sec. 2.6. After discussing the implications of these results for the WGC, we conclude in Sec. 2.7.

2.2 Proof of $\Delta S > 0$

In this section, we study corrections to the Bekenstein-Hawking entropy of a thermodynamically stable black hole at fixed mass and charge. We prove that these contributions are positive whenever they come from higher-dimension operators generated at tree level by quantum fields.

Assumptions

Let us state our assumptions explicitly. First, we assume the existence of quantum fields ϕ at a characteristic mass scale $m_\phi \ll \Lambda$, where Λ is the energy scale at which quantum field theory breaks down. This parametric separation is required so that quantum field theory has some regime of validity. By the usual rules of effective field theory, the higher-dimension operators in Eq. (2.4) receive small contributions suppressed by the cutoff Λ . In general, Λ can be parametrically smaller than the Planck scale.

Second, we assume that the ϕ degrees of freedom couple to photons and gravitons such that integrating them out generates the higher-dimension operators in Eq. (2.4) classically, i.e., at tree level. Since $m_\phi \ll \Lambda$, these states induce the dominant contributions to the higher-dimension operators in Eq. (2.4). Specifically, the corresponding operator coefficients scale as $c_i \propto 1/m_\phi^2 \gg 1/\Lambda^2$ since tree-level ϕ exchange is always accompanied by a single factor of $1/m_\phi^2$ coming from the propa-

gator denominator. Thus, effects arising from the cutoff Λ will be negligible in any context in which quantum field theory is applicable.

As noted previously, states like ϕ are a common feature in string theory, whose low energy spectrum includes particles like the dilaton and moduli, which are massless in the supersymmetric limit. In the presence of supersymmetry breaking, these flat directions are lifted, thus inducing masses $m_\phi \ll \Lambda$, where Λ is the string scale.

While our arguments are perfectly consistent with a scale Λ far below the Planck scale, we will frequently refer to pure Einstein-Maxwell theory and the pure Reissner-Nordström solution as a baseline of comparison. We do so entirely out of convenience and not because any component of our argument requires that quantum field theory be applicable up to the Planck scale. Hence, in an abuse of nomenclature, we hereafter refer to the higher-dimension operator contributions of order $1/m_\phi^2$ as corrections to pure Einstein-Maxwell theory, bearing in mind that we actually mean pure Einstein-Maxwell theory *plus* contributions of order $1/\Lambda^2$, which are parametrically smaller than all the contributions of interest.

Third, we focus on black holes that are thermodynamically stable, i.e., have positive specific heat. As we will see, this is necessary for technical reasons so that we can exploit certain properties of the Euclidean path integral.

Positivity Argument

Consider a positively charged black hole of mass M and charge Q perturbed by higher-dimension operator corrections in general spacetime dimension D . As we will show in detail in Sec. 2.4, the perturbed metric $g_{\mu\nu} = \tilde{g}_{\mu\nu} + \Delta g_{\mu\nu}$ can be computed from the perturbed Lagrangian $\mathcal{L} = \tilde{\mathcal{L}} + \Delta\mathcal{L}$, where unless otherwise stated all quantities are expressed as perturbations on a Reissner-Nordström black hole of the same mass M and charge Q in pure Einstein-Maxwell theory.

From the perturbed entropy we can define the corresponding inverse temperature $\beta = \partial_M S$, which we write as

$$\beta = \tilde{\beta} + \Delta\beta, \quad (2.12)$$

where $\tilde{\beta} = \partial_M \tilde{S}$ is the inverse temperature of the Reissner-Nordström black hole and $\Delta\beta = \partial_M \Delta S$ is the shift of the inverse temperature. The latter appears because higher-dimension operators will in general change the temperature of a black hole at a fixed mass and charge.

Next, we compute the free energy $F(\beta)$ of the perturbed black hole in a canonical

ensemble at inverse temperature β . The free energy is calculated from the Euclidean path integral,

$$e^{-\beta F(\beta)} = Z(\beta) = \int d[\widehat{g}]d[\widehat{A}] e^{-I[\widehat{g}, \widehat{A}]}, \quad (2.13)$$

where \widehat{g} and \widehat{A} are integration variables running over metric and gauge field configurations. The Euclidean action $I = \widetilde{I} + \Delta I$ is the spacetime integral of the Wick-rotated Lagrangian plus boundary terms appropriate to our choice of the canonical ensemble [113]. Here, the boundary conditions at asymptotic infinity are defined by periodicity β in Euclidean time, with a total electric flux Q at the boundary [114], though we suppress all dependence on the latter throughout.

By assumption, the higher-dimension operators in the low-energy effective theory are dominated by tree-level contributions from heavy fields. The Euclidean path integral including these ultraviolet modes is

$$\int d[\widehat{g}]d[\widehat{A}]d[\widehat{\phi}] e^{-I_{\text{UV}}[\widehat{g}, \widehat{A}, \widehat{\phi}]} = \int d[\widehat{g}]d[\widehat{A}] e^{-I[\widehat{g}, \widehat{A}]}, \quad (2.14)$$

where $\widehat{\phi}$ is a collective integration variable running over all configurations of the heavy fields. As a convention, we choose $\widehat{\phi} = 0$ as the boundary condition at asymptotic infinity, thus defining zero as the vacuum expectation value of the field in flat space. In the classical limit, the right-hand side of Eq. (2.14) is obtained by solving the equations of motion for the heavy fields and plugging these solutions back into the action.

Now consider an *alternative* field configuration that instead sets all the heavy fields to zero, thus rendering them non-dynamical. This field configuration does *not* satisfy the equations of motion, but this will have no bearing on the following argument. For this configuration the massive fields are decoupled and their contributions to higher-dimension operators are set strictly to zero. It is then a simple mathematical fact that

$$I_{\text{UV}}[\widehat{g}, \widehat{A}, 0] = \widetilde{I}[\widehat{g}, \widehat{A}], \quad (2.15)$$

where the right-hand side is the Euclidean action for pure Einstein-Maxwell theory for any choice of metric and gauge field. The statement of Eq. (2.15) encodes our assumption that the dominant contributions to the higher-dimension operators in the effective field theory come from heavy fields.

Putting this all together, we obtain a simple inequality relating the free energy of the

perturbed black hole and a Reissner-Nordström black hole at the same temperature,³

$$-\log Z(\beta) = I_{\text{UV}}[g_\beta, A_\beta, \phi_\beta] < I_{\text{UV}}[\tilde{g}_\beta, \tilde{A}_\beta, 0] = \tilde{I}[\tilde{g}_\beta, \tilde{A}_\beta] = -\log \tilde{Z}(\beta). \quad (2.16)$$

To obtain the first equality we compute $\log Z(\beta)$ via the saddle-point approximation. Here g_β , A_β , and ϕ_β are the solutions to the classical equations of motion with subscripts to emphasize their consistency with boundary conditions enforcing inverse temperature β . By definition, $I_{\text{UV}}[g_\beta, A_\beta, \phi_\beta]$ extremizes the Euclidean action. The subsequent inequality then holds if this extremum is *also* a local minimum, in which case off-shell field configurations slightly displaced from the classical solutions will increase the Euclidean action. For this off-shell field configuration we choose the pure Reissner-Nordström metric \tilde{g}_β subject to the same boundary condition dictating inverse temperature β , while pinning all heavy fields to zero. Since this configuration differs only marginally from the true solution of the equations of motion, the displacement from the local minimum will be tiny as required. From Eq. (2.15) we see that the resulting expression is formally equal to the Euclidean path integral for pure Einstein-Maxwell theory evaluated on the Reissner-Nordström background. Using the saddle-point approximation once more, we obtain the final equality with $-\log \tilde{Z}(\beta)$, which is β times the free energy $\tilde{F}(\beta)$ for a Reissner-Nordström black hole at inverse temperature β .

Crucially, $\log \tilde{Z}(\beta)$ does *not* correspond to the free energy of a Reissner-Nordström black hole of mass M , which has an inverse temperature $\tilde{\beta}$. To relate Eq. (2.16) to the latter, we plug Eq. (2.12) into the right-hand side of Eq. (2.16), yielding

$$\log \tilde{Z}(\beta) = \log \tilde{Z}(\tilde{\beta}) - M \partial_M \Delta S, \quad (2.17)$$

where $\log \tilde{Z}(\tilde{\beta})$ is the free energy of a Reissner-Nordström black hole of mass M and inverse temperature $\tilde{\beta}$. To obtain Eq. (2.17), we inserted the thermodynamic relation, $M = -\partial_{\tilde{\beta}} \log \tilde{Z}(\tilde{\beta})$, together with the formula for the inverse temperature shift, $\Delta\beta = \partial_M \Delta S$. From the definition of the free energy of the canonical ensemble, we then obtain

$$\begin{aligned} \log Z(\beta) &= S - \beta M = (1 - M \partial_M) S \\ \log \tilde{Z}(\tilde{\beta}) &= \tilde{S} - \tilde{\beta} M = (1 - M \partial_M) \tilde{S}, \end{aligned} \quad (2.18)$$

where we have used the fact that the perturbed black hole at inverse temperature β has the same mass as the unperturbed black hole at inverse temperature $\tilde{\beta}$. Combining

³Strictly speaking, the free energy of a black hole is obtained only after subtracting the free energy contribution from hot flat space or some other reference spacetime [115]. However, since $\log Z(\beta)$ and $\log \tilde{Z}(\beta)$ have the same asymptotic boundary conditions, any such reference dependence will cancel from either side of Eq. (2.16).

Eqs. (2.16), (2.17), and (2.18), we cancel terms to obtain

$$\Delta S > 0, \tag{2.19}$$

establishing our claim. The above argument accords with the natural intuition that constraining microscopic states, i.e., heavy fields, to be non-dynamical will decrease the entropy.

Let us comment briefly on a subtle but important caveat to the above arguments. The inequality in Eq. (2.16) crucially assumes that on the black hole solution the Euclidean action is not just an extremum but specifically a local minimum. The latter condition guarantees the stability of the Euclidean action under small off-shell perturbations. As is well known, however, the Euclidean path integral suffers from saddle-point instabilities mediated by conformal perturbations of the metric that are unbounded from below. Fortunately, it was shown in Refs. [116, 117] that these particular modes are actually a gauge artifact. For a certain orthogonal decomposition of the metric, the offending conformal mode can be completely decoupled from the physical degrees of freedom. With an appropriate contour of integration it is then possible to path integrate over this mode to yield a convergent final expression.

Later on, an analysis of the Euclidean Schwarzschild solution [118] revealed a bona fide instability coming from a certain non-conformal perturbation about the background solution. This result has been interpreted as evidence that this solution actually describes a tunneling event from a hot background spacetime into a large black hole [119, 120]. Later analyses [121–123] support these claims and moreover show a direct correlation between the existence of negative modes and the thermodynamic instability that arises from negative specific heat. To our knowledge, in all cases considered these saddle-point instabilities disappear when the specific heat is positive, which for example in $D = 4$ requires a black hole with $q/m > \sqrt{3}/2$ in natural units.

For the remainder of this paper we restrict to black holes within this thermodynamically stable window of charge-to-mass ratios so that the extremum of the Euclidean action is a local minimum rather than a saddle point and our proof of Eq. (2.19) applies. Crucially, this range of parameters includes highly charged black holes, so the results of this section can be used in our discussion of the WGC later on.⁴

⁴The stability results of Refs. [116–123] were obtained in the context of pure gravity and Einstein-Maxwell theory. However, they should also apply in the presence of additional heavy fields,

We believe that Eq. (2.19) is likely true even after relaxing some of the assumptions outlined in Sec. 2.2, specifically those requiring a tree-level quantum field theoretic ultraviolet completion. In particular, from Eqs. (2.17) and (2.18) it is obvious that the positivity condition in Eq. (2.19) is mathematically equivalent to an inequality of free energies,

$$F(\beta) < \widetilde{F}(\beta), \quad (2.20)$$

which says that the free energy of the perturbed black hole is less than that of a Reissner-Nordström black hole at the same temperature. Here we emphasize that the former is computed in the theory defined by \mathcal{L} and the latter corresponds to $\widetilde{\mathcal{L}}$. It is quite possible that the free energy condition in Eq. (2.20) holds in complete generality, e.g., including quantum corrections.

Explicit Example

It is instructive to examine the above arguments for the explicit example of a massive, gravitationally-coupled scalar field. The Euclidean action for the ultraviolet completion is⁵

$$I_{\text{UV}}[g, A, \phi] = \int d^D x \sqrt{g} \left[-\frac{1}{2\kappa^2} R + \frac{1}{4} F_{\mu\nu} F^{\mu\nu} + \left(\frac{a_\phi}{\kappa} R + b_\phi \kappa F_{\mu\nu} F^{\mu\nu} \right) \phi + \frac{1}{2} \nabla_\mu \phi \nabla^\mu \phi + \frac{1}{2} m_\phi^2 \phi^2 \right], \quad (2.21)$$

where out of notational convenience the hatted convention employed previously is dropped. The coupling constants a_ϕ and b_ϕ are dimensionless and have indefinite sign. The classical solution for ϕ is

$$\phi = \frac{1}{\nabla^2 - m_\phi^2} \left(\frac{a_\phi}{\kappa} R + b_\phi \kappa F_{\mu\nu} F^{\mu\nu} \right). \quad (2.22)$$

Plugging back into the Euclidean action, we obtain

$$I[g, A] = \int d^D x \sqrt{g} \left[-\frac{1}{2\kappa^2} R + \frac{1}{4} F_{\mu\nu} F^{\mu\nu} - \frac{1}{2m_\phi^2} \left(\frac{a_\phi}{\kappa} R + b_\phi \kappa F_{\mu\nu} F^{\mu\nu} \right)^2 \right], \quad (2.23)$$

which at low energies only produce small corrections to the leading-order black hole solutions. The precise crossover from positive to negative specific heat may be slightly shifted by the effects of the corresponding higher-dimension operators but this has no impact on the thermodynamic stability of highly charged black holes, which are safely within this window.

⁵Here we ignore boundary terms since we will be interested only in the low-energy corrections generated from integrating out heavy fields. These states produce higher-derivative effective operators whose effects fall off quickly with distance and are thus subdominant to bulk action contributions.

where all gradient terms from the ϕ solution are negligible in the low-energy limit. Next, consider the Euclidean action for the full theory, given a field configuration where ϕ is set strictly to zero. The resulting expression is the Euclidean action for pure Einstein-Maxwell theory,

$$I_{\text{UV}}[g, A, 0] = \int d^D x \sqrt{g} \left[-\frac{1}{2\kappa^2} R + \frac{1}{4} F_{\mu\nu} F^{\mu\nu} \right] = \tilde{I}[g, A]. \quad (2.24)$$

Putting this all together, we learn that

$$I[g, A] < I[\tilde{g}, \tilde{A}] < \tilde{I}[\tilde{g}, \tilde{A}]. \quad (2.25)$$

The first inequality follows because the action is minimized on the solutions to the classical equations of motion for thermodynamically stable black holes. The second inequality follows because Eq. (2.23) differs from Eq. (2.24) by a negative-definite contribution. This relation between Euclidean actions then implies Eq. (2.20) in the saddle-point approximation.

Unitarity and Monotonicity

From Sec. 2.2 it is clear that the entropy inequality $\Delta S > 0$ is very closely related to unitarity. In particular, the relative signs derived in the previous example hinged critically on the absence of tachyons or ghosts in the ultraviolet completion. This is not so surprising, since the presence of such pathologies introduce saddle-point instabilities on a general background, be it flat space or a black hole. It would be interesting to draw a direct connection between our results and previous discussions of unitarity and analyticity [108, 124].

There is also an interesting connection between our results and monotonicity theorems along renormalization group flows [125]. Our proof of $\Delta S > 0$ was framed in terms of integrating out all heavy fields at once. However, if the spectrum of particles is hierarchical, then this logic can be applied at each mass threshold in sequence. The total entropy shift is then

$$\Delta S = \int_{\text{UV}}^{\text{IR}} dS, \quad (2.26)$$

where the differential entropy $dS > 0$ contributed by each state is positive. Extrapolating from this classical result, it is reasonable to conjecture that such a positivity condition persists at the quantum level. Indeed, as we will see in Sec. 2.6, the renormalization of pure Einstein-Maxwell theory accords with this expectation.

It is known that the quantum entropy corrections computed from the Euclidean path integral are in close relation with the entanglement entropies of the corresponding modes, where the horizon is the entangling surface (see Refs. [126, 127] and references therein). Since entanglement entropy is intrinsically positive, so too are the quantum entropy corrections, to the extent to which they are equivalent. We will comment on this connection in more detail in Sec. 2.3.

2.3 Classical vs. Quantum

Up until now we have focused on classical corrections to the entropy, ignoring all loop effects. As we will see, there exists a regime of black hole masses in which the classical contributions dominate over the quantum. In this case, $\Delta S > 0$ according to the proof presented in the previous section. In what follows, we estimate and compare the characteristic size of the leading tree-level and loop-level corrections to the black hole entropy.

Leading Contributions

For concreteness, consider a scalar ϕ of mass m_ϕ . As per the assumptions of the previous section, we assume that this field has the usual minimal coupling to gravitons but also direct couplings to the curvature and electromagnetic field strength. Conservatively, we assume that these couplings are at least of gravitational strength, so the interactions go as $\sim \phi R/\kappa$ and $\sim \kappa \phi F^2$. Here it will be convenient to define a set of rescaled higher-dimension operator coefficients,

$$d_{1,2,3} = \kappa^2 c_{1,2,3}, \quad d_{4,5,6} = c_{4,5,6}, \quad d_{7,8} = \kappa^{-2} c_{7,8}, \quad (2.27)$$

which are the dimensionally natural basis in which to express quantities. All of these rescaled coefficients have mass dimension $[d_i] = -2$.

Tree Level. The dominant contributions coming from tree-level ϕ particle exchange enter as corrections to the R^2 , RF^2 , and F^4 operators of size

$$\delta(d_i) \sim \frac{1}{m_\phi^2} \quad (\text{tree}). \quad (2.28)$$

Here each contribution scales with a factor of $1/m_\phi^2$ coming from the ϕ propagator denominator.

Loop Level. First, let us consider loop corrections involving purely gravitational interactions. At one loop, the leading contributions enter through the renormalization

of the gravitational constant,

$$\delta(\kappa^{-2}) \sim m_\phi^{D-2} \quad (\text{loop}), \quad (2.29)$$

which follows straightforwardly from dimensional analysis. At loop level, gravitational interactions also yield contributions to higher-dimension operators,

$$\delta(d_i) \sim \kappa^2 m_\phi^{D-4} \quad (\text{loop}), \quad (2.30)$$

which are always subdominant to Eq. (2.28).

Loops involving gauge interactions will similarly renormalize the gauge coupling as well as the higher-dimension operator coefficients, yielding contributions that scale as Eq. (2.29) and Eq. (2.30) but with enhancement factors proportional to the charge-to-mass ratios of fundamental charged particles. In principle, these contributions can dominate. For example, in the standard model, the leading contributions to the Euler-Heisenberg Lagrangian come from loops of electrons. However, as shown in ??, this only happens when there are fundamental charged particles with large charge-to-mass ratios. In this case there is no claim to prove, since WGC is already satisfied. For this reason, we restrict our consideration to theories where all fundamental charged particles fail or are near the WGC bound without satisfying it. In this limit gauge interactions are of the same strength as gravitational interactions so the leading tree-level and loop-level corrections from both scale as in Eq. (2.28) and Eq. (2.29).

Region of Interest

From Eqs. (2.28), (2.29), and (2.30), we can estimate the corresponding corrections to the black hole entropy, which takes the schematic form

$$S \sim \frac{\rho^{D-2}}{\kappa^2} + \rho^{D-2} m_\phi^{D-2} + \rho^{D-4} m_\phi^{D-4} + \frac{\rho^{D-4}}{\kappa^2 m_\phi^2} + \dots, \quad (2.31)$$

where ρ is the radius of the black hole. The first term is the Bekenstein-Hawking entropy, the second term is the quantum correction to the gravitational constant, and the third and fourth terms are the quantum and classical corrections to the higher dimension operators, respectively. Demanding that classical entropy corrections dominate over all quantum corrections requires that

$$\rho \ll \frac{1}{\kappa m_\phi^{D/2}}. \quad (2.32)$$

Crucially, since m_ϕ is much smaller than the Planck scale, this constraint is consistent with $\rho \gg 1/m_\phi$, which is necessary to remain within the regime of validity of the effective field theory. For the remainder of this paper we focus on this regime of black hole masses.

Before moving on, let us comment briefly on the expectation of positivity for the quantum entropy corrections. While our results only rely on positivity of the classical contribution, it is reasonable to conjecture that the same might apply to quantum corrections. It is known, however, that the quantum contributions in Eq. (2.30) have indefinite sign and in $D = 4$ these correspond to well-studied logarithmic corrections to black hole entropy [128–131]. Nevertheless, these signs do not matter because we have already shown that these corrections are parametrically subdominant to the contributions from Eq. (2.29) related to the renormalization of the gravitational constant.

Meanwhile, corrections of the latter type have also been computed via heat kernel methods and found to be positive for minimally-coupled spin 0 and 1/2 particles but negative for spin 0 particles with non-minimal couplings [132] as well as spin 1 and spin 2 particles [133, 134]. There is, however, a longstanding debate over the physical meaning of these negative corrections. They indicate a naive mismatch with calculations of quantum field theoretic entanglement entropy, which is manifestly positive. While these contributions have been understood as the entanglement of certain edge modes [135, 136], the sign of the leading power-law divergence was also shown to be regulator-dependent. In general, these negative corrections are formally power-law divergent and scheme-dependent and such quantities should be at least partly absorbed into the renormalized gravitational constant [128, 134, 137, 138]. For a consistent ultraviolet completion, all divergences will disappear and the residual corrections will be finite. On physical grounds, it is expected that, if properly regulated, these quantum entropy corrections will be manifestly positive as expected from the manifest positivity of entanglement entropy.

2.4 Black Hole Spacetime

We now turn to the study of a spherically symmetric, positively charged black hole of mass M and charge Q in the presence of low-energy corrections to pure Einstein-Maxwell theory. For simplicity, we restrict to $D = 4$ dimensions for the remainder of the body of this paper, but all of our results generalize to arbitrary spacetime dimension $D \geq 4$, as shown in App. A.1.

Our aim is to derive new bounds on the higher-dimension operator coefficients c_i . As noted previously, this restricts our consideration to black holes large enough that the effective field theory is valid but small enough to satisfy Eq. (2.32), so $1/m_\phi \ll \rho \ll 1/\kappa m_\phi^2$, where m_ϕ is the mass scale of the new states. This range always exists provided there is a parametric separation between m_ϕ and the Planck scale. Furthermore, we consider the thermodynamically stable regime where $q/m > \sqrt{3}/2$ so the specific heat is positive.

Note that the mass and charge are defined at spatial infinity. Since we will only consider static spacetimes, the ADM and Komar formulations of these quantities are equivalent. Explicitly, the Komar mass and charge are⁶

$$M \sim \frac{1}{\kappa^2} \int_{i^0} n_\mu \sigma_\nu \nabla^\mu K^\nu \quad \text{and} \quad Q \sim \int_{i^0} n_\mu \nabla_\nu F^{\mu\nu}, \quad (2.33)$$

where the integral region i^0 is spatial infinity, n is the unit timelike normal vector, σ is the unit spatial outward-pointing normal vector, and K is the timelike Killing vector. Since the integral is evaluated at spatial infinity, only the leading behavior at large r contributes to these expressions. Because higher-dimension operators correct the metric and gauge field at subleading order in r , they do not affect the definition of the asymptotic mass and charge.

Unperturbed Solution

The unperturbed theory is described by the Lagrangian for Einstein-Maxwell theory in Eq. (2.3). For notational convenience we will sometimes describe the mass and charge in natural units of the gravitational constant,⁷

$$m = \frac{\kappa^2 M}{8\pi} \quad \text{and} \quad q = \frac{\kappa Q}{4\sqrt{2}\pi}. \quad (2.34)$$

We also define the extremality parameter

$$\xi = \sqrt{1 - \frac{q^2}{m^2}}, \quad (2.35)$$

⁶Here we take all black holes to be of definite mass even though in practice they have a small width given by their inverse lifetime. For instance, as classically stable objects, black holes can only decay quantum mechanically via Hawking emission and Schwinger pair production processes, which are suppressed by additional factors of the gravitational constant. Moreover, decays into smaller black holes will proceed via non-perturbative gravitational effects, which are exponentially suppressed.

⁷In D dimensions, the mass dimensions of various quantities are $[\kappa^2] = 2 - D$, $[R] = 2$, $[F] = D/2$, $[M] = 1$, $[Q] = 2 - D/2$, $[m] = [q] = 3 - D$, $[c_{1,2,3}] = D - 4$, $[c_{4,5,6}] = -2$, $[c_{7,8}] = -D$, and $[d_i] = -2$.

where a neutral black hole corresponds to $\xi = 1$ and an extremal black hole corresponds to $\xi = 0$. As noted previously, we will consider black holes with positive specific heat, corresponding to $q/m > \sqrt{3}/2$, or equivalently, $\xi < 1/2$.

The solution is the Reissner-Nordström black hole, whose metric takes the static and spherically symmetric form

$$ds^2 = \tilde{g}_{\mu\nu} dx^\mu dx^\nu = -\tilde{f}(r) dt^2 + \frac{1}{\tilde{g}(r)} dr^2 + r^2 d\Omega^2, \quad (2.36)$$

where the unperturbed metric components are

$$\tilde{f}(r) = \tilde{g}(r) = 1 - \frac{2m}{r} + \frac{q^2}{r^2} \quad (2.37)$$

and the unperturbed electromagnetic field strength is

$$\tilde{F}_{\mu\nu} dx^\mu \wedge dx^\nu = \frac{Q}{4\pi r^2} dt \wedge dr. \quad (2.38)$$

The unperturbed event horizon is the outer horizon of the Reissner-Nordström black hole and is located at the radius $r = \tilde{\rho}$, where

$$\tilde{\rho} = m + \sqrt{m^2 - q^2} = m(1 + \xi). \quad (2.39)$$

The absence of a naked singularity implies that the charge is bounded by the inequality

$$\frac{q}{m} \leq 1, \quad (2.40)$$

which is saturated in the case of an extremal black hole.

Perturbed Solution

In the presence of the higher-dimension operators in Eq. (2.4), the perturbed metric takes the form

$$ds^2 = g_{\mu\nu} dx^\mu dx^\nu = -f(r) dt^2 + \frac{1}{g(r)} dr^2 + r^2 d\Omega^2, \quad (2.41)$$

where the metric components are complicated functions of the coefficients c_i . However, as shown in Refs. [139, 140], it is straightforward to compute corrections to the Reissner-Nordström solution order-by-order in c_i . Following the prescription in ?? applied to the higher-dimension operators in Eq. (2.4), we find that at first order in c_i the radial component of the metric is

$$g(r) = 1 - \frac{2m}{r} + \frac{q^2}{r^2} - \frac{q^2}{r^6} \left\{ \begin{array}{l} \frac{4}{5}(d_2 + 4d_3)(6q^2 - 15mr + 10r^2) \\ + 8d_4(3q^2 - 7mr + 4r^2) + \frac{4}{5}d_5(11q^2 - 25mr + 15r^2) \\ + \frac{4}{5}d_6(16q^2 - 35mr + 20r^2) + \frac{8}{5}(2d_7 + d_8)q^2 \end{array} \right\}, \quad (2.42)$$

where the coefficients d_i are defined in terms of c_i in Eq. (2.27).

2.5 Calculation of Entropy

Wald Entropy Formula

We now compute the entropy corrections to black holes of size much greater than the Compton wavelengths of the heavy modes. A major advantage of this approach is that the effects of all short-distance degrees of freedom are encoded purely by higher-dimension operators. Moreover, even though these states are absent from the low-energy theory, their contributions to the entropy are fully accounted for by the Wald formula in Eq. (2.6).

For a spherically symmetric spacetime, the integral in Eq. (2.6) is trivial, yielding

$$S = -2\pi A \frac{\delta \mathcal{L}}{\delta R_{\mu\nu\rho\sigma}} \epsilon_{\mu\nu} \epsilon_{\rho\sigma} \Big|_{g_{\mu\nu}, \rho}, \quad (2.43)$$

where all quantities are evaluated for the perturbed metric and perturbed horizon radius, $\rho = \tilde{\rho} + \Delta\rho$. The perturbed horizon area is $A = 4\pi\rho^2$ and the binormal is

$$\epsilon_{\mu\nu}(r) = \sqrt{\frac{f(r)}{g(r)}} (\delta_\mu^t \delta_\nu^r - \delta_\mu^r \delta_\nu^t). \quad (2.44)$$

Expanding the area $A = \tilde{A} + \Delta A$ and the Lagrangian $\mathcal{L} = \tilde{\mathcal{L}} + \Delta\mathcal{L}$ in perturbations, we obtain

$$S = -2\pi \left(\tilde{A} \frac{\delta \tilde{\mathcal{L}}}{\delta R_{\mu\nu\rho\sigma}} + \tilde{A} \frac{\delta \Delta\mathcal{L}}{\delta R_{\mu\nu\rho\sigma}} + \Delta A \frac{\delta \tilde{\mathcal{L}}}{\delta R_{\mu\nu\rho\sigma}} + \dots \right) \epsilon_{\mu\nu} \epsilon_{\rho\sigma} \Big|_{g_{\mu\nu}, \rho}, \quad (2.45)$$

where $\tilde{A} = 4\pi\tilde{\rho}^2$ and the ellipses denote terms that are higher order in perturbations. The first term is straightforwardly obtained by differentiating Eq. (2.3) with respect to the Riemann tensor,

$$\frac{\delta \tilde{\mathcal{L}}}{\delta R_{\mu\nu\rho\sigma}} = \frac{1}{2\kappa^2} g^{\mu\rho} g^{\nu\sigma}, \quad (2.46)$$

where the proper (anti)symmetrization of indices on the right-hand side is implicit. Since the binormal is normalized as $\epsilon_{\mu\nu} \epsilon^{\mu\nu} = -2$, the first term in Eq. (2.45) is simply the unperturbed black hole entropy \tilde{S} defined in Eq. (2.7). Moving this term to the left-hand side of Eq. (2.45), we obtain an expression for the difference in entropies,

$$\Delta S = \Delta S_I + \Delta S_H, \quad (2.47)$$

split into an "interaction" and "horizon" contribution. Because we are working at first order in perturbations, both of these terms should be evaluated on the unperturbed metric and horizon radius. The interaction contribution,

$$\Delta S_I = -2\pi\tilde{A} \left. \frac{\delta\Delta\mathcal{L}}{\delta R_{\mu\nu\rho\sigma}} \epsilon_{\mu\nu}\epsilon_{\rho\sigma} \right|_{\tilde{g}_{\mu\nu}, \tilde{\rho}}, \quad (2.48)$$

appears because the interactions of photons and gravitons are modified at low energies. Meanwhile, the horizon contribution,

$$\Delta S_H = -2\pi\Delta A \left. \frac{\delta\tilde{\mathcal{L}}}{\delta R_{\mu\nu\rho\sigma}} \epsilon_{\mu\nu}\epsilon_{\rho\sigma} \right|_{\tilde{g}_{\mu\nu}, \tilde{\rho}} = \frac{2\pi}{\kappa^2} \Delta A, \quad (2.49)$$

is present because higher-dimension operators modify the black hole background, thus shifting the location of the horizon. Here we have substituted in Eq. (2.46) to write the right-hand side of this expression as simply the shift of the horizon area.

Interaction Contribution

To obtain the interaction contribution to the entropy shift we compute

$$\begin{aligned} \frac{\delta\Delta\mathcal{L}}{\delta R_{\mu\nu\rho\sigma}} = & 2c_1 R g^{\mu\rho} g^{\nu\sigma} + 2c_2 R^{\mu\rho} g^{\nu\sigma} + 2c_3 R^{\mu\nu\rho\sigma} \\ & + c_4 F_{\alpha\beta} F^{\alpha\beta} g^{\mu\rho} g^{\nu\sigma} + c_5 F^\mu{}_\alpha F^{\rho\alpha} g^{\nu\sigma} + c_6 F^{\mu\nu} F^{\rho\sigma}, \end{aligned} \quad (2.50)$$

where proper (anti)symmetrization on indices is left implicit as before. Substituting the unperturbed black hole background into Eq. (2.50) and evaluating Eq. (2.48), we obtain

$$\Delta S_I = \tilde{S} \times \frac{2}{m^2(1+\xi)^3} [8d_3 - 2(1-\xi)(d_2 + 6d_3 + 2d_4 + d_5 + 2d_6)], \quad (2.51)$$

written in terms of the coefficients defined in Eq. (2.27). Setting $\xi = 1$ in our expression for ΔS_I in Eq. (2.51) agrees with the expressions in ?? as well as their generalization to arbitrary dimension in ??.

Horizon Contribution

The horizon contribution to the entropy shift depends on the location of the perturbed horizon. Since the spacetime is static, the horizon is determined by zeros of the metric components $f(r)$ and $g(r)$ defined in Eq. (2.41). On general grounds, $f(r)$ and $g(r)$ have coincident zeros since otherwise the spacetime would contain a region with non-Lorentzian signature. Moreover, we have verified by explicit calculation that $f(r)$ and $g(r)$ share the same zeros at first order in perturbations.

The perturbed horizon is located at radius $\rho = \tilde{\rho} + \Delta\rho$. To compute ρ , we expand $g(r) = \tilde{g}(r) + \Delta g(r)$ at first order in perturbations, as defined in Eq. (2.42). The perturbed horizon radius then satisfies the equation

$$0 = g(\rho) = \tilde{g}(\tilde{\rho}) + \Delta g(\tilde{\rho}) + \Delta\rho \partial_{\tilde{\rho}} \tilde{g}(\tilde{\rho}). \quad (2.52)$$

The first term on the right-hand side vanishes by the definition of the unperturbed horizon radius. Solving for the horizon shift, we find

$$\Delta\rho = -\frac{\Delta g(\tilde{\rho})}{\partial_{\tilde{\rho}} \tilde{g}(\tilde{\rho})}. \quad (2.53)$$

At first order, the perturbed horizon area is then given by

$$\Delta A = A - \tilde{A} = 8\pi\tilde{\rho}\Delta\rho = -\frac{8\pi\tilde{\rho}\Delta g(\tilde{\rho})}{\partial_{\tilde{\rho}} \tilde{g}(\tilde{\rho})}. \quad (2.54)$$

Inputting the perturbed metric in Eq. (2.42) and evaluating Eq. (2.49), we obtain

$$\Delta S_{\text{H}} = \tilde{S} \times \frac{4(1-\xi)}{5m^2\xi(1+\xi)^3} [(1+4\xi)(d_2 + 4d_3 + d_5 + d_6) + 10\xi d_4 + 2(1-\xi)(2d_7 + d_8)]. \quad (2.55)$$

Note that the horizon contribution to the entropy shift is divergent in the $\xi \rightarrow 0$ limit corresponding to an extremal black hole. Physically, this occurs because the inner and outer horizons become degenerate, so $\partial_{\tilde{\rho}} \tilde{g}(\tilde{\rho}) \rightarrow 0$. In this case, Eq. (2.52) implies that for some fixed contribution $\Delta g(\tilde{\rho})$ from higher-dimension operators, the horizon must shift by a parametrically large amount $\Delta\rho$ in order to maintain the horizon condition.

Of course, the strict $\xi \rightarrow 0$ limit is pathological since this produces an infinite entropy shift, signaling a breakdown of perturbation theory. Demanding that the shift in entropy be much smaller than the unperturbed entropy, we obtain the constraint

$$\xi \gg \frac{|d_i|}{m^2}. \quad (2.56)$$

As shown in Eq. (2.32), the classical effects of higher-dimension operators are only dominant over the quantum for black hole radii smaller than a certain value, $\rho \ll 1/\kappa m_\phi^2$. Using that $d_i \sim 1/m_\phi^2$ for a tree-level ultraviolet completion, Eq. (2.56) becomes $\xi \gg \kappa^2 m_\phi^2$.

Perturbativity also requires that the shift in the inverse temperature $\Delta\beta$ be subdominant to the background inverse temperature $\tilde{\beta}$ of the unperturbed Reissner-Nordström black hole. As a consistency check, we have verified that $\beta = \partial_M S$ agrees with the

surface gravity of the perturbed black hole metric. For highly charged black holes, the unperturbed inverse temperature goes as $\tilde{\beta} \sim m/\xi$ while $\Delta\beta \sim d_i/m\xi^3$. Demanding that the correction be smaller than the leading contribution, $\Delta\beta \ll \tilde{\beta}$, we obtain the stronger condition

$$\xi \gg \frac{|d_i|^{1/2}}{m}. \quad (2.57)$$

Combining this with the upper bound on ρ from Eq. (2.32) and the scaling of d_i , we obtain

$$\xi \gg \kappa m_\phi. \quad (2.58)$$

Thus, it is always possible to take the limit of a highly charged black hole, $\xi \ll 1$, provided the mass scale m_ϕ of the heavy fields is far below the Planck scale as we have assumed throughout.

2.6 New Positivity Bounds

General Bounds

The total entropy shift $\Delta S = \Delta S_I + \Delta S_H$ is obtained by adding Eq. (2.51) and Eq. (2.55), yielding

$$\Delta S = \tilde{S} \times \frac{4}{5m^2\xi(1+\xi)^3} \times \left[(1-\xi)^2(d_2+d_5) + 2(2+\xi+7\xi^2)d_3 + (1-\xi)(1-6\xi)d_6 + 2(1-\xi)^2(2d_7+d_8) \right]. \quad (2.59)$$

As proven in Sec. 2.2, the entropy shift is positive under the assumptions we have stated. Combining Eq. (2.8) and Eq. (2.59), we obtain a family of positivity bounds,

$$(1-\xi)^2 d_0 + 20\xi d_3 - 5\xi(1-\xi)(2d_3+d_6) > 0, \quad (2.60)$$

where we have defined the parameter

$$d_0 = d_2 + 4d_3 + d_5 + d_6 + 4d_7 + 2d_8. \quad (2.61)$$

The bound in Eq. (2.60) is the main result of this work: a consistency condition on the coefficients of higher-dimension operator corrections to Einstein-Maxwell theory following from the positivity of corrections to the black hole entropy. The generalizations of Eqs. (2.59), (2.60), and (2.61) to arbitrary dimension D are derived and presented in Eqs. (A.18), (A.19), and (A.20) in App. A.1.

As discussed in Sec. 2.2, our proof of $\Delta S > 0$ applies to thermodynamically stable black holes, restricting consideration to the window $\xi \in (0, 1/2)$. The full space of bounds over this range defines a convex region in the space of coefficients d_i . Thus

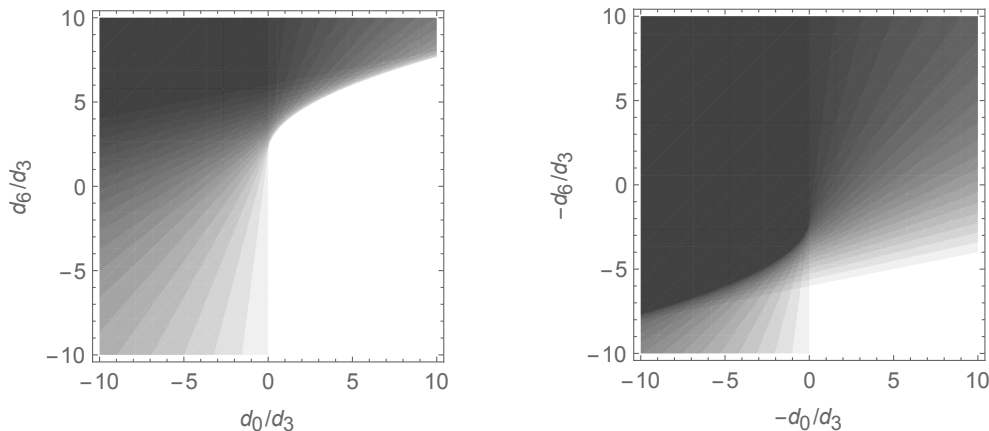


Figure 2.2: Constraints on higher-dimension operator coefficients derived from black hole entropy. The shaded regions are excluded, with the gradations corresponding to incremental values of $\xi \in (0, 1/2)$. The left and right panels correspond to $d_3 > 0$ and $d_3 < 0$, respectively. In either case, $d_0 < 0$ is forbidden so $d_0 > 0$ and the WGC is automatically satisfied.

the full space of positivity constraints, depicted in Fig. 2.2 for $D = 4$, is stronger than those implied by any finite set of choices for ξ .

We have derived these positivity conditions from a particular physical setup: a black hole of a given charge-to-mass ratio corresponding to $\xi \in (0, 1/2)$ and mass consistent with Eq. (2.32) so that our proof of $\Delta S > 0$ applies. Despite this specificity, we emphasize that the resulting bounds in Eq. (2.60) are consistency conditions on the effective action and thus hold *independently of the background*.

Examples and Consistency Checks

Our bound in Eq. (2.60) and its higher-dimensional generalization in Eq. (A.19) pass a number of explicit checks. To begin, we emphasize that these inequalities are invariant under a change of the field basis, which by reparameterization theorems should leave physical observables unchanged. As discussed in App. A.2, metric field redefinitions shift the higher-dimension operator coefficients d_i in a way that renders individual coefficients operationally meaningless. By studying these transformations, one can build a basis of field redefinition invariant combinations of coefficients, of which d_0, d_3, d_6 are a subset. Remarkably, while the separate contributions to the entropy from ΔS_I and ΔS_H are *not* invariant under field redefinitions, their sum ΔS is invariant for all ξ in arbitrary dimension D , as shown in App. A.2. Field redefinition invariance of the inequality $\Delta S > 0$ is a prerequisite for this bound

to have physical meaning.

On physical grounds, it is natural to expect that any positivity condition is preserved under renormalization group flow into the infrared. This is true because a consistent theory should continue to be consistent at arbitrarily long distances. Interestingly, this expectation agrees with known results on the one-loop divergences of pure Einstein-Maxwell theory in $D = 4$, which enter solely through the $R_{\mu\nu}R^{\mu\nu}$ operator [98]. The sign of this divergence is consistent with a negative beta function, indicating that the coefficient of this operator indeed increases in the infrared, consistent with Eq. (2.60).

We can also study Eq. (A.19) in simple concrete examples. First, consider any theory in general dimension D in which the strength of gravity is negligible relative to gauge interactions. In this limit all higher-dimension operators are vanishing except for d_7 and d_8 , which control the leading contributions to photon self-interactions in the Euler-Heisenberg effective action. Applying the logic of ??, we have computed the four-photon scattering amplitude at low energies and found that dispersion relations imply the positivity conditions $2d_7 + d_8 > 0$ and $d_8 > 0$, corresponding to different choices of external polarizations. In this case, the former inequality exactly implies that $d_0 > 0$ in general dimension D , thus providing a consistency check of Eqs. (2.60) and (A.19).

Second, we examine the scalar model described in Sec. 2.2. Translating from Euclidean to Lorentzian signature, we obtain the higher-dimension operator coefficients

$$d_i = \frac{1}{2m_\phi^2} \times \{a_\phi^2, 0, 0, 2a_\phi b_\phi, 0, 0, b_\phi^2, 0\}, \quad (2.62)$$

which, written in terms of d_0 using Eq. (A.20), give

$$d_0 = \frac{D-3}{8m_\phi^2} [(D-4)a_\phi + 2(D-2)b_\phi]^2, \quad (2.63)$$

which is a perfect square, so the bound in Eq. (A.19) is again satisfied.

Third, we study the low-energy description of the heterotic string, for which the higher-dimension operators have coefficients as given in Refs. [139, 141],

$$d_i = \frac{\alpha'}{64} \times \{4, -16, 4, 0, 0, 0, -3, 12\}, \quad (2.64)$$

where we have absorbed the dependence on the dilaton expectation value into α' . Plugging these parameters into Eq. (A.19) yields $(6D^2 - 30D + 37)\xi^2 + 2(D -$

$2)\xi + 2D - 5 > 0$, which holds for all $\xi \in (0, 1)$ and $D > 3$. Thus, we find that Eq. (A.19) is actually satisfied even beyond the range of thermodynamic stability and the critical dimension of the string.

The Weak Gravity Conjecture

In the limit of a highly charged black hole we take $\xi \ll 1$ and our general bound in Eq. (2.60) becomes

$$d_0 > 0, \quad (2.65)$$

with d_0 defined in terms of the other d_i in Eq. (2.61).

As it turns out, this inequality is intimately connected with the extremality condition for a black hole. To see why, consider the unperturbed Reissner-Nordström solution, for which the extremal charge-to-mass ratio is $\tilde{z} = q/m = 1$. In general, quantum corrections to the gravitational constant and electric charge will renormalize the right-hand side of this condition. Since these contributions affect black holes of all masses universally, their effects can simply be absorbed into the definitions of mass and charge. Meanwhile, higher-dimension operators also shift the maximum charge-to-mass ratio permitted for a physical black hole, i.e., a black hole free from naked singularities. In contrast, these corrections are mass-dependent, so they induce a physical shift of the extremality condition to $z = \tilde{z} + \Delta z$ [139].

To compute this shift, we analyze the metric component $g(r, z)$, interpreted as a function of both the radius and the charge-to-mass ratio. The shifted horizon is defined by the condition $g(\rho, z) = 0$. At linear order in perturbations, this condition becomes

$$0 = g(\rho, z) = \tilde{g}(\tilde{\rho}, \tilde{z}) + \Delta g(\tilde{\rho}, \tilde{z}) + \Delta \rho \partial_{\tilde{\rho}} \tilde{g}(\tilde{\rho}, \tilde{z}) + \Delta z \partial_{\tilde{z}} \tilde{g}(\tilde{\rho}, \tilde{z}). \quad (2.66)$$

Since the unperturbed black hole is extremal, the first and third terms on the right-hand side are zero. Solving for the shift in the charge-to-mass ratio yields

$$\Delta z = -\frac{\Delta g(\tilde{\rho}, \tilde{z})}{\partial_{\tilde{z}} \tilde{g}(\tilde{\rho}, \tilde{z})}. \quad (2.67)$$

By explicit calculation, the charge-to-mass ratio shift is

$$\Delta z = \frac{2d_0}{5m^2} > 0, \quad (2.68)$$

which is positive according to Eq. (2.65).

As shown in ??, if Δz is positive then small black holes *automatically* satisfy the WGC [104], which posits that an Abelian gauge theory consistently coupled

to quantum gravity must contain a state with charge-to-mass ratio greater than unity. In its original formulation [104], the WGC was presented with several compelling justifications. This included overwhelming circumstantial evidence from a long list of explicit examples in quantum field theory and string theory. A more direct argument was also presented in the form of an elegant thought experiment involving stable black hole remnants [142–146]. In particular, due to mass and charge conservation, a charged black hole is stable unless there exist lighter states with a higher charge-to-mass ratio, into which the black hole can decay. In the infinite-mass limit, the charge-to-mass ratio of an extremal black hole is dictated by the Reissner-Nordström solution and approaches unity. Violation of the WGC would then imply the existence of an infinite tower of stable remnants labeled by the extremal black hole mass, asserted as pathological in [147]. While this thought experiment offers some crucial physical intuition for the WGC, it falls short since there do not exist formal proofs that stable black hole remnants are actually inconsistent with more established principles like the covariant entropy bound. In many cases the number of black hole remnants is very large but still finite; furthermore, the states are labeled by distinct charges and are thus in principle distinguishable [147].

On the other hand, if the WGC is satisfied then extremal black holes are unstable to decay. We have shown here that considerations of black hole entropy imply that the charge-to-mass ratio of an extremal black hole increases with decreasing size. In particular, higher-dimension operators induce a positive shift of the extremality bound, but these corrections decouple for large black hole masses. The upshot is then that an extremal black hole of a given mass can always decay into smaller extremal black holes of a greater charge-to-mass ratio, following the upper curve in Fig. 2.1. Our bound in Eq. (2.65)—and thus our proof of the WGC—generalizes to D spacetime dimensions, as shown in App. A.1.

Let us comment on the relation between our results and previous work connecting black holes and the WGC. First, while the argument in this paper makes critical use of extremal black holes, our reasoning is completely different from the original proposal of [147], hinging instead on the thermodynamic entropy of black holes rather than their stability. More recently, the WGC has also been linked to the cosmic censorship conjecture [148]. We leave an analysis of this and its relationship to black hole entropy for future work.

In other recent studies [147, 149], the WGC has also been evaluated in the context of

black hole entropy using methodologies that differ substantially from our own. Both [147] and [149] examine the leading logarithmic corrections to black hole entropy due to the quantum effects of light matter particles. Such effects are relevant for black holes of size parametrically smaller than the Compton wavelength of the matter. We, in contrast, consider the opposite regime, which effectively corresponds to a gapped spectrum.

Furthermore, Refs. [147, 149] argue for the inconsistency of WGC violation through quite different means: [147] makes the argument through the appearance of a low cutoff, while [149] employs the second law of thermodynamics. It is crucial to note that our assertion of a positive entropy shift is logically distinct from the second law of thermodynamics, which applies to the difference in entropy before and after a physical process but within the same physical system. Our construction is instead based on the positivity of classical entropy corrections proven in Sec. 2.2.

Finally, Refs. [147, 149] and also another interesting approach [150] all consider concrete models with explicit spectra of charged and neutral scalars and fermions. For this reason, these works at best show that certain WGC-violating theories are inconsistent. This leaves the logical possibility that more complicated theories that violate the WGC might still be judged valid by their analyses. In comparison, our work applies to large black holes in a general low-energy effective theory, which is insensitive to the precise details of the spectrum and hence constitutes a model-independent argument for the WGC.

Entropy, Area, and Extremality

A priori, it is somewhat miraculous that the entropy constraint in Eq. (2.65) is literally equivalent to the extremality condition in Eq. (2.68). To briefly summarize, we have shown that

$$\Delta S \sim \Delta\rho \sim \Delta z > 0, \quad (2.69)$$

so the low-energy corrections to the near-extremal black hole entropy, area, and extremality condition are all proportional to each other and all positive.

Why does the same combination of coefficients d_0 appear in all of these inequalities? As it turns out, this connection is not so mysterious once one considers the perturbed metric component $g(\rho, z)$ in Eq. (2.66) as a function of the shift in horizon radius $\Delta\rho$ and the shift in the charge-to-mass ratio Δz . For a near-extremal black hole of fixed charge and mass, we set $\Delta z = 0$ and thus $\Delta\rho = -\Delta g / \partial_{\tilde{\rho}} g$. On the other hand, if the charge and mass are free but the unperturbed system is exactly extremal, then

the $\Delta\rho$ term drops out and the charge-to-mass ratio shift is $\Delta z = -\Delta g/\partial_z \tilde{g}$. At the same time, the radial component of the metric \tilde{g} is by definition spacelike outside the horizon, so $\partial_\rho \tilde{g} > 0$. Moreover, since \tilde{g} dictates the gravitational potential at long distances, it decreases with m and thus increases with the charge-to-mass ratio, so $\partial_z \tilde{g} > 0$. This logic implies that $\Delta\rho$ and Δz have the same sign. Since the entropy shift for a near-extremal black hole is dominated by the shift in the horizon, $\Delta S \sim \Delta\rho$, we discover that $\Delta S > 0$, $\Delta\rho > 0$, and $\Delta z > 0$ are equivalent bounds.

Conveniently, the above logic immediately extends to the multi-charge generalization of the WGC proposed in ???. For a theory with multiple Abelian factors, the charge-to-mass ratio defines a vector \mathbf{z} in charge space. The WGC then mandates that the unit ball representing all possible large black holes be contained within the convex hull spanned by the set of all \mathbf{z} for the lighter states in the theory. Crucially, for a multi-charged black hole, the perturbed metric only depends on the magnitude of its charge and not the direction. Hence, Eq. (2.66) still applies, provided we define $\tilde{z} = |\mathbf{z}|$ as the magnitude of the charge-to-mass ratio vector of the black hole and $\Delta z = \Delta\mathbf{z} \cdot \tilde{\mathbf{z}}/|\tilde{\mathbf{z}}|$ as its shift. Repeating exactly the argument of the previous paragraph, we learn that $\Delta S > 0$, $\Delta\rho > 0$, and $\Delta\mathbf{z} \cdot \tilde{\mathbf{z}} > 0$ are all equivalent. The last inequality implies that the extremality condition for a multi-charged extremal black hole is perturbed so that the corresponding unit ball is expanded outward in every direction, thus proving the multi-charge version of the WGC given by the convex hull condition in ???.

2.7 Discussion and Conclusions

In this paper, we derived a positivity condition on classical corrections to the Bekenstein-Hawking entropy. For near-extremal black holes this enforces positivity of a certain linear combination of coefficients of higher-dimension operators. This very same combination of couplings corrects the extremality condition for black holes so that their charge-to-mass ratios approach unity from above for increasing size. Large extremal black holes are thus unstable to decay to smaller extremal black holes. Since the latter have charge-to-mass ratios greater than unity, they automatically fulfill the requirement of the WGC.

Our findings leave a number of avenues for future work. First, it would be interesting to determine if entropy considerations have any additional implications for the swampland program, for example by introducing new operators in extended theories like Einstein-dilaton gravity or by considering black holes embedded in asymptot-

ically AdS or dS space, rotating black holes, or black holes of different topologies. Second, one would ideally like to understand the relationship, if any, between these entropy bounds and other constraints on low-energy dynamics coming from causality, analyticity, and unitarity. Indeed, the positivity of entropy shifts discussed in this paper stems from state counting in the ultraviolet, which is highly reminiscent of dispersion relation bounds utilizing the positivity of forward cross-sections [108–111, 124, 151–153] and amplitudes approaches based on the positivity of spectral representations [112, 154, 155].

Acknowledgments

We thank Nima Arkani-Hamed, Raphael Bousso, Sean Carroll, William Cottrell, Daniel Harlow, Tom Hartman, Yasunori Nomura, Hiroshi Ooguri, Matthew Reece, Prashant Saraswat, Gary Shiu, Leo Stein, and Aron Wall for helpful discussions. C.C. and J.L. are supported by a Sloan Research Fellowship and DOE Early Career Award under grant no. DE-SC0010255. G.N.R. is supported by the Miller Institute for Basic Research in Science at the University of California, Berkeley.

BOOTSTRAPPING HEISENBERG MAGNETS AND THEIR CUBIC INSTABILITY

This chapter is based on S. M. Chester, W. Landry, **J. Liu**, D. Poland, D. Simmons-Duffin, N. Su, and A. Vichi (**alphabetical order**), *Bootstrapping Heisenberg Magnets and their Cubic Instability*, Phys. Rev. D **104**, 105013, Editors' Suggestion, (2021), arxiv:2011.14647 [hep-th].

Abstract: We study the critical $O(3)$ model using the numerical conformal bootstrap. In particular, we use a recently developed cutting-surface algorithm to efficiently map out the allowed space of CFT data from correlators involving the leading $O(3)$ singlet s , vector ϕ , and rank-2 symmetric tensor t . We determine their scaling dimensions to be $(\Delta_s, \Delta_\phi, \Delta_t) = (0.518942(51), 1.59489(59), 1.20954(23))$, and also bound various OPE coefficients. We additionally introduce a new "tip-finding" algorithm to compute an upper bound on the leading rank-4 symmetric tensor t_4 , which we find to be relevant with $\Delta_{t_4} < 2.99056$. The conformal bootstrap thus provides a numerical proof that systems described by the critical $O(3)$ model, such as classical Heisenberg ferromagnets at the Curie transition, are unstable to cubic anisotropy.

3.1 Introduction

Numerical bootstrap methods [156, 157] (see [158, 159] for recent reviews) have led to powerful new results in the study of conformal field theories (CFTs). In [4, 5] we developed an approach to large-scale bootstrap problems which allowed for precise determinations of the CFT data of the 3d critical $O(2)$ model. In this work, we continue the exploration of large-scale bootstrap problems by applying the technology introduced in [4] to the study of the 3d critical $O(3)$ model.

Concretely, we apply these methods to study correlation functions of the lowest-dimension singlet, vector, and rank-2 scalars in the three-dimensional critical $O(3)$ model. Using the "cutting surface" algorithm introduced in [4], we compute the allowed region for the CFT data of these leading scalar operators. Our results, together with comparisons to results from Monte Carlo simulations, are summarized in table 3.1. We also introduce a new algorithm and software implementation called

`tiptop`, which allows us to efficiently test allowed gaps for other operators across this region. We use it to determine an upper bound on the dimension of the lowest-dimension rank-4 scalar.

The 3d $O(3)$ model is a well-studied renormalization group (RG) fixed point, and its critical exponents have been computed using many methods, both theoretical and experimental. This model describes the critical behavior of isotropic magnets, such as the Curie transition in isotropic ferromagnets, and antiferromagnets at the Néel transition point. Moreover, since disorder corresponds to an irrelevant perturbation,¹ the model also describes isotropic magnets with quenched disorder.

One of the main open questions about the $O(3)$ model is its stability under cubic deformations. The majority of magnets present in nature are indeed not isotropic: this means that the microscopic Hamiltonian describing the system in the ultraviolet (UV) is not invariant under the full $O(3)$ symmetry group but only under a discrete subgroup, such as the cubic symmetry group. This implies that additional terms will be generated at the microscopic level that are invariant under cubic symmetry but transform in a non-trivial representation of $O(3)$. If any of those deformations turn out to be relevant, the $O(3)$ fixed point would be unstable and could not be reached without further tuning in the UV theory. The attractive, stable, fixed point would instead be the 3d cubic model. Field theory computations and Monte Carlo simulations have shown that these two models have very similar critical exponents: hence, if the cubic perturbation is relevant, it should be very close to marginality and the RG flow connecting the two theories is very short. We will come back to this point in section 3.1.

We give a definite answer to the above question: the $O(3)$ model is unstable under cubic deformations. This information is encoded in the dimension of the lowest rank-4 scalar t_4 , which in the $O(3)$ model satisfies $\Delta_{t_4} < 3$. As we will discuss, this implies that the $O(3)$ model is also unstable with respect to the biconal fixed point with $\mathbb{Z}_2 \times O(2)$ symmetry. Relevance of t_4 has been previously suggested by Monte Carlo [8] and perturbative expansions [162], but the proximity to marginality and near degeneracy of the critical exponents between the cubic, biconal, and $O(3)$ fixed points makes this a subtle question ideal for the precision and rigor of the conformal bootstrap.

¹This is the case in any $O(N)$ model with $N \geq 2$.

CFT data	method	value	ref
Δ_s	MC	1.5948(2)	[7]
	CB	1.5957(55)	[160]
	CB	1.59488(81)	this work
Δ_ϕ	MC	0.518920(25)	[7]
	CB	0.51928(62)	[160]
	CB	0.518936(67)	this work
Δ_t	MC	1.2094(3)	[8]
	CB	1.2095(55*)	[161]
	CB	1.20954(32)	this work
Δ_{t_4}	MC	2.987(4)	[8]
	CB	< 2.99056	this work
$\lambda_{\phi\phi s}$	CB	0.5244(11*)	[160]
	CB	0.524261(59*)	this work
λ_{sss}	CB	0.499(12*)	[160]
	CB	0.5055(11*)	this work
λ_{tts}	CB	0.98348(39*)	this work
$\lambda_{\phi\phi t}$	CB	0.87451(22*)	this work
λ_{ttt}	CB	1.49957(49*)	this work

Table 3.1: Comparison of conformal bootstrap (CB) results with previous determinations from Monte Carlo (MC) simulations. We denote the leading rank-0, rank-1, rank-2, and rank-4 scalars by s, ϕ, t, t_4 , respectively. Bold uncertainties correspond to rigorous intervals from bootstrap bounds. Uncertainties marked with a * indicate that the value is estimated non-rigorously by sampling points.

Theoretical approaches to the 3d $O(3)$ model

We start by briefly reviewing past approaches to the 3d $O(3)$ model, including field theory studies, Monte Carlo, and past results obtained by conformal bootstrap techniques. We also describe related models and motivate the calculations in this work.

The simplest continuum field theory in the $O(3)$ universality class is the theory of a scalar field $\vec{\phi}$ transforming in the fundamental representation of $O(3)$ with Lagrangian

$$\mathcal{L} = \frac{1}{2}|\partial\vec{\phi}|^2 + \frac{1}{2}m^2|\vec{\phi}|^2 + \frac{g}{4!}|\vec{\phi}|^4. \quad (3.1)$$

A large negative mass-squared for the scalar induces spontaneous symmetry breaking and leads to the ordered phase, while a large positive mass-squared leads to

the disordered phase. The critical point is achieved by tuning the UV mass so that the infrared (IR) correlation length diverges. The β function of the coupling g has been computed in the ε -expansion and in a fixed-dimension scheme. After a Borel-resummation, both methods predict the existence of an IR stable fixed point. We will review these results in the next sections.

The IR limit of the above field theory captures the same physics as the Heisenberg model. This model consists of a lattice of classical spins \vec{S}_i , which can take values on a three-dimensional sphere. The Hamiltonian has only nearest-neighbor interactions:

$$\mathcal{H} = -J \sum_{\langle i,j \rangle} \vec{S}_i \cdot \vec{S}_j + H \sum_i S_i, \quad (3.2)$$

where we also introduced an external magnetic field H . When the parameter J is positive, the ground state corresponds to all spins aligned, corresponding to ferromagnets. When $J < 0$, the energy is minimized when neighboring spins are anti-aligned, corresponding to antiferromagnets.

For small J , the line $H = 0$ separates a ferromagnetic phase from the paramagnetic one. This line represents a first-order transition and terminates at a value $J = J_c$, where the correlation length of the system diverges, and the transition becomes second order. For $J > J_c$, there is only a disordered phase. At $J = J_c$, the theory in the IR is in the same universality class of the field theory defined in (3.1). The critical exponents are related to operator dimensions at the fixed point as

$$\Delta_\phi = \frac{1 + \eta}{2}, \quad \Delta_s = 3 - \frac{1}{\nu}, \quad \Delta_t = 3 - Y_2. \quad (3.3)$$

Here, $s \sim |\vec{\phi}|^2$ denotes the lowest-dimension singlet scalar, while $t_{ij} \sim (\phi_i \phi_j - \text{trace})$ denotes the lowest rank-2 scalar. More generically the exponents Y_r are associated to the dimensions of the lowest rank- r scalar operator.² In the $O(N)$ model, the dimension of the lowest traceless symmetric operator t describes the instability of the theory against anisotropic perturbations. Because of this, it plays an important role in the description of multicritical phenomena. For instance, the critical behavior near a bicritical point where two critical lines with $O(n_1)$ and $O(n_2)$ symmetry meet gives rise to a critical theory with enlarged $O(n_1 + n_2)$ symmetry.

The Hamiltonian (3.2) is a simplified model of magnetic interactions, since in a real crystalline solid other interactions are present. For instance, the crystal lattice structure could give rise to magnetic anisotropy. In cubic-symmetric lattices this

²Sometimes in the literature they are replaced by the crossover exponents $\phi_r = \nu Y_r$.

effect produces an interaction localized at each lattice point i of the form $\sum_{k=1}^3 (S_i^k)^4$. This perturbation breaks the $O(3)$ global symmetry of the Heisenberg Hamiltonian, and therefore it cannot be generated by an RG transformation. As such, the IR fixed point of (3.2) will be described by an $O(3)$ invariant CFT.

$O(N)$ vs. multi-critical models

The $O(3)$ model described above can be generalized to $O(N)$ by promoting $\vec{\phi}$ to an N component field. We can also consider the closely related cubic model, which describes the continuum limit of the Hamiltonian (3.2) with the addition of the $O(N)$ breaking term $\sum_{k=1}^N (S_i^k)^4$. This interaction is indeed invariant under the symmetries of a hyper-cubic lattice, namely permutations and reflection of the three axes. The field ϕ_i , $i = 1, \dots, N$, transforms in the fundamental representation of the permutation group \mathcal{S}_N . Moreover, each component is odd under a reflection of the corresponding axis. The composition of these transformations gives rise to the hypercubic symmetry group $C_N = \mathbb{Z}_N \times \mathcal{S}_N$.

Compared to (3.1), the Lagrangian of the hypercubic model has an additional term in the potential:

$$\mathcal{L} = \frac{1}{2} \sum_{i=1}^N \left((\partial_\mu \phi_i)^2 + m^2 \phi_i^2 \right) + \frac{g}{4!} \left(\sum_{i=1}^N \phi_i^2 \right)^2 + \frac{h}{4!} \sum_{i=1}^N \phi_i^4. \quad (3.4)$$

The computation of the two β -functions β_g and β_h reveals the existence of four fixed points: the trivial fixed point ($g = h = 0$), the N decoupled copies of the Ising model ($h \neq 0, g = 0$), the $O(N)$ fixed point ($g \neq 0, h = 0$) and the cubic model ($g \neq 0, h \neq 0$). It is straightforward to see that the first two are unstable since the quartic operator parametrized by g is relevant in both theories.³ Determining which one of the other two fixed points is stable is a more complicated issue, and it turns out to be N dependent.

One way to rephrase the above question is to notice that the additional term in (3.4) can be rewritten as

$$\sum_{i=1}^N \phi_i^4 = \sum_{i=1}^N t_4^{iiii} + \frac{3}{N+2} \left(\sum_{i=1}^N \phi_i^2 \right)^2, \quad (3.5)$$

where t_4^{ijkl} is the traceless symmetric combination of four fields. The added term in the potential, in $O(N)$ notation, can be written as a combination of a rank-4 field

³The case of N decoupled Ising model corresponds to products of operators $\epsilon_i \sim \phi_i^2$ belonging to different copies where $2\Delta_\epsilon < 3$ in the Ising model.

and a singlet. We know that the singlet is irrelevant at the $O(N)$ fixed point, by definition. Thus the stability of the $O(N)$ fixed point or the cubic point is linked to the value of the dimension of the operator t_4 .

In the $O(2)$ model the operator t_4 is irrelevant. A simple proof of this is to notice that for $N = 2$, as long as $h \neq 0$, the cubic Lagrangian can be mapped in the Lagrangian of two decoupled Ising models. This cubic fixed point coincides with the decoupled Ising fixed point, which is unstable. Field theory and Monte Carlo determinations of the dimension of t_4 agree with this argument. This is also consistent with the assumptions made in [4].

On the contrary, at large N , the operator t_4 is relevant, and the cubic fixed point is stable. Thus, it is important to know at which value $N = N_c > 2$ the operator t_4 becomes relevant.

A second closely related model is the multi-critical point with $O(n_1) \times O(n_2)$ symmetry. A field theory description is given in terms of two sets of scalar fields $\vec{\phi}_1$ and $\vec{\phi}_2$, transforming respectively in the fundamental representation of $O(n_1)$ and $O(n_2)$, with Lagrangian:

$$\mathcal{L} = \frac{1}{2} \sum_{i=1}^2 |\partial_\mu \vec{\phi}_i|^2 + \frac{g_1}{4!} \left(|\vec{\phi}_1|^2 \right)^2 + \frac{g_2}{4!} \left(|\vec{\phi}_2|^2 \right)^2 + \frac{h}{4} |\vec{\phi}_1|^2 |\vec{\phi}_2|^2, \quad (3.6)$$

where we have already set to zero all the mass terms. The analysis of the perturbative β functions shows the existence of six fixed points. Some we already know: the free one ($g_i = 0, h = 0$), the two Wilson Fisher fixed points ($g_1 \neq 0, g_2 = h = 0$ and same with $1 \leftrightarrow 2$), the decoupled fixed point (DFP, $g_i \neq 0, h = 0$), the symmetry enhanced $O(n_1 + n_2)$ Wilson Fisher fixed point, and lastly the biconal fixed point (BFP). The latter one also has all couplings nonvanishing, but the global symmetry is not enhanced.

The problem of understanding the stable fixed point can be again reduced to studying the (ir)relevance of given deformations in the various CFTs. For instance, by inspecting the dimension of the composite operator built out of the lowest dimension scalar singlets in $O(n_1)$ and $O(n_2)$ theories, one can conclude that the DFP is stable for any $N = n_1 + n_2 \geq 4$. It is unstable for $N \leq 3$, although the perturbation is close to being marginal.⁴

The issue of stability of $O(N)$ vs. the BFP is again related to the dimension of a certain operator. In the Lagrangian formulation, this is a combination of quartic

⁴The most precise bootstrap determination [4, 160] gives $\Delta_{[s_{Z_2}, s_{O(2)}]} = \Delta_{s_{Z_2}} + \Delta_{s_{O(2)}} = 2.92398(23) < 3$.

interactions. At the $O(N)$ fixed point this term is mapped in a combination of the second-lowest rank-0 (S'), second-lowest rank-2 (t'_2) and leading rank-4 scalar operator t_4 . If any of these operators is relevant, then the $O(N)$ fixed point is unstable. While the former two are known to be always irrelevant for any N , the latter is the object of investigations. In particular, if $\Delta_{t_4} < 3$ for $N = 3$, then among the fixed points, the BFP will be the stable one.

Field theory results

CFT data	method	value	ref
Δ_s	$d = 3$ exp	1.5840(14)	[163]
	ε -exp	1.580(11)	[164]
	HT	1.603(4)	[165]
Δ_ϕ	$d = 3$ exp	0.5175(4)	[163]
	ε -exp	0.5188(23)	[164]
	HT	0.5180(35)	[165]
Δ_t	$d = 3$ exp	1.20(3)	[166]
	ε -exp	1.210(3)	[166]
	HT	1.24(2)	[167]
Δ_{t_4}	$d = 3$ exp	2.987(6)	[162]
	ε -exp	2.997(4)	[162]

Table 3.2: Comparison of field theory results using various techniques: fixed-dimensional expansion in three dimensions ($d = 3$ exp), epsilon expansion (ε -exp) and high temperature expansion (HT). We denote the leading rank-0, rank-1, rank-2, and rank-4 scalars by s, ϕ, t, t_4 , respectively. Another estimate of Δ_t in the fixed-dimensional expansion can be found in [13] in terms of the crossover exponents $\phi_T = Y_2\nu$, with $Y_2 = 3 - \Delta_t$. We do not report it here because the errors depend on the value of ν used.

Both the $O(3)$ model and the cubic model have been extensively studied using different expansion techniques. β -functions for these models are known up to high order in both the ε -expansion and fixed-dimension expansion, and critical exponents have been computed by Borel resumming the respective series.⁵ We

⁵Both approaches are based on a perturbative expansion in the quartic interaction g up to a certain loop order. In the fixed dimension approach one works directly in $d = 3$ dimension and looks for solutions of the Borel resummed β -function $\beta^{\text{BR}}(g_*) = 0$. Critical exponents are then computed as $\nu^{\text{BR}}(g_*)$. In order to remove the divergences one imposes suitable renormalization conditions. Historically the term "fixed dimension" refers to renormalization conditions at zero momentum; the use of a minimal subtraction scheme is instead called a "minimal subtraction scheme without ε -expansion". In the proper ε -expansion approach one works in $d = 4 - \varepsilon$ dimensions and solves

report in table 3.2 the latest results obtained with field theory techniques.

The question of stability of fixed points has also been discussed in the literature. As we discussed in the previous section, this question can be addressed in two ways: by computing the dimension of the lowest dimension rank-4 scalar in the $O(3)$ model, or by computing the value N_c at which the dimension of the second-lowest rank-0 scalar in the cubic model becomes exactly marginal.⁶ Results from both methods support the conclusion that $O(3)$ is unstable while the cubic model is stable. The formula for N_c in the ε -expansion is [168, 169]:

$$N_c = 4 - 2\varepsilon + 2.58847559\varepsilon^2 - 5.87431189\varepsilon^3 + 16.82703902\varepsilon^4 + O[\varepsilon^5], \quad (3.7)$$

and after resummation gives $N_c = 2.89(2)$.

Analysis of the ε -expansion or fixed-dimension perturbative series in the cubic model [166, 170, 171] shows that the critical exponents of the two models are very close:

$$\nu_{O(3)} - \nu_{\text{cubic}} = 0.0003(3), \quad \eta_{O(3)} - \eta_{\text{cubic}} = 0.0001(1). \quad (3.8)$$

These differences are much smaller than the typical experimental error (e.g., [172]). This makes distinguishing the two models experimentally very challenging. Curiously, the first few terms in the of the ε -expansion of the critical exponents in (3.8) are quite different, and it is only after the Borel resummation that the two values appear quite close.

Similarly, also the biconal $\mathbb{Z}_2 \times O(2)$ model and the $O(3)$ critical exponents are very close, as the flow connecting the two is driven by the same almost marginal operator as in the cubic case:

$$|\nu_{O(3)} - \nu_{\text{BFP}}| \lesssim 0.001, \quad |\eta_{O(3)} - \eta_{\text{BFP}}| = 0.0005, \quad |\eta_{O(3)} - \eta'_{\text{BFP}}| = 0.0001, \quad (3.9)$$

where η_{BFP} and η'_{BFP} correspond to the two relevant order parameters charged respectively under \mathbb{Z}_2 or $O(2)$.

the condition $\beta(g_*) = 0$ order by order in ε . Plugging the solution $g_*(\varepsilon)$ into the expression for the critical exponent one gets a series in ε that can be Borel resummed. The final critical exponents are then computed as $\nu^{\varepsilon\text{-BR}}(\varepsilon = 1)$.

⁶The lowest dimension one corresponds to the mass deformation and is always relevant; the second-lowest corresponds to a combination of the two quartic interactions. The orthogonal combination is related to the Lagrangian operator via the equation of motion and is irrelevant.

Monte Carlo results

Using Monte Carlo (MC) techniques, it is possible to obtain precise estimates of the critical exponents for both the $O(3)$ model and the cubic model, as well as information about their stability. Such determinations can also be improved when combined with finite-size scaling (FSS) or high-temperature expansion (HT) methods. A precise determination of the ν and η critical exponents was made using MC and FSS methods in [173]. A more precise analysis combining MC with HT techniques was carried out in [174], while a more precise MC and FSS study was performed in [8]. A very precise MC and FSS analysis of an icosahedral model, as well as improved MC and HT analyses were recently presented in [7]. Several other less precise determinations can be found in [172]. The dimensions relevant to anisotropic perturbations of rank-2,3,4 were computed in [8, 175] using MC and FSS methods, and support the conjecture that the $O(3)$ model is unstable under cubic deformations. These results are summarized in table 3.1.

The conformal bootstrap

Three dimensional $O(3)$ models have been studied with bootstrap methods in a series of papers [160, 161, 176], first by considering the correlation function $\langle \phi_i \phi_j \phi_k \phi_l \rangle$, where ϕ_i is the lowest-dimension scalar transforming in the vector representation of $O(N)$, and then by also including correlation functions involving the lowest-dimension singlet scalar s . The most precise determination of the critical exponents was obtained in [160], which isolated a three dimensional region in the space $\{\Delta_\phi, \Delta_s, \lambda_{sss}/\lambda_{\phi\phi s}\} = \{0.51928(62), 1.5957(55), 1.205(9)\}$, under the assumption that ϕ_i and s are the unique relevant scalar operators in their representations. In addition, by scanning over this island, [160] determined the magnitude of the leading OPE coefficient to be $\lambda_{\phi\phi s} = 0.5244(11)$.

Theories invariant under the cubic symmetry group were also studied using bootstrap methods using single correlators [177, 178], and mixed correlators [179, 180]. In particular [178] analyzed the bootstrap equations assuming the hypercubic symmetry group $C_N = \mathbb{Z}_N \rtimes \mathcal{S}_N$ and observed a series of kinks for various values of N . However, the locations of the kinks in the singlet sector were degenerate with the $O(N)$ kinks (and hence compatible with (3.8)), likely reflecting a symmetry enhancement in the extremal bootstrap solutions [181–185], while the bounds in other sectors did not seem to be saturated by the cubic model. The mixed-correlator analysis of [179, 180] also did not manage to isolate the cubic model but rather found evidence of a new

theory, called the "Platonic CFT," with cubic symmetry and operator dimensions not matching any known CFT.

In this work, we study the $O(3)$ model with numerical bootstrap techniques using a larger system of correlation functions than before: in addition to ϕ_i and s , we incorporate the lowest-dimension rank-2 scalar $t_{ij} \sim \phi_{(i}\phi_{j)}$. This setup is similar to the one leading to the successful results obtained in [4] for the $O(2)$ model. Following the strategy detailed in [4], we first scan over the three operator dimensions $\{\Delta_\phi, \Delta_s, \Delta_t\}$ and the OPE coefficients $\{s_{ss}, \phi\phi s, t_{ts}, \phi\phi t, t_{tt}\}$ (or more precisely their ratios) and we determine a three dimensional island in the space of operator dimensions, along with an associated allowed set of OPE coefficient ratios. Next, we compute upper and lower bounds on the magnitude $\lambda_{\phi\phi s}$, as well as on the current and stress-tensor central charges C_J and C_T . Finally, we enlarge the parameter space to include one more parameter: the dimension of the lowest rank-4 scalar Δ_{t_4} . Using the new `tiptop` algorithm, which we describe in section 3.3, we carve out the allowed region in the enlarged four-dimensional space and obtain an upper bound on Δ_{t_4} .

Structure of this work

The remainder of this work is structured as follows. In section 3.2 we describe the crossing equations and relevant $O(3)$ representation theory. In section 3.3 we describe the new `tiptop` algorithm that we use in order to bound Δ_{t_4} . In section 3.4 we describe the results of our numerical bootstrap calculations and in section 3.5 we describe directions for future research. Various appendices describe the code availability, software setup, details about our tensor structures, and give a list of allowed and disallowed points that we have computed.

3.2 The $O(3)$ model

Crossing equations

We begin by describing the representation theory of $O(3) = \mathbb{Z}_2 \times SO(3)$. We label the irreducible representations \mathbf{q}^\pm of $O(3)$ by the usual $SO(3)$ rank \mathbf{q} tensor of dimension $2q + 1$ for $q \in \frac{1}{2}\mathbb{Z}_{\geq 0}$, as well as the \mathbb{Z}_2 parity \pm . Tensor products of these irreps are given by

$$\mathbf{q}_1^\pm \otimes \mathbf{q}_2^\pm = \bigoplus_{q_a=|q_1-q_2|}^{q_1+q_2} \mathbf{q}_a^+, \quad \mathbf{q}_1^\pm \otimes \mathbf{q}_2^\mp = \bigoplus_{q_a=|q_1-q_2|}^{q_1+q_2} \mathbf{q}_a^-, \quad (3.10)$$

where if $\mathbf{q}_1^\pm = \mathbf{q}_2^\pm$, then the even/odd \mathbf{q}_a are in the symmetric/antisymmetric part of the tensor product.

Operators $O_{\mathbf{q}^\pm}(x)$ in the irrep \mathbf{q}^\pm can be written in terms of $SO(3)$ fundamental indices $i = 1, 2, 3$ as rank- q symmetric traceless tensors $O_\pm^{i_1 \dots i_q}(x)$ with the extra \mathbb{Z}_2 labels \pm . Four-point functions of scalar operators $\varphi_\pm^{i_1 \dots i_q}(x)$ can be expanded in the s -channel in terms of conformal blocks as⁷

$$\begin{aligned} & \left\langle \varphi_{\pm_1}^{i_1 \dots i_{q_1}}(x_1) \varphi_{\pm_2}^{j_1 \dots j_{q_2}}(x_2) \varphi_{\pm_3}^{k_1 \dots k_{q_3}}(x_3) \varphi_{\pm_4}^{l_1 \dots l_{q_4}}(x_4) \right\rangle \\ &= \frac{\left(\frac{x_{24}}{x_{14}}\right)^{\Delta_{12}} \left(\frac{x_{14}}{x_{13}}\right)^{\Delta_{34}}}{x_{12}^{\Delta_1 + \Delta_2} x_{34}^{\Delta_3 + \Delta_4}} \sum_{\mathcal{O}} (-1)^\ell \lambda_{\varphi_1 \varphi_2 \mathcal{O}} \lambda_{\varphi_3 \varphi_4 \mathcal{O}} T_{\mathcal{R}_1 \mathcal{R}_2 \mathcal{R}_3 \mathcal{R}_4}^{\mathcal{R}, i_1 \dots i_{q_1}, j_1 \dots j_{q_2}, k_1 \dots k_{q_3}, l_1 \dots l_{q_4}} g_{\Delta, \ell}^{\Delta_{12}, \Delta_{34}}(u, v), \end{aligned} \quad (3.11)$$

where $\Delta_{ij} \equiv \Delta_i - \Delta_j$, the conformal cross ratios u, v are

$$u \equiv \frac{x_{12}^2 x_{34}^2}{x_{13}^2 x_{24}^2}, \quad v \equiv \frac{x_{14}^2 x_{23}^2}{x_{13}^2 x_{24}^2}, \quad (3.12)$$

and the operators \mathcal{O} that appear both OPEs $\varphi_1 \times \varphi_2$ and $\varphi_3 \times \varphi_4$ have scaling dimension Δ , spin ℓ , and transform in an irrep \mathcal{R} that appears in both the tensor products $\mathcal{R}_1 \otimes \mathcal{R}_2$ and $\mathcal{R}_3 \otimes \mathcal{R}_4$. For each \mathcal{R} , the $SO(3)$ structure $T^{\mathcal{R}}$ can be constructed using the $SO(3)$ Casimir and normalized to give consistent OPE coefficients under crossing using the free theory as described in appendix B.3. The \mathbb{Z}_2 irrep of \mathcal{O} follows from trivial multiplication of \pm_1 and \pm_2 , and so does not require a structure. If $\varphi_1 = \varphi_2$ (or $\varphi_3 = \varphi_4$), then Bose symmetry requires that \mathcal{O} have only even/odd ℓ for \mathcal{R} in the symmetric/antisymmetric product of $\mathcal{R}_1 \otimes \mathcal{R}_2$ (or $\mathcal{R}_3 \otimes \mathcal{R}_4$).

We are interested in four-point functions of the lowest dimension scalar operators transforming in the $\mathbf{0}^+$, $\mathbf{1}^-$, and $\mathbf{2}^+$ representations, which we will denote following [160, 161, 176] as s , ϕ , and t , respectively.⁸ These operators are normalized via their two point functions as

$$\langle s(x_1) s(x_2) \rangle = \frac{1}{x_{12}^{2\Delta_s}}, \quad \langle \phi^i(x_1) \phi^j(x_2) \rangle = \frac{\delta^{ij}}{x_{12}^{2\Delta_\phi}}, \quad \langle t^{i_1 i_2}(x_1) t^{j_1 j_2}(x_2) \rangle = \frac{\delta^{i_1 j_1} \delta^{i_2 j_2}}{x_{12}^{2\Delta_t}}, \quad (3.13)$$

⁷Our conformal blocks are normalized as in the second line of table 1 in [158].

⁸The singlet S , traceless symmetric T , vector V , and antisymmetric A irreps considered in previous $O(N)$ bootstrap papers [160, 161, 176] correspond for $O(3)$ to the $\mathbf{0}^+$, $\mathbf{2}^+$, $\mathbf{1}^-$, and $\mathbf{1}^-$ irreps, respectively, where now $A \cong V$.

Correlator	s -channel	t -channel	Eqs
$\langle\phi\phi\phi\phi\rangle$	$(\ell^+, \mathbf{0}^+), (\ell^-, \mathbf{1}^+), (\ell^+, \mathbf{2}^+)$	same	3
$\langle tttt\rangle$	$(\ell^+, \mathbf{0}^+), (\ell^-, \mathbf{1}^+), (\ell^+, \mathbf{2}^+), (\ell^-, \mathbf{3}^+), (\ell^+, \mathbf{4}^+)$	same	5
$\langle t\phi t\phi\rangle$	$(\ell^\pm, \mathbf{1}^-), (\ell^\pm, \mathbf{2}^-), (\ell^\pm, \mathbf{3}^-)$	same	3
$\langle tt\phi\phi\rangle$	$(\ell^+, \mathbf{0}^+), (\ell^-, \mathbf{1}^+)$	$(\ell^\pm, \mathbf{1}^-), (\ell^\pm, \mathbf{2}^-), (\ell^\pm, \mathbf{3}^-)$	6
$\langle ssss\rangle$	$(\ell^+, \mathbf{0}^+)$	same	1
$\langle\phi s\phi s\rangle$	$(\ell^\pm, \mathbf{1}^-)$	same	1
$\langle tsts\rangle$	$(\ell^\pm, \mathbf{2}^+)$	same	1
$\langle ttss\rangle$	$(\ell^+, \mathbf{0}^+)$	$(\ell^\pm, \mathbf{2}^+)$	2
$\langle\phi\phi ss\rangle$	$(\ell^+, \mathbf{0}^+)$	$(\ell^\pm, \mathbf{1}^-)$	2
$\langle\phi s\phi t\rangle$	$(\ell^\pm, \mathbf{1}^-)$	same	1
$\langle\phi\phi st\rangle$	$(\ell^+, \mathbf{2}^+)$	$(\ell^\pm, \mathbf{1}^-)$	2
$\langle sttt\rangle$	$(\ell^\pm, \mathbf{2}^+)$	same	1

Table 3.3: Four-point function configurations that give independent crossing equations under equating their s - and t -channels, along with whether even or odd spins ℓ^\pm appear for each irrep in each channel, and the number of crossing equations that each configuration yields.

where $x_{12} \equiv |x_1 - x_2|$ and all indices of the same letter should be symmetrized with their trace removed. In table 3.3 we list the 4-point functions of s , ϕ , and t that are allowed by $O(3)$ symmetry⁹ and whose s and t -channel configurations lead to independent crossing equations, along with the irreps and spins of the operators that appear in the OPE, and the number of crossing equations that they yield. These 4-point functions can be written explicitly as in (3.11), where the explicit $SO(3)$ structures $T^{\mathcal{R}}$ are computed in appendix B.3. Equating each of these s -channel

⁹If we had just $SO(3)$ symmetry, then in addition to these 4-point functions we would also have $\langle s\phi\phi\phi\rangle$, $\langle stt\phi\rangle$, $\langle t\phi\phi\phi\rangle$, and $\langle\phi ttt\rangle$, which can be constructed using the $SO(3)$ invariant tensor ϵ_{ijk} . These correlators give an additional 9 crossing equations for 37 total. As discussed in [161], to distinguish between $SO(3)$ and $O(3)$, one needs to set some of the OPE coefficients in these additional correlators to be nonzero. Otherwise, the extra crossing equations have no effect.

4-point functions with their respective t -channels yields the crossing equations

$$\begin{aligned}
0 = & \sum_{O_{0^+,\ell^+}} \left(\lambda_{ssO_{0^+}} \quad \lambda_{\phi\phi O_{0^+}} \quad \lambda_{ttO_{0^+}} \right) \vec{V}_{0^+,\Delta,\ell^+} \begin{pmatrix} \lambda_{ssO_{0^+}} \\ \lambda_{\phi\phi O_{0^+}} \\ \lambda_{ttO_{0^+}} \end{pmatrix} \\
& + \sum_{O_{1^+,\ell^-}} \left(\lambda_{\phi\phi O_{1^+}} \quad \lambda_{ttO_{1^+}} \right) \vec{V}_{1^+,\Delta,\ell^-} \begin{pmatrix} \lambda_{\phi\phi O_{1^+}} \\ \lambda_{ttO_{1^+}} \end{pmatrix} + \sum_{O_{1^-,\ell^\pm}} \left(\lambda_{t\phi O_{1^-}} \quad \lambda_{\phi s O_{1^-}} \right) \vec{V}_{1^-,\Delta,\ell^\pm} \begin{pmatrix} \lambda_{t\phi O_{1^-}} \\ \lambda_{\phi s O_{1^-}} \end{pmatrix} \\
& + \sum_{O_{2^+,\ell^+}} \left(\lambda_{\phi\phi O_{2^+}} \quad \lambda_{ttO_{2^+}} \quad \lambda_{tsO_{2^+}} \right) \vec{V}_{2^+,\Delta,\ell^+} \begin{pmatrix} \lambda_{\phi\phi O_{2^+}} \\ \lambda_{ttO_{2^+}} \\ \lambda_{tsO_{2^+}} \end{pmatrix} + \sum_{O_{2^+,\ell^-}} \lambda_{tsO_{2^+}}^2 \vec{V}_{2^+,\Delta,\ell^-} \\
& + \sum_{O_{2^-,\ell^\pm}} \lambda_{t\phi O_{2^-}}^2 \vec{V}_{2^-,\Delta,\ell^\pm} + \sum_{O_{3^+,\ell^-}} \lambda_{ttO_{3^+}}^2 \vec{V}_{3^+,\Delta,\ell^-} + \sum_{O_{3^-,\ell^\pm}} \lambda_{t\phi O_{3^-}}^2 \vec{V}_{3^-,\Delta,\ell^\pm} + \sum_{O_{4^+,\ell^+}} \lambda_{ttO_{4^+}}^2 \vec{V}_{4^+,\Delta,\ell^+},
\end{aligned} \tag{3.14}$$

where ℓ^\pm denotes which spins appear, and the V 's are 28-dimensional vectors of matrix or scalar crossing equations that are ordered as table 3.3 and written in terms of

$$F_{\mp,\Delta,\ell}^{ij,kl}(u, v) = v^{\frac{\Delta_k + \Delta_j}{2}} g_{\Delta,\ell}^{\Delta_{ij},\Delta_{kl}}(u, v) \mp u^{\frac{\Delta_k + \Delta_j}{2}} g_{\Delta,\ell}^{\Delta_{ij},\Delta_{kl}}(v, u). \tag{3.15}$$

The explicit form of the V 's is given in the Mathematica notebook associated with the arxiv link [186].¹⁰

Ward identities

The OPE coefficients of J^μ and $T^{\mu\nu}$ are constrained by Ward identities in terms of the two-point coefficients C_J and C_T . In our conventions, we have

$$\lambda_{OO_T}^2 = \frac{\Delta_O^2}{3C_T/C_T^{\text{free}}}, \quad \lambda_{OO_J}^2 = \frac{q_O^2}{2C_J/C_J^{\text{free}}}, \tag{3.16}$$

where $C_{J,T}^{\text{free}}$ are the two-point coefficients of J and T in the free $O(3)$ model described in appendix B.3. Thus, the contribution of these operators to the crossing equation can be parametrized purely in terms of C_T and C_J , together with the dimensions and charges of the external scalars ϕ, s, t .

3.3 The tiptop algorithm

While our primary search for the $O(3)$ bootstrap island will follow the same methods and software tools used for the $O(2)$ model described in [4], we will also need to

¹⁰These crossing equations can also be derived using the software package `autoboot` [187].

compute the maximum value of the scaling dimension Δ_{t_4} over this island. This employs a new search strategy and software implementation that we describe in this section.

Software and algorithm

To automate finding the maximally allowed value of some gap across the allowed region, we have written `tiptop`, software for generating successive points for searching for the maximum value of a coordinate achieved by a region in $(N + 1)$ -dimensional space (see Appendix B.1). It has many optimizations specifically for finding the maximum gap. It is meant to be invoked by a driver that takes these points, computes whether they are feasible, and then asks for more points to check.

The number of dimensions is arbitrary but fixed at compile time. For concreteness and ease of visualization, we assume that $N + 1 = 3$ for the rest of this discussion, where the dimensions are Δ_ϕ , Δ_s , and Δ_{gap} . The algorithm operates unchanged for higher dimensions.

We start with at least one feasible point, a cloud of infeasible points, a cloud of points that are in-progress, and a maximum gap ($\Delta_{\text{max_gap}}$). In-progress points are points that the driver already knows about and is working on, but does not yet know if they are feasible. For example, those calculations may have been submitted as calculations to an HPC cluster but not yet completed.

We assume that there are no feasible points with $\Delta_{\text{gap}} \geq \Delta_{\text{max_gap}}$. We also assume that islands only shrink at larger gaps. So if a point is infeasible at one gap, it will continue to be infeasible at larger gaps. The last assumption is that each N -dimensional island at a fixed value of Δ_{gap} is convex and simply connected, so each island never become a horseshoe or splits into two pieces. While there are many examples of islands splitting at low Λ , islands at high Λ have been well behaved for a wide variety of theories.

The basic outline of the algorithm for generating points is:

- Set Δ_{feasible} to the largest Δ_{gap} with a feasible point.
- Explore parameters at Δ_{feasible} to find the size of the island there. If there are any corners of parameter space left to map out, return one point from there. (Section 3.3)

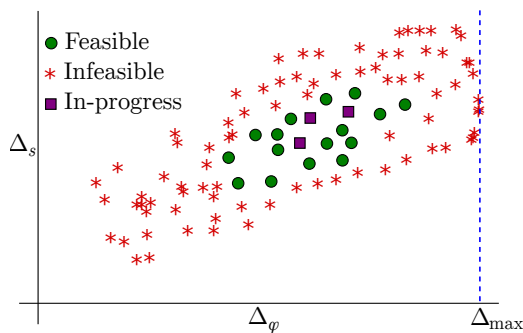


Figure 3.1: The max coordinates Δ_{\max} for a collection of feasible, infeasible, and in-progress points.

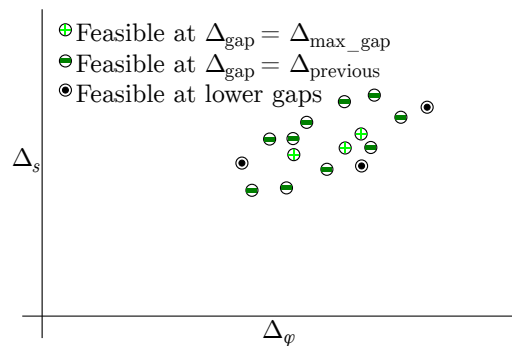


Figure 3.2: Different types of feasible points. Only the points feasible at $\Delta_{\text{gap}} = \Delta_{\text{previous}}$ are used for rescaling.

- If the island at Δ_{feasible} is thoroughly mapped out, generate one point at a higher gap. (Section 3.3)

The non-gap dimensions (Δ_{ϕ} , Δ_s) are represented as regular floating-point numbers, while the gap dimension (Δ_{gap}) is represented as a 64 bit integer. This reduces numerical errors where two points at very similar gaps are mistakenly considered to be at the same gap.

`tiptop` will not return a point in two cases:

- The current gap Δ_{feasible} might be fully explored, but it needs to know the outcome of some in-progress points to be sure.
- There are no valid larger gaps left. For example, consider the case where $\Delta_{\text{feasible}} = 10000$ and `tiptop` has ruled out any jumps to $\Delta_{\text{gap}} = 10001$. There are no integers between 10000 and 10001, so the algorithm terminates.

Exploring the current gap

Rescaling

The islands often have extreme aspect ratios in the 'natural' coordinates. This causes difficulties when exploring an island, so `tiptop` rescales the coordinates. The first step in rescaling is to get an overall scale for all of the points (feasible, infeasible, and in-progress) from all gaps. We define Δ_{\max} as a scalar equal to the largest absolute coordinate value in all dimensions, as shown in Figure 3.1.

For a given Δ_{\max_gap} , we define Δ_{previous} as the largest gap with feasible points but less than Δ_{\max_gap} . This is usually a previous value for Δ_{\max_gap} . Figure 3.2 shows an example of feasible points at Δ_{\max_gap} , Δ_{previous} , and lower gaps.

Using the m feasible points at Δ_{previous} , we scale the points using a principle component analysis. Specifically, we construct the matrix

$$M = \begin{pmatrix} \Delta_{\phi 0} & \Delta_{s 0} \\ \Delta_{\phi 1} & \Delta_{s 1} \\ \Delta_{\phi 2} & \Delta_{s 2} \\ \Delta_{\phi 3} & \Delta_{s 3} \\ \vdots & \vdots \end{pmatrix} .$$

We then compute the singular value decomposition (SVD) of this matrix

$$M = U\Sigma V^* , \quad (3.17)$$

where Σ is a rectangular $m \times N$ diagonal matrix with non-negative real numbers $\sigma_i = \Sigma_{ii}$ on the diagonal ranging from the smallest (σ_{\min}) to the largest (σ_{\max}). U is an $m \times m$ unitary matrix, and V is an $N \times N$ (here 2×2) unitary matrix.

We define the $N \times N$ matrix Ω as the first N rows of Σ . This is a diagonal matrix with the entries σ_i , so the inverse is trivial. Putting this all together, we define the rescaling matrix

$$R \equiv \sigma_{\min} \Omega^{-1} V^T / (1.75 \times \Delta_{\max}) . \quad (3.18)$$

It may be that there are so few points at Δ_{previous} that they are not linearly independent. For example, in the beginning, there may not be any points at Δ_{previous} . If the ratio between the smallest (σ_{\min}) and largest (σ_{\max}) of these singular values is less than a tolerance (we use 10^{-8}), then we only scale by Δ_{\max}

$$R \equiv I / (1.75 \times \Delta_{\max}) , \quad (3.19)$$

where I is the identity.

Everything is scaled by the largest coordinate value Δ_{\max} to guarantee that all points are mapped into a box with extents $(-1,1)$ in every dimension. The factor of 1.75 (about $\sqrt{3}$) is to ensure that all points will fit into the unit box even after rotation.

The transformation has the effect of a rotation and then rescaling of the rotated coordinates, so the feasible region remains convex. However, the feasible points

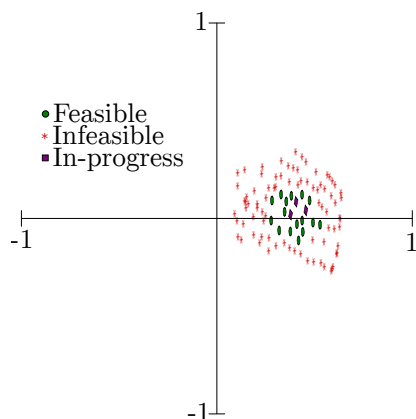


Figure 3.3: Points from Figure 3.1 after rescaling.

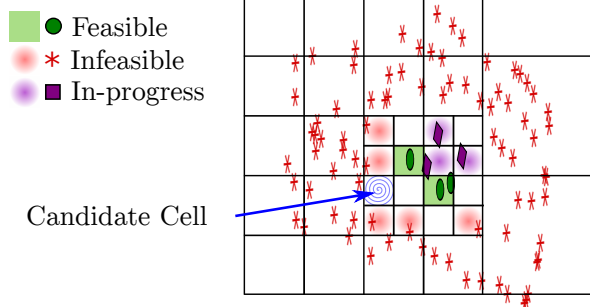


Figure 3.4: Points from Figure 3.3 with an adapted mesh. Points that are feasible at $\Delta_{\text{gap}} < \Delta_{\text{feasible}}$ have been removed. The blue spiral indicates an empty candidate cell. The other empty cells are not diagonal from a feasible cell, so they are not considered.

should outline a more circular shape than the extended ellipse we started with, as shown in Figure 3.3.

One concern with this rescaling algorithm is that it weighs dense regions with more points more than equivalently sized regions with fewer points. So it may not produce an optimal transform. In practice, the later steps spread out the points very evenly, so this concern turns out not to be a problem in practice.

Adaptively meshing the box

While the distribution of points in Figure 3.3 no longer has extreme aspect ratios, the points are still clustered in a small region of the unit box.

Based on the assumption that the feasible island only shrinks as the gap increases, we now only consider three sets of points: feasible at the current $\Delta_{\text{max_gap}}$, and infeasible or in-progress at $\Delta_{\text{gap}} \leq \Delta_{\text{max_gap}}$. For the rest of this step, we will be treating in-progress and infeasible points identically.

The strategy is to place points in regions that are empty. To quantify this emptiness, we create a regular mesh covering the points. Empty regions are then cells that have no points. We start with a very coarse mesh consisting of a single cell covering the entire unit box. Then we loop over all cells, splitting each cell a point into 2^N cells (4 for our example). We recursively loop over these new cells, continuing until we have reached the minimum cell size.

The minimum cell size is set by multiplying the *minimum* coordinate extents of the rescaled feasible points by a fixed fraction f_{cutoff} . In Figure 3.3, this minimum extent is about 0.5 in both dimensions. We use $f_{\text{cutoff}} = 2$, which is deliberately very coarse. If $f_{\text{cutoff}} < 1$, then the algorithm will feel the need to completely fill in internal regions, even though, by assumption, the internal spaces do not need to be checked.

Just after a jump to a higher gap, there is only one feasible point at Δ_{feasible} . In this case, the extents are zero, so we use a default minimum cell width of 2^{-47} . This is quite small, but a little bigger than the minimum resolution of an IEEE-754 double-precision number (2^{-53}). This helps reduce errors from round-tripping the number through different systems.

Most of these cells will be empty. We select the largest empty cell that is adjacent to a cell containing only feasible points. If there are multiple empty cells next to a feasible cell, then we select a new cell in the order $(+, +)$, $(-, -)$, $(+, -)$, $(-, +)$ as in Figure 3.4. We only check diagonals, so points get laid out in a checkerboard pattern.

If there are two candidate empty cells, we choose the cell adjacent to the first feasible point given to `tiptop`. So when driving `tiptop`, we always list the feasible points in the same order.

The new point is not placed at the center of the new cell, but rather simply offset from the existing feasible point. So if the feasible point is in a corner of a cell, the new point will be in the same corner of the empty cell.

The observed behavior of this algorithm is that it quickly finds a rough estimate for the boundary between feasible and unfeasible, but can spend a lot of effort finding the exact boundaries. In-progress points are treated as infeasible, so too many in-progress points will lead to extra work. In practice, we have up to 16 points in-progress at any one time.

Jumping to a larger gap

If the previous section does not yield a new point, and there are no in-progress points, then we try to jump to a larger gap.

We start by rescaling the points as in section 3.3. We draw a coordinate box around all of the points feasible at Δ_{feasible} and shrink it by a factor of 2. Then we find the largest gap Δ_{ceiling} that can accommodate this box without containing any infeasible

or in-progress points with $\Delta_{\text{gap}} \leq \Delta_{\text{ceiling}}$. At the beginning, there are no infeasible points at large gaps, so $\Delta_{\text{ceiling}} = \Delta_{\text{max_gap}}$.

We return the center of the box at $\Delta_{\text{gap}} = (\Delta_{\text{feasible}} + \Delta_{\text{ceiling}}) / 2$, thus bisecting the range of feasible gaps. This underscores the need for a good estimate of $\Delta_{\text{max_gap}}$. If the estimate is too high, then the algorithm will recommend too many points that are far too large.

Overall, we have found this approach to work reasonably well. More importantly, it is very robust. It is very easy to be too clever, resulting in odd failures.

3.4 Results

Dimension bounds with OPE scans

Next we present our conformal bootstrap island computed using `sdpb`, along with its comparison with various Monte Carlo results. Computing the conformal bootstrap island requires scanning over the three operator dimensions $\{\Delta_\phi, \Delta_s, \Delta_t\}$ using the Delaunay search algorithm described in [4], and for each point using the "cutting surface" algorithm presented in [4] to decide if there exists an allowed point in the space of OPE coefficient ratios $\left\{ \frac{sss}{\phi\phi s}, \frac{tts}{\phi\phi s}, \frac{\phi\phi t}{\phi\phi s}, \frac{ttt}{\phi\phi s} \right\}$.

When computing the island we make the following assumptions about the spectrum unless stated otherwise. We assume that ϕ , s , and t are the only relevant operators in their respective symmetry representations, so that $\Delta_{\phi', s', t'} \geq 3$. In addition, we assume that the leading rank-4 scalar has a dimension satisfying $\Delta_{t_4} \geq 2$. We assume an $O(3)$ current with $\Delta_J = 2$ and stress tensor with $\Delta_T = 3$, with coefficients satisfying the Ward identity constraints. We also impose a twist gap above them, as well as in all other sectors not mentioned above, of size 10^{-6} .

In Figure 3.5 we show the conformal bootstrap island we have computed at $\Lambda = 43$ using these assumptions, compared to the Monte Carlo results of [7, 8]. In Figure 3.6 we show various 2d projections of the bootstrap island. In appendix B.4 we give the full set of allowed and disallowed points we computed at $\Lambda = 43$, along with Figure B.1 which shows the convergence of the allowed points as a function of Λ after performing an affine transformation to make the allowed regions roughly spherical.

In these plots we show our best determination of the allowed region at a given Λ , constructed by computing a Delaunay triangulation of the tested points, choosing triangles that contain both allowed and disallowed points, and plotting the convex

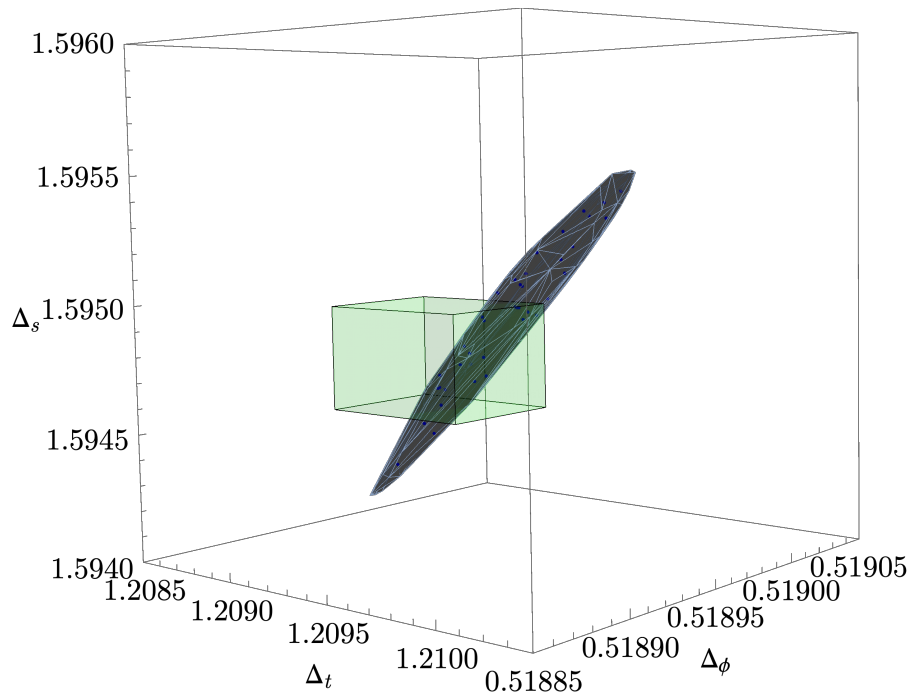


Figure 3.5: The $\Lambda = 43$ conformal bootstrap dimension island (black) compared with the Monte Carlo results [7, 8] (green).

hull of the points that are midway between the allowed and disallowed vertices in these triangles. At $\Lambda = 43$, this "best-fit" region gives

$$\begin{aligned}\Delta_\phi &= 0.518942(51^*), \\ \Delta_s &= 1.59489(59^*), \\ \Delta_t &= 1.20954(23^*).\end{aligned}\tag{3.20}$$

A more rigorous determination can be made by taking the convex hull of the disallowed points in these boundary Delaunay triangles. This region gives the rigorous error bars

$$\Delta_\phi = 0.518936(\mathbf{67}),\tag{3.21}$$

$$\Delta_s = 1.59488(\mathbf{81}),\tag{3.22}$$

$$\Delta_t = 1.20954(\mathbf{32}),\tag{3.23}$$

which we have quoted in table 3.1.

The allowed points at $\Lambda = 43$ are associated with OPE coefficient ratios which live

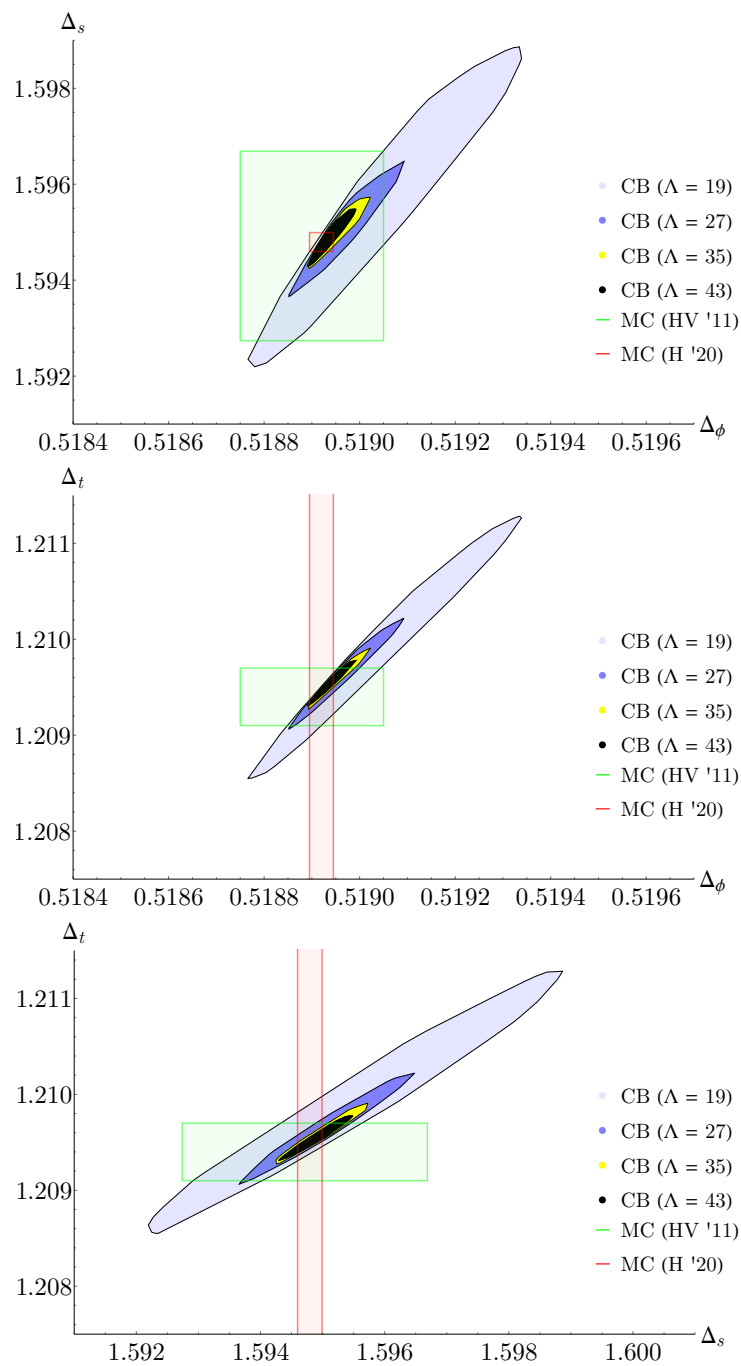


Figure 3.6: Comparison between the conformal bootstrap islands at $\Lambda = 19, 27, 35, 43$ projected to the $\{\Delta_\phi, \Delta_s\}$, $\{\Delta_\phi, \Delta_t\}$, and $\{\Delta_s, \Delta_t\}$ planes and the Monte Carlo results of [7, 8].

in the ranges¹¹

$$\begin{aligned}
\frac{\lambda_{sss}}{\lambda_{\phi\phi s}} &= 0.9643(20^*), \\
\frac{\lambda_{ttt}}{\lambda_{\phi\phi s}} &= 1.87593(53^*), \\
\frac{\lambda_{\phi\phi t}}{\lambda_{\phi\phi s}} &= 1.66808(23^*), \\
\frac{\lambda_{ttt}}{\lambda_{\phi\phi s}} &= 2.86034(61^*).
\end{aligned} \tag{3.24}$$

These should be viewed as an approximation to the full allowed region of OPE coefficients, which may be slightly larger.

Central charges and $\lambda_{\phi\phi s}$

Next, we compute upper and lower bounds on the magnitude of the OPE coefficient $\lambda_{\phi\phi s}$, the central charge C_T , and the current central charge C_J . We compute these bounds over a small sample of points in our allowed region so the results will be inherently non-rigorous. However, we believe that this treatment gives reasonable estimates for these quantities that are more precise than previous results.

The strategy is similar to the method we employed in [4]. We take seven primal points in the $\Lambda = 43$ island, consisting of the scaling dimensions and allowed OPE coefficients. The points are chosen to be sufficiently symmetrized and sparse across the $\Lambda = 43$ island we have computed. For each of these points, we extremize C_T , C_J , and the external OPE norm parameterized by $\lambda_{\phi\phi s}$, to obtain upper and lower bounds. This calculation was limited to $\Lambda = 35$ due to our available computational resources. The data points and SDPB parameters we used are summarized in tables B.5 and B.2, respectively.

There is an important comment we want to make about the upper bound computation on C_T and C_J (a similar comment was made in [4]). For computing upper bounds on C_T and C_J , we have to assume a gap $\Delta_{T'/J'}$ above the unitarity bound for the next operators in the T or J sectors. Note that this gap was not assumed in our OPE scan, so this extra constraint might turn an allowed point into a disallowed point. If we do not have such a gap, the upper bound is loose and may not give reasonable results. On the other hand, large gaps can make SDPB unable to find a solution.

¹¹Note that there is an ambiguity in the signs of these coefficients, related to performing the operator redefinitions $s \rightarrow -s$ and $t \rightarrow -t$. This freedom can be used to fix $\lambda_{\phi\phi s}$ and $\lambda_{\phi\phi t}$ to be positive, after which all other signs in (3.24) are determined to be positive by the conformal bootstrap.

In table B.5, we summarize the gaps $\Delta_{T'/J'}$ we assume in the upper bound calculations. From spectrum determinations using the extremal functional method (see [188, 189]), we have noticed that a gap $\Delta_{T'/J'} = \Delta_{T/J} + 1$ above T and J is generally favored. We were able to compute bounds with this gap for three of the points, but for the other four we could not find solutions. For those points, we adopted the weaker assumption $\Delta_{\text{ext},T(J)} = \Delta_{T/J} + 0.1$.

Following this procedure, we obtain our estimates of C_T , C_J , and $\lambda_{\phi\phi_s}$ in the critical $O(3)$ model,

$$\begin{aligned} C_J/C_J^{\text{free}} &= 0.90632(16^*), \\ C_T/C_T^{\text{free}} &= 0.944524(28^*), \\ \lambda_{\phi\phi_s} &= 0.524261(59^*). \end{aligned} \tag{3.25}$$

These results agree with and are more precise than previous determinations of these quantities (see [160, 161, 176]).

Upper bound on Δ_{t_4}

Our last result is the maximum value of the rank-4 scalar dimension Δ_{t_4} . In conjunction with the `tiptop` algorithm described in section 3.3, we computed points at $\Lambda = 19, 27$, and 35 . Allowed points at lower values of Λ were used to initiate the search at larger values of Λ . Figure 3.7 shows a projection of a subset of the 1311 disallowed points and 172 allowed points at $\Lambda = 35$, and Figure 3.8 shows how the island shrinks as we approach the maximum Δ_{t_4} .

The largest allowed value of Δ_{t_4} was 2.99052 , with the tip centered around the scaling dimensions $\{\Delta_\phi, \Delta_s, \Delta_t\} = \{0.518962, 1.59527, 1.20969\}$. We can also consider the nearest disallowed point. To compute the nearest, we first use the affine transformation (B.8) which makes the dimension island roughly spherical with $O(1)$ size, and we additionally rescale $\Delta_{t_4} - 3$ by a factor of ~ 100 so that the tip's curvature also ranges over an $O(1)$ distance. Then we compute the Euclidean norm. The algorithm is very well converged, so the result is robust against the precise form of these transformations. This gives us a conservative bound of

$$\Delta_{t_4} < 2.99056. \tag{3.26}$$

This implies that the leading rank-4 tensor in the critical $O(3)$ model is relevant, in agreement with other studies.

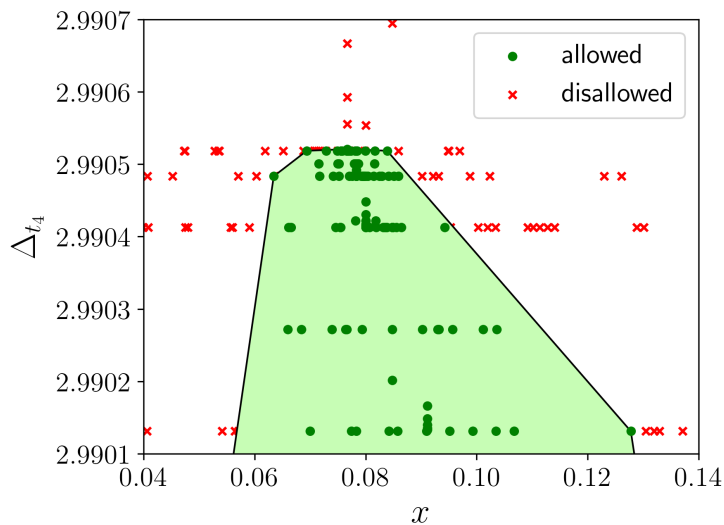


Figure 3.7: Two-dimensional projection of the results of the `tiptop` search at $\Lambda = 35$. The x coordinate is related to the three scalar dimensions via (B.8). Projections in y and z look similar. We have superimposed a convex hull encompassing the allowed points on top, obscuring some of the disallowed points. We can see the behaviour of the `tiptop` algorithm, exploring the island at one Δ_{t_4} before jumping to a larger Δ_{t_4} . The jumps become progressively smaller, indicating convergence. We computed 16 points simultaneously, and this calculation took several months during which the `tiptop` algorithm was being developed. So the points reflect occasional crashes and small inefficiencies in the set of computed points.

3.5 Future directions

In this work we have applied the methods developed in [4, 5] for large-scale bootstrap problems to the critical $O(3)$ model in three dimensions. This has led to results for scaling dimensions which are competitive with the most precise Monte Carlo simulations, and results for OPE coefficients which are significantly more precise than previous determinations. In addition, we have computed a rigorous bound on the scaling dimension of the leading rank-4 tensor, showing that it is relevant. Thus, any $O(3)$ system with cubic anisotropy should flow to the cubic fixed point (discussed in section 3.1) instead of the Heisenberg fixed point.

An interesting direction for future research will be the application of conformal perturbation theory to this flow. The cubic model can be reached by perturbing the $O(3)$ CFT with the operator $X \equiv \sum_{i=1}^3 t_4^{iii}$, which breaks $O(3)$ symmetry to the discrete symmetry $\mathbb{Z}_3 \times \mathcal{S}_3$. From the $O(3)$ point of view, this term is a certain component of the $O(3)$ rank-4 tensor with dimension $\Delta_{t_4} \simeq 2.99$. On the other

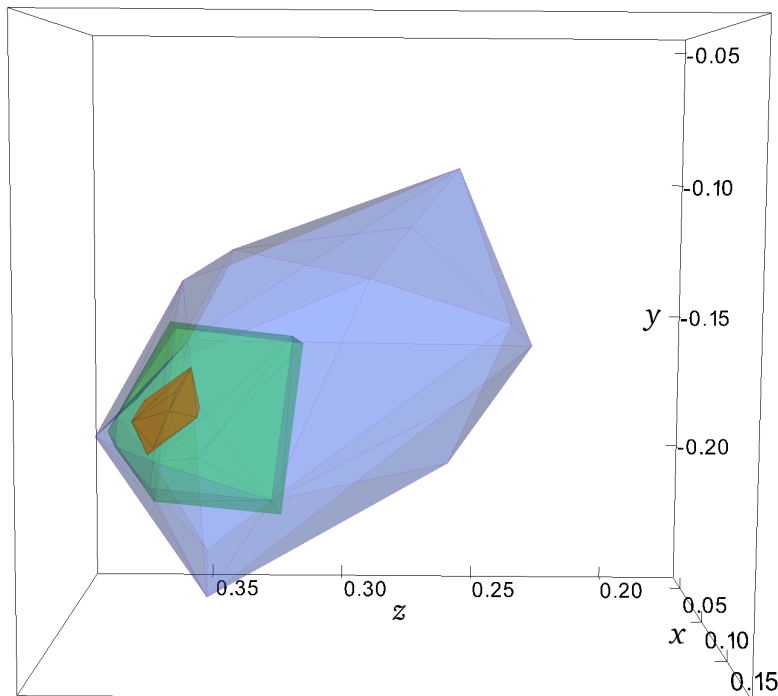


Figure 3.8: Three-dimensional islands of allowed points at different Δ_{t_4} at $\Lambda = 35$, demonstrating how the islands shrink as we approach the maximum Δ_{t_4} . The x , y , and z coordinates are related to the three scalar dimensions via (B.8). The values for Δ_{t_4} , from the largest region to smallest, are 2.989, 2.99025, and 2.9905, with smaller values including all allowed points at larger values.

hand, in the cubic fixed point conformal perturbation theory predicts $\Delta_X \simeq 3.01$. Because this term is marginally irrelevant with $\delta = \Delta_X - 3 \simeq 0.01$, if we want to reach the cubic fixed point by a Monte Carlo simulation, the size of the lattice has to be around the order of $2^{1/\delta}$, which is impractical to implement.

An alternative way to estimate the cubic CFT data is using conformal perturbation theory. We start with the perturbed action $S = S_{O(3)} + g \int d^3x X$. Using the formalism in [190], one finds the beta function to be

$$\beta_g = -\delta g - \frac{\text{vol } S^{d-1}}{2} \lambda_{XXX} g^2. \quad (3.27)$$

The dimension of an operator \mathcal{O} at the cubic fixed point is then given at linear order in δ by $\Delta_{\mathcal{O}} = \Delta_0 + 2\delta \lambda_{\mathcal{O}OX} / \lambda_{XXX}$, where Δ_0 is the dimension of corresponding operator in the $O(3)$ CFT. Specifically one obtains $\Delta_X = \Delta_0 + 2\delta$, which justifies the estimate $\Delta_X \simeq 3.01$.

The OPE coefficient λ_{XXX} is proportional to $\lambda_{t_4 t_4 t_4}$. Unfortunately, using the setup of the present paper, we don't have access to $\lambda_{t_4 t_4 t_4}$. To access $\lambda_{t_4 t_4 t_4}$, one needs to bootstrap all four-point functions involving $\{\phi, s, t, t_4\}$, which is a concrete task for future research. Here we can estimate that the correction to Δ_t in the cubic fixed-point is of order $\delta = 0.01$. On the other hand, the corrections to Δ_ϕ, Δ_s start at order $\delta^2 \simeq 0.0001$ since $\lambda_{\phi\phi t_4} = \lambda_{s s t_4} = 0$. Note that in this work the error bar for Δ_t is much smaller than δ . Therefore a careful study of the $\{\phi, s, t, t_4\}$ system should yield a solid prediction for the correction to Δ_t in the cubic model.

Of course, it will also be interesting to understand how to isolate the cubic fixed point more directly using the conformal bootstrap, perhaps using a larger system of correlators than was considered in [177, 179, 180]. One can also straightforwardly apply the large-scale bootstrap techniques we have developed to other $O(N)$ models, as well as to 3d CFTs with fermions (using the newly developed software [191]) or to study conserved currents [192–194]. Using these methods one can also continue exploring larger systems of correlators that may help us to isolate CFTs containing gauge fields, such as 3d QED [195, 196] and 4d QCD.

Now that we have precisely isolated the $O(3)$ model, we are also in position to do a more detailed study of its low-twist trajectories of operators as a function of spin, which can be compared to analytical calculations using the Lorentzian Inversion formula [37, 197], following the approach of [5, 198, 199]. Such analytical techniques can also be used to estimate the leading Regge intercepts and related Lorentzian data of the $O(3)$ model. In future work it will also be important to understand how to better incorporate insights from the analytical bootstrap, such as our precise understanding of the large spin asymptotics, into making large-scale numerical methods even more powerful.

Acknowledgments

We thank Yinchen He, Igor Klebanov, Filip Kos, Zhijin Li, João Penendones, Junchen Rong, Slava Rychkov, Andreas Stergiou, and Ettore Vicari for discussions. WL, JL, and DSD are supported by Simons Foundation grant 488657 (Simons Collaboration on the Nonperturbative Bootstrap). DSD and JL are also supported by a DOE Early Career Award under grant no. DE-SC0019085. DP is supported

by Simons Foundation grant 488651 (Simons Collaboration on the Nonperturbative Bootstrap) and DOE grants DE-SC0020318 and DE-SC0017660. This project has received funding from the European Research Council (ERC) under the European Union's Horizon 2020 research and innovation programme (grant agreement no. 758903). AV is also supported by the Swiss National Science Foundation (SNSF) under grant no. PP00P2-163670. SMC is supported by a Zuckerman STEM Leadership Fellowship.

This work used the Extreme Science and Engineering Discovery Environment (XSEDE) Comet Cluster at the San Diego Supercomputing Center (SDSC) through allocation PHY190023, which is supported by National Science Foundation grant number ACI-1548562. This work also used the EPFL SCITAS cluster, which is supported by the SNSF grant PP00P2-163670, the Caltech High Performance Cluster, partially supported by a grant from the Gordon and Betty Moore Foundation, and the Grace computing cluster, supported by the facilities and staff of the Yale University Faculty of Sciences High Performance Computing Center.

Chapter 4

COLLISIONS OF FALSE-VACUUM BUBBLE WALLS IN A QUANTUM SPIN CHAIN

This chapter is based on A. Milsted, **J. Liu**, J. Preskill, and G. Vidal, *Collisions of false-vacuum bubble walls in a quantum spin chain*, PRX Quantum **3**, 020316, (2022), arXiv:2012.07243 [quant-ph].

Abstract: We study the real-time dynamics of a small bubble of "false vacuum" in a quantum spin chain near criticality, where the low-energy physics is described by a relativistic (1+1)-dimensional quantum field theory. Such a bubble can be thought of as a confined kink-antikink pair (a meson). We carefully construct bubbles so that particle production does not occur until the walls collide. To achieve this in the presence of strong correlations, we extend a Matrix Product State (MPS) ansatz for quasiparticle wavepackets [Van Damme et al., arXiv:1907.02474 (2019)] to the case of confined, topological quasiparticles. By choosing the wavepacket width and the bubble size appropriately, we avoid strong lattice effects and observe relativistic kink-antikink collisions. We use the MPS quasiparticle ansatz to detect scattering outcomes: In the Ising model, with transverse and longitudinal fields, we do not observe particle production despite nonintegrability (supporting recent observations of nonthermalizing mesonic states). With additional interactions, we see production of confined and unconfined particle pairs. Although we simulated these low-energy, few-particle events with moderate resources, we observe significant growth of entanglement with energy and with the number of collisions, suggesting that increasing either will ultimately exhaust our methods. Quantum devices, in contrast, are not limited by entanglement production, and promise to allow us to go far beyond classical methods. We anticipate that kink-antikink scattering in 1+1 dimensions will be an instructive benchmark problem for relatively near-term quantum devices.

It is possible that the known universe is built on top of a metastable, or "false" vacuum state. In this scenario, there is a small but nonzero probability of a small bubble of "true" vacuum forming via tunneling, whose interior has a lower energy density. Thus the bubble expands, its walls accelerating, bulldozing everything in their path. If multiple bubbles of true vacuum form far apart, their walls will rush toward each other and eventually collide, producing showers of particles. It

is possible that such events have already occurred, and are thus relevant for the evolution of the early universe [200–204]. Simulations could provide an important window into these high-energy, strongly-coupled dynamical processes.

However, one does not easily simulate the dynamics of a strongly interacting quantum field theory (QFT), at least using classical computers. Quantum Monte Carlo – the workhorse for simulations of equilibrium phenomena in lattice systems (such as lattice QCD [1]) – suffers from the sign problem that blocks its application to real-time dynamics. Tensor-network methods show promise, and have been used to simulate nontrivial dynamical phenomena in (1+1)D systems, such as string breaking in lattice gauge theory [205–210]. Nevertheless, the computational cost increases exponentially with time in the general case (due to linear scaling of entanglement entropy) and also dramatically with the number of spatial dimensions.

In principle, quantum computers (both analog and digital) can simulate dynamics of quantum field theories at long timescales with polynomial costs [27, 28], a topic which has recently attracted great interest [23, 211–218, 218–231]. However, existing or near-term digital quantum devices are noisy, such that only shallow quantum circuits can avoid being overwhelmed by errors. Analog quantum simulators can support longer coherence times but are typically limited to a small set of Hamiltonians and initial states. As such, for the time being, we expect classical simulations of physical systems to perform better, with quantum devices catching up as the hardware improves, ultimately beating classical computers by an exponential margin. Thus dynamical simulations of phenomena like false-vacuum collapse are physically-motivated applications for quantum computers and analog quantum simulators, and can be used as benchmark problems as quantum devices improve.

In this paper, we develop a framework for simulating the full quantum dynamics of false-vacuum bubble-wall collisions in (1+1) dimensions using Matrix Product States [232, 233], demonstrating the production of new particles (see Fig. 4.1). Note that, in (1+1) dimensions, a false-vacuum bubble can be viewed as an excited *meson* state consisting of a kink-antikink pair, where the kink and antikink are localized, spatially separated topological particles. The false vacuum plays the role of a low-energy string that binds the kink to the antikink (confinement). Furthermore, metastability of the false vacuum corresponds to suppression of string breaking [234]. We simulate the relaxation of such mesonic states, which we simply call "bubbles", in which both the kink and antikink are of low mass. During relaxation, the kink and antikink will collide. This can be thought of as a scattering event, hence

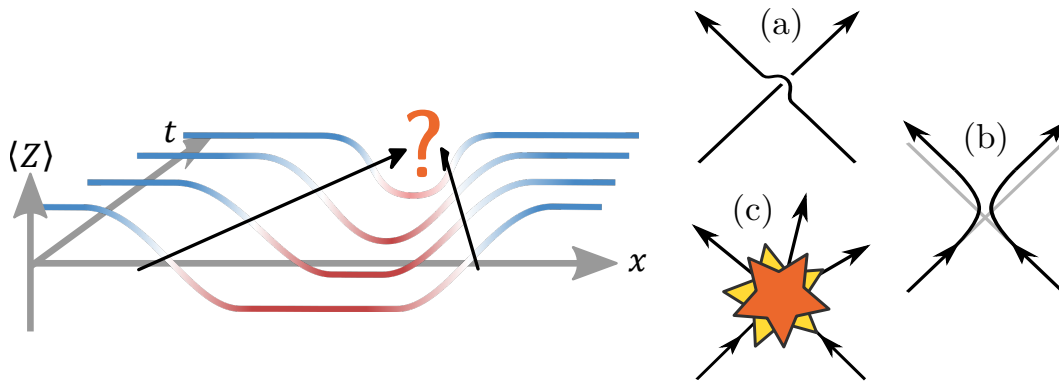


Figure 4.1: Cartoon showing the collapse of a false-vacuum bubble in a spin chain. The magnetization $\langle Z \rangle$ is positive in the true vacuum, but negative in the false vacuum. A bubble-wall collision is a scattering process, which may be (a) free (no interaction), (b) elastic (no particle production), or (c) inelastic (particle production). Note that in free and elastic scattering of topological particles the left (right) particle always remains a kink (antikink).

falling into one of three categories: free (no interaction), elastic (interaction, but no particle production), and inelastic (particle production). We successfully simulate inelastic kink-antikink collisions over ~ 1000 lattice sites at energies of up to $\sim 5m_\mu$, where m_μ is the mass of the lightest meson. We characterize scattering outcomes in our simulations by tracking the energy density and entanglement entropy, as well as by projecting the quantum state into different particle "sectors".

Previous work on related phenomena includes MPS simulations of meson decay in the Schwinger model [206–210, 235], where the initial state is typically prepared by applying a bare string operator to the vacuum. This generally creates multiple highly-localized particles of varying energy at the string edges, leading to relatively complex dynamics. The rapid resulting entanglement growth can make it difficult to reach long times and to treat large systems. Such strings can be smeared out into wavepackets (as considered, for example in some recent work on mesonic excitations in spin chains [229, 236]), which focuses the wavepacket momenta, significantly reducing the energy and entanglement growth. Nevertheless, the smeared string will still generally create multiple species of topological excitation. Recently, however, techniques have been developed [237] to construct wavepacket states with selective particle content in generic (1+1)-dimensional systems using MPS ¹. A main result of our paper is that we can extend those techniques to build *quasistable* initial bubble states which, aside from the acceleration of the walls under the confining force, do

¹Also see [238] for a Bethe-ansatz approach.

not change significantly *until the walls collide*. We achieve this by selecting a single species of kink and antikink quasiparticle for the bubble-wall wavepackets, together with the metastable false vacuum for the interior. Apart from further reducing the energy and the rate of entanglement growth, which enables us to treat larger systems and simulate for longer times, this greatly improves the *interpretability* of our simulations, since the only scattering events that occur come from bubble-wall collisions. We contrast this with the smeared bare string construction, in which meson pairs are generally observed immediately, at the initial bubble walls, as shown in Fig. 4.2.

One approach to simulating the dynamics of QFT phenomena on the lattice is to spatially discretize a chosen QFT Hamiltonian [2, 28, 205–210, 239]. In many cases involving bosonic fields, however, this results in an infinite-dimensional Hilbert space for each lattice site that must then be truncated. In this study, we consider a *quantum spin chain*, chosen and tuned so that its low-energy physics is governed by an *emergent* relativistic QFT. This is known to occur in the vicinity of many continuous phase transitions, where the emergent QFT is often a (by definition relativistic) conformal field theory (CFT) (see e.g. [240]).

To summarize, partially motivated by a potential connection with early universe cosmology, we have studied inelastic particle production arising from collisions of confined kink-antikink pairs in a relativistic scalar field theory. We probe the quantum field theory by tuning close to a critical point of the spin chain described in Sec. 4.1, ensuring that the kink and antikink lattice velocities remain below their maximum values, thus avoiding strong lattice artifacts. Our classical simulations use MPS approximations to the evolving quantum state, which are computationally feasible as long as the state does not become too highly entangled. By highlighting the limitations of such classical methods, our work clarifies where quantum advantage might potentially arise in relatively near-term quantum simulators.

The initial state preparation for our dynamical simulations is subtle, because the kink-antikink pair is not an energy eigenstate. As discussed in Sec. 4.2, we take care to prepare initial kink and antikink wavepackets which are broad compared to the lattice spacing, and not contaminated by additional unwanted excitations. We also develop tools for analysis of the outgoing particles produced in inelastic kink-antikink collisions. We show in Sec. 4.3 that particle production is strongly suppressed in the Ising model with intrinsic \mathbb{Z}_2 symmetry breaking, even though the model is nonintegrable in that case, and we show that copious particle production

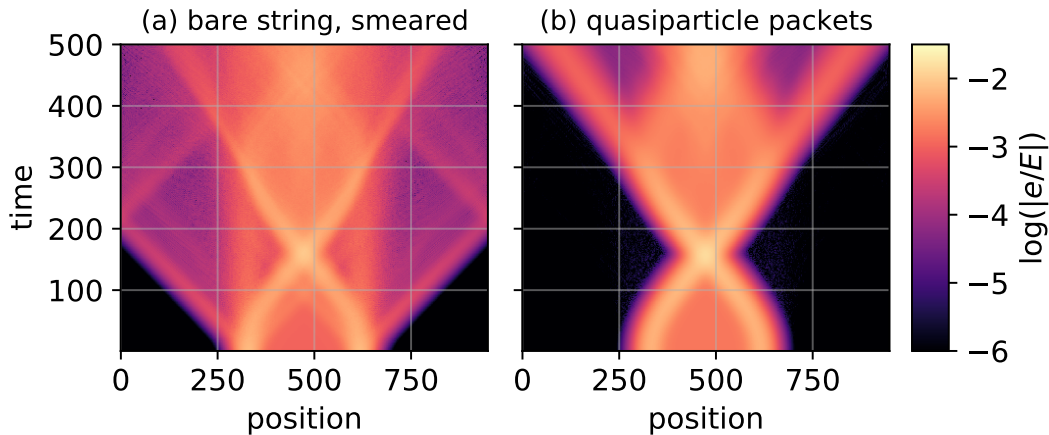


Figure 4.2: Evolution of the excess energy density e (relative to vacuum), as a fraction of total excess energy E , in a spin chain for two initial states: (a) created by applying a spatially smeared string operator to the vacuum and (b) constructed from MPS tensors to contain kink and antikink quasiparticle wavepackets. In (a) meson pairs are produced immediately at the string edges, whereas in (b) there is no particle production until the initial kink and antikink collide. The dynamics are restricted to a window of ~ 1000 sites, leading to boundary effects in (a). For more details, see App. C.6.

occurs once a \mathbb{Z}_2 -symmetric three-site local interaction turns on. We also quantitatively track the growth of entanglement entropy during repeated kink-antikink collisions, thus inferring how large a bond dimension is needed to provide an accurate approximation to the evolving quantum state. Sec. 4.4 contains concluding remarks, and further details of our methods and results are provided in the appendices.

4.1 Selecting a spin chain

We seek a spin chain whose IR physics is described by a relativistic emergent field theory supporting confined kinks. In principle, there are many suitable models: An emergent field theory of confined kink-antikink pairs can be engineered by starting with a spontaneously-broken discrete symmetry, which provides multiple vacua and topological excitations. We then tune close to a symmetry-breaking phase transition, typically described by a CFT, and finally add a weak symmetry-breaking field to lift the vacuum degeneracy and confine the kinks. We must take care, however, since emergent field theories of such spin chains are sometimes *integrable* [241–244], in which case scattering, including kink collision, is *elastic*. If we want to observe particle production in the emergent field theory, we must avoid integrability.

We choose an extension [9, 10] of the transverse-field Ising chain

$$H = \sum_{j=1}^N \left[-Z_j Z_{j+1} - g X_j - h Z_j + \lambda (X_j Z_{j+1} Z_{j+2} + Z_j Z_{j+1} X_{j+2}) \right], \quad (4.1)$$

which at $h = 0$ has \mathbb{Z}_2 symmetry ($Z_j \rightarrow -Z_j$, $X_j \rightarrow X_j$) that is spontaneously broken when $g < 1$ for a large range of λ : see Fig. 4.3 for a phase diagram. For $\lambda = 0$, we have the transverse-field Ising chain, which already supports confined kinks for $g < 1$ and $0 < |h| \ll 1$ [11, 245]. However, for small $|h|$ it is very close to being integrable [11, 242] (both the emergent field theory and the spin chain itself are noninteracting for $h = 0$). Previous work has shown that mesonic states in this model can have extremely long lifetimes [246–250], with recent numerical studies suggesting that these long-lived states can have energies well above the threshold for inelastic scattering [234, 251, 252]. This is despite the lack of any exact conservation law protecting these excited meson states from decay.

Turning on λ allows us to go beyond this "almost-integrable" regime, since both the spin chain itself and the emergent field theory are nonintegrable for $\lambda > 0$, $g < 1$, even at $h = 0$ [12, 244, 253, 254]. We present simulations at a point along the Ising line $\lambda = 0$, labelled (i) in Fig. 4.3, as well as at two points, labelled (ii) and (iii), closer to the Tri-Critical Ising (TCI) point at $\lambda \rightarrow 0.428$, $g = 1$, $h = 0$.

4.2 Methods

Constructing bubble states

Here we describe how to construct the bubble states used to initialize our simulations. For simplicity, we begin with the construction of bubble states in the *bare* setting $\lambda = 0$, $g = 0$, where quantum fluctuations vanish, before moving onto the *dressed* setting, where we use MPS to capture the fluctuations that appear. In both cases we first describe the true and false vacua, then the kink and antikink states, before explaining how to combine them into a bubble. We work in the Z -basis throughout: $Z|\uparrow\rangle = |\uparrow\rangle$, $Z|\downarrow\rangle = -|\downarrow\rangle$.

Let us first consider $\lambda = 0$, $g = 0$, for which the terms in H commute and there are no quantum fluctuations (all eigenstates of H have definite spin orientations in the Z basis). In this bare case, the true and false vacua are simply $|\Omega^{\text{bare}}\rangle := |\dots \uparrow\uparrow\uparrow \dots\rangle$ and $|\bar{\Omega}^{\text{bare}}\rangle := |\dots \downarrow\downarrow \dots\rangle$, respectively. A kink is a domain wall $|\kappa_j^{\text{bare}}\rangle := |\dots \uparrow\downarrow_j \dots\rangle$, here located at position j , and an antikink is $|\bar{\kappa}_k^{\text{bare}}\rangle := |\dots \downarrow_k \uparrow \dots\rangle$. These highly-localized excitations have maximal momentum uncertainty. By smearing them out into *wavepackets*, e.g. $\sum_j f_j |\kappa_j^{\text{bare}}\rangle$, we can make them quasilocal

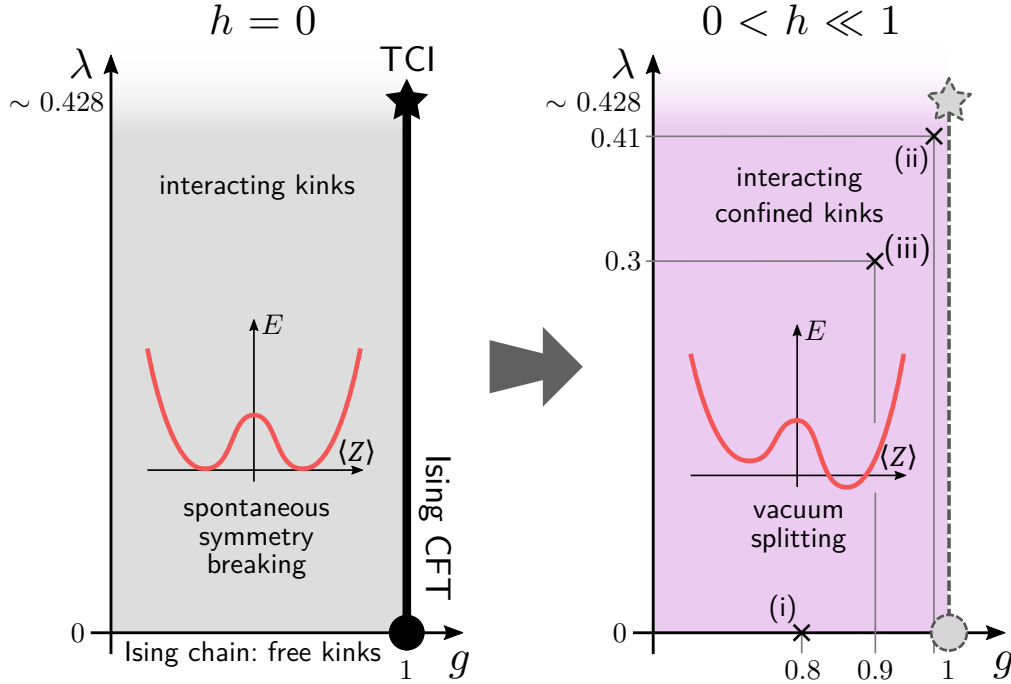


Figure 4.3: Partial phase diagrams of the extended Ising chain [9, 10], both without and with a small longitudinal field h that breaks the \mathbb{Z}_2 symmetry. At $h = 0$, $g = 1$ there is a continuous (symmetry-breaking) phase transition described by the Ising CFT for $\lambda \lesssim 0.428$, and by the Tri-Critical Ising (TCI) CFT at $\lambda \approx 0.428$. By studying the spin chain near to these transitions ($g \rightarrow 1$, $h \rightarrow 0$), we can access emergent, relativistic quantum field theories with confined kinks [11, 12]. Points (i), (ii), and (iii) correspond to the data shown in the figures below.

in both position and momentum space. We consider Gaussian packets

$$f_j(x, p) := e^{ipj} e^{-\frac{(j-x)^2}{\sigma^2}}, \quad (4.2)$$

centered at position x and momentum p , with spatial width σ . In the maximally delocalized limit $\sigma \rightarrow \infty$ we obtain a momentum eigenstate with momentum p . By combining kink and antikink wavepackets we can construct a false-vacuum bubble with quasilocalized walls at positions x_L and x_R

$$|\Psi^{\text{bare}}\rangle = \sum_{j < k} f_j(x_L, p_L) f_k(x_R, p_R) |\kappa \bar{\kappa}_{jk}^{\text{bare}}\rangle, \quad (4.3)$$

where $x_R - x_L$ determines the size of the bubble, p_L and p_R specify the expected momenta of the bubble walls, and we define the localized kink-antikink pair states

$$|\kappa \bar{\kappa}_{jk}^{\text{bare}}\rangle := |\dots \uparrow \downarrow_j \dots \downarrow_k \uparrow \dots\rangle. \quad (4.4)$$

Note that the restriction $j < k$ (the kink must be to the left of the antikink) means that the Gaussian packets (4.2) are truncated. In practice, one can ensure that this truncation is negligible by choosing x_L , x_R , and σ so that the coefficients are very small when $j \sim k$.

While these bare states illustrate many relevant properties of the states we wish to construct for $H(g > 0, \lambda \geq 0)$, they are all *eigenstates* of the bare Hamiltonian $H(g = 0, \lambda = 0)$, implying that kinks and antikinks do not propagate². They are also *product states*, devoid of entanglement. To obtain interesting dynamics, we need $g > 0$, for which all the bare states have counterparts dressed by fluctuations, possessing exponentially decaying correlations and entanglement between lattice sites. This entanglement can be efficiently captured by Matrix Product States (MPS)[232, 233, 255], a variational class of states with the form

$$|\psi\rangle = \sum_{\{s\}} A_1^{(s_1)} A_2^{(s_2)} \dots A_N^{(s_N)} |s_1 s_2 \dots s_N\rangle, \quad (4.5)$$

where N is the number of lattice sites, $s_j = 0, 1$ for our model and each $A_j^{(s)}$ is a $D_{j-1} \times D_j$ matrix, making A_j a rank-3 tensor. The dimensions D_j , called *bond dimensions*, limit the amount of entanglement that can be represented: the entropy of the subsystem consisting of all sites $> j$, which we call the *cut entropy* at location j , is upper-bounded by $\log_2 D_j$. In a finite chain with open boundaries, $D_0 = D_N = 1$. In our constructions, we consider infinite MPS in which the boundaries are decoupled from the bulk due to exponential decay of correlations (see App. C.1).

MPS can also be specified using tensor network diagrams. For example, we can rewrite (4.5) as

$$|\psi\rangle = \left| \begin{array}{c} \boxed{A_1} - \boxed{A_2} \cdots \boxed{A_N} \end{array} \right\rangle, \quad (4.6)$$

where $\boxed{}$ represents a rank-3 tensor. In Fig. 4.4, we illustrate the localized bare states and their dressed MPS counterparts, using tensor-network diagrams to indicate how the MPS are constructed. The MPS $|\Omega\rangle$ and $|\bar{\Omega}\rangle$ are approximations to the dressed true and false vacua. They are uniform, infinite MPS built from tensors $\boxed{}$ and $\boxed{}$, respectively. We optimize $\boxed{}$ using variational methods [205, 256–259] to minimize the energy of $|\Omega\rangle$. To find the metastable false vacuum $|\bar{\Omega}\rangle$, we first apply a global spin-flip to $|\Omega\rangle$, resulting in another uniform MPS, whose energy we then minimize. For sufficiently small $g \ll 1$, we observe that the energy-minimization

² $H(g = 0, \lambda = 0)$ is an RG fixed-point and one can think of the kinks and antikinks as having infinite mass.

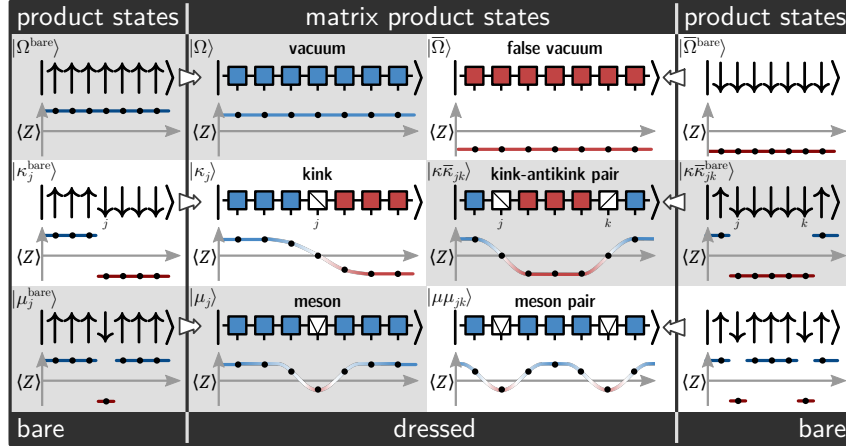


Figure 4.4: Diagram illustrating the various types of states, and their spin profiles, relevant for simulations. For example, our initial states are *wavepackets* constructed from kink-antikink pairs (a type of excited meson). The product states listed are eigenstates of H when $g = 0$, $\lambda = 0$. Away from this regime, we use MPS to accurately capture fluctuations in the vacua and excited states.

procedure does not find a path to the true ground state, resulting in a *metastable* false vacuum state $|\bar{\Omega}\rangle$, with MPS tensor \blacksquare , that behaves as an energy eigenstate for all practical purposes (up to numerical precision – see App. C.2).

The MPS $|\kappa_j\rangle$ approximates a dressed, localized kink state. It is constructed by introducing a new tensor \boxplus that sits at position j , between two semi-infinite chains, one consisting of \blacksquare on the left and one of \blacksquare on the right. The tensor \boxplus parameterizes the spatial transition between the true and false vacuum regions. Unlike in the bare case, the transition region may encompass many lattice sites, as illustrated by the $\langle Z \rangle$ plots in Fig. 4.4. The antikink $|\bar{\kappa}_k\rangle$ is similarly constructed by introducing a tensor \boxminus between a chain of \blacksquare on the left and \blacksquare on the right. We select \boxplus and \boxminus using an MPS Bloch-state approach [233, 257, 258, 260] so that $|\kappa_j\rangle$ and $|\bar{\kappa}_k\rangle$ states can be thought of as "position bases" for the kink and antikink *quasiparticles* of lowest energy. We use these states to construct topological quasiparticle wavepackets $\sum_j f_j |\kappa_j\rangle$ and $\sum_k f_k |\bar{\kappa}_k\rangle$ [237]. If D is the bond dimension of the vacuum MPS, such wavepackets have MPS representations with bond dimension $2D$ (see App. C.3 for details).

The Bloch-state approach for finding \boxplus and \boxminus is conceptually simpler when $h = 0$, so that there is no confining force acting on the kinks and antikinks. We consider the $h \neq 0$ case further below. For $h = 0$, we solve an effective Hamiltonian for \boxplus and \boxminus

such that the momentum eigenstates, $\sum_j e^{ipj} |\kappa_j\rangle$ and $\sum_k e^{ipk} |\bar{\kappa}_k\rangle$, approximate the lowest-energy topological eigenstates of H with momentum p [258]. The resulting tensors $\tilde{\chi}$, $\tilde{\chi}^\dagger$ (and hence $|\kappa_j\rangle$, $|\bar{\kappa}_k\rangle$) generally depend on the momentum p , but we ignore this dependence when building wavepackets, aside from choosing the p used to solve for $\tilde{\chi}$ and $\tilde{\chi}^\dagger$ to match the expectation value of momentum in the wavepacket state. This is justified for Gaussian wavepackets with large σ , and hence small momentum variance, if the tensors vary sufficiently slowly with p .

There is also an important physical reason for choosing σ to be large: In the presence of fluctuations, localized packets can no longer be truly static, since they are not eigenstates of H . Instead, they will spread out as time passes, at a rate dependent on σ . Wavepackets can be made to spread slowly relative to other processes, such as the collapse of a false-vacuum bubble, by choosing $\sigma \gg \xi$, where ξ is the correlation length in lattice units. It is desirable for the kink and antikink wavepackets comprising a bubble to spread only minimally prior to collision, since then the wavepackets of *outgoing* quasiparticles also tend to be well localized, which makes them easier to characterize.

We now explain how to find $\tilde{\chi}$ and $\tilde{\chi}^\dagger$ in case $|h| > 0$, where the confining force on kinks and antikinks means that $\sum_j e^{ipj} |\kappa_j\rangle$ and $\sum_k e^{ipk} |\bar{\kappa}_k\rangle$ can no longer be eigenstates of H . In this case, we optimize $\tilde{\chi}$ and $\tilde{\chi}^\dagger$ by optimizing *modified* energy functions that subtract away the false-vacuum contributions, which in $|\kappa_j\rangle$ and $|\bar{\kappa}_k\rangle$ depend on the positions j and k (thus providing an accelerating force). We explain this for the case of $|\kappa_j\rangle$ and $\tilde{\chi}$, since the procedure is completely analogous for $|\bar{\kappa}_k\rangle$ and $\tilde{\chi}^\dagger$. We first note that it is possible to choose $\tilde{\chi}$, by exploiting a redundancy in the representation of momentum eigenstates, to achieve $\langle \kappa_j | \kappa_k \rangle = \delta_{jk}$ (see App. C.3). After making this choice, we minimize

$$\tilde{E} = \sum_{jk} e^{ip(k-j)} \langle \kappa_j | (H - \Delta E_j \mathbb{1}) | \kappa_k \rangle, \quad (4.7)$$

where $\Delta E_j := \sum_{-\infty}^j e_{\text{true}} + \sum_{j+1}^{\infty} e_{\text{false}}$ captures the infinite bulk contributions to the energy present in $|\kappa_j\rangle$, coming from the true and false vacua (e_{true} and e_{false} are the energy densities of the true and false vacua). Subtracting them in this position-dependent way makes the contribution of each $|\kappa_j\rangle$ term to \tilde{E} finite and independent of j . Note that the ΔE_j correction does not affect off-diagonal terms $\langle \kappa_j | \kappa_{k \neq j} \rangle$. The energy minimization procedure is easily carried out by slightly adapting the methods of [257] (see App. C.3 for details).

To build dressed bubble states $|\Psi\rangle$ as MPS, we proceed analogously to the bare case by combining a kink and an antikink wavepacket

$$|\Psi\rangle = \sum_{j < k} f_j(x_L, p_L) f_k(x_R, p_R) |\kappa\bar{\kappa}_{jk}\rangle, \quad (4.8)$$

where, in our simulations, we choose the momenta $p_L = p_R = 0$ and set $x_R - x_L \gg \sigma$ so that $f_j(x_L) f_k(x_R)$ is small for small $k - j$. The kink-antikink pair states $|\kappa\bar{\kappa}_{jk}\rangle$ are constructed by combining the tensors , ,  and  (already optimized to represent the vacua, kinks, and antikinks) without further modification, as illustrated in Fig. 4.4, using the aforementioned reflection-symmetry condition to fix  and  completely (see App. C.3). With this scheme, $|\kappa\bar{\kappa}_{jk}\rangle$ accurately describes a kink-antikink pair at asymptotically large separations $k - j$. However, at small separations, corrections would generally be needed due to interaction effects³. We again rely on $x_R - x_L \gg \sigma$ here, which ensures that terms with small separation are strongly suppressed, so that the error incurred by ignoring interactions is small.

Time evolution

To evolve an initial MPS $|\Psi(t = 0)\rangle$ in time, we apply the time-dependent variational principle (TDVP) [256] within a finite window of the infinite chain surrounding the initial bubble [259]. The TDVP provides effective equations of motion for the MPS tensors so that the evolution of the MPS approximates evolution by H . We primarily use the Runge-Kutta 4/5 algorithm to numerically integrate these equations, which we find provides a good balance of speed and accuracy except at very early times, where we use the better-conditioned, but more computationally intensive, "split-step" integrator of [261]. These methods are implemented in the *evoMPS* python package [262]. To capture growing entanglement, the bond dimensions of the MPS are allowed to increase during the evolution up to some chosen maximum [261, 263].

As the state evolves, we monitor its spin and energy expectation values as well as its entanglement properties. This allows us to draw conclusions about collision (scattering) outcomes. For instance, elastic and inelastic scattering are easily distinguished from the trivial case, as interaction generically results in *entanglement* between any outgoing kinks or particles⁴, whereas trivial scattering never does. We can also easily distinguish elastic and inelastic scattering in many cases. For example, if a

³A priori, the MPS tensors may also need modifying at short distances even in the absence of interactions.

⁴This is true for wavepackets of finite width. In the limit of infinitely-broad spatial wavepackets (momentum eigenstates), elastic scattering does not produce entanglement in (1+1)D. see App. C.9.

collision produces a pair of mesons, their wavepackets will spread *ballistically* since two mesons are not subject to a confining force. Indeed, any sustained ballistic spread of energy implies particle production. Importantly, the converse does not always hold, since confined topological particles different from those of the initial state may also be produced.

Particle detection

Aside from constructing the initial state $|\Psi\rangle$, we can also use the MPS $|\kappa\bar{\kappa}_{jk}\rangle$, representing kink-antikink pairs, as a kind of *particle detector*, the inner product $\langle\kappa\bar{\kappa}_{jk}|\Psi(t)\rangle$ corresponding approximately to the amplitude of a kink-antikink pair with position j, k at time t . Conveniently, these states can be made to fulfill $\langle\kappa\bar{\kappa}_{jk}|\kappa\bar{\kappa}_{lm}\rangle = \delta_{jl}\delta_{kl}$ (see App. C.3). We can treat the subspace spanned by these basis states as an approximate kink-antikink pair "sector", which we denote $\kappa\bar{\kappa}$. One reason for its approximate nature should be familiar from the discussion above: The basis captures a kink-antikink pair most accurately if the kink and antikink are smeared out into wavepackets that are sufficiently broad, so that the wavepacket momenta are focused around the momentum p used to compute \mathbb{V} and \mathbb{W} . Additionally, the kink and antikink must be sufficiently separated so that interaction effects are insignificant. Fortunately, these two properties can be checked *after* projecting the wavefunction into the $|\kappa\bar{\kappa}_{jk}\rangle$ subspace. The simplest way to deal with terms in which the kink and antikink are too close together is to simply exclude them from the projection subspace. Inaccuracies due to the momentum-dependence of \mathbb{V} and \mathbb{W} can be mitigated in a few ways: Assuming the momentum dependence is not too strong, the simplest strategy is to tune \mathbb{V} and \mathbb{W} to match the expected momentum of the projected wavefunction. A more precise result can be had via a Fourier analysis, in which the detection subspace is further restricted to a range of momenta that match \mathbb{V} and \mathbb{W} . See App. C.4 for a more detailed, technical discussion.

The $\kappa\bar{\kappa}$ subspace is already sufficient to detect inelastic scattering: if the portion of the wavefunction within the subspace drops significantly during evolution, particle production has likely occurred. Going further, we can construct quasiparticle position bases for other quasiparticle types, both topological and nontopological. To this end, we define the MPS $|\kappa_j^{(a)}\rangle$, $|\bar{\kappa}_j^{(a)}\rangle$, and $|\mu_j^{(a)}\rangle$, with corresponding tensors $\mathbb{V}^{(a)}$, $\mathbb{W}^{(a)}$, and $\mathbb{M}^{(a)}$, to be approximate position bases for the a^{th} kink, antikink, and meson quasiparticles, with $a = 0, 1, \dots$ in ascending order of energy. We sometimes suppress the superscript a when considering the lowest-energy

quasiparticles of each type $a = 0$. The meson states $|\mu_j\rangle$ are constructed from the vacuum tensor \mathbb{V} and the meson tensor \mathbb{M} , as illustrated in Fig. 4.4. We compute $\mathbb{V}^{(a)}$, $\mathbb{M}^{(a)}$, and $\mathbb{K}^{(a)}$ by simply solving for multiple energies in the Bloch-state approach used above to generate the lowest-energy kink and antikink tensors \mathbb{K} , \mathbb{A} [257, 260]⁵. This procedure can deliver accurate quasiparticle states for quasiparticles with energy E_a below the two-particle threshold [258]. Above that threshold, these tensors may correspond to unstable excitations. The procedure also guarantees that $\langle \kappa_j^{(a)} | \kappa_k^{(b)} \rangle = \langle \bar{\kappa}_j^{(a)} | \bar{\kappa}_k^{(b)} \rangle = \langle \mu_j^{(a)} | \mu_k^{(b)} \rangle = \delta_{jk} \delta_{ab}$. The kink, antikink and meson single-particle bases are mutually orthogonal by construction, due to the orthogonality of the true and false vacua in the thermodynamic limit.

We can construct pair states $|\kappa \bar{\kappa}_{jk}^{(a,b)}\rangle$ and $|\mu \mu_{jk}^{(a,b)}\rangle$ from this extended set of single-quasiparticle states following Fig. 4.4. These extended bases are *not* orthonormal at small separations $k - j$ due to interaction effects. Nevertheless, we can compute a minimum separation d for each set of Hamiltonian parameters g, Δ, h so that the bases are *approximately* orthonormal when $k - j \geq d$ (see App. C.3). These restricted bases give us access to extended kink-antikink $\kappa \bar{\kappa}^{(a,b)}$ and meson-pair $\mu \mu^{(a,b)}$ "sectors", allowing a much finer analysis of particle content.

4.3 Results

Kink dynamics

In the following we consider kinks, but the discussion applies equally to antikinks. The evolution of a kink-quasiparticle wavepacket will generically involve propagation and spreading (delocalization). We wish to construct wavepackets that are sufficiently broad so that they spread slowly, relative to propagation. Broader spatial wavepackets lead to slower spread because they have narrower momentum support; furthermore, spreading is reduced for wavepackets with higher momentum, because the relevant part of the kink-quasiparticle dispersion relation $E_\kappa(p)$ looks increasingly linear.

For $h = 0$, we observe that our kink wavepackets indeed spread slowly as they propagate at their initial set momentum (see App. C.8). In the presence of a confining force from a symmetry-breaking field $h > 0$, kinks undergo acceleration, as expected. A stationary kink is initially accelerated in the direction of the false vacuum, as the energy of the false vacuum is converted into kinetic energy of the kink, as would also be expected in a relativistic QFT, but the long term behavior

⁵These methods also deliver approximate quasiparticle dispersion relations.

is strongly influenced by the lattice (see App. C.7 for single-kink simulation data). The lattice momentum p is bounded $-\pi < p \leq \pi$, and the momentum expectation value of the kink wavepacket precesses around the unit circle with $\dot{p} = \text{constant}$. To understand how the *position* of the kink evolves as this happens, we must consider the wavepacket group velocity $v(p) := \partial E_\kappa(p)/\partial p$. With an emergent relativistic QFT governing the IR physics, the dispersion relation is approximately relativistic ($E_\kappa(p) \sim \sqrt{p^2 + m_\kappa^2}$ for a kink of mass m_κ) for small $|p|$, becoming almost linear as p increases. However, due to the bounded nature of p on the lattice, $E_\kappa(p)$ must deviate from relativistic behavior as $|p|$ continues to increase. Indeed, assuming $E_\kappa(p)$ is smooth, including at the boundary value $E_\kappa(\pi) = E_\kappa(-\pi)$, it is *also* bounded from above and below. As such, a wavepacket will typically reach a maximum group velocity for some $p(v_{\max})$, after which it will begin to *slow down*. Assuming $E_\kappa(p) = E_\kappa(-p)$ it will ultimately *reverse* and retrace its path back to its original position and momentum (with some wavepacket spread), performing *Bloch oscillations*.

Bubble dynamics

Instead of Bloch oscillations of individual kinks, we wish to study the emergent relativistic dynamics of false-vacuum *bubbles* comprised of a kink wavepacket and an antikink wavepacket. In particular, we want to simulate kink-antikink collisions at large kinetic energies (to increase particle-production amplitudes). Since the kink and antikink accelerate toward each other under the confining force, we can increase the kinetic energy at the time of collision by increasing the initial bubble size $x_R - x_L$ (and hence the amount of energy stored in the false vacuum). However, if we allow the kink and antikink to evolve for too long prior to collision, their momenta will exceed $|p(v_{\max})|$ and they will begin to undergo Bloch oscillations, deviating from their relativistic behavior. We can ensure that this does not occur by limiting the initial bubble size, with the maximum size depending on the Hamiltonian parameters g, λ, h . In general, a smaller mass gap (since $h \neq 0$, this is the meson mass m_μ), measured in lattice units, increases the maximum bubble size, measured in physical units (multiples of the lattice correlation length ξ). Moving closer to criticality thus allows us to reach higher collision energies relative to the mass gap while staying below $p(v_{\max})$.

We simulated bubble dynamics for the Ising model ($\lambda = 0$) as well as near to the Tri-Critical Ising point of the extended model ($\lambda > 0$) for a range of parameters. We first focus on the two points marked (i) and (ii) in Fig. 4.3.

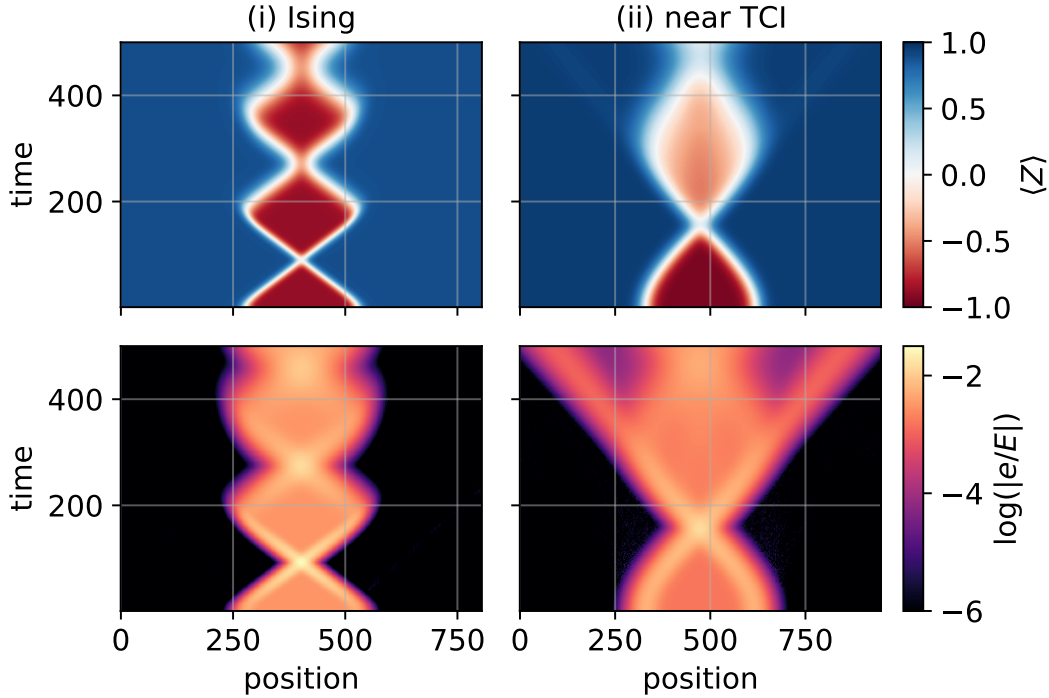


Figure 4.5: Spin expectation values and relative energy density e/E for (i) the Ising model ($\lambda = 0$, $g = 0.8$, $h = 0.007$) and (ii) the generalized Ising model nearer to the Tricritical Ising CFT fixed point (TCI) ($\lambda = 0.41$, $g = 0.98$, $h = 0.001$). For (i), the initial wavepackets have $\sigma = 25$ and are 248.5 sites apart ($E/m_\mu = 3.72$). For (ii), $\sigma = 40$ with separation 287.4 ($E/m_\mu = 2.62$). The MPS bond dimensions are $D = 10$ and $D = 18$ for the vacua of (i) and (ii), respectively. During the simulation the dimensions are restricted to $D \leq 128$ and the integration step size is $\delta t = 0.05$.

The Ising model

In the Ising case ($\lambda = 0$) with $h = 0$, known to be a theory of free kinks, our simulations reproduce the expected trivial scattering: kinks given an initial nonzero momentum collide without generating any additional entanglement. With explicit symmetry-breaking ($0 < h \ll 1$) we find nontrivial scattering, as evidenced by entanglement between the post-collision kink wavepackets. However, even when the energy is significantly above the meson pair-production threshold $E > 2m_\mu$ there is no obvious ballistic spread to indicate production of unconfined particles (see Fig. 4.5). Furthermore, the system is found to be within the bubble "sector" $\kappa\bar{\kappa}^{(0,0)}$ after the first collision to high numerical precision, as shown for $g = 0.8$ in Fig. 4.6, consistent with purely elastic scattering of kinks. The probability $1 - P_{\kappa\bar{\kappa}}$ of being in a *different* sector is estimated to be around $O(10^{-5})$ both before and after the first collision, with the difference closing as the maximum bond dimension

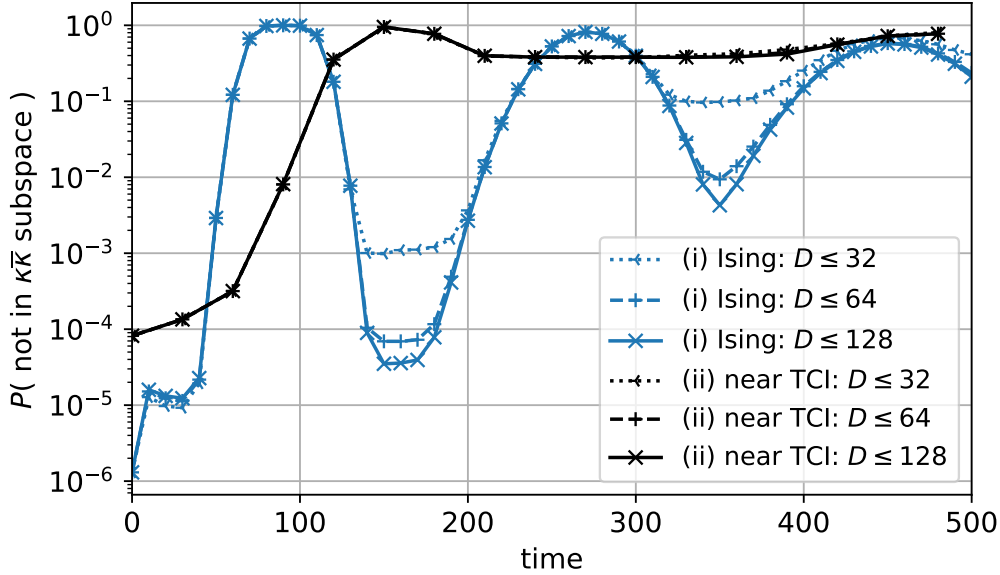


Figure 4.6: Portion of state (by probability) outside of the MPS bubble subspace $\kappa\bar{\kappa}^{(0,0)}$ for simulations (i) and (ii) of Fig. 4.5. Here we fully account for momentum dependence of the basis states $|\kappa\bar{\kappa}_{j,k}\rangle$ via a Fourier analysis and count only contributions with $k - j \geq 60$ (see App. C.4). For Ising (i), the small probability after the first collision of $t \approx 90$ indicates elastic scattering of kinks, in stark contrast with the TCI case (ii), where the probability remains high after the first collision at $t \approx 150$. In (i), the growth of the post-collision probability with subsequent collisions is consistent with increasingly inaccurate representation of accumulating entanglement (due to the limit imposed on the MPS bond dimension D), as well with delocalization of the wavepackets, since contributions from kink-antikink pairs with small separation $k - j$ are not counted.

increases. This probability is consistent with a numerical estimate of the accuracy of the kink-antikink quasiparticle basis states, as detailed in App. C.3. That $P_{\kappa\bar{\kappa}} < 1$ during collisions, as well as later in the evolution as the wavepackets delocalize, is due to components of the state leaving the space of well-separated localized quasiparticles as the kink and antikink interact. While we cannot entirely rule out inelastic scattering using this data, any inelastic process would have to be extremely unlikely to be consistent with our results.

This observation is surprising given that the spin chain and its emergent field theory are not integrable, but consistent with recent observations of nonthermalizing states in the Ising model [234, 251, 252]. We further find that elastic scattering persists even if we allow the kink velocity to exceed v_{\max} , as it does in simulation (i) of Figs. 4.5 and 4.6 (see App. C.7), so that the emergent relativistic field theory is

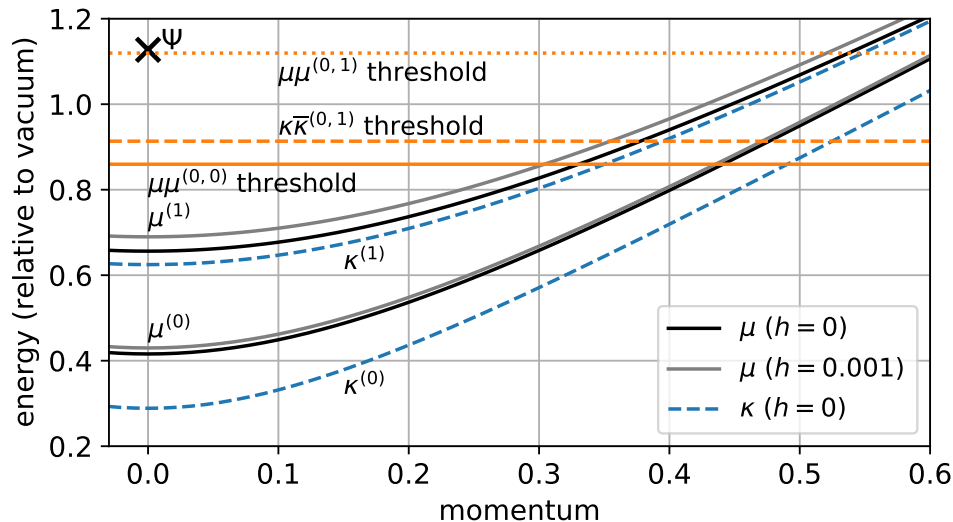


Figure 4.7: Dispersion relations (numerical, using MPS) of kinks κ and mesons μ for $\lambda = 0.41$, $g = 0.98$. For mesons, energies are shown with and without a weak longitudinal field. Individual kinks do not have a finite energy for $h > 0$. Threshold energies for pair production are shown (computed assuming $h = 0$ for kinks and $h = 0.001$ for mesons), as is the energy (labelled Ψ) of the simulation shown in Fig. 4.5 for parameter-set (ii).

no longer a good description of the physics. This is strong evidence that, in the Ising chain with a weak longitudinal field, bubbles are stable up to *arbitrarily* high energies: When a bubble is large enough, its walls will not meet due to Bloch oscillations, so no scattering can occur while it remains localized. When bubbles are small enough for the kinks to collide, our evidence suggests they always do so elastically.

Near the Tri-Critical Ising point

Turning on $\lambda > 0$, we choose the initial bubble size so that the energy, shown in Fig. 4.7, is well above the pair-production threshold (but still low enough to keep the kink velocity $\ll v_{\max}$). Here we find clear evidence that unconfined particles are produced. Most apparently, Fig. 4.5 (ii) clearly shows *ballistic* spread of wavepackets emanating from the first collision event. To further resolve the scattering outcomes, we project onto meson-pair and kink-antikink-pair quasiparticle bases, finding four dominant "sectors", illustrated in Fig. 4.8, where we tune the quasiparticle basis MPS to match the momentum expectation value of the outgoing quasiparticle wavepackets (as estimated from the Fourier transform of the projected wavefunctions) and

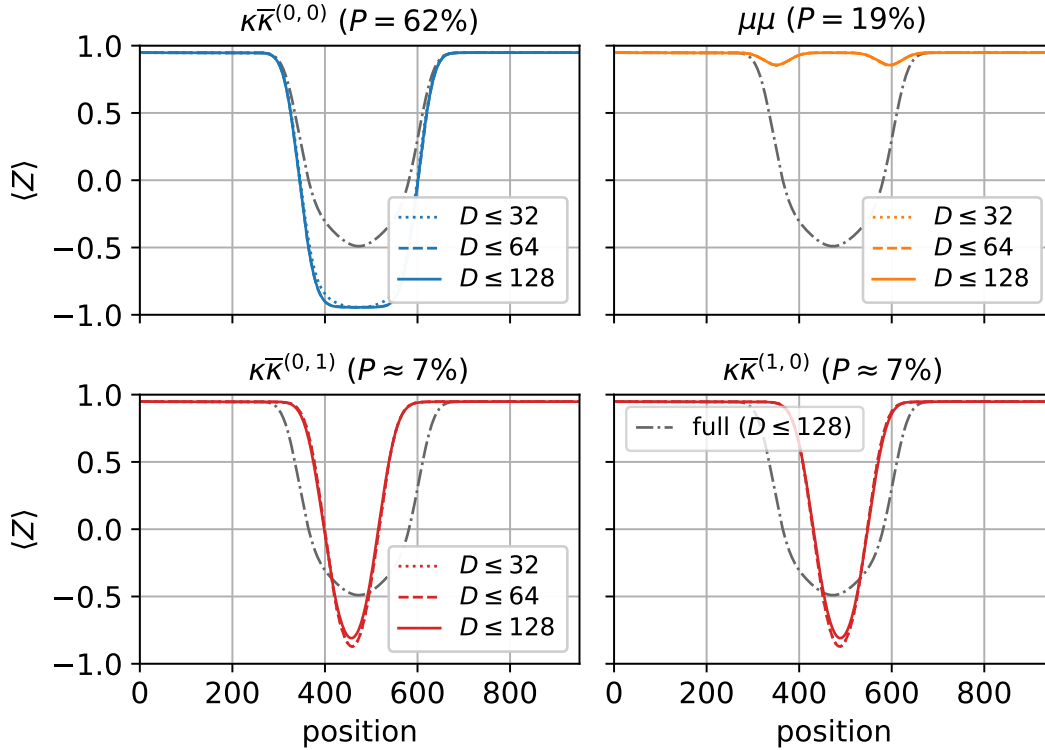


Figure 4.8: Spin expectation values for simulation (ii) of Fig. 4.5 at time $t = 270$ (bond dimension $D \leq 128$) after projection into selected quasiparticle subspaces and normalization. The amount of wavefunction captured by each (approximately orthogonal) subspace is given as a probability P (see App. C.4). Included subspaces are $\mu\mu$, a pair of mesons of lowest energy, and $\kappa\bar{\kappa}^{(a,b)}$, a bubble made of a kink of type a and an antikink of type b (where 0 is the lowest-energy kink quasiparticle, and 1 is the next highest – see Fig. 4.7).

compute the spin expectation values of the projected wavefunction for each sector. We also compute the scattering outcome probabilities (the norms of the projected wavefunctions)⁶. We find the most likely outgoing configurations to be: a bubble made of type-0 kinks $\kappa\bar{\kappa}^{(0,0)}$ (elastic channel) with probability $P = 62\%$, then a type-0 meson pair $\mu\mu^{(0,0)}$ with $P = 19\%$, and finally a bubble made either of a type-0 kink paired with a type-1 antikink (higher energy) $\kappa\bar{\kappa}^{(0,1)}$, or a type-1 kink paired with a type-0 antikink $\kappa\bar{\kappa}^{(1,0)}$, each with $P \approx 7\%$ (reflection symmetry). These outcomes are all kinematically allowed, according to the energetic thresholds shown in Fig. 4.7.

We note that the (rounded) projection probabilities in Fig. 4.8 only add to 95%.

⁶For this we use a more sophisticated Fourier analysis that more fully accounts for the momentum dependence of the quasiparticle basis MPS. see App. C.4.

This may indicate the presence of other sectors we have not accounted for, such as a $\mu^{(0)}$ paired with a small $\kappa\bar{\kappa}^{(0,0)}$ bubble, or a $\kappa\bar{\kappa}^{(0,0)}$ bubble containing one or more quasiparticle-excitations of the false vacuum. Unfortunately, since these "sectors" each involve at least three quasiparticles, the corresponding position bases have many more terms ($O(N^3)$ versus $O(N^2)$ for pairs), making them difficult to work with⁷.

It is also possible that various sources of error have affected results: (i) when excitation tensors in a 2-quasiparticle MPS are close together, so that interactions are relevant, the state may not accurately represent quasiparticles, (ii) the MPS representations of the quasiparticle position states are variational approximations subject to some error (which also affects the initial state of the simulation), and (iii) although we allow the MPS bond dimension to increase up to some maximum during simulations ($D \leq 128$ in this case), errors can still accumulate if that maximum is insufficient to capture all entanglement, as well as due to errors in the numerical integration steps. We did not explicitly characterize the effects of (ii), but expect them to be small, because the true and false vacuum MPS, upon which the excitations are built, are already accurate to $\sim 10^{-6}$ in norm. By varying the minimum quasiparticle separation used in the projection, as well as the maximum bond dimension of the simulation, we were able to characterize effects (i) and (iii), finding them to amount to changes in the outcome probabilities of $\ll 0.01$, except in the case of $\kappa\bar{\kappa}^{(0,1)}$ and $\kappa\bar{\kappa}^{(1,0)}$, in which one of the quasiparticles is heavier than the other, leading to a smaller separation between the kink and antikink. In this case, our analysis suggests the error here amounts to a change of around ± 0.01 in the outcome probability, possibly more (see App. C.4). This outcome might be better resolved at higher energies, at which the kink-antikink separations would increase.

In case of the $\mu\mu$ outcome, we cross-check the computed outcome probability by comparing it with the excess energy (relative to the vacuum) E_{pkts} of the regions containing the ballistic wavepackets, visible in Fig. 4.5 (ii). If these wavepackets belong to a two-meson "branch" of the wavefunction, that branch (the portion of the wavefunction in the $\mu\mu$ subspace) must contribute EP to the energy, where E is the total energy and P is the probability of the $\mu\mu$ scattering outcome. We can therefore estimate P as E_{pkts}/E . This gives us a P within the range 19% to 20% at $t = 480$ (after separation), depending on the precise extent of the region we sum over (e.g. from site 0 to site 250 for the left packet), compatible with the projected

⁷Not only computationally, but also because basis orthogonality is harder to achieve.

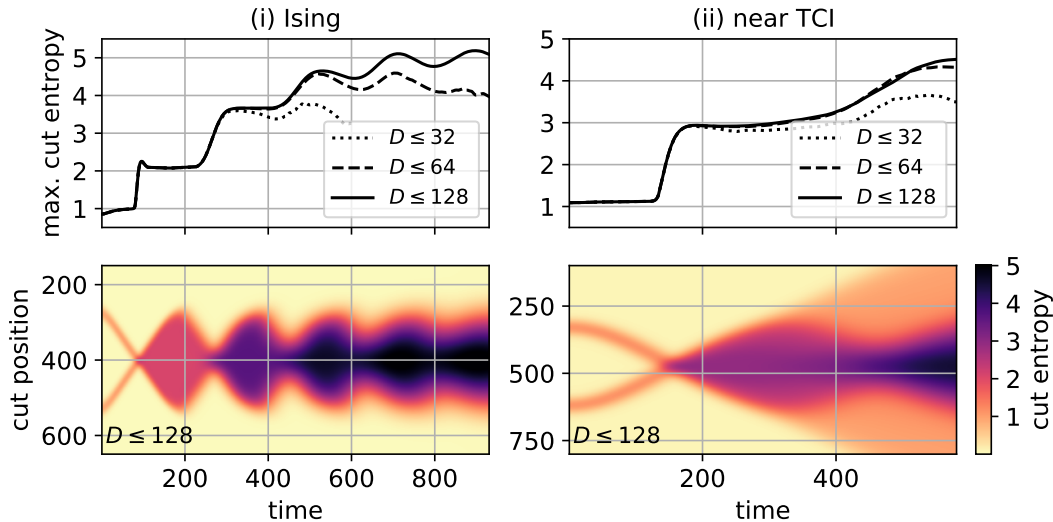


Figure 4.9: Entanglement entropy (base 2) for cuts (left-right bipartitions) of the spin chain as a function of time for the simulations (i) and (ii) of Fig. 4.5. Convergence with the bond dimension D slows as time goes on. For example, in (i) the max. cut entropy at $D \leq 128$ is very likely not converged after $t \approx 400$.

$\mu\mu$ wavefunction.

Entropy and computational cost

As evidenced by Fig. 4.6, the bond dimension of the MPS representing the evolving state must continue to grow as time goes on, in order to maintain accuracy. The cut entropy at location j is a proxy for the required bond dimension D_j . Fig. 4.9 shows the evolution of the maximum cut entropy for the simulations of Fig. 4.5. At early times, we observe that the maximum cut entropy jumps dramatically during scattering events, whether elastic or inelastic, remaining almost constant in between. This is consistent with a model of interacting quasiparticle wavepackets: Separated wavepackets undergo stable propagation until they collide, at which point interactions generate entanglement corresponding to the different possible scattering outcomes. At late times, we observe a temporal broadening of the jumps, consistent with spatial broadening of the wavepackets involved. Fig. 4.9 also shows that, although there is cut entropy associated with the wavepackets themselves, this is quickly surpassed by the cut entropy in the center of the chain, associated with entanglement between the left and right outgoing packets. It is this entanglement between outgoing quasiparticles that is responsible for the post-collision plateaus visible in the maximum cut entropy.

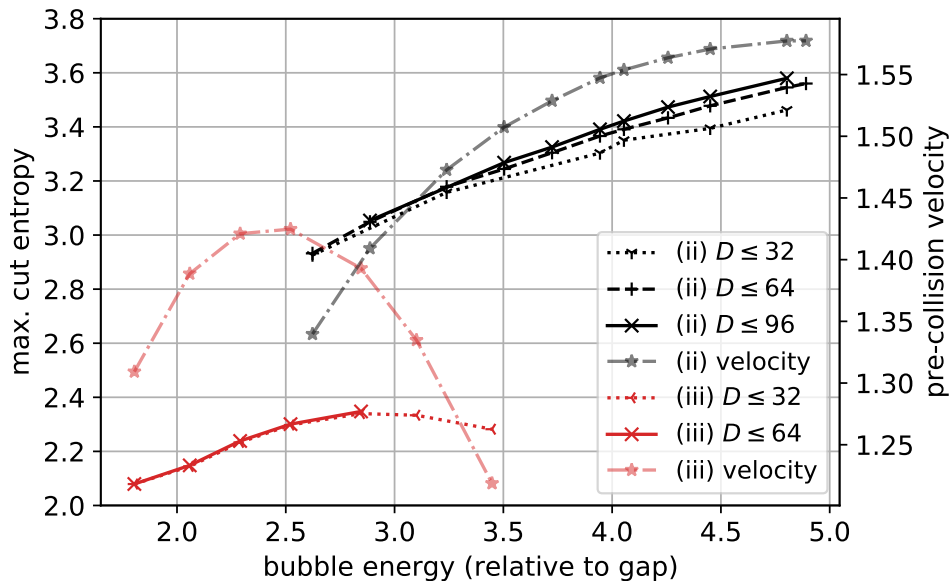


Figure 4.10: Peak maximum cut entropy during the first collision as a function of energy (ii) close to ($\lambda = 0.41$, $g = 0.98$, $h = 0.001$) and (iii) further from the TCI point ($\lambda = 0.3$, $g = 0.9$, $h = 0.0069$), with the energy controlled by the initial kink separation. The meson mass m_μ in lattice units is 0.43 for (ii) vs. 0.97 for (iii), while the vacuum correlation length ξ is 3.6 sites for (ii) and 1.8 sites for (iii), both indicating that (ii) is closer to criticality. The initial wavepacket width is $\sigma = 40$ for (ii) and $\sigma = 19$ for (iii). The kink velocity (lattice units) at the start of the first entropy jump (see Fig. 4.9) is also shown. Decreasing velocity with energy indicates the onset of Bloch oscillations.

The entropy jumps clearly make MPS simulations of long-time dynamics demanding. However, for the purposes of studying the quasiparticle content of scattering outcomes, with the incoming quasiparticles chosen via the initial state, it is enough to accurately simulate a single collision and then wait until the outgoing wavepackets have separated sufficiently so that interactions between outgoing quasiparticles may be neglected (we assume the simulation parameters are chosen such that wavepackets remain localized for sufficiently long times)⁸.

We expect the entropy generated in a collision of localized quasiparticle wavepackets to depend on the collision energy relative to the masses of quasiparticles: the more scattering outcomes there are, and the greater the probability of those outcomes, the larger the post-collision entanglement entropy can be. In Fig. 4.10, we explore the

⁸Simulating for only relatively short times also increases the likelihood that these tasks can be carried out on NISQ-era quantum devices.

maximum cut entropy as a function of energy, controlled via the initial kink separation, for two sets of Hamiltonian parameters, one (ii) closer and one (iii) further from criticality. We find that the entropy indeed grows with energy, smoothly increasing even as thresholds are crossed, e.g. the $2m_{\mu^{(1)}}$, $3m_{\mu^{(0)}}$, and $4m_{\mu^{(0)}}$ thresholds in case of (ii) (see also Fig. 4.7).

The entropy continues to increase at least until the energy is sufficient for the kinks to approach the maximum possible kink velocity prior to collision, at which point we expect deviations from the emergent relativistic dynamics to become apparent as Bloch oscillations emerge. In the case of (iii), Fig. 4.10 shows that the post-collision entropy eventually decreases as lattice effects kick in, coincident with deceleration of the kinks prior to collision. Note that we are able to reach much higher relative energies with parameters (ii) before encountering obvious lattice effects. This illustrates the general principle that more of the emergent relativistic QFT is revealed as one approaches criticality: the relative energies accessible by quasiparticles, while avoiding Bloch oscillations (momenta $< p(v_{\max})$), grows as the lattice meson mass drops.

We also observe that much more entropy is generated in the first collision for parameters (ii) than for parameters (iii), even when the relative energy is similar⁹. A significant part of this difference likely comes from a much higher probability of meson pair production, as well as the availability of the $\kappa\bar{\kappa}^{(0,1)}$ outcomes, in case (ii): the probability of particle production is $< 10\%$ in case (iii) at energy $E/m_{\mu} \approx 2.52$, in contrast with $\sim 38\%$ at energy $E/m_{\mu} \approx 2.62$ in case (ii), according to $\kappa\bar{\kappa}^{(0,0)}$ basis overlaps. This is possible, since these two parameter sets were not chosen to be part of an RG trajectory, so that their emergent QFTs need not be the same.

4.4 Discussion

Building on recent innovations in the classical simulation of quasiparticle dynamics using Matrix Product States [237], we proposed a framework for simulating and characterizing the full (nonperturbative) quantum dynamics of false-vacuum bubbles in relativistic QFTs that govern the IR physics of one-dimensional lattice systems. While we chose to simulate a quantum spin chain, the methods we use are general and could also be applied directly to, for instance, a spatially-discretized QFT such as the Schwinger model or $\lambda\phi^4$ theory [2, 28, 205–210, 239]. We also demonstrated that the MPS quasiparticle ansatz, with which we initialized our simulations, can

⁹The difference in post-collision entropy is not attributable to different vacuum entropies, since these are < 0.1 in both cases.

be used to *detect* quasiparticles that are produced as time evolves. This allowed us to verify quasiparticle pair-production in the modified Ising model we studied, including production of different species of confined kink that were not obvious from examining energy density and spin expectation values alone. We used the same kind of analysis to confirm a *lack of* particle-production in the unmodified Ising model (with transverse field and small longitudinal field), supporting other recent studies that suggest particle production is very strongly suppressed [234, 251, 252].

We were able to significantly improve the efficiency and interpretability of our simulations by carefully choosing our initial states in two different ways: Firstly, constructing spatially broad wavepackets allowed us to access the dynamics of the emergent IR QFT without the spoiling effects of UV, high-momentum components that are strongly influenced by the lattice. Broad wavepackets also lead to localization of quasiparticles over long times, making it easier to characterize scattering outcomes, and improve the numerical conditioning of the dynamical simulation (see App. C.6). Secondly, by precisely tuning the quasiparticle content of the initial wavepackets [237], we were able to study individual scattering events in isolation, while further reducing the computational demands of the simulation by lowering entanglement.

Entanglement growth is the most significant barrier to dynamical simulations with MPS, as the computational cost of each time step scales exponentially with the cut entropy. By choosing broad quasiparticle wavepackets, we reduce entanglement growth at the expense of growing the number of lattice sites involved in the simulation. This is a good tradeoff for MPS simulations, as the computational cost scales only linearly in the number of lattice sites. Even with this tradeoff, we found that the large jumps in cut entanglement with each collision (of confined quasiparticles in the system) preclude simulating more than a handful of successive collisions. Furthermore, we found clear evidence of entanglement growth with the collision energy, although the onset of Bloch oscillations prevented us from drawing strong conclusions about how this growth continues in the emergent IR QFT. Nevertheless, in the absence of lattice effects that obscure the IR QFT, it seems reasonable to expect the entropy to continue to grow with energy, which would eventually preclude accurate simulation using MPS.

A natural next step would be to identify RG trajectories in the Hamiltonian parameter space so that results can be extrapolated to the continuum. This is equivalent to finding paths toward criticality of the lattice model, along which the low-energy

spectrum remains consistent with a particular emergent (IR) QFT. Moving closer to the continuum would also allow us to reach higher (relative) collision energies while avoiding lattice effects, such as Bloch oscillations. In turn, this would permit a more thorough exploration of the energy-dependence of the entanglement generated in collisions.

As we approach criticality, the bond dimension of the MPS vacua must grow to maintain accuracy, as must the size of the simulation window, since the wavepacket width in lattice units would have to increase with the lattice correlation length in order to maintain localization. Getting closer to criticality seems feasible: The simulations featured in the main text, with maximum MPS bond dimension 128 and time-step size 0.05, took between one and two weeks to complete on 8 cores each and this time could likely be reduced significantly with further work to optimize the code¹⁰ and the use of a numerical integrator with an adaptive time-step size.

Increasing the number of spatial dimensions presents a significantly greater challenge for classical algorithms: while the computational cost of MPS simulations scales with the bond dimension D as $O(D^3)$, the scaling for tensor-networks capable of handling large (2+1)-dimensional systems, such as PEPS [265], is much worse (albeit still polynomial)¹¹. As an intermediate step, one could consider systems with a small, compactified second dimension of space, which are often within reach of MPS methods. By performing a Fourier transform of the Hamiltonian in the compactified direction only [267], one could study scattering of quasiparticles that are spatially localized in one direction, while being momentum eigenstates of the other. Compared to the purely (1+1)-dimensional case, the additional "Kaluza-Klein" excitations associated with the Fourier modes of the compactified dimension would already open up a much greater range of scattering outcomes.

Compared to the simulations we performed, increasing the variety of scattering outcomes, whether by raising the relative energy in a given model, choosing a lattice model with a richer set of low-energy excitations (e.g. near a phase transition described by a CFT with larger central charge), or adding spatial dimensions, seems necessary in order to find problems that exhaust tensor-network methods due to the additional entanglement generated. Such problems appear more amenable to

¹⁰GPU acceleration may also be useful [264].

¹¹Some methodological changes would also be needed: false-vacuum bubbles in > 1 spatial dimensions, having extensive boundaries, no longer look like mesons. As such, localized quasiparticle techniques (such as those developed for PEPS [266]) are not directly applicable. Instead, suitable initial states could likely be prepared via energy minimization in the presence of a nonuniform symmetry-breaking field.

simulation on quantum hardware, which is not *a priori* limited in the amount of entanglement it can deal with. However, raising the energy may be problematic for near-term quantum devices, which are limited both in their size and coherence times, since avoiding lattice effects (such as Bloch oscillations) at higher relative energies requires moving closer to criticality while increasing system sizes and evolution times. Instead, increasing the richness of low-energy excitations by changing the model or adding (compactified) dimensions, while avoiding coming too close to criticality, may be a more promising route toward quantum advantage using near-term devices.

Acknowledgments

We thank Alex Buser, Marcela Carena, Cliff Cheung, Natalie Klco, Ying-Ying Li, Spiros Michalakis, Nicola Pancotti, Burak Şahinoğlu, Martin Savage, and Eugene Tang for useful discussions and comments.

This material is based upon work supported in part by the U.S. Department of Energy Office of Science, Office of Advanced Scientific Computing Research, (DE-NA0003525, DE-SC0020290), and Office of High Energy Physics (DE-ACO2-07CH11359, DE-SC0018407).

AM, JL, and JP also acknowledge funding provided by the Institute for Quantum Information and Matter, an NSF Physics Frontiers Center (NSF Grant PHY-1733907), the Simons Foundation It from Qubit Collaboration, and the Air Force Office of Scientific Research (FA9550-19-1-0360). GV is a CIFAR fellow in the Quantum Information Science Program. Sandbox is a team within the Alphabet family of companies, which includes Google, Verily, Waymo, X, and others. Research at Perimeter Institute is supported in part by the Government of Canada through the Department of Innovation, Science and Economic Development Canada and by the Province of Ontario through the Ministry of Colleges and Universities. Some of the computations presented here were conducted on the Caltech High Performance Cluster, partially supported by a grant from the Gordon and Betty Moore Foundation.

BIBLIOGRAPHY

- [1] S. Durr *et al.*, “Ab-Initio Determination of Light Hadron Masses,” *Science* **322** (2008) 1224–1227, arXiv:0906.3599 [hep-lat].
- [2] J. Liu, J. Preskill, and B. Şahinoğlu, “Simulating kink scattering in a quantum computer,” to appear.
<https://drive.google.com/file/d/1wOrPm071futZ1LEj-12JiMUAvg4n0dQr/view>.
- [3] A. Milsted, J. Liu, J. Preskill, and G. Vidal, “Collisions of false-vacuum bubble walls in a quantum spin chain,” arXiv:2012.07243 [quant-ph].
- [4] S. M. Chester, W. Landry, J. Liu, D. Poland, D. Simmons-Duffin, N. Su, and A. Vichi, “Carving out OPE space and precise $O(2)$ model critical exponents,” *JHEP* **06** (2020) 142, arXiv:1912.03324 [hep-th].
- [5] J. Liu, D. Meltzer, D. Poland, and D. Simmons-Duffin, “The Lorentzian inversion formula and the spectrum of the 3d $O(2)$ CFT,” *JHEP* **09** (2020) 115, arXiv:2007.07914 [hep-th].
- [6] E. Palti, “The Swampland: Introduction and Review,” *Fortsch. Phys.* **67** no. 6, (2019) 1900037, arXiv:1903.06239 [hep-th].
- [7] M. Hasenbusch, “Monte Carlo study of a generalized icosahedral model on the simple cubic lattice,” *Phys. Rev. B* **102** no. 2, (2020) 024406, arXiv:2005.04448 [cond-mat.stat-mech].
- [8] M. Hasenbusch and E. Vicari, “Anisotropic perturbations in three-dimensional $o(n)$ -symmetric vector models,” *Physical Review B* **84** no. 12, (Sep, 2011) 125136.
<http://dx.doi.org/10.1103/PhysRevB.84.125136>.
- [9] E. O’Brien and P. Fendley, “Lattice supersymmetry and order-disorder coexistence in the tricritical Ising model,” *Phys. Rev. Lett.* **120** no. 20, (2018) 206403, arXiv:1712.06662 [cond-mat.stat-mech].
- [10] N. Sannomiya and H. Katsura, “Supersymmetry Breaking and Nambu-Goldstone Fermions in Interacting Majorana Chains,” *Phys. Rev. D* **99** no. 4, (2019) 045002, arXiv:1712.01148 [cond-mat.str-el].
- [11] P. Fonseca and A. Zamolodchikov, “Ising spectroscopy. I. Mesons at $T < T(c)$,” 12, 2006.
- [12] G. Mussardo and G. Takacs, “Effective potentials and kink spectra in non-integrable perturbed conformal field theories,” *J. Phys. A* **42** (2009) 304022, arXiv:0901.3537 [hep-th].

- [13] P. Calabrese, A. Pelissetto, and E. Vicari, “Critical structure factors of bilinear fields in $o(n)$ vector models,” *Physical Review E* **65** no. 4, (Apr, 2002) 046115. <http://dx.doi.org/10.1103/PhysRevE.65.046115>.
- [14] E. Schrödinger, “Nature and the greeks, science and humanism,”.
- [15] “See, <https://www.forbes.com/sites/niallmccarthy/2016/01/06/americas-best-phd-majors-by-salary-infographic/?sh=1596ba603ed5>,”.
- [16] “See, <https://www.ftc.gov/news-events/press-releases/2019/07/ftc-imposes-5-billion-penalty-sweeping-new-privacy-restrictions>,”.
- [17] N. Y. Halpern, “Quantum steampunk: Quantum information, thermodynamics, their intersection, and applications thereof across physics,” *PhD. Thesis, Caltech, 2018*, [arxiv:1807.09786](https://arxiv.org/abs/1807.09786) (2018) .
- [18] Z. Ahmed *et al.*, “Quantum Sensing for High Energy Physics,” in *First workshop on Quantum Sensing for High Energy Physics*. 3, 2018. [arXiv:1803.11306](https://arxiv.org/abs/1803.11306) [hep-ex].
- [19] D. Simmons-Duffin, “The Conformal Bootstrap,” in *Theoretical Advanced Study Institute in Elementary Particle Physics: New Frontiers in Fields and Strings*, pp. 1–74. 2017. [arXiv:1602.07982](https://arxiv.org/abs/1602.07982) [hep-th].
- [20] L. F. Alday, J. Maldacena, A. Sever, and P. Vieira, “Y-system for Scattering Amplitudes,” *J. Phys. A* **43** (2010) 485401, [arXiv:1002.2459](https://arxiv.org/abs/1002.2459) [hep-th].
- [21] J. M. Maldacena, “The Large N limit of superconformal field theories and supergravity,” *Int. J. Theor. Phys.* **38** (1999) 1113–1133, [arXiv:hep-th/9711200](https://arxiv.org/abs/hep-th/9711200).
- [22] R. P. Feynman, “Simulating physics with computers,” *Int. J. Theor. Phys.* **21** (1982) 467–488.
- [23] J. Preskill, “Simulating quantum field theory with a quantum computer,” *PoS LATTICE2018* (2018) 024, [arXiv:1811.10085](https://arxiv.org/abs/1811.10085) [hep-lat].
- [24] J. Preskill, “Quantum computing in the nisq era and beyond,” *Quantum* **2** (2018) 79.
- [25] F. Arute, K. Arya, R. Babbush, D. Bacon, J. C. Bardin, R. Barends, R. Biswas, S. Boixo, F. G. Brandao, D. A. Buell, *et al.*, “Quantum supremacy using a programmable superconducting processor,” *Nature* **574** no. 7779, (2019) 505–510.
- [26] G. Ortiz, J. Gubernatis, E. Knill, and R. Laflamme, “Quantum algorithms for fermionic simulations,” *Phys. Rev. A* **64** (2001) 022319, [arXiv:cond-mat/0012334](https://arxiv.org/abs/cond-mat/0012334). [Erratum: *Phys.Rev.A* 65, 029902 (2002)].

- [27] S. P. Jordan, K. S. Lee, and J. Preskill, “Quantum Algorithms for Quantum Field Theories,” *Science* **336** (2012) 1130–1133, arXiv:1111.3633 [quant-ph].
- [28] S. P. Jordan, K. S. Lee, and J. Preskill, “Quantum Computation of Scattering in Scalar Quantum Field Theories,” *Quant. Inf. Comput.* **14** (2014) 1014–1080, arXiv:1112.4833 [hep-th].
- [29] S. P. Jordan, K. S. M. Lee, and J. Preskill, “Quantum Algorithms for Fermionic Quantum Field Theories,” arXiv:1404.7115 [hep-th].
- [30] S. P. Jordan, H. Krovi, K. S. M. Lee, and J. Preskill, “BQP-completeness of Scattering in Scalar Quantum Field Theory,” arXiv:1703.00454 [quant-ph].
- [31] S. R. Coleman, “Classical Lumps and their Quantum Descendents,” *Subnucl. Ser.* **13** (1977) 297.
- [32] T. Lee and Y. Pang, “Nontopological solitons,” *Phys. Rept.* **221** (1992) 251–350.
- [33] G. F. Chew, “S-Matrix Theory of Strong Interactions without Elementary Particles,” *Rev. Mod. Phys.* **34** no. 3, (1962) 394–401.
- [34] A. Polyakov, “Nonhamiltonian approach to conformal quantum field theory,” *Zh. Eksp. Teor. Fiz.* **66** (1974) 23–42.
- [35] D. Simmons-Duffin, “A Semidefinite Program Solver for the Conformal Bootstrap,” *JHEP* **06** (2015) 174, arXiv:1502.02033 [hep-th].
- [36] S. El-Showk, M. F. Paulos, D. Poland, S. Rychkov, D. Simmons-Duffin, and A. Vichi, “Solving the 3D Ising Model with the Conformal Bootstrap,” *Phys. Rev. D* **86** (2012) 025022, arXiv:1203.6064 [hep-th].
- [37] S. Caron-Huot, “Analyticity in Spin in Conformal Theories,” *JHEP* **09** (2017) 078, arXiv:1703.00278 [hep-th].
- [38] S. M. Chester, W. Landry, J. Liu, D. Poland, D. Simmons-Duffin, N. Su, and A. Vichi, “Bootstrapping Heisenberg Magnets and their Cubic Instability,” arXiv:2011.14647 [hep-th].
- [39] W. Landry and D. Simmons-Duffin, “Scaling the semidefinite program solver SDPB,” arXiv:1909.09745 [hep-th].
- [40] N. Bao and J. Liu, “Quantum algorithms for conformal bootstrap,” *Nucl. Phys. B* **946** (2019) 114702, arXiv:1811.05675 [hep-th].
- [41] CMS Collaboration, A. M. Sirunyan *et al.*, “Identification of heavy, energetic, hadronically decaying particles using machine-learning techniques,” *JINST* **15** no. 06, (2020) P06005, arXiv:2004.08262 [hep-ex].

- [42] T. Roxlo and M. Reece, “Opening the black box of neural nets: case studies in stop/top discrimination,” arXiv:1804.09278 [hep-ph].
- [43] R. Bousso and J. Polchinski, “Quantization of four form fluxes and dynamical neutralization of the cosmological constant,” *JHEP* **06** (2000) 006, arXiv:hep-th/0004134.
- [44] L. Susskind, “The Anthropic landscape of string theory,” arXiv:hep-th/0302219.
- [45] S. Ashok and M. R. Douglas, “Counting flux vacua,” *JHEP* **01** (2004) 060, arXiv:hep-th/0307049.
- [46] C. Cheung, J. Liu, and G. N. Remmen, “Proof of the Weak Gravity Conjecture from Black Hole Entropy,” *JHEP* **10** (2018) 004, arXiv:1801.08546 [hep-th].
- [47] F. Denef and M. R. Douglas, “Computational complexity of the landscape. I.,” *Annals Phys.* **322** (2007) 1096–1142, arXiv:hep-th/0602072.
- [48] M. R. Douglas, “Spaces of Quantum Field Theories,” *J. Phys. Conf. Ser.* **462** no. 1, (2013) 012011, arXiv:1005.2779 [hep-th].
- [49] F. Denef, M. R. Douglas, B. Greene, and C. Zukowski, “Computational complexity of the landscape II—Cosmological considerations,” *Annals Phys.* **392** (2018) 93–127, arXiv:1706.06430 [hep-th].
- [50] J. Liu, “Artificial Neural Network in Cosmic Landscape,” *JHEP* **12** (2017) 149, arXiv:1707.02800 [hep-th].
- [51] Y.-H. He, “Deep-Learning the Landscape,” arXiv:1706.02714 [hep-th].
- [52] F. Ruehle, “Data science applications to string theory,” *Phys. Rept.* **839** (2020) 1–117.
- [53] J. Halverson and C. Long, “Statistical Predictions in String Theory and Deep Generative Models,” *Fortsch. Phys.* **68** no. 5, (2020) 2000005, arXiv:2001.00555 [hep-th].
- [54] S. Hawking, “Particle Creation by Black Holes,” *Commun. Math. Phys.* **43** (1975) 199–220. [Erratum: *Commun.Math.Phys.* 46, 206 (1976)].
- [55] S. Hawking, “Black hole explosions,” *Nature* **248** (1974) 30–31.
- [56] S. Ryu and T. Takayanagi, “Holographic derivation of entanglement entropy from AdS/CFT,” *Phys. Rev. Lett.* **96** (2006) 181602, arXiv:hep-th/0603001.

- [57] A. Almheiri, X. Dong, and D. Harlow, “Bulk Locality and Quantum Error Correction in AdS/CFT,” *JHEP* **04** (2015) 163, arXiv:1411.7041 [hep-th].
- [58] P. Hayden and J. Preskill, “Black holes as mirrors: Quantum information in random subsystems,” *JHEP* **09** (2007) 120, arXiv:0708.4025 [hep-th].
- [59] A. R. Brown, D. A. Roberts, L. Susskind, B. Swingle, and Y. Zhao, “Holographic Complexity Equals Bulk Action?,” *Phys. Rev. Lett.* **116** no. 19, (2016) 191301, arXiv:1509.07876 [hep-th].
- [60] “*It from qubit*, <https://www.simonsfoundation.org/mathematics-physical-sciences/it-from-qubit/>.”
- [61] L. McGough, M. Mezei, and H. Verlinde, “Moving the CFT into the bulk with $T\bar{T}$,” *JHEP* **04** (2018) 010, arXiv:1611.03470 [hep-th].
- [62] P. Kraus, J. Liu, and D. Marolf, “Cutoff AdS₃ versus the $T\bar{T}$ deformation,” *JHEP* **07** (2018) 027, arXiv:1801.02714 [hep-th].
- [63] X. Dong, E. Silverstein, and G. Torroba, “De Sitter Holography and Entanglement Entropy,” *JHEP* **07** (2018) 050, arXiv:1804.08623 [hep-th].
- [64] V. Gorbenko, E. Silverstein, and G. Torroba, “dS/dS and $T\bar{T}$,” *JHEP* **03** (2019) 085, arXiv:1811.07965 [hep-th].
- [65] A. Lewkowycz, J. Liu, E. Silverstein, and G. Torroba, “ $T\bar{T}$ and EE, with implications for (A)dS subregion encodings,” *JHEP* **04** (2020) 152, arXiv:1909.13808 [hep-th].
- [66] “*The non-perturbative bootstrap*, <https://bootstrapcollaboration.com/>.”
- [67] L. Susskind, “Horizons Protect Church-Turing,” arXiv:2003.01807 [hep-th].
- [68] M. Hogarth, *Predictability, computability, and spacetime*. PhD thesis, University of Cambridge, 1996.
- [69] R. Geroch and J. B. Hartle, “Computability and physical theories,” *Foundations of Physics* **16** no. 6, (1986) 533–550.
- [70] A. Bouland, B. Fefferman, and U. Vazirani, “Computational pseudorandomness, the wormhole growth paradox, and constraints on the AdS/CFT duality,” arXiv:1910.14646 [quant-ph].
- [71] I. Kim, E. Tang, and J. Preskill, “The ghost in the radiation: Robust encodings of the black hole interior,” *JHEP* **20** (2020) 031, arXiv:2003.05451 [hep-th].

- [72] B. Yoshida, “Remarks on Black Hole Complexity Puzzle,” [arXiv:2005.12491 \[hep-th\]](#).
- [73] E. Witten, “String theory dynamics in various dimensions,” *Nucl. Phys. B* **443** (1995) 85–126, [arXiv:hep-th/9503124](#).
- [74] P.-S. Hsin and N. Seiberg, “Level/rank Duality and Chern-Simons-Matter Theories,” *JHEP* **09** (2016) 095, [arXiv:1607.07457 \[hep-th\]](#).
- [75] E. H. Lieb and M. B. Ruskai, “A Fundamental Property of Quantum-Mechanical Entropy,” *Phys. Rev. Lett.* **30** (1973) 434–436.
- [76] E. Lieb and M. Ruskai, “Proof of the strong subadditivity of quantum-mechanical entropy,” *J. Math. Phys.* **14** (1973) 1938–1941.
- [77] M. Headrick and T. Takayanagi, “A Holographic proof of the strong subadditivity of entanglement entropy,” *Phys. Rev. D* **76** (2007) 106013, [arXiv:0704.3719 \[hep-th\]](#).
- [78] T. C. Bohdanowicz and F. G. Brandao, “Universal Hamiltonians for Exponentially Long Simulation,” [arXiv:1710.02625 \[quant-ph\]](#).
- [79] F. G. Brandao, W. Chemissany, N. Hunter-Jones, R. Kueng, and J. Preskill, “Models of quantum complexity growth,” [arXiv:1912.04297 \[hep-th\]](#).
- [80] L. Susskind, “Computational Complexity and Black Hole Horizons,” *Fortsch. Phys.* **64** (2016) 24–43, [arXiv:1403.5695 \[hep-th\]](#).
[Addendum: *Fortsch.Phys.* 64, 44–48 (2016)].
- [81] P. Hayden and G. Penington, “Black hole microstates vs. the additivity conjectures,” [arXiv:2012.07861 \[hep-th\]](#).
- [82] P. Mehta and D. J. Schwab, “An exact mapping between the variational renormalization group and deep learning,” *arXiv preprint arXiv:1410.3831* (2014).
- [83] E. Dyer and G. Gur-Ari, “Asymptotics of Wide Networks from Feynman Diagrams,” [arXiv:1909.11304 \[cs.LG\]](#).
- [84] A. R. Brown, H. Gharibyan, S. Leichenauer, H. W. Lin, S. Nezami, G. Salton, L. Susskind, B. Swingle, and M. Walter, “Quantum Gravity in the Lab: Teleportation by Size and Traversable Wormholes,” [arXiv:1911.06314 \[quant-ph\]](#).
- [85] D. M. Hofman and J. Maldacena, “Conformal collider physics: Energy and charge correlations,” *JHEP* **05** (2008) 012, [arXiv:0803.1467 \[hep-th\]](#).
- [86] S. W. Hawking, M. J. Perry, and A. Strominger, “Soft Hair on Black Holes,” *Phys. Rev. Lett.* **116** no. 23, (2016) 231301, [arXiv:1601.00921 \[hep-th\]](#).

- [87] L. J. Dixon, M.-X. Luo, V. Shtabovenko, T.-Z. Yang, and H. X. Zhu, “Analytical Computation of Energy-Energy Correlation at Next-to-Leading Order in QCD,” *Phys. Rev. Lett.* **120** no. 10, (2018) 102001, arXiv:1801.03219 [hep-ph].
- [88] M. Kologlu, P. Kravchuk, D. Simmons-Duffin, and A. Zhiboedov, “The light-ray OPE and conformal colliders,” arXiv:1905.01311 [hep-th].
- [89] “<https://news.fnal.gov/2018/09/department-of-energy-awards-fermilab-more-than-10-million-for-quantum-science/>,”.
- [90] “<http://www.xact.es>,”.
- [91] J. Polchinski, “Memories of a Theoretical Physicist,” arXiv:1708.09093 [physics.hist-ph].
- [92] “Private communications with Ning Su,”.
- [93] “The man who knew infinity, [https://en.wikipedia.org/wiki/The_Man_Who_Knew_Infinity_\(film\)](https://en.wikipedia.org/wiki/The_Man_Who_Knew_Infinity_(film)),”.
- [94] G. Raayoni, S. Gottlieb, G. Pisha, Y. Harris, Y. Manor, U. Mendlovic, D. Haviv, Y. Hadad, and I. Kamnitzer, “The ramanujan machine: automatically generated conjectures on fundamental constants,” *arXiv preprint arXiv:1907.00205* (2019) .
- [95] “The ramanujan machine. <http://www.ramanujanmachine.com/>,”.
- [96] “Number theorist fears all published math is wrong. https://www.vice.com/en_us/article/8xwm54/number-theorist-fears-all-published-math-is-wrong-actually,”.
- [97] P. Huang, A. J. Long, and L.-T. Wang, “Probing the Electroweak Phase Transition with Higgs Factories and Gravitational Waves,” *Phys. Rev. D* **94** no. 7, (2016) 075008, arXiv:1608.06619 [hep-ph].
- [98] S. Deser and P. van Nieuwenhuizen, “One Loop Divergences of Quantized Einstein-Maxwell Fields,” *Phys. Rev.* **D10** (1974) 401.
- [99] R. M. Wald, “Black hole entropy is the Noether charge,” *Phys. Rev.* **D48** (1993) R3427, arXiv:gr-qc/9307038 [gr-qc].
- [100] X. Dong, “Holographic Entanglement Entropy for General Higher Derivative Gravity,” *JHEP* **01** (2014) 044, arXiv:1310.5713 [hep-th].
- [101] J. D. Bekenstein, “Black holes and entropy,” *Phys. Rev.* **D7** (1973) 2333.
- [102] S. W. Hawking, “Black Holes and Thermodynamics,” *Phys. Rev.* **D13** (1976) 191.

- [103] P. C. W. Davies, “Thermodynamics of Black Holes,” *Proc. Roy. Soc. Lond.* **A353** (1977) 499.
- [104] N. Arkani-Hamed, L. Motl, A. Nicolis, and C. Vafa, “The string landscape, black holes and gravity as the weakest force,” *JHEP* **06** (2007) 060, arXiv:hep-th/0601001 [hep-th].
- [105] C. Cheung and G. N. Remmen, “Naturalness and the Weak Gravity Conjecture,” *Phys. Rev. Lett.* **113** (2014) 051601, arXiv:1402.2287 [hep-ph].
- [106] C. Vafa, “The String Landscape and the Swampland,” arXiv:hep-th/0509212 [hep-th].
- [107] H. Ooguri and C. Vafa, “On the Geometry of the String Landscape and the Swampland,” *Nucl. Phys.* **B766** (2007) 21, arXiv:hep-th/0605264 [hep-th].
- [108] A. Adams, N. Arkani-Hamed, S. Dubovsky, A. Nicolis, and R. Rattazzi, “Causality, analyticity and an IR obstruction to UV completion,” *JHEP* **10** (2006) 014, arXiv:hep-th/0602178 [hep-th].
- [109] C. Cheung and G. N. Remmen, “Infrared Consistency and the Weak Gravity Conjecture,” *JHEP* **12** (2014) 087, arXiv:1407.7865 [hep-th].
- [110] B. Bellazzini, C. Cheung, and G. N. Remmen, “Quantum Gravity Constraints from Unitarity and Analyticity,” *Phys. Rev.* **D93** (2016) 064076, arXiv:1509.00851 [hep-th].
- [111] C. Cheung and G. N. Remmen, “Positive Signs in Massive Gravity,” *JHEP* **04** (2016) 002, arXiv:1601.04068 [hep-th].
- [112] C. Cheung and G. N. Remmen, “Positivity of Curvature-Squared Corrections in Gravity,” *Phys. Rev. Lett.* **118** (2017) 051601, arXiv:1608.02942 [hep-th].
- [113] G. W. Gibbons and S. W. Hawking, “Action Integrals and Partition Functions in Quantum Gravity,” *Phys. Rev.* **D15** (1977) 2752.
- [114] H. W. Braden, J. D. Brown, B. F. Whiting, and J. W. York, Jr., “Charged black hole in a grand canonical ensemble,” *Phys. Rev.* **D42** (1990) 3376.
- [115] J. D. Brown and J. W. York, Jr., “Quasilocal energy and conserved charges derived from the gravitational action,” *Phys. Rev.* **D47** (1993) 1407, arXiv:gr-qc/9209012 [gr-qc].
- [116] G. W. Gibbons, S. W. Hawking, and M. J. Perry, “Path Integrals and the Indefiniteness of the Gravitational Action,” *Nucl. Phys.* **B138** (1978) 141.

- [117] G. W. Gibbons and M. J. Perry, “Quantizing Gravitational Instantons,” *Nucl. Phys.* **B146** (1978) 90.
- [118] D. J. Gross, M. J. Perry, and L. G. Yaffe, “Instability of Flat Space at Finite Temperature,” *Phys. Rev.* **D25** (1982) 330.
- [119] J. W. York, Jr., “Black hole thermodynamics and the Euclidean Einstein action,” *Phys. Rev.* **D33** (1986) 2092.
- [120] S. W. Hawking and D. N. Page, “Thermodynamics of Black Holes in Anti-de Sitter Space,” *Commun. Math. Phys.* **87** (1983) 577.
- [121] T. Prestidge, “Dynamic and thermodynamic stability and negative modes in Schwarzschild-anti-de Sitter,” *Phys. Rev.* **D61** (2000) 084002, arXiv:hep-th/9907163 [hep-th].
- [122] H. S. Reall, “Classical and thermodynamic stability of black branes,” *Phys. Rev.* **D64** (2001) 044005, arXiv:hep-th/0104071 [hep-th].
- [123] R. Monteiro and J. E. Santos, “Negative modes and the thermodynamics of Reissner-Nordström black holes,” *Phys. Rev.* **D79** (2009) 064006, arXiv:0812.1767 [gr-qc].
- [124] A. Nicolis, R. Rattazzi, and E. Trincherini, “Energy’s and amplitudes’ positivity,” *JHEP* **05** (2010) 095, arXiv:0912.4258 [hep-th]. [Erratum: *JHEP*11,128(2011)].
- [125] Z. Komargodski and A. Schwimmer, “On Renormalization Group Flows in Four Dimensions,” *JHEP* **12** (2011) 099, arXiv:1107.3987 [hep-th].
- [126] S. N. Solodukhin, “Entanglement entropy of black holes,” *Living Rev. Rel.* **14** (2011) 8, arXiv:1104.3712 [hep-th].
- [127] D. Harlow, “Jerusalem Lectures on Black Holes and Quantum Information,” *Rev. Mod. Phys.* **88** (2016) 015002, arXiv:1409.1231 [hep-th].
- [128] S. N. Solodukhin, “Conical singularity and quantum corrections to the entropy of a black hole,” *Phys. Rev.* **D51** (1995) 609, arXiv:hep-th/9407001 [hep-th].
- [129] S. N. Solodukhin, “‘Nongeometric’ contribution to the entropy of a black hole due to quantum corrections,” *Phys. Rev.* **D51** (1995) 618, arXiv:hep-th/9408068 [hep-th].
- [130] D. V. Fursaev, “Temperature and entropy of a quantum black hole and conformal anomaly,” *Phys. Rev.* **D51** (1995) 5352, arXiv:hep-th/9412161 [hep-th].

- [131] S. Carlip, “Logarithmic corrections to black hole entropy from the Cardy formula,” *Class. Quant. Grav.* **17** (2000) 4175, arXiv:gr-qc/0005017 [gr-qc].
- [132] S. N. Solodukhin, “One loop renormalization of black hole entropy due to nonminimally coupled matter,” *Phys. Rev.* **D52** (1995) 7046, arXiv:hep-th/9504022 [hep-th].
- [133] D. N. Kabat, “Black hole entropy and entropy of entanglement,” *Nucl. Phys.* **B453** (1995) 281, arXiv:hep-th/9503016 [hep-th].
- [134] S. N. Solodukhin, “Newton constant, contact terms, and entropy,” *Phys. Rev.* **D91** (2015) 084028, arXiv:1502.03758 [hep-th].
- [135] W. Donnelly and A. C. Wall, “Do gauge fields really contribute negatively to black hole entropy?,” *Phys. Rev.* **D86** (2012) 064042, arXiv:1206.5831 [hep-th].
- [136] W. Donnelly and A. C. Wall, “Entanglement entropy of electromagnetic edge modes,” *Phys. Rev. Lett.* **114** (2015) 111603, arXiv:1412.1895 [hep-th].
- [137] L. Susskind and J. Uglum, “Black hole entropy in canonical quantum gravity and superstring theory,” *Phys. Rev.* **D50** (1994) 2700, arXiv:hep-th/9401070 [hep-th].
- [138] J.-G. Demers, R. Lafrance, and R. C. Myers, “Black hole entropy without brick walls,” *Phys. Rev.* **D52** (1995) 2245, arXiv:gr-qc/9503003 [gr-qc].
- [139] Y. Kats, L. Motl, and M. Padi, “Higher-order corrections to mass-charge relation of extremal black holes,” *JHEP* **12** (2007) 068, arXiv:hep-th/0606100 [hep-th].
- [140] M. Campanelli, C. O. Lousto, and J. Audretsch, “A perturbative method to solve fourth-order gravity field equations,” *Phys. Rev.* **D49** (1994) 5188, arXiv:gr-qc/9401013 [gr-qc].
- [141] D. J. Gross and J. H. Sloan, “The Quartic Effective Action for the Heterotic String,” *Nucl. Phys.* **B291** (1987) 41.
- [142] L. Susskind, “Trouble for remnants,” arXiv:hep-th/9501106 [hep-th].
- [143] S. B. Giddings, “Black holes and massive remnants,” *Phys. Rev.* **D46** (1992) 1347, arXiv:hep-th/9203059 [hep-th].
- [144] G. ’t Hooft, “Dimensional reduction in quantum gravity,” in *Conference on Highlights of Particle and Condensed Matter Physics (SALAMFEST)*, vol. C930308, p. 284. 1993. arXiv:gr-qc/9310026 [gr-qc].

- [145] R. Bousso, “The holographic principle,” *Rev. Mod. Phys.* **74** (2002) 825, arXiv:hep-th/0203101 [hep-th].
- [146] T. Banks, M. Johnson, and A. Shomer, “A Note on Gauge Theories Coupled to Gravity,” *JHEP* **09** (2006) 049, arXiv:hep-th/0606277 [hep-th].
- [147] G. Shiu, P. Soler, and W. Cottrell, “Weak Gravity Conjecture and Extremal Black Holes,” arXiv:1611.06270 [hep-th].
- [148] G. T. Horowitz, J. E. Santos, and B. Way, “Evidence for an Electrifying Violation of Cosmic Censorship,” *Class. Quant. Grav.* **33** (2016) 195007, arXiv:1604.06465 [hep-th].
- [149] Z. Fisher and C. J. Moggi, “A Semiclassical, Entropic Proof of a Weak Gravity Conjecture,” arXiv:1706.08257 [hep-th].
- [150] S. Hod, “A proof of the weak gravity conjecture,” *Int. J. Mod. Phys.* **D26** (2017) 1742004, arXiv:1705.06287 [gr-qc].
- [151] B. Bellazzini, “Softness and amplitudes’ positivity for spinning particles,” *JHEP* **02** (2017) 034, arXiv:1605.06111 [hep-th].
- [152] C. de Rham, S. Melville, A. J. Tolley, and S.-Y. Zhou, “UV complete me: positivity bounds for particles with spin,” *JHEP* **03** (2018) 011, arXiv:1706.02712 [hep-th].
- [153] B. Bellazzini, F. Riva, J. Serra, and F. Sgarlata, “Beyond Positivity Bounds and the Fate of Massive Gravity,” *Phys. Rev. Lett.* **120** (2018) 161101, arXiv:1710.02539 [hep-th].
- [154] G. Dvali, A. Franca, and C. Gomez, “Road Signs for UV-Completion,” arXiv:1204.6388 [hep-th].
- [155] A. Jenkins and D. O’Connell, “The story of \mathcal{O} : Positivity constraints in effective field theories,” arXiv:hep-th/0609159 [hep-th].
- [156] R. Rattazzi, V. S. Rychkov, E. Tonni, and A. Vichi, “Bounding scalar operator dimensions in 4D CFT,” *JHEP* **0812** (2008) 031, arXiv:0807.0004 [hep-th].
- [157] V. S. Rychkov and A. Vichi, “Universal Constraints on Conformal Operator Dimensions,” *Phys.Rev.* **D80** (2009) 045006, arXiv:0905.2211 [hep-th].
- [158] D. Poland, S. Rychkov, and A. Vichi, “The Conformal Bootstrap: Theory, Numerical Techniques, and Applications,” *Rev. Mod. Phys.* **91** no. 1, (2019) 15002, arXiv:1805.04405 [hep-th]. [Rev. Mod. Phys.91,015002(2019)].

- [159] S. M. Chester, “Weizmann Lectures on the Numerical Conformal Bootstrap,” arXiv:1907.05147 [hep-th].
- [160] F. Kos, D. Poland, D. Simmons-Duffin, and A. Vichi, “Precision Islands in the Ising and $O(N)$ Models,” *JHEP* **08** (2016) 036, arXiv:1603.04436 [hep-th].
- [161] F. Kos, D. Poland, D. Simmons-Duffin, and A. Vichi, “Bootstrapping the $O(N)$ Archipelago,” *JHEP* **11** (2015) 106, arXiv:1504.07997 [hep-th].
- [162] J. M. Carmona, A. Pelissetto, and E. Vicari, “The N component Ginzburg-Landau Hamiltonian with cubic anisotropy: A Six loop study,” *Phys. Rev.* **B61** (2000) 15136–15151, arXiv:cond-mat/9912115 [cond-mat].
- [163] F. Jasch and H. Kleinert, “Fast-convergent resummation algorithm and critical exponents of ϕ^4 -theory in three dimensions,” *Journal of Mathematical Physics* **42** no. 1, (Jan, 2001) 52–73.
<http://dx.doi.org/10.1063/1.1289377>.
- [164] R. Guida and J. Zinn-Justin, “Critical exponents of then-vector model,” *Journal of Physics A: Mathematical and General* **31** no. 40, (Oct, 1998) 8103–8121. <http://dx.doi.org/10.1088/0305-4470/31/40/006>.
- [165] P. Butera and M. Comi, “Renormalized couplings and scaling correction amplitudes in then-vector spin models on the sc and the bcc lattices,” *Physical Review B* **58** no. 17, (Nov, 1998) 11552–11569.
<http://dx.doi.org/10.1103/PhysRevB.58.11552>.
- [166] P. Calabrese, A. Pelissetto, and E. Vicari, “Randomly dilute spin models with cubic symmetry,” *Physical Review B* **67** no. 2, (Jan, 2003) 024418.
<http://dx.doi.org/10.1103/PhysRevB.67.024418>.
- [167] P. Pfeuty, D. Jasnow, and M. E. Fisher, “Crossover scaling functions for exchange anisotropy,” *Phys. Rev. B* **10** (Sep, 1974) 2088–2112.
<https://link.aps.org/doi/10.1103/PhysRevB.10.2088>.
- [168] H. Kleinert and V. Schulte-Frohlinde, “Exact five-loop renormalization group functions of θ^4 -theory with $o(n)$ -symmetric and cubic interactions. critical exponents up to ϵ^5 ,” *Physics Letters B* **342** no. 1-4, (Jan, 1995) 284–296. [http://dx.doi.org/10.1016/0370-2693\(94\)01377-0](http://dx.doi.org/10.1016/0370-2693(94)01377-0).
- [169] K. Varnashev, “Stability of a cubic fixed point in three-dimensions: Critical exponents for generic N ,” *Phys. Rev. B* **61** (2000) 14660, arXiv:cond-mat/9909087.
- [170] R. Folk, Y. Holovatch, and T. Yavorskii, “Pseudo- ϵ expansion of six-loop renormalization-group functions of an anisotropic cubic model,” *Physical*

- Review B* **62** no. 18, (Nov, 2000) 12195–12200.
<http://dx.doi.org/10.1103/PhysRevB.62.12195>.
- [171] J. Manuel Carmona, A. Pelissetto, and E. Vicari, “N-component ginzburg-landau hamiltonian with cubic anisotropy: A six-loop study,” *Physical Review B* **61** no. 22, (Jun, 2000) 15136–15151.
<http://dx.doi.org/10.1103/PhysRevB.61.15136>.
- [172] A. Pelissetto and E. Vicari, “Critical phenomena and renormalization-group theory,” *Phys. Rept.* **368** (2002) 549–727, [arXiv:cond-mat/0012164](https://arxiv.org/abs/cond-mat/0012164).
- [173] M. Hasenbusch, “Eliminating leading corrections to scaling in the three-dimensional $o(n)$ -symmetric ϕ^4 model: $N=3$ and 4,” *Journal of Physics A: Mathematical and General* **34** no. 40, (Oct, 2001) 8221–8236.
<http://dx.doi.org/10.1088/0305-4470/34/40/302>.
- [174] M. Campostrini, M. Hasenbusch, A. Pelissetto, P. Rossi, and E. Vicari, “Critical exponents and equation of state of the three-dimensional Heisenberg universality class,” *Phys.Rev.* **B65** (2002) 144520, [arXiv:cond-mat/0110336](https://arxiv.org/abs/cond-mat/0110336) [cond-mat].
- [175] M. Caselle and M. Hasenbusch, “The Stability of the $O(N)$ invariant fixed point in three-dimensions,” *J. Phys.* **A31** (1998) 4603–4617, [arXiv:cond-mat/9711080](https://arxiv.org/abs/cond-mat/9711080) [cond-mat].
- [176] F. Kos, D. Poland, and D. Simmons-Duffin, “Bootstrapping the $O(N)$ vector models,” *JHEP* **06** (2014) 091, [arXiv:1307.6856](https://arxiv.org/abs/1307.6856) [hep-th].
- [177] J. Rong and N. Su, “Scalar CFTs and Their Large N Limits,” *JHEP* **09** (2018) 103, [arXiv:1712.00985](https://arxiv.org/abs/1712.00985) [hep-th].
- [178] A. Stergiou, “Bootstrapping hypercubic and hypertetrahedral theories in three dimensions,” *JHEP* **05** (2018) 035, [arXiv:1801.07127](https://arxiv.org/abs/1801.07127) [hep-th].
- [179] S. R. Kousvos and A. Stergiou, “Bootstrapping Mixed Correlators in Three-Dimensional Cubic Theories,” *SciPost Phys.* **6** no. 3, (2019) 035, [arXiv:1810.10015](https://arxiv.org/abs/1810.10015) [hep-th].
- [180] S. R. Kousvos and A. Stergiou, “Bootstrapping Mixed Correlators in Three-Dimensional Cubic Theories II,” *SciPost Phys.* **8** no. 6, (2020) 085, [arXiv:1911.00522](https://arxiv.org/abs/1911.00522) [hep-th].
- [181] D. Poland, D. Simmons-Duffin, and A. Vichi, “Carving Out the Space of 4D CFTs,” *JHEP* **1205** (2012) 110, [arXiv:1109.5176](https://arxiv.org/abs/1109.5176) [hep-th].
- [182] Y. Nakayama, “Bootstrap experiments on higher dimensional CFTs,” *Int. J. Mod. Phys.* **A33** no. 07, (2018) 1850036, [arXiv:1705.02744](https://arxiv.org/abs/1705.02744) [hep-th].
- [183] Z. Li, “Solving QED₃ with Conformal Bootstrap,” [arXiv:1812.09281](https://arxiv.org/abs/1812.09281) [hep-th].

- [184] Z. Li and D. Poland, “Searching for gauge theories with the conformal bootstrap,” arXiv:2005.01721 [hep-th].
- [185] Z. Li, “Symmetries of conformal correlation functions,” arXiv:2006.05119 [hep-th].
- [186] “Arxiv link of this chapter, [https://arxiv.org/abs/2011.14647/.](https://arxiv.org/abs/2011.14647/)”.
- [187] M. Go and Y. Tachikawa, “autoboot: A generator of bootstrap equations with global symmetry,” *JHEP* **06** (2019) 084, arXiv:1903.10522 [hep-th].
- [188] D. Poland and D. Simmons-Duffin, “Bounds on 4D Conformal and Superconformal Field Theories,” *JHEP* **1105** (2011) 017, arXiv:1009.2087 [hep-th].
- [189] S. El-Showk and M. F. Paulos, “Bootstrapping Conformal Field Theories with the Extremal Functional Method,” *Phys. Rev. Lett.* **111** no. 24, (2013) 241601, arXiv:1211.2810 [hep-th].
- [190] Z. Komargodski and D. Simmons-Duffin, “The Random-Bond Ising Model in 2.01 and 3 Dimensions,” *J. Phys. A* **50** no. 15, (2017) 154001, arXiv:1603.04444 [hep-th].
- [191] R. S. Erramilli, L. V. Iliesiu, P. Kravchuk, W. Landry, D. Poland, and D. Simmons-Duffin, “blocks_3d: Software for general 3d conformal blocks,” arXiv:2011.01959 [hep-th].
- [192] A. Dymarsky, J. Penedones, E. Trevisani, and A. Vichi, “Charting the space of 3D CFTs with a continuous global symmetry,” *JHEP* **05** (2019) 098, arXiv:1705.04278 [hep-th].
- [193] A. Dymarsky, F. Kos, P. Kravchuk, D. Poland, and D. Simmons-Duffin, “The 3d Stress-Tensor Bootstrap,” *JHEP* **02** (2018) 164, arXiv:1708.05718 [hep-th].
- [194] M. Reehorst, E. Trevisani, and A. Vichi, “Mixed Scalar-Current bootstrap in three dimensions,” arXiv:1911.05747 [hep-th].
- [195] S. M. Chester and S. S. Pufu, “Towards bootstrapping QED₃,” *JHEP* **08** (2016) 019, arXiv:1601.03476 [hep-th].
- [196] S. M. Chester, L. V. Iliesiu, M. Mezei, and S. S. Pufu, “Monopole Operators in $U(1)$ Chern-Simons-Matter Theories,” *JHEP* **05** (2018) 157, arXiv:1710.00654 [hep-th].
- [197] D. Simmons-Duffin, D. Stanford, and E. Witten, “A spacetime derivation of the Lorentzian OPE inversion formula,” *JHEP* **07** (2018) 085, arXiv:1711.03816 [hep-th].

- [198] S. Albayrak, D. Meltzer, and D. Poland, “More Analytic Bootstrap: Nonperturbative Effects and Fermions,” *JHEP* **08** (2019) 040, arXiv:1904.00032 [hep-th].
- [199] S. Caron-Huot, Y. Gobeil, and Z. Zahraee, “The leading trajectory in the 2+1D Ising CFT,” arXiv:2007.11647 [hep-th].
- [200] S. R. Coleman, “The Fate of the False Vacuum. 1. Semiclassical Theory,” *Phys. Rev. D* **15** (1977) 2929–2936. [Erratum: *Phys. Rev. D* **16**, 1248 (1977)].
- [201] J. Callan, Curtis G. and S. R. Coleman, “The Fate of the False Vacuum. 2. First Quantum Corrections,” *Phys. Rev. D* **16** (1977) 1762–1768.
- [202] M. S. Turner and F. Wilczek, “Might our vacuum be metastable?,” *Nature* **298** (1982) 633–634.
- [203] S. R. Coleman and F. De Luccia, “Gravitational Effects on and of Vacuum Decay,” *Phys. Rev. D* **21** (1980) 3305.
- [204] T. Markkanen, A. Rajantie, and S. Stopyra, “Cosmological Aspects of Higgs Vacuum Metastability,” *Front. Astron. Space Sci.* **5** (2018) 40, arXiv:1809.06923 [astro-ph.CO].
- [205] A. Milsted, J. Haegeman, and T. J. Osborne, “Matrix product states and variational methods applied to critical quantum field theory,” *Phys. Rev. D* **88** (2013) 085030, arXiv:1302.5582 [hep-lat].
- [206] S. Kühn, J. I. Cirac, and M. C. Bañuls, “Non-Abelian string breaking phenomena with Matrix Product States,” *JHEP* **07** (2015) 130, arXiv:1505.04441 [hep-lat].
- [207] T. Pichler, M. Dalmonte, E. Rico, P. Zoller, and S. Montangero, “Real-time Dynamics in U(1) Lattice Gauge Theories with Tensor Networks,” *Phys. Rev. X* **6** no. 1, (2016) 011023, arXiv:1505.04440 [cond-mat.quant-gas].
- [208] B. Buyens, J. Haegeman, F. Hebenstreit, F. Verstraete, and K. Van Acoleyen, “Real-time simulation of the Schwinger effect with Matrix Product States,” *Phys. Rev. D* **96** no. 11, (2017) 114501, arXiv:1612.00739 [hep-lat].
- [209] T. Chanda, J. Zakrzewski, M. Lewenstein, and L. Tagliacozzo, “Confinement and lack of thermalization after quenches in the bosonic Schwinger model,” *Phys. Rev. Lett.* **124** no. 18, (2020) 180602, arXiv:1909.12657 [cond-mat.stat-mech].
- [210] G. Magnifico, M. Dalmonte, P. Facchi, S. Pascazio, F. V. Pepe, and E. Ercolessi, “Real Time Dynamics and Confinement in the \mathbb{Z}_n Schwinger-Weyl lattice model for 1+1 QED,” *Quantum* **4** (2020) 281, arXiv:1909.04821 [quant-ph].

- [211] A. Mezzacapo, E. Rico, C. Sabín, I. Egusquiza, L. Lamata, and E. Solano, “Non-Abelian $SU(2)$ Lattice Gauge Theories in Superconducting Circuits,” *Phys. Rev. Lett.* **115** no. 24, (2015) 240502, arXiv:1505.04720 [quant-ph].
- [212] E. Martinez *et al.*, “Real-time dynamics of lattice gauge theories with a few-qubit quantum computer,” *Nature* **534** (2016) 516–519, arXiv:1605.04570 [quant-ph].
- [213] D. González-Cuadra, E. Zohar, and J. I. Cirac, “Quantum Simulation of the Abelian-Higgs Lattice Gauge Theory with Ultracold Atoms,” *New J. Phys.* **19** no. 6, (2017) 063038, arXiv:1702.05492 [quant-ph].
- [214] E. Zohar, A. Farace, B. Reznik, and J. I. Cirac, “Digital quantum simulation of \mathbb{Z}_2 lattice gauge theories with dynamical fermionic matter,” *Phys. Rev. Lett.* **118** no. 7, (2017) 070501, arXiv:1607.03656.
- [215] C. Muschik, M. Heyl, E. Martinez, T. Monz, P. Schindler, B. Vogell, M. Dalmonte, P. Hauke, R. Blatt, and P. Zoller, “U(1) Wilson lattice gauge theories in digital quantum simulators,” *New J. Phys.* **19** no. 10, (2017) 103020, arXiv:1612.08653 [quant-ph].
- [216] J. Bender, E. Zohar, A. Farace, and J. I. Cirac, “Digital quantum simulation of lattice gauge theories in three spatial dimensions,” *New J. Phys.* **20** no. 9, (2018) 093001, arXiv:1804.02082 [quant-ph].
- [217] NuQS Collaboration, H. Lamm, S. Lawrence, and Y. Yamauchi, “General Methods for Digital Quantum Simulation of Gauge Theories,” *Phys. Rev. D* **100** no. 3, (2019) 034518, arXiv:1903.08807 [hep-lat].
- [218] F. M. Surace, P. P. Mazza, G. Giudici, A. Leroise, A. Gambassi, and M. Dalmonte, “Lattice gauge theories and string dynamics in Rydberg atom quantum simulators,” *Phys. Rev. X* **10** no. 2, (2020) 021041, arXiv:1902.09551 [cond-mat.quant-gas].
- [219] M. Kreshchuk, W. M. Kirby, G. Goldstein, H. Beauchemin, and P. J. Love, “Quantum simulation of quantum field theory in the light-front formulation,” 2020.
- [220] J. Liu and Y. Xin, “Quantum simulation of quantum field theories as quantum chemistry,” *JHEP* **12** (2020) 011, arXiv:2004.13234 [hep-th].
- [221] S. Notarnicola, M. Collura, and S. Montangero, “Real-time-dynamics quantum simulation of (1+1)-dimensional lattice QED with Rydberg atoms,” *Phys. Rev. Res.* **2** no. 1, (2020) 013288, arXiv:1907.12579 [cond-mat.quant-gas].

- [222] Z. Davoudi, M. Hafezi, C. Monroe, G. Pagano, A. Seif, and A. Shaw, “Towards analog quantum simulations of lattice gauge theories with trapped ions,” *Phys. Rev. Res.* **2** no. 2, (2020) 023015, arXiv:1908.03210 [quant-ph].
- [223] A. Celi, B. Vermersch, O. Viyuela, H. Pichler, M. D. Lukin, and P. Zoller, “Emerging Two-Dimensional Gauge Theories in Rydberg Configurable Arrays,” *Phys. Rev. X* **10** no. 2, (2020) 021057, arXiv:1907.03311 [quant-ph].
- [224] M. Bañuls *et al.*, “Simulating Lattice Gauge Theories within Quantum Technologies,” *Eur. Phys. J. D* **74** no. 8, (2020) 165, arXiv:1911.00003 [quant-ph].
- [225] W. Du, J. P. Vary, X. Zhao, and W. Zuo, “Quantum Simulation of Nuclear Inelastic Scattering,” 6, 2020.
- [226] T. Farrelly and J. Streich, “Discretizing quantum field theories for quantum simulation,” 2, 2020.
- [227] A. F. Shaw, P. Lougovski, J. R. Stryker, and N. Wiebe, “Quantum Algorithms for Simulating the Lattice Schwinger Model,” *Quantum* **4** (2020) 306, arXiv:2002.11146 [quant-ph].
- [228] N. Klco, J. R. Stryker, and M. J. Savage, “SU(2) non-Abelian gauge field theory in one dimension on digital quantum computers,” *Phys. Rev. D* **101** no. 7, (2020) 074512, arXiv:1908.06935 [quant-ph].
- [229] F. M. Surace and A. Lerose, “Scattering of mesons in quantum simulators,” 11, 2020.
- [230] J. Vovrosh and J. Knolle, “Confinement and entanglement dynamics on a digital quantum computer,” 2020.
- [231] Y.-Z. Li and J. Liu, “On Quantum Simulation Of Cosmic Inflation,” 9, 2020.
- [232] M. Fannes, B. Nachtergaele, and R. F. Werner, “Finitely correlated states on quantum spin chains,” *Commun. Math. Phys.* **144** no. 3, (1992) 443–490.
- [233] S. Rommer and S. Ostlund, “Class of ansatz wave functions for one-dimensional spin systems and their relation to the density matrix renormalization group,” *Phys. Rev. B* **55** (1997) 2164–2181, arXiv:cond-mat/9606213.
- [234] A. Lerose, F. M. Surace, P. P. Mazza, G. Peretto, M. Collura, and A. Gambassi, “Quasilocalized dynamics from confinement of quantum excitations,” *Phys. Rev. B* **102** no. 4, (2020) 041118, arXiv:1911.07877 [cond-mat.stat-mech].

- [235] C. Nagele, J. E. Cejudo, T. Byrnes, and M. Kleban, “Flux unwinding in the lattice schwinger model,” *Physical Review D* **99** no. 9, (May, 2019) –, arXiv:1811.03096 [hep-th].
<http://dx.doi.org/10.1103/PhysRevD.99.094501>.
- [236] P. Karpov, G. Zhu, M. Heller, and M. Heyl, “Spatiotemporal dynamics of particle collisions in quantum spin chains,” 11, 2020.
- [237] M. Van Damme, L. Vanderstraeten, J. De Nardis, J. Haegeman, and F. Verstraete, “Real-time scattering of interacting quasiparticles in quantum spin chains,” 2019.
- [238] R. Vlijm, M. Ganahl, D. Fioretto, M. Brockmann, M. Haque, H. G. Evertz, and J.-S. Caux, “Quasi-soliton scattering in quantum spin chains,” *Phys. Rev. B* **92** no. 21, (2015) 214427, arXiv:1507.08624 [cond-mat.str-el].
- [239] T. Sugihara, “Density matrix renormalization group in a two-dimensional lambda phi⁴ Hamiltonian lattice model,” *JHEP* **05** (2004) 007, arXiv:hep-lat/0403008.
- [240] D. Friedan, Z.-a. Qiu, and S. H. Shenker, “Conformal Invariance, Unitarity and Two-Dimensional Critical Exponents,” *Phys. Rev. Lett.* **52** (1984) 1575–1578.
- [241] A. Zamolodchikov, “Integrable field theory from conformal field theory,” *Adv. Stud. Pure Math.* **19** (1989) 641–674.
- [242] A. Zamolodchikov, “Integrals of Motion and S Matrix of the (Scaled) T=T(c) Ising Model with Magnetic Field,” *Int. J. Mod. Phys. A* **4** (1989) 4235.
- [243] G. Delfino, G. Mussardo, and P. Simonetti, “Nonintegrable quantum field theories as perturbations of certain integrable models,” *Nucl. Phys. B* **473** (1996) 469–508, arXiv:hep-th/9603011.
- [244] G. Mussardo, “Integrability, Non-integrability and confinement,” *J. Stat. Mech.* **1101** (2011) P01002, arXiv:1010.5519 [cond-mat.stat-mech].
- [245] B. M. McCoy and T. T. Wu, “Two-dimensional Ising Field Theory in a Magnetic Field: Breakup of the Cut in the Two Point Function,” *Phys. Rev. D* **18** (1978) 1259.
- [246] T. Rakovszky, M. Mestyán, M. Collura, M. Kormos, and G. Takács, “Hamiltonian truncation approach to quenches in the ising field theory,” *Nucl. Phys. B* **911** (Oct, 2016) 805–845, arXiv:1607.01068.
<http://dx.doi.org/10.1016/j.nuclphysb.2016.08.024>.

- [247] M. Kormos, M. Collura, G. Takács, and P. Calabrese, “Real-time confinement following a quantum quench to a non-integrable model,” *Nature Physics* **13** no. 3, (2017) 246–249, arXiv:1604.03571 [cond-mat.stat-mech].
- [248] C.-J. Lin and O. I. Motrunich, “Quasiparticle explanation of the weak-thermalization regime under quench in a nonintegrable quantum spin chain,” *Phys. Rev. A* **95** no. 2, (2017) 023621, arXiv:1610.04287.
- [249] K. Hódsági, M. Kormos, and G. Takács, “Quench dynamics of the ising field theory in a magnetic field,” *SciPost Phys.* **5** no. 3, (Sep, 2018) –, arXiv:1803.01158.
- [250] O. A. Castro-Alvaredo, M. Lencsés, I. M. Szécsényi, and J. Viti, “Entanglement Oscillations near a Quantum Critical Point,” *Phys. Rev. Lett.* **124** no. 23, (2020) 230601, arXiv:2001.10007 [cond-mat.stat-mech].
- [251] A. J. James, R. M. Konik, and N. J. Robinson, “Nonthermal states arising from confinement in one and two dimensions,” *Phys. Rev. Lett.* **122** no. 13, (2019) 130603, arXiv:1804.09990 [cond-mat.stat-mech].
- [252] J. Wurtz and A. Polkovnikov, “Emergent conservation laws and nonthermal states in the mixed-field ising model,” *Phys. Rev. B* **101** no. 19, (2020) 195138, arXiv:2002.08969 [cond-mat.str-el].
- [253] M. Lassig, G. Mussardo, and J. L. Cardy, “The scaling region of the tricritical Ising model in two-dimensions,” *Nucl. Phys. B* **348** (1991) 591–618.
- [254] L. Lepori, G. Mussardo, and G. Z. Toth, “The particle spectrum of the Tricritical Ising Model with spin reversal symmetric perturbations,” *J. Stat. Mech.* **0809** (2008) P09004, arXiv:0806.4715 [hep-th].
- [255] F. Verstraete and J. I. Cirac, “Matrix product states represent ground states faithfully,” *Phys. Rev. B* **73** no. 9, (2006) 094423, arXiv:cond-mat/0505140.
- [256] J. Haegeman, J. Cirac, T. J. Osborne, I. Pizorn, H. Verschelde, and F. Verstraete, “Time-Dependent Variational Principle for Quantum Lattices,” *Phys. Rev. Lett.* **107** (2011) 070601, arXiv:1103.0936 [cond-mat.str-el].
- [257] J. Haegeman, B. Pirvu, D. J. Weir, J. I. Cirac, T. J. Osborne, H. Verschelde, and F. Verstraete, “Variational matrix product ansatz for dispersion relations,” *Phys. Rev. B* **85** no. 10, (2012) 100408, arXiv:1103.2286 [quant-ph].

- [258] J. Haegeman, S. Michalakis, B. Nachtergaele, T. J. Osborne, N. Schuch, and F. Verstraete, “Elementary excitations in gapped quantum spin systems,” *Phys. Rev. Lett.* **111** no. 8, (2013) 080401, arXiv:1305.2176 [quant-ph].
- [259] A. Milsted, J. Haegeman, T. J. Osborne, and F. Verstraete, “Variational matrix product ansatz for nonuniform dynamics in the thermodynamic limit,” *Phys. Rev. B* **88** no. 15, (2013) 155116, arXiv:1207.0691 [cond-mat.str-el].
- [260] L. Vanderstraeten, F. Verstraete, and J. Haegeman, “Scattering particles in quantum spin chains,” *Phys. Rev. B* **92** no. 12, (2015) 125136, arXiv:1506.01008 [cond-mat.str-el].
- [261] J. Haegeman, C. Lubich, I. Oseledets, B. Vandereycken, and F. Verstraete, “Unifying time evolution and optimization with matrix product states,” *Phys. Rev. B* **94** no. 16, (2016) 165116, arXiv:1408.5056 [quant-ph].
- [262] A. Milsted, “evoMPS,” July, 2020. <https://github.com/amilsted/evoMPS>.
- [263] J. Haegeman, T. J. Osborne, and F. Verstraete, “Post-matrix product state methods: To tangent space and beyond,” *Phys. Rev. B* **88** no. 7, (2013) 075133, arXiv:1305.1894 [quant-ph].
- [264] W. Li, J. Ren, and Z. Shuai, “Numerical assessment for accuracy and gpu acceleration of td-dmrg time evolution schemes,” *J. Chem. Phys.* **152** no. 2, (2020) 024127, arXiv:1907.12044.
- [265] F. Verstraete, M. Wolf, D. Pérez-García, and J. I. Cirac, “Projected entangled states: Properties and applications,” *Int. J. Mod. Phys. B* **20** no. 30n31, (2006) 5142–5153.
- [266] L. Vanderstraeten, J. Haegeman, and F. Verstraete, “Simulating excitation spectra with projected entangled-pair states,” *Phys. Rev. B* **99** no. 16, (2019) 165121, arXiv:1809.06747.
- [267] J. Motruk, M. P. Zaletel, R. S. Mong, and F. Pollmann, “Density matrix renormalization group on a cylinder in mixed real and momentum space,” *Phys. Rev. B* **93** no. 15, (2016) 155139, arXiv:1512.03318.
- [268] Boost Authors, “Boost C++ Libraries.” <http://www.boost.org/>, 2003-2020.
- [269] G. Guennebaud, B. Jacob, *et al.*, “Eigen v3.” <http://eigen.tuxfamily.org>, 2010.
- [270] W. Schroeder, K. Martin, and B. Lorensen, *The Visualization Toolkit*. Kitware, fourth ed., 2006.

- [271] J. Towns, T. Cockerill, M. Dahan, I. Foster, K. Gaither, A. Grimshaw, V. Hazlewood, S. Lathrop, D. Lifka, G. D. Peterson, R. Roskies, J. Scott, and N. Wilkins-Diehr, “Xsede: Accelerating scientific discovery,” *Computing in Science and Engineering* **16** no. 05, (Sep, 2014) 62–74.
- [272] L. Vanderstraeten, J. Haegeman, and F. Verstraete, “Tangent-space methods for uniform matrix product states,” *SciPost Phys. Lect. Notes* (2019) 7, [arXiv:1810.07006](https://arxiv.org/abs/1810.07006) [cond-mat.str-el].
- [273] E. Tang *private communication* (2020) .

Appendix A

APPENDICES OF CHAPTER 2

A.1 Generalization to Arbitrary Dimension

Black Hole Spacetime

In this appendix we generalize all of our results to arbitrary spacetime dimension $D \geq 4$. See footnote 7 for the mass dimensions of various quantities. To begin, we consider the Reissner-Nordström metric in D dimensions,

$$ds^2 = -\tilde{f}(r)dt^2 + \frac{1}{\tilde{g}(r)}dr^2 + r^2 d\Omega_{D-2}^2, \quad (\text{A.1})$$

where $d\Omega_{D-2}^2$ is line element on the unit $(D-2)$ -sphere and

$$\tilde{f}(r) = \tilde{g}(r) = 1 - \frac{2\kappa^2 M}{(D-2)\Omega_{D-2}r^{D-3}} + \frac{Q^2\kappa^2}{(D-2)(D-3)\Omega_{D-2}^2 r^{2(D-3)}}, \quad (\text{A.2})$$

as before denoting $\kappa^2 = 8\pi G$. The electromagnetic field strength is

$$\tilde{F}_{\mu\nu} dx^\mu \wedge dx^\nu = \frac{Q}{\Omega_{D-2}r^{D-2}} dt \wedge dr, \quad (\text{A.3})$$

where the $(D-2)$ -dimensional area of the unit codimension-two sphere is

$$\Omega_{D-2} = \frac{2\pi^{\frac{D-1}{2}}}{\Gamma\left(\frac{D-1}{2}\right)}. \quad (\text{A.4})$$

Next, let us define new variables for mass and charge in units of the Planck scale,

$$m = \frac{\kappa^2 M}{(D-2)\Omega_{D-2}}, \quad q = \frac{\kappa Q}{\sqrt{(D-2)(D-3)\Omega_{D-2}}}, \quad (\text{A.5})$$

along with a rescaled radial coordinate,

$$x = r^{D-3}, \quad (\text{A.6})$$

in terms of which the metric component can be written simply as

$$\tilde{g}(r) = 1 - \frac{2m}{x} + \frac{q^2}{x^2}. \quad (\text{A.7})$$

The outer horizon is located at $x = \tilde{\chi} = \tilde{\rho}^{D-3}$, where

$$\tilde{\chi} = m + \sqrt{m^2 - q^2} = m(1 + \xi) \quad (\text{A.8})$$

and ξ is defined as in Eq. (2.35). The extremality condition for the background Reissner-Nordström spacetime as before requires $q/m \leq 1$. The requirement of thermodynamic stability restricts our consideration to black holes with $\xi < \frac{D-3}{D-2}$, for which the specific heat is positive.

Following the perturbative methods of Refs. [139, 140], we can compute the metric components at first order in perturbations, finding

$$g(r) = 1 - \frac{2m}{x} + \frac{q^2}{x^2} - \frac{q^2}{x^{\frac{2(2D-5)}{D-3}}} \sum_{i=1}^8 \alpha_i c_i, \quad (\text{A.9})$$

where the coefficients are

$$\begin{aligned} \alpha_1 &= \frac{(D-3)(D-4)}{D-2} \left[2 \frac{13D^2 - 47D + 40}{3D-7} q^2 - 8(3D-5)mx + 16(D-2)x^2 \right] \\ \alpha_2 &= 2 \frac{D-3}{D-2} \left[\frac{8D^3 - 55D^2 + 117D - 76}{3D-7} q^2 - 4(2D^2 - 10D + 11)mx \right. \\ &\quad \left. + 2(3D-10)(D-2)x^2 \right] \\ \alpha_3 &= 4 \frac{D-3}{D-2} \left[\frac{8D^3 - 48D^2 + 87D - 44}{3D-7} q^2 - 2(4D^2 - 17D + 16)mx \right. \\ &\quad \left. + 8(D-2)(D-3)x^2 - 2(D-2)(D-4) \frac{m^2 x^2}{q^2} \right] \\ \alpha_4 &= 4(D-3) \left[\frac{(7D-13)(D-2)}{3D-7} q^2 - 2(3D-5)mx + 4(D-2)x^2 \right] \\ \alpha_5 &= 2(D-3) \left[\frac{(5D-9)(D-2)}{3D-7} q^2 - 2(2D-3)mx + 3(D-2)x^2 \right] \\ \alpha_6 &= 4(D-3) \left[4 \frac{(D-2)^2}{3D-7} q^2 - (3D-5)mx + 2(D-2)x^2 \right] \\ \alpha_7 &= 8 \frac{(D-2)(D-3)^2}{3D-7} q^2 \\ \alpha_8 &= 4 \frac{(D-2)(D-3)^2}{3D-7} q^2. \end{aligned} \quad (\text{A.10})$$

Calculation of Entropy

As before, the total entropy shift is $\Delta S = \Delta S_I + \Delta S_H$, where ΔS_I , defined in Eq. (2.48), arises from modifications of the low-energy graviton interactions and ΔS_H , defined in Eq. (2.49), is induced by the shift of the black hole horizon.

To compute the entropy contribution from interactions, we substitute the unperturbed

black hole background from Sec. A.1 into Eq. (2.50), yielding

$$\Delta S_I = \tilde{S} \times \frac{2(D-3)}{m^{\frac{2}{D-3}}(1+\xi)^{\frac{D-1}{D-3}}} \left\{ 4(D-2)d_3 - 2(1-\xi) \left[(D-4)d_1 + (D-3)d_2 + 2(2D-5)d_3 + (D-2) \left(d_4 + \frac{1}{2}d_5 + d_6 \right) \right] \right\}. \quad (\text{A.11})$$

To obtain the entropy contribution from the shift in the horizon, we apply Eq. (2.53).

The shift in the horizon area is then

$$\Delta A = A - \tilde{A} = (D-2)\Omega_{D-2}\tilde{\rho}^{D-3}\Delta\rho = -\frac{(D-2)\Omega_{D-2}\tilde{\chi}\Delta g(\tilde{\rho})}{\partial_{\tilde{\rho}}\tilde{g}(\tilde{\rho})}, \quad (\text{A.12})$$

where the unperturbed area is $\tilde{A} = \Omega_{D-2}\tilde{\rho}^{D-2}$. Inserting the perturbed metric in Eqs. (A.9) and (A.10), we then obtain

$$\begin{aligned} \Delta S_H = \tilde{S} \times & \frac{1}{(3D-7)m^{\frac{2}{D-3}}\xi(1+\xi)^{\frac{D-1}{D-3}}} \times \\ & \times \left\{ d_1(1-\xi)(D-3)(D-4)[(11D-24)\xi + D-4] \right. \\ & + d_2(1-\xi)(D-3)[(10D^2-53D+68)\xi + 2D^2-11D+16] \\ & + 2d_3[-(16D^3-128D^2+337D-292)(1-\xi)^2 \\ & \quad + 2(3D-7)(4D^2-23D+32)(1-\xi) \\ & \quad - 2(D-2)(D-4)(3D-7)] \\ & + 2d_4(1-\xi)(D-2)(D-3)[5(D-2)\xi + D-4] \\ & + 2(d_5+d_6)(D-2)(D-3)(1-\xi)[2(D-2)\xi + D-3] \\ & \left. + 2(2d_7+d_8)(D-2)^2(D-3)(1-\xi)^2 \right\}. \quad (\text{A.13}) \end{aligned}$$

As before, we can consider a near-extremal limit in which $\xi \ll 1$ but $\Delta S \ll \tilde{S}$ so that perturbation theory still applies. This requires that

$$\xi \gg \frac{|d_i|}{m^{\frac{2}{D-3}}}, \quad (\text{A.14})$$

which permits arbitrarily small ξ for a sufficiently large black hole. However, for the classical higher-dimension operators to dominate, we again require $\rho \ll 1/\kappa m_\phi^{D/2}$ according to Eq. (2.32). Hence, for a tree-level ultraviolet completion with $d_i \sim 1/m_\phi^2$, Eq. (A.14) becomes $\xi \gg \kappa^2 m_\phi^{D-2}$. Additionally, our argument in Sec. 2.2 imposes a further perturbativity criterion on the inverse temperature shift, $\Delta\beta \ll \tilde{\beta}$. The background inverse temperature is

$$\tilde{\beta} = \frac{2\pi m^{\frac{1}{D-3}}(1+\xi)^{\frac{D-2}{D-3}}}{(D-3)\xi}, \quad (\text{A.15})$$

while in the near-extremal limit the inverse temperature shift goes as $\Delta\beta \sim d_i/\xi^3 m^{1/(D-3)}$. Hence, requiring $\Delta\beta \ll \tilde{\beta}$, we have

$$\xi \gg \frac{|d_i|^{1/2}}{m^{\frac{1}{D-3}}}. \quad (\text{A.16})$$

Along with the scaling of the d_i and the bound on ρ imposed by Eq. (2.32), this becomes just the requirement that

$$\xi \gg \kappa m_\phi^{(D-2)/2}, \quad (\text{A.17})$$

so ξ can still be made parametrically small provided the heavy states are sub-Planckian.

New Positivity Bounds

Combining Eqs. (A.11) and (A.13), we obtain the total shift in entropy in D dimensions,

$$\begin{aligned} \Delta S = \tilde{S} \times & \frac{1}{(3D-7)m^{\frac{2}{D-3}}\xi(1+\xi)^{\frac{D-1}{D-3}}} \times \\ & \times \{d_1(D-3)(D-4)^2(1-\xi)^2 \\ & + d_2(D-3)(2D^2-11D+16)(1-\xi)^2 \\ & + 2d_3[(8D^3-60D^2+151D-128)(1-\xi)^2 \\ & - 2(D-2)(2D-5)(3D-7)(1-\xi) \\ & + 2(D-2)^2(3D-7)] \\ & + 2d_4(D-2)(D-3)(D-4)(1-\xi)^2 \\ & + 2d_5(D-2)(D-3)^2(1-\xi)^2 \\ & + 2d_6(D-2)(D-3)(1-\xi)[-2(2D-5)\xi + D-3] \\ & + 4d_7(D-2)^2(D-3)(1-\xi)^2 \\ & + 2d_8(D-2)^2(D-3)(1-\xi)^2\}. \end{aligned} \quad (\text{A.18})$$

Positivity of this entropy shift for all $\xi \in \left(0, \frac{D-3}{D-2}\right)$ then implies a family of new constraints on the higher-dimension operator coefficients, which generalizes Eq. (2.60),

$$(1-\xi)^2 d_0 + (D-2)^2(3D-7)\xi d_3 - \frac{1}{2}(D-2)(D-3)(3D-7)\xi(1-\xi)(2d_3+d_6) > 0, \quad (\text{A.19})$$

where in analogy with Eq. (2.61) we have defined

$$\begin{aligned}
d_0 = & \frac{1}{4}(D-3)(D-4)^2 d_1 + \frac{1}{4}(D-3)(2D^2 - 11D + 16)d_2 \\
& + \frac{1}{2}(2D^3 - 16D^2 + 45D - 44)d_3 + \frac{1}{2}(D-2)(D-3)(D-4)d_4 \quad (\text{A.20}) \\
& + \frac{1}{2}(D-2)(D-3)^2(d_5 + d_6) + (D-2)^2(D-3) \left(d_7 + \frac{1}{2}d_8 \right).
\end{aligned}$$

As before, the bound in Eq. (A.19) is stronger than any finite set of bounds obtained for fixed values of ξ , i.e., each ξ yields a linearly independent bound. As shown in App. A.2, the bound in Eq. (A.19) is field redefinition invariant for all values of ξ .

In the near-extremal limit, $\xi \ll 1$, the bound in Eq. (A.19) becomes

$$d_0 > 0. \quad (\text{A.21})$$

The above inequality is closely related to the perturbation of the extremality condition discussed in Sec. 2.6. Applying the same reasoning to general dimension D , we find that the extremality condition for the perturbed black hole is shifted by

$$\Delta z = \frac{4(D-3)}{(3D-7)(D-2)m^{\frac{2}{D-3}}} d_0, \quad (\text{A.22})$$

where d_0 is exactly the same combination of coefficients defined in Eq. (A.20). Thus, the requirement of Eq. (2.8) mandating positive entropy shift implies a constraint on the coefficients of higher-dimension operators that increases the charge-to-mass ratio of extremal black holes in the theory. In turn, large black holes can decay to smaller black holes of a higher charge-to-mass-ratio, thus establishing the WGC in general dimension D .

A.2 Field Redefinition Invariance

Any physical observable should be invariant under a reparameterization of the field variables. Let us consider an arbitrary field redefinition,

$$g_{\mu\nu} \rightarrow g_{\mu\nu} + \delta g_{\mu\nu}, \quad (\text{A.23})$$

where the perturbation is second order in derivatives, so

$$\delta g_{\mu\nu} = r_1 R_{\mu\nu} + r_2 g_{\mu\nu} R + r_3 \kappa^2 F_{\mu\rho} F_\nu{}^\rho + r_4 \kappa^2 g_{\mu\nu} F_{\rho\sigma} F^{\rho\sigma} \quad (\text{A.24})$$

for a set of four arbitrary constants r_i . Inserting this field redefinition into the action for Einstein-Maxwell theory induces new terms in the action proportional to the

equations of motion,¹

$$\delta\mathcal{L} = \frac{1}{2\kappa^2}\delta g^{\mu\nu}\left(R_{\mu\nu} - \frac{1}{2}Rg_{\mu\nu} - \kappa^2T_{\mu\nu}\right). \quad (\text{A.25})$$

This has the net effect of shifting the higher-dimension operator coefficients in the action by

$$\begin{aligned} d_1 &\rightarrow d_1 - \frac{1}{4}r_1 - \frac{D-2}{4}r_2 \\ d_2 &\rightarrow d_2 + \frac{1}{2}r_1 \\ d_3 &\rightarrow d_3 \\ d_4 &\rightarrow d_4 + \frac{1}{8}r_1 + \frac{D-4}{8}r_2 - \frac{1}{4}r_3 - \frac{D-2}{4}r_4 \\ d_5 &\rightarrow d_5 - \frac{1}{2}r_1 + \frac{1}{2}r_3 \\ d_6 &\rightarrow d_6 \\ d_7 &\rightarrow d_7 + \frac{1}{8}r_3 + \frac{D-4}{8}r_4 \\ d_8 &\rightarrow d_8 - \frac{1}{2}r_3. \end{aligned} \quad (\text{A.26})$$

Because the field redefinition depends on four arbitrary constants, this reduces the naive basis of eight higher-dimension operator coefficients down to a set of four combinations that are automatically field redefinition invariant:

$$d_0, d_3, d_6, d_9, \quad (\text{A.27})$$

where d_0 is defined in Eq. (A.20) and $d_9 = d_2 + d_5 + d_8$. All physical quantities, like the bounds in Eqs. (2.60) and (A.19), depend only on these combinations of coefficients.

¹The particular field redefinition in which the pure Einstein-Maxwell equations of motion are substituted into the higher-dimension operators is a special case of the transformation in Eq. (A.24).

Appendix B

APPENDICES OF CHAPTER 3

B.1 Code availability

All code used in this work is available online. This includes the various codes described in appendix A of [4], as well as `tiptop`, available at <https://gitlab.com/bootstrapcollaboration/tiptop>. `tiptop` is implemented in C++17 and uses the Boost [268], Eigen [269], and VTK [270] libraries. The version used in this paper has the Git commit hash

23774017b8726699bd838cf138a65e29405f0907

B.2 Software setup and parameters

The computations of the $O(3)$ model islands described in section 3.4 with $\Lambda = 19, 27$ were performed on the Caltech HPC Cluster, the Yale Grace Cluster, and the EPFL SCITAS cluster. For the computations with $\Lambda = 35, 43$, we tested possible primal points using the Caltech and Yale clusters. After finding a few initial primal points, the main Delaunay triangulation search was performed on the XSEDE Comet Cluster [271] at the San Diego Supercomputing Center through allocation PHY190023. Together, the computations of the $\Lambda = 35$ island, the $\Lambda = 43$ island, and the $\Lambda = 35$ `tiptop` search took 2.94M CPU hours on the Comet Cluster. The optimization computations of section 3.4 were performed at $\Lambda = 35$ and completed on the Caltech and Yale clusters.

We used the following choices for the set of spins at each value of Λ :

$$\begin{aligned}
 S_{19} &= \{0, \dots, 26\} \cup \{49, 50\}, \\
 S_{27} &= \{0, \dots, 31\} \cup \{49, 50\}, \\
 S_{35} &= \{0, \dots, 44\} \cup \{47, 48, 51, 52, 55, 56, 59, 60, 63, 64, 67, 68\}, \\
 S_{43} &= \{0, \dots, 64\} \cup \{67, 68, 71, 72, 75, 76, 79, 80, 83, 84, 87, 88\}. \quad (\text{B.1})
 \end{aligned}$$

The `sdpb` parameters used in our computations are given in tables B.1 and B.2.

B.3 Tensor structures

In this appendix we compute the $SO(3)$ tensor structures T^R that appear in the conformal block expansions (3.11) for the 4-point functions listed in table 3.3. We

Λ	19	27	35	43
keptPoleOrder	14	14	32	40
order	60	60	80	90
spins	S_{19}	S_{27}	S_{35}	S_{43}
precision	768	768	960	1024
dualityGapThreshold	10^{-30}	10^{-30}	10^{-30}	10^{-75}
primalErrorThreshold	10^{-200}	10^{-200}	10^{-200}	10^{-200}
dualErrorThreshold	10^{-200}	10^{-200}	10^{-200}	10^{-200}
initialMatrixScalePrimal	10^{40}	10^{50}	10^{50}	10^{60}
initialMatrixScaleDual	10^{40}	10^{50}	10^{50}	10^{60}
feasibleCenteringParameter	0.1	0.1	0.1	0.1
infeasibleCenteringParameter	0.3	0.3	0.3	0.3
stepLengthReduction	0.7	0.7	0.7	0.7
maxComplementarity	10^{100}	10^{130}	10^{160}	10^{200}

Table B.1: Parameters used for the computations of the conformal bootstrap islands in section 3.4. The sets S_Λ are defined in (B.1).

Λ	35
keptPoleOrder	30
order	60
spins	S_{35}
precision	768
dualityGapThreshold	10^{-20}
primalErrorThreshold	10^{-50}
dualErrorThreshold	10^{-60}
initialMatrixScalePrimal	10^{50}
initialMatrixScaleDual	10^{50}
feasibleCenteringParameter	0.1
infeasibleCenteringParameter	0.3
stepLengthReduction	0.7
maxComplementarity	10^{160}

Table B.2: Parameters used for the optimization computations in section 3.4. The set S_{35} is defined in (B.1).

start by defining a basis of tensors for each configuration in table 3.3:

$$\begin{aligned}
B_{\phi\phi\phi\phi}^I &= \begin{pmatrix} \delta_{ij}\delta_{kl} \\ \delta_{ik}\delta_{jl} \\ \delta_{il}\delta_{jk} \end{pmatrix}, \\
B_{tttt}^I &= \begin{pmatrix} \delta_{i_1j_1}\delta_{i_2j_2}\delta_{k_1l_1}\delta_{k_2l_2} \\ \delta_{i_1k_1}\delta_{i_2k_2}\delta_{j_1l_1}\delta_{j_2l_2} \\ \delta_{i_1l_1}\delta_{i_2l_2}\delta_{k_1j_1}\delta_{k_2j_2} \\ \delta_{i_1j_1}\delta_{i_2k_2}\delta_{k_1l_1}\delta_{j_2l_2} \\ \delta_{i_1j_1}\delta_{i_2l_1}\delta_{j_2k_1}\delta_{k_2l_2} \end{pmatrix}, \\
B_{t\phi t\phi}^I &= \begin{pmatrix} \delta_{i_1k_1}\delta_{i_2k_2}\delta_{j_1l_1} \\ \delta_{i_1j_1}\delta_{i_2k_2}\delta_{k_1l_1} \\ \delta_{i_1l_1}\delta_{i_2k_2}\delta_{j_1k_1} \end{pmatrix}, \\
B_{tt\phi\phi}^I &= \begin{pmatrix} \delta_{i_1j_1}\delta_{i_2j_2}\delta_{k_1l_1} \\ \delta_{i_1k_1}\delta_{i_2j_2}\delta_{j_1l_1} \\ \delta_{i_1l_1}\delta_{i_2j_2}\delta_{k_1j_1} \end{pmatrix}, \\
B_{ssss} &= 1, \\
B_{\phi s\phi s} &= \delta_{ik}, \\
B_{tsts} &= \delta_{i_1k_1}\delta_{i_2k_2}, \\
B_{ttss} &= \delta_{i_1j_1}\delta_{i_2j_2}, \\
B_{\phi\phi ss} &= \delta_{ij}, \\
B_{\phi s\phi t} &= \delta_{il_1}\delta_{kl_2}, \\
B_{\phi\phi st} &= \delta_{il_1}\delta_{jl_2}, \\
B_{sttt} &= \delta_{j_1k_1}\delta_{j_2l_1}\delta_{k_2l_2},
\end{aligned} \tag{B.2}$$

where the indices for each of the four operators are labeled as i, j, k, l respectively, all indices with the same letter should be symmetrized with the trace removed, and for simplicity we suppress the indices on the left-hand side. For the first four configurations with non-trivial bases, we can find the tensor structure using the rank-2 $SO(3)$ Casimir C acting on a basis B with n, m number of i, j indices, respectively, as:

$$CB^I = \sum_J M^{IJ} B^J, \quad C \equiv (G_{i'_1}^{i_1} \oplus \cdots \oplus G_{i'_n}^{i_n} \oplus G_{j'_1}^{j_1} \oplus \cdots \oplus G_{j'_m}^{j_m})^2, \tag{B.3}$$

where G are the usual $SO(3)$ generators. The K eigenvectors $(T_K)^J$ of M^{IJ} are eigenvectors of C :

$$(CT_K)^I = \sum_J M^{IJ} (T_K)^J = c_K (T_K)^I, \quad (\text{B.4})$$

where the eigenvalue c for a rank q $SO(3)$ irrep is $q(q+1)$, which allows us to identify each T_K with an irrep. Up to an overall normalization, these T_K are then the desired tensor structures. For the last 8 configurations there is only one basis element, so the tensor structure is simply that element also up to an overall

normalization. The final list of tensor structures is then

$$\begin{aligned}
\langle \phi\phi\phi\phi \rangle : \quad & T_{1^-1^-1^-1^-}^{0^+} = B_{\phi\phi\phi\phi}^1, \\
& T_{1^-1^-1^-1^-}^{1^+} = B_{\phi\phi\phi\phi}^2 - B_{\phi\phi\phi\phi}^3, \\
& T_{1^-1^-1^-1^-}^{2^+} = B_{\phi\phi\phi\phi}^2 + B_{\phi\phi\phi\phi}^3 - \frac{2}{3}B_{\phi\phi\phi\phi}^1, \\
\langle tttt \rangle : \quad & T_{2^+2^+2^+2^+}^{0^+} = B_{tttt}^1, \\
& T_{2^+2^+2^+2^+}^{1^+} = B_{tttt}^4 - B_{tttt}^5, \\
& T_{2^+2^+2^+2^+}^{2^+} = B_{tttt}^4 + B_{tttt}^5 - \frac{2}{3}B_{tttt}^1, \\
& T_{2^+2^+2^+2^+}^{3^+} = B_{tttt}^5 - B_{tttt}^4 - \frac{5}{4}B_{tttt}^3 + \frac{5}{4}B_{tttt}^2, \\
& T_{2^+2^+2^+2^+}^{4^+} = -B_{tttt}^5 - B_{tttt}^4 + \frac{7}{12}B_{tttt}^3 + \frac{7}{12}B_{tttt}^2 + \frac{13}{30}B_{tttt}^1, \\
\langle t\phi t\phi \rangle, \langle \phi t t\phi \rangle : \quad & T_{2^+1^-2^+1^-}^{1^-} = 2B_{t\phi t\phi}^2, \\
& T_{2^+1^-2^+1^-}^{2^-} = -4B_{t\phi t\phi}^1 + 2B_{t\phi t\phi}^2 + 4B_{t\phi t\phi}^3, \\
& T_{2^+1^-2^+1^-}^{3^-} = 10B_{t\phi t\phi}^1 - 8B_{t\phi t\phi}^2 + 20B_{t\phi t\phi}^3, \\
\langle t t\phi\phi \rangle : \quad & T_{2^+2^+1^-1^-}^{0^+} = B_{tt\phi\phi}^1, \\
& T_{2^+2^+1^-1^-}^{1^+} = B_{tt\phi\phi}^2 - B_{tt\phi\phi}^3, \\
& T_{2^+2^+1^-1^-}^{2^+} = B_{tt\phi\phi}^2 + B_{tt\phi\phi}^3 - \frac{2}{3}B_{tt\phi\phi}^1, \\
\langle ssss \rangle : \quad & T_{0^+0^+0^+0^+}^{0^+} = B_{ssss}, \\
\langle \phi s\phi s \rangle, \langle s\phi\phi s \rangle : \quad & T_{1^-0^+1^-2^+}^{1^-} = B_{\phi s\phi s}, \\
\langle tsts \rangle, \langle stts \rangle : \quad & T_{2^+0^+2^+0^+}^{2^+} = B_{tsts}, \\
\langle ttss \rangle : \quad & T_{2^+2^+0^+0^+}^{0^+} = B_{ttss}, \\
\langle \phi\phi ss \rangle : \quad & T_{1^-1^-0^+0^+}^{0^+} = B_{\phi\phi ss}, \\
\langle \phi s\phi t \rangle, \langle s\phi\phi t \rangle : \quad & T_{1^-0^+1^-2^+}^{1^-} = \sqrt{2}B_{\phi s\phi t}, \\
\langle \phi\phi st \rangle : \quad & T_{1^-1^-0^+2^+}^{2^+} = \sqrt{2}B_{\phi\phi st}, \\
\langle sttt \rangle, \langle ttst \rangle : \quad & T_{0^+2^+2^+2^+}^{2^+} = \sqrt{2}B_{sttt}.
\end{aligned} \tag{B.5}$$

The overall normalization of these tensor structures has been chosen so that the OPE coefficients $\lambda_{\varphi_1\varphi_2\mathcal{O}}$ and $\lambda_{\varphi_3\varphi_4\mathcal{O}}$ in (3.11) are consistent under permutation of their subscripts. This can be checked using the free theory, where we have the operators

$$s(x) \equiv \frac{1}{\sqrt{6}}\phi^i(x)\phi^i(x), \quad t^{ij}(x) \equiv \frac{1}{\sqrt{2}}\phi^i(x)\phi^j(x) - \text{trace}, \tag{B.6}$$

which have been normalized consistent with the 2-point function normalization in (3.13). We can then compute all the 4-point functions in table 3.3 using Wick contractions and expand in blocks as in (3.11) using the tensor structures in (B.5) to verify this consistency.¹

B.4 Computed points

In table B.3 we list the 38 primal points we have computed in the $\Lambda = 43$ island and in table B.4 we list the 270 dual points we computed at $\Lambda = 43$. In table B.5 we list the 7 primal points we use for the optimization computations described in section 3.4.

In Figure B.1 we show a plot of the allowed regions at $\Lambda = 19, 27, 35, 43$ after performing an affine transformation which makes the $\Lambda = 19$ region roughly spherical. The precise affine transformation is given by

$$\begin{aligned} x &= 228.67 - 107.177\Delta_s - 43.8661\Delta_t - 8.77302\Delta_\phi, \\ y &= -1061.39 - 694.406\Delta_s + 1612.44\Delta_t + 420.885\Delta_\phi, \\ z &= 2590.87 - 221.685\Delta_s + 2629.52\Delta_t - 10439.6\Delta_\phi. \end{aligned} \tag{B.8}$$

¹Note that there is another convention generated by the package `autoboot` [187]. Our results for scanned external OPEs are different from the `autoboot` (ab) convention by

$$\left(\lambda_{sss}^{\text{us}}, \lambda_{tts}^{\text{us}}, \lambda_{\phi\phi t}^{\text{us}}, \lambda_{\phi\phi s}^{\text{us}}, \lambda_{ttt}^{\text{us}} \right) = \left(\lambda_{sss}^{\text{ab}}, \frac{1}{\sqrt{3}}\lambda_{tts}^{\text{ab}}, \frac{1}{\sqrt{5}}\lambda_{\phi\phi t}^{\text{ab}}, \frac{1}{\sqrt{10}}\lambda_{\phi\phi s}^{\text{ab}}, \sqrt{\frac{6}{35}}\lambda_{ttt}^{\text{ab}} \right). \tag{B.7}$$

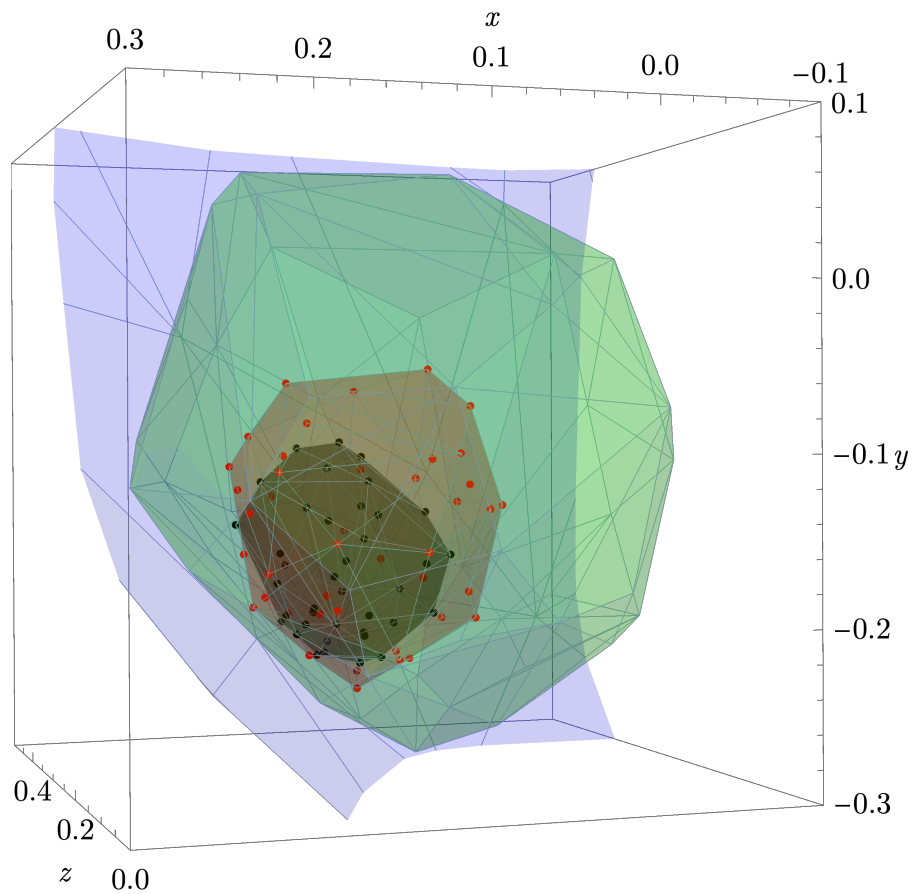


Figure B.1: The convex hulls of the allowed points in the affine space (B.8) at derivative orders $\Lambda = 19, 27, 35, 43$. The red and black data points are the allowed points at derivative orders $\Lambda = 35, 43$.

Δ_ϕ	Δ_s	Δ_t	$\frac{\lambda_{sss}}{\lambda_{\phi\phi s}}$	$\frac{\lambda_{tts}}{\lambda_{\phi\phi s}}$	$\frac{\lambda_{\phi\phi t}}{\lambda_{\phi\phi s}}$	$\frac{\lambda_{ttt}}{\lambda_{\phi\phi s}}$
0.5189783882	1.5953612741	1.2097311776	0.9658557781	1.8764272526	1.6683150562	2.8608280295
0.5189583670	1.5949959168	1.2096121876	0.9637866930	1.8759071995	1.6681321958	2.8604010933
0.5189461401	1.5949711389	1.2095536502	0.9650503920	1.8758868056	1.6680723076	2.8601976693
0.5189272852	1.5948074081	1.2094888929	0.9652812111	1.8758487781	1.6680235398	2.8603061675
0.5189613339	1.5952564268	1.2096662222	0.9662461846	1.8763712143	1.6682528867	2.8607475247
0.5189198114	1.5946719225	1.2094285955	0.9639220579	1.8755694851	1.6679344313	2.8599409571
0.5189172850	1.5946165394	1.2094312995	0.9634877179	1.8756194443	1.6679524398	2.8599835329
0.5189500473	1.5951798121	1.2096307308	0.9661780974	1.8763286685	1.6682360908	2.8607267382
0.5189649901	1.5951958587	1.2096821376	0.9647455098	1.8763265571	1.6682560921	2.8608385887
0.5189431822	1.5950799657	1.2095793546	0.9658559545	1.8761787760	1.6681550694	2.8604066434
0.5189526027	1.5949370220	1.2096034154	0.9633651701	1.8758925982	1.6681462865	2.8605568949
0.5189301757	1.5949315300	1.2095370407	0.9653175705	1.8761152596	1.6681181238	2.8605816730
0.5189168372	1.5946844827	1.2094296026	0.9642949506	1.8756631385	1.6679573604	2.8599418324
0.5189483062	1.5950509260	1.2095711164	0.9654214538	1.8760347497	1.6681115766	2.8602582414
0.5189153515	1.5946825124	1.2094352034	0.9643765341	1.8757126829	1.6679642216	2.8601068005
0.5189440155	1.5949715807	1.2095885922	0.9644538043	1.8760784038	1.6681817119	2.8607365030
0.5189150284	1.5945099455	1.2094139921	0.9622684128	1.8754680443	1.6679176085	2.8599290431
0.5189347282	1.5947841912	1.2094914029	0.9639498317	1.8756547299	1.6679896459	2.8599829650
0.5189802791	1.5952998277	1.2097251950	0.9649312284	1.8762516023	1.6682831892	2.8609105511
0.5189248611	1.5948368279	1.2094835818	0.9649249785	1.8759055628	1.6680304724	2.8600899846
0.5189306747	1.5946954535	1.2094799696	0.9630209667	1.8756016368	1.6679818979	2.8600556364
0.5189217812	1.5947698290	1.2094894198	0.9646493947	1.8759369337	1.6680732162	2.8603682382
0.5189121284	1.5945494559	1.2093932170	0.9632128469	1.8754599512	1.6678971836	2.8597295069
0.5189738261	1.5953116389	1.2096932265	0.9658322350	1.8762663003	1.6682491526	2.8606277206
0.5189145348	1.5947341024	1.2094532479	0.9650247104	1.8759430722	1.6680183536	2.8602402387
0.5189014384	1.5944048949	1.2093555400	0.9627737264	1.8753951336	1.6678520403	2.8597952050
0.5189305457	1.5947604700	1.2094652572	0.9640748832	1.8756103384	1.6679623986	2.8598809964
0.5189623990	1.5950949062	1.2096629593	0.9640070854	1.8761554772	1.6682313428	2.8608189553
0.5189460789	1.5950582403	1.2095808918	0.9654253734	1.8761261589	1.6681362224	2.8605045135
0.5189301505	1.5949452685	1.2095278745	0.9657542568	1.8760854806	1.6681017321	2.8604962327
0.5189685635	1.5953320391	1.2097096529	0.9660028358	1.8764583565	1.6683135549	2.8609575117
0.5189497511	1.5949209137	1.2095606097	0.9638109344	1.8758202300	1.6680711351	2.8601899822
0.5189337664	1.5947155621	1.2095107201	0.9623655424	1.8757184969	1.6680386790	2.8602450223
0.5189453714	1.5951023898	1.2096147301	0.9659065454	1.8763651079	1.6682206940	2.8607919521
0.5189862601	1.5954028918	1.2097515683	0.9654844905	1.8763339257	1.6683105873	2.8607881451
0.5189476979	1.5949533896	1.2096010827	0.9637175659	1.8760304271	1.6681861098	2.8606729585
0.5189346015	1.5950348003	1.2095678602	0.9659534043	1.8763062992	1.6681684361	2.8606248190
0.5189598320	1.5951484795	1.2096664021	0.9647455098	1.8763265571	1.6682560921	2.8608385887

Table B.3: Allowed points in the $\Lambda = 43$ island.

Δ_ϕ	Δ_s	Δ_T	Δ_ϕ	Δ_s	Δ_T	Δ_ϕ	Δ_s	Δ_T
0.5187966798	1.5921850401	1.2086228804	0.5189424979	1.5947703013	1.2093601723	0.5190663597	1.5958743309	1.2100957055
0.5189025751	1.5940617801	1.2092954008	0.5189661102	1.5944802637	1.2095417129	0.5190718073	1.5968585432	1.2101543103
0.5189114364	1.5946504985	1.2093872462	0.5189611442	1.5952505758	1.2096113811	0.5191015148	1.5964779979	1.2103179313
0.5189189599	1.5941920882	1.2092297471	0.5189509729	1.5951396676	1.2096608087	0.5191201873	1.5971879432	1.2103557229
0.5189289736	1.5938535802	1.2091078506	0.5189524092	1.5951856771	1.2095713650	0.5191327281	1.5966679522	1.2102157357
0.5189045881	1.5924442671	1.2084245865	0.5189561829	1.5950657026	1.2096530941	0.5192390608	1.5909575125	1.2111650118
0.5187375387	1.5921586352	1.2084312743	0.5189575751	1.5955303099	1.2096401327	0.5189384637	1.5945786868	1.2092964612
0.5187762022	1.5918820333	1.2086546005	0.5189576562	1.5952325581	1.2096851550	0.5189388374	1.5940295775	1.2094866518
0.518726937	1.5914255278	1.2085310641	0.5189595475	1.594833608	1.2097148970	0.5189406470	1.5951736959	1.2096602578
0.5188353864	1.5944222782	1.2090020249	0.5189682325	1.595196784	1.2096321472	0.5189435236	1.5946628177	1.2095079508
0.5188362222	1.5935429810	1.2089818386	0.5189696503	1.594254718	1.2094617876	0.5189501857	1.5947201370	1.2094479043
0.5188416799	1.5933781659	1.2089481869	0.5189733687	1.5940010519	1.2095786660	0.5189609300	1.5947551012	1.2095700139
0.5188478354	1.5938857812	1.2091362879	0.5189772029	1.5939593535	1.2096440413	0.5189728490	1.5955014573	1.2097394518
0.5188535669	1.5932852488	1.2088214042	0.5189800482	1.5949200496	1.2097035540	0.5189785861	1.5948000056	1.2096217602
0.5188541349	1.5932916366	1.2089652272	0.5189804744	1.5953372481	1.2097875328	0.5189943897	1.5951836165	1.2096726877
0.5188547707	1.5939362785	1.2090312421	0.5189818184	1.5960833573	1.2098711894	0.5190020000	1.5955721180	1.2098149448
0.5188571369	1.5931900946	1.2090569647	0.5189828015	1.5952764767	1.2099175729	0.5190031045	1.5956425756	1.2098237701
0.5188574085	1.5927203987	1.2089917699	0.5189871624	1.5963425034	1.20989915261	0.5190089551	1.5959677551	1.2099418222
0.5188612075	1.5939110280	1.2091455740	0.5189966010	1.596234958	1.2098589501	0.5190262023	1.5960422185	1.2100190836
0.5188615855	1.5937167137	1.2090998988	0.5190066292	1.5959897652	1.2099481084	0.5190349642	1.5958180255	1.2099716558
0.5188768144	1.5938159784	1.2090216235	0.5190086343	1.5954797940	1.2098872690	0.5190621203	1.5957337543	1.209838282
0.5188830465	1.5941282784	1.2092443533	0.5190093925	1.5948495201	1.2095311073	0.5191180161	1.5968444953	1.2103456280
0.5188846453	1.5942465723	1.2092589387	0.5190140405	1.5948232716	1.2098887955	0.5191470052	1.5962315204	1.2104571613
0.5188859294	1.5941864473	1.2092761662	0.5190158019	1.5958546312	1.2098800029	0.5191921249	1.5963777247	1.2105975545
0.5188862012	1.5941115729	1.2092259695	0.5190176624	1.5957396035	1.2099524800	0.5192666256	1.5975999519	1.2109769054
0.5188873828	1.5941321791	1.2092596161	0.5190182636	1.5959290569	1.2097197608	0.5192844446	1.5981834807	1.2109478678
0.5188874108	1.5939452740	1.2091859961	0.5190222887	1.5962382824	1.2100406599	0.5192153931	1.5971409678	1.2108619123
0.5188875107	1.5943066473	1.2093007722	0.5190234338	1.5944921267	1.2097386508	0.5190126129	1.5960328832	1.2098411820
0.5188880552	1.5943163631	1.2093081233	0.5190268914	1.5946488779	1.2099549543	0.5189965698	1.5957079384	1.2098781545
0.5188955343	1.5940849591	1.2092127567	0.5190379431	1.5958717009	1.2099655030	0.5190070117	1.5964405597	1.2102546468
0.5189058185	1.5944141764	1.2092795081	0.5190482917	1.5959334075	1.2099669689	0.5189972378	1.5954623091	1.2097288249
0.5189025610	1.5945285109	1.2093580928	0.5190584519	1.5959584074	1.2099840028	0.5190240028	1.5977739605	1.2108758412
0.5189038211	1.5943538031	1.209070892	0.5190598740	1.5957892478	1.2100080216	0.5192967458	1.5978374167	1.2109654958
0.5189054986	1.5948072619	1.2094766226	0.5190647361	1.5962663627	1.2101523145	0.5190531962	1.5957547434	1.2100253487
0.5189060888	1.5943304453	1.2093294643	0.5190652599	1.5960263900	1.2101090017	0.5190490017	1.5969430017	1.2109405017
0.5189083086	1.5946728229	1.2094131489	0.5190725277	1.5960088046	1.2100991203	0.5189939710	1.5943081218	1.2094518082
0.5189105727	1.5946766232	1.2094486445	0.5190732857	1.5962583225	1.2100744510	0.5189583814	1.5947940605	1.2094896280
0.5189114164	1.5941494552	1.2091446525	0.5190754469	1.5961544869	1.2100450000	0.5189549480	1.5948539419	1.2095000000
0.5189153608	1.5942042741	1.2092824092	0.5190839106	1.5962931060	1.2101834489	0.5189639253	1.5945186785	1.2094725381
0.5189179786	1.5948735383	1.2094980656	0.5190846538	1.5964564464	1.2101828248	0.5189636657	1.5957551038	1.2098219526
0.5189191601	1.5941295191	1.2093520548	0.5190925018	1.596592328	1.2102438238	0.5189948238	1.5948941949	1.2098519173
0.5189241090	1.5941509824	1.2094002783	0.5191014483	1.5962764902	1.2102433612	0.5189919017	1.5941900169	1.2095288310
0.5189333103	1.5939599259	1.2094523297	0.5191200121	1.5963878404	1.2104256692	0.5189979105	1.5956955072	1.2097796640
0.5189339920	1.5943501521	1.2094632463	0.5191238375	1.5961605267	1.2101530223	0.5189956657	1.5957402879	1.2109458216
0.5189346097	1.5944851028	1.2095740716	0.5191427139	1.5977670021	1.2106878967	0.5190123754	1.5941402932	1.2095300773
0.5189379786	1.5944279251	1.2093909591	0.5191466549	1.5971361619	1.2105308642	0.5190157406	1.5958569876	1.2099200545
0.5189403629	1.5926407786	1.2091965625	0.5191695884	1.5970766016	1.2106599584	0.5190278431	1.5958918751	1.2100251015
0.5189419788	1.5940503654	1.2091664050	0.5191747564	1.5961581015	1.2104165938	0.5190325131	1.5959081051	1.2099969538
0.5189448544	1.5939659673	1.2093669005	0.5191752118	1.5973309222	1.2104867529	0.5190520384	1.5963152404	1.2100841277
0.5189453134	1.5945586909	1.2094861573	0.5191772163	1.597425702	1.2107843442	0.5190586609	1.5969509826	1.2099085486
0.5189469431	1.5938359757	1.2091138392	0.5191984066	1.5976763974	1.2108343370	0.5190715439	1.5959012797	1.2101497826
0.5189471783	1.5931200581	1.2091539461	0.5192110760	1.5974046747	1.2105784428	0.5190826625	1.5965090465	1.2102403519
0.5189471553	1.5940468208	1.2092711976	0.5192315872	1.5976397828	1.2109134929	0.5191170800	1.5974916154	1.2105045310
0.5189236080	1.593067503	1.2087833097	0.5192577054	1.5985002420	1.2110002270	0.5191778676	1.5977308111	1.2107843923
0.5189236880	1.5929291631	1.2086556537	0.5192699179	1.5978096662	1.2108726994	0.5192844980	1.5971285489	1.2107746440
0.5189254081	1.5938577238	1.2089727162	0.5192751871	1.5986516951	1.2111692313	0.5192666651	1.5983714488	1.2105056823
0.5189270708	1.5920193042	1.2085475222	0.5193182009	1.5988546582	1.2112832624	0.5192812420	1.5987160882	1.21111101581
0.5189286720	1.5940780889	1.2092200213	0.5193313955	1.5984303599	1.211533312	0.519340795	1.5983604551	1.2112010479
0.5189375787	1.5938867482	1.2091282102	0.5193414850	1.598641969	1.211569121	0.5189685870	1.5947403353	1.2095546973
0.51893791085	1.5938475441	1.2092269843	0.5193551883	1.5998541317	1.2115607995	0.5189469362	1.5948003211	1.2094569806
0.51893860122	1.5944086593	1.2093181142	0.5193481340	1.5991038253	1.2114973155	0.5190080327	1.5999140301	1.2106738444
0.51893881256	1.5943425103	1.2092606077	0.5193498892	1.5989679837	1.2114217221	0.5190853457	1.5968203648	1.2103356646
0.5189396192	1.5944000610	1.2093369626	0.5190798632	1.5964346557	1.2102066791	0.5189402432	1.5947339426	1.2095132572
0.5189399836	1.5944714851	1.2093479909	0.5189741917	1.5958585985	1.2097697715	0.5189866072	1.5952602047	1.2097386641
0.5189402967	1.5942907732	1.2093450874	0.5189927891	1.5951952177	1.2097327291	0.5189466850	1.5949712041	1.2095429276
0.5189406160	1.5944245329	1.2093054811	0.5189996154	1.5950788378	1.2097054113	0.5189977338	1.5955819151	1.2098187686
0.5189130711	1.5943416289	1.2092938887	0.5190167890	1.595602397	1.2098873787	0.5189417109	1.5948151822	1.2095116242
0.5189282439	1.5948669505	1.2094354495	0.5190038122	1.5949189011	1.2096389844	0.5189887395	1.5955311410	1.209798738
0.5189381636	1.5945869176	1.2095373290	0.5190339170	1.5955996031	1.2098749137	0.5189905152	1.5954860043	1.2097574571
0.518920952	1.5946145223	1.2093971626	0.519041371	1.5962115376	1.2100881124	0.5189868037	1.5944541540	1.2096312400
0.5189252255	1.5932931016	1.2088647649	0.5191177942	1.5966893312	1.2103147962	0.5189664963	1.5953900793	1.209788870
0.5189378367	1.5937600844	1.2090049206	0.5190979149	1.598977149	1.2110282728	0.5189404136	1.5944739467	1.2093498390
0.5189044036	1.5938713707	1.2092753786	0.5192965929	1.598599729	1.2109290808	0.5189471051	1.596143706	1.2096143706
0.5189335453	1.5923524886	1.2088551025	0.5193036599	1.5986614215	1.2113279731	0.5189476015	1.5951048660	1.209587135
0.518928340	1.592538527	1.2086181825	0.5192445691	1.5971357017	1.2106354701	0.5189924665	1.5947319121	1.2095257880
0.5188672706	1.5938569690	1.2091784902	0.5189651690	1.595181240	1.209518338	0.5189758138	1.5951104102	1.2097131902
0.5189271453	1.5939744974	1.2092114019	0.5191751265	1.5980350400	1.2107387866	0.5189281878	1.5946813688	1.209496850
0.5189815521	1.5940429270							

Appendix C

APPENDICES OF CHAPTER 4

C.1 Infinite MPS

In the main text, we define a Matrix Product State on a finite number of sites with open boundary conditions. To represent the true and false vacua of a spin chain, we use infinite MPS (iMPS), in which the number of sites $\rightarrow \infty$

$$|\psi\rangle = \sum_{\{s\}} v_L^\dagger \dots A_{-1}^{(s_{-1})} A_0^{(s_0)} A_1^{(s_1)} \dots v_R |\dots s_{-1} s_0 s_1 \dots\rangle, \quad (\text{C.1})$$

where $A_j^{(s)}$ is a $D_{j-1} \times D_j$ matrix assigned to site j in basis-state s and v_L and v_R are appropriately-sized boundary vectors. In a *uniform* (translation invariant) iMPS, we use the same tensor A everywhere: $A_j^{(s)} = A^{(s)} \forall j \in \mathbb{Z}$. Such a state has a well defined norm for generic choices of v_L and v_R if the $D^2 \times D^2$ "transfer matrix"

$$\begin{array}{c} \boxed{A} \\ \text{---} \\ \boxed{A^*} \end{array} = \sum_s A^{(s)} \otimes A^{(s)*}, \quad (\text{C.2})$$

where $*$ indicates the complex conjugate has a nondegenerate eigenvalue of largest magnitude, with A normalized so that this eigenvalue is equal to 1 [232]. This condition implies exponential decay of correlations with distance. By additionally normalizing v_L and v_R appropriately, we can achieve $\langle \psi | \psi \rangle = 1$. The precise choice of boundary vectors does not affect bulk expectation values due to the aforementioned exponential decay of correlators.

Nonuniform windows

To build the bubble states of the main text, and to simulate their evolution in time, we allow the tensors of an otherwise uniform iMPS to vary within a "window", consisting of N contiguous sites. These states have the form

$$|\psi\rangle = \sum_{\{s\}} |\dots s_1 \dots s_N \dots\rangle \times v_L^\dagger \left(\prod_{i=-\infty}^0 A_L^{(s_i)} \right) A_1^{(s_1)} \dots A_N^{(s_N)} \left(\prod_{j=N+1}^{\infty} A_R^{(s_j)} \right) v_R, \quad (\text{C.3})$$

where A_L and A_R parameterize the semi-infinite left and right bulk parts of the chain and $A_1 \dots A_N$ parameterize the nonuniform window. The above transfer-matrix conditions for a well-defined uniform iMPS must be satisfied for both the

A_L and A_R tensors. The norm of the state is then determined by the content of the window tensors $A_1 \dots A_N$. For the bubble states, we let $A_L = A_R = \text{blue square}$, where blue square is the tensor optimized for the uniform ground state (true vacuum) of the spin chain. We then choose $A_1 \dots A_N$ to represent a false-vacuum bubble, as described below in App. C.3. For example, a fully localized bubble state (the kink-antikink state of Fig. 4.4) has $A_1 = \text{blue square with arrow}$ (representing a kink), $A_2 \dots A_{N-1} = \text{red square}$ (representing the false vacuum), and $A_N = \text{blue square with arrow}$ (representing the antikink).

C.2 Finding the true and false vacua

Finding the true vacuum

The tensor A defining a uniform iMPS (C.1) can be optimized to represent low-energy, translation-invariant states of gapped quantum spin chains using various algorithms. We use the nonlinear conjugate-gradient method described in [205] and implemented in the *evoMPS* package [262] to find a uniform iMPS that approximately describe the ground states of gapped quantum spin chains. We denote the optimized iMPS tensor blue square .

Finding the false vacuum

We explain how we obtain an iMPS representation of the false vacuum in practice in App. C.2 below. In this section, we consider the nature of the false vacuum more generally.

For the broken \mathbb{Z}_2 symmetry of the Ising-like chain in the main text, the false vacuum $|\bar{\Omega}\rangle$ is a state that has opposite spin orientation to the true vacuum $|\Omega\rangle$. It should also be *like* a vacuum, in that it should be a spatially uniform, approximately static state near a local energetic minimum with respect to some constraint, such as locality.

A candidate state is the "flipped" vacuum

$$\left(\prod_j X_j \right) |\Omega\rangle. \quad (\text{C.4})$$

It is spatially uniform and typically close to an energetic minimum in the following sense: If we apply a finite string $\prod_{j=1}^L X_j$ of length L , the change in energy will be *positive* for small values of L , becoming negative only after the $O(2hL)$ energy lost by replacing false vacuum with true vacuum on L sites is larger than the $O(1)$ energy penalty of spin anti-alignment at the boundaries. However, the flipped vacuum is generally *not* close to being an eigenstate in case of a nonzero symmetry-breaking field parameter h and therefore is not suitably static. Nevertheless, one might begin

with the flipped vacuum and attempt to bring it closer to a false-vacuum eigenstate by lowering the energy, for example via imaginary time evolution:

$$|\bar{\Omega}\rangle = e^{-\tau H} \left(\prod_j X_j \right) |\Omega\rangle. \quad (\text{C.5})$$

A problem with this approach is that, since we are not in a true energetic minimum, imaginary time evolution will ultimately take us back to the *true* vacuum $|\Omega\rangle$. At finite system sizes, this corresponds to a nonzero inner product between the flipped vacuum and the vacuum. Let us consider the \mathbb{Z}_2 -broken Ising Hamiltonian ($\lambda = 0$, $h > 0$) at finite system size N . Although in our simulations we work directly in the thermodynamic limit $N \rightarrow \infty$ using iMPS, finite N is more convenient for the following calculation. We will see that the key result is independent of N . If we perturb around the bare theory of $g = 0$, we find

$$\langle \Omega | \left(\prod_j X_j \right) | \Omega \rangle = 0 + \mathcal{O}(g^N), \quad (\text{C.6})$$

where $g \ll 1$. Overlaps $\langle E_i | \left(\prod_j X_j \right) | \Omega \rangle$ with energy eigenstates $|E_i\rangle$ that are close to the true vacuum (e.g. low-energy excitations) are also exponentially suppressed.

A simplified model allows us to estimate the timescale for "decay" to the true vacuum under imaginary time evolution. Take $|\psi\rangle := \psi_\Omega |\Omega\rangle + \sum_i \psi_i |\bar{E}_i\rangle$, where $\langle \psi | \psi \rangle = 1$ and $|\bar{E}_i\rangle$ represents an eigenstate in the false-vacuum "sector", i.e. with a flipped spin orientation versus $|\Omega\rangle$. This will be our model for the flipped vacuum $\left(\prod_j X_j \right) |\Omega\rangle$. From our perturbative calculation, we take $|\psi_\Omega| \approx g^N$, so that $\sum_i |\psi_i|^2 \approx 1 - g^{2N}$. Imaginary-time evolution give us

$$e^{-\tau H} |\psi\rangle = e^{-\tau E_\Omega} \psi_\Omega |\Omega\rangle + \sum_i e^{-\tau \bar{E}_i} \psi_i |\bar{E}_i\rangle. \quad (\text{C.7})$$

Now we take $\bar{E}_i - E_\Omega \sim 2Nh$, since $|\bar{E}_i\rangle$ are flipped states which suffer an extensive energy penalty compared to $|\Omega\rangle$. The relative contribution of the vacuum after a time τ is then

$$g^N e^{\tau 2Nh}, \quad (\text{C.8})$$

which goes to 1 at τ_Ω , independently of N :

$$\tau_\Omega = -\frac{1}{2h} \log g. \quad (\text{C.9})$$

Hence, for small h , one must evolve for a "long" time to see a significant vacuum contribution. For sufficiently large τ still satisfying $\tau \ll \tau_\Omega$, assuming initial occupancy and energetic separation of the $|\bar{E}_0\rangle$ state, we end up with:

$$e^{-\tau H}|\psi\rangle \approx e^{-\tau E_\Omega}\psi_\Omega|\Omega\rangle + e^{-\tau \bar{E}_0}\psi_0|\bar{E}_0\rangle, \quad (\text{C.10})$$

where $|\bar{E}_0\rangle$ is a hypothetical lowest-energy contribution from the false-vacuum "sector". This picture is supported by numerical observations in which performing some imaginary-time evolution on $(\prod_j X_j)|\Omega\rangle$ quickly results in something that is (numerically) approximately an eigenstate.

Finding an iMPS for the false vacuum

To find an iMPS for the false vacuum, we begin with an iMPS approximation of the *flipped vacuum* (C.4), obtained from the iMPS approximation of the true vacuum. Instead of using imaginary time evolution to reduce the energy of this state, as considered in the previous section, we use the same conjugate-gradient optimization method used to find the true vacuum [262]. Like imaginary time evolution, such variational methods should eventually take the flipped state to the true vacuum state. In practice, however, we observe that for small symmetry-breaking fields $|h| \ll 1$ this does not happen. Instead, the state converges to a false-vacuum iMPS (parameterized by a tensor we denote \blacksquare) that is numerically indistinguishable from an energy eigenstate. This may be because of the limited available numerical precision¹, which could preclude accurate representation of the gradient components that would lead to the true vacuum.

C.3 MPS quasiparticle states

We use a Bloch-state approach to represent low-energy excitations [233, 257, 258]. A localized quasiparticle state is constructed from vacuum tensors A_L and A_R , which remain constant, together with an "excitation tensor" B that can be chosen to represent different excitations:

$$|\phi_j(A_L, B, A_R)\rangle := \sum_{\vec{s}} v_L^\dagger \left(\prod_{i=-\infty}^{j-1} A_L^{s_i} \right) B^{s_j} \left(\prod_{k=j+1}^{\infty} A_R^{s_k} \right) v_R |\vec{s}\rangle. \quad (\text{C.11})$$

This ansatz can represent topological excitations, in case A_L and A_R refer to different vacua, as well as nontopological excitations, in case A_L and A_R represent the same

¹We use a double-precision floating-point representation, although the effective precision may be lower due to inversion of small Schmidt coefficients [261].

vacuum state. We use the symbol ϕ to denote a generic excitation, and κ , $\bar{\kappa}$, or μ to refer to kinks, antikinks, or mesons specifically. For example, the kink states $|\kappa_j\rangle$ of the main text have $A_L = \text{blue square with arrow}$, $B = \text{blue square with arrow and cross}$ and $A_R = \text{red square with arrow}$, while the meson states $|\mu_j\rangle$ have $A_L = \text{blue square with arrow}$, $B = \text{blue square with arrow and cross}$ and $A_R = \text{blue square with arrow}$. For tensor-network diagrams showing the parts of the tensor networks surrounding B (for $|\kappa_j\rangle$ and $|\mu_j\rangle$) see Fig. 4.4. Due to exponential decay of correlations in the vacua represented by A_L and A_R , the tensor B represents a *quasilocal* excitation and may affect expectation values across many lattice sites. In the following, we assume for simplicity that the MPS $|\phi_j\rangle$ have uniform bond dimension D .

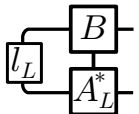
Momentum eigenstates can be constructed as Fourier modes of the spatially localized excitations:

$$|\phi(A_L, B, A_R, p)\rangle := \sum_j e^{ipj} |\phi_j(A_L, B, A_R)\rangle. \quad (\text{C.12})$$

These momentum eigenstates enjoy a "gauge" freedom (parameter redundancy): the B tensor may be transformed as

$$B^s \rightarrow B^s + A_L^s x - e^{-ip} x A_R^s, \quad (\text{C.13})$$

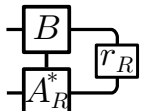
where x is a $D \times D$ matrix, without affecting the Fourier mode $|\phi(A_L, B, A_R, p)\rangle$. This freedom can be fixed in many ways. For example, the "left orthogonality"² conditions [257, 272] are

$$\langle l_L | \left(\sum_s B^{(s)} \otimes A_L^{(s)*} \right) = 0, \quad (\text{C.14})$$


where $\langle l_L |$ is the dominant left eigenvector of the MPS transfer matrix of the left uniform bulk:

$$\langle l_L | \left(\sum_s A_L^{(s)} \otimes A_L^{(s)*} \right) = \langle l_L |. \quad (\text{C.15})$$

Similarly, the "right orthogonality" conditions are

$$\left(\sum_s B^{(s)} \otimes A_R^{(s)*} \right) |r_R\rangle = 0, \quad (\text{C.16})$$


where $|r_R\rangle$ is the dominant right eigenvector of the MPS transfer matrix of the right uniform bulk:

$$\left(\sum_s A_R^{(s)} \otimes A_R^{(s)*} \right) |r_R\rangle = |r_R\rangle. \quad (\text{C.17})$$

²Called "left gauge-fixing" in [257].

These conditions can be achieved for any initial tensor B by transforming it with an appropriate choice of x in (C.13). Imposing either the left or right conditions, (C.14) or (C.16), implies orthogonality of the position states: $\langle \phi_j(A_L, B, A_R) | \phi_k(A_L, B, A_R) \rangle = \delta_{jk}$. This is particularly convenient for working with the momentum eigenstates, as it greatly simplifies the computation of their inner products and expectation values [257].

Optimizing the excitation tensor B

To find a tensor B that accurately represents a *particular* quasiparticle excitation, we use the methods of [257] with some modifications for dealing with the case in which one of A_L and A_R represents a *false* vacuum (with a different energy density compared to the true vacuum). The basic idea is to project the Hamiltonian onto the ansatz space of momentum eigenstates $|\phi(A_L, B, A_R, p)\rangle$, resulting in an effective Hamiltonian for the tensor B that can be solved using a standard sparse eigenvalue solver.

Note that, since $\langle \phi(A_L, B, A_R, p) | \phi(A_L, B, A_R, p') \rangle = \delta(p - p')$, it is natural to do this for a particular, chosen value of p . By solving for multiple eigenvalue-eigenvector pairs, a set of orthogonal tensors $B^{(a)}$ (the eigenvectors) can be found that accurately approximate several different low-energy excitations (labeled by the index a), as long as they are all below the two-particle threshold [258]. The eigenvalues are the energies of these excitations. By computing them for a range of p , one can obtain an approximate dispersion relation $E(p)$ for the quasiparticles in the system.

Importantly, not only the energies, but also the optimized tensors $B^{(a)}(p)$, and hence the position states $|\phi_j(B)\rangle$, generally depend nontrivially on the value of p . This is illustrated in Fig. C.3, which shows the error made in using a tensor $B^{(0)}(p = 0)$ optimized for $p = 0$, to represent the lowest-lying excitations at other momenta.

Broken symmetry and kinks

In the presence of explicit symmetry breaking ($h \neq 0$), *topological excitations* such as kinks and antikinks involve the false vacuum. The energy of a localized kink (or antikink) depends on its position, since different positions lead to different extensive contributions from the false vacuum³. As such, there are no energy-momentum

³In an infinite system, as considered here, all kinks have *infinite* energy with respect to the vacuum. However, the energy difference between two kinks is finite when their positions differ by a finite amount.

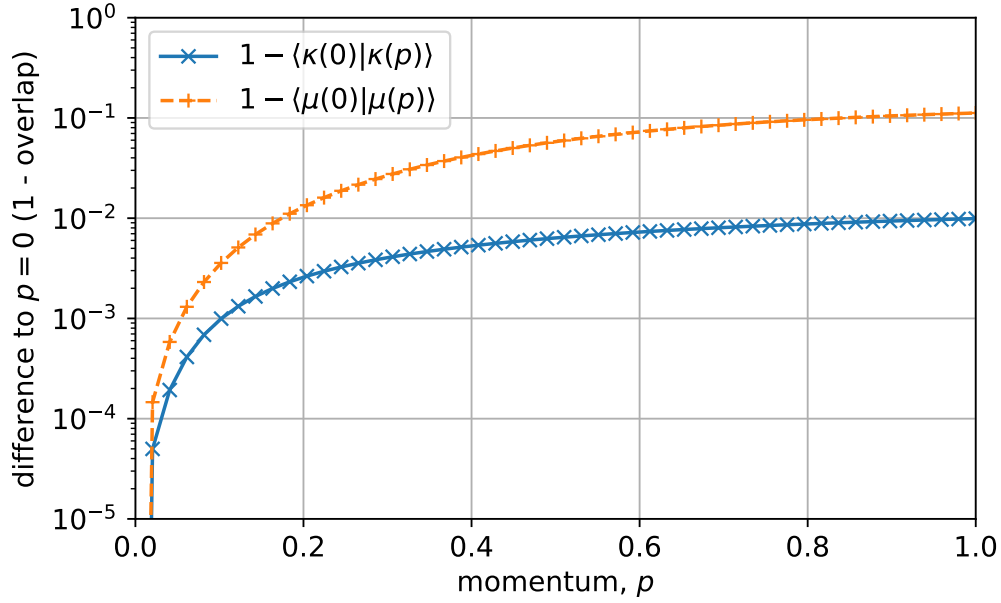
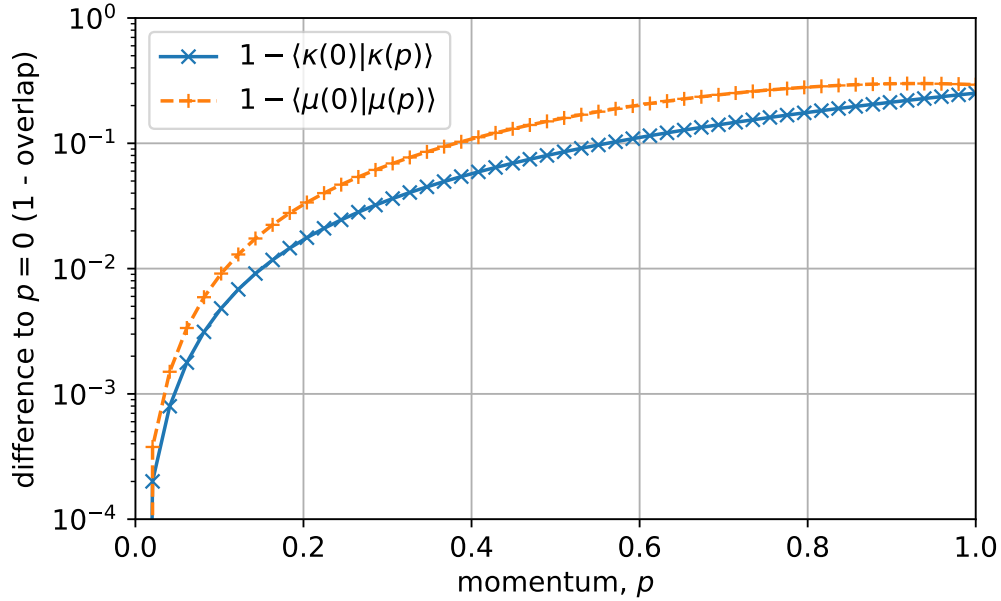
(i) Ising: $g = 0.8, h = 0.007$ (ii) near TCI: $\lambda = 0.41, g = 0.98, h = 0.001$ 

Figure C.1: Error made $(1 - \langle \phi_j(B) | \phi_j(B(p)) \rangle)$ in ignoring the momentum dependence of the tensor B used to construct MPS quasiparticle states, for both kink and meson excitations, for the Hamiltonian parameters used in simulations (i) and (ii) of the main text. The momentum-eigenstate freedom on $B(p)$ is fixed so that $\langle \phi_j(B) | \phi_k(B') \rangle = \delta_{jk}$.

eigenstates (of the Hamiltonian and momentum operators) corresponding to these excitations and we cannot find them by solving the effective Hamiltonian for the B tensors considered above. Nevertheless, we expect there to be excitations that behave as quasiparticles subject to a confining force (which makes them accelerate). If one could somehow negate the confining force, as if by accelerating at the same rate as the quasiparticle, the latter would appear to propagate freely.

With this picture in mind, we define a modified energy function

$$\tilde{E} = \sum_{jk} e^{ip(k-j)} \langle \phi_j | (H - \Delta E_j \mathbb{1}) | \phi_k \rangle, \quad (\text{C.18})$$

where $\Delta E_j := \sum_{-\infty}^j e_L + \sum_{j+1}^{\infty} e_R$ and e_L, e_R are the energy densities of the vacua parameterized by A_L and A_R , respectively. Here, it is assumed that the momentum-eigenstate gauge-freedom on B , (C.13), has been fixed so that $\langle \phi_j | \phi_k \rangle = \delta_{jk}$. With orthogonality of the position states, the identity term simply shifts the energy of the excitation in a position-dependent way, cancelling the position-dependent contribution due to the differing bulk energy densities. One can also write down a modified Hamiltonian

$$\tilde{H} = H - \sum_j P_j \Delta E_j, \quad (\text{C.19})$$

where P_j is a projector onto the space of states spanned by $|\phi_j(B)\rangle$ for all B satisfying the chosen orthogonality conditions: for such B , we thus have $P_j |\phi_k(B)\rangle = \delta_{jk} |\phi_k(B)\rangle$. We can then rewrite \tilde{E} as

$$\tilde{E} = \langle \phi(A_L, B, A_R, p) | \tilde{H} | \phi(A_L, B, A_R, p) \rangle. \quad (\text{C.20})$$

We can thus optimize B by computing eigenvalue-eigenvector pairs of \tilde{H} , after pushing it into the ansatz space, analogously to the symmetric case above.

In this formulation it is manifest that the optimization procedure *depends on the conditions used to achieve position-state orthogonality*, since different conditions will lead to different P_j in (C.19). In practice, we find that the difference this makes to the resulting optimized states $|\phi(A_L, B, A_R, p)\rangle$ is small: We consider the infidelity per site

$$\begin{aligned} 1 - |\mathbb{Z}|^{-1} |\langle \phi(B_{LF}, p) | \phi(B_{RF}, p) \rangle| = \\ 1 - |\langle \phi_j(B_{LF}) | \phi(B_{RF}, p) \rangle|, \end{aligned} \quad (\text{C.21})$$

where B_{LF} and B_{RF} are optimized for the same quasiparticle (and momentum p) using the *left* and *right* orthogonality conditions, (C.14) and (C.16), respectively,

and $|\mathbb{Z}|$ is the cardinality of the integers (accounting for the infinite norm of the momentum eigenstates). We find empirically the infidelity scales as h^2 , where $h \ll 1$ is the symmetry-breaking parameter of the Hamiltonian, for the lowest-energy kink states and the Hamiltonian parameters considered in this paper. This dependence is shown in Fig. C.2.

It may be possible to design improved optimization techniques that avoid this ambiguity. A prerequisite would be a cost function other than $\langle \tilde{H} \rangle$, presumably related to the stability of the quasiparticle wavepackets, that distinguishes usefully between the different choices that can be made in parameterizing B .

Another important observation is that, in (C.19), we assume that the location j of the B tensor reliably indicates the position of the kink (or antikink). In fact, since the excitation described by B is *quasilocal*, the location of the kink (defined as the point in space at which the spin expectation value crosses zero) may differ from j . Indeed, as shown below in Fig. C.3, there may be a relative shift of several lattice sites, depending on the choice of left or right orthogonality conditions on B . The shift will generally also depend on the momentum p , such that a dispersion relation $E(p)$ computed from the eigenvalues of \tilde{H} should really be interpreted as a function of the B -tensor momentum, derived from the position j of B , considered distinct from the kink momentum, derived from the kink position.

The momentum-dependent energy-shift due to these position shifts can be calculated by first computing the actual kink positions, relative to j , for each $|\phi_j(p)\rangle$, as a function of p . These shifts can then be multiplied by the false-vacuum excess energy density to compute the energy shift, which can in turn be used to "correct" the dispersion relation. This provides a more intuitive definition of the kink dispersion in the symmetry-broken setting. Note also, however, that since kink quasiparticles do not have a well-defined energy gap with respect to the vacuum state, these dispersion relations still cannot be used to compute particle-production thresholds. They could, however, be used to estimate the kink velocity $dE(p)/dp$, this being independent of energy shifts $E(p) \rightarrow E(p) + c$.

Wavepackets

Analogously to the momentum eigenstates of (C.12), we can construct wavepackets from the localized quasiparticle states as

$$|\phi(A_L, B, A_R, f)\rangle := \sum_i f_i |\phi_i(A_L, B, A_R)\rangle, \quad (\text{C.22})$$

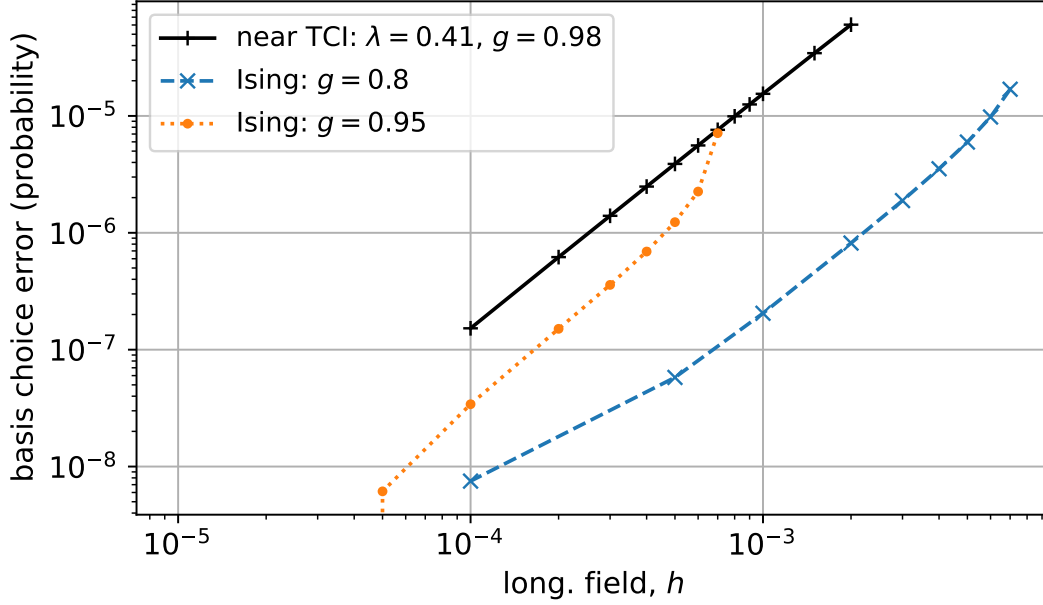


Figure C.2: Estimated error (1 - infidelity per site) on momentum eigenstates $|\phi(B, p)\rangle$ for kink quasiparticles, due to the choice of orthogonality conditions on B used to achieve $\langle \phi_j(B) | \phi_k(B) \rangle = \delta_{jk}$. Here we compare the left and right orthogonality conditions, (C.14) and (C.16).

where in our simulations we choose f_i to be a Gaussian centered at position x with width σ . Importantly for our purposes, it is straightforward to turn such a wavepacket state into a *single* MPS:

$$|\phi(A_L, B, A_R, f)\rangle = \sum_{\vec{s}} w_L^\dagger \left(\prod_{i=-\infty}^{\infty} A_i^{s_i} \right) w_R |\vec{s}\rangle, \quad (\text{C.23})$$

where

$$A_i^s := \begin{pmatrix} A_L^s & f_i B^s \\ 0 & A_R^s \end{pmatrix} \quad (\text{C.24})$$

is a $2D \times 2D$ matrix, given that A_L^s , A_R^s , and B^s are all $D \times D$ matrices. We set the boundary conditions to be

$$\begin{aligned} w_L^\dagger &:= (v_L^\dagger, 0) \\ w_R &:= \begin{pmatrix} 0 \\ v_R \end{pmatrix} \end{aligned} \quad (\text{C.25})$$

for some generic choice of v_L and v_R . If $|f_i|$ falls below some numerical threshold for all i less than some i_L and for all i greater than some $i_R > i_L$, we can truncate it to zero and reduce the bond dimension to D in those regions without introducing significant

errors. This allows us to represent a truncated wavepacket in the thermodynamic limit using the nonuniform window ansatz (C.3).

As discussed in the main text, this wavepacket construction *ignores* any momentum dependence of the tensor B . While this introduces errors in the form of contributions from other excitations, as shown in Fig. C.3, these become small for large σ , as indicated in Fig. C.5 below.

Localized states and Bloch-state parameter redundancy

The parameter redundancy, or "gauge freedom", on the B -tensors of the momentum eigenstates (C.12) *does not* leave the localized states $|\phi_j(B)\rangle$ of (C.11) unchanged. These states, as well as the wavepacket states (C.22) built from them, depend on how these degrees of freedom are fixed. However, the procedure we use for choosing optimal B tensors is based on momentum eigenstates and does not tell us how to optimally fix the remaining freedom.

That said, the impact of this choice on Gaussian wavepacket states must vanish in the limit $\sigma \rightarrow \infty$, where packets become momentum eigenstates. Hence we can reasonably expect the impact on wavepackets with finite width to become small as σ increases. Since we already have a physical reason to choose broad wavepackets in our simulations (for slow wavepacket spread), this issue is not as severe as it may at first appear.

Nevertheless, we choose to use the *reflection-symmetric* conditions of [237], slightly adapted for the topologically nontrivial setting, to fix the remaining freedom on the B tensors used to construct our initial bubble states. To be precise, we fix B by choosing x in (C.13) as

$$x = \arg \min_{x'} \left(\left| \sum_s B(x')^{(s)} \otimes A_L^{(s)*} \right|^2 + \left| \sum_s B(x')^{(s)} \otimes A_R^{(s)*} \right|^2 \right). \quad (\text{C.26})$$

In terms of tensor networks, we can rewrite this as

$$x = \arg \min_{x'} \left(\left| \begin{array}{c} \boxed{B(x')} \\ \boxed{A_L^*} \end{array} \right|^2 + \left| \begin{array}{c} \boxed{B(x')} \\ \boxed{A_R^*} \end{array} \right|^2 \right). \quad (\text{C.27})$$

Unlike the left and right orthogonality conditions, (C.14) and (C.16), these conditions are manifestly symmetric under spatial reflections. The reflection-symmetric

conditions can be formulated as an overdetermined linear-least-squares optimization problem and then solved using standard techniques.

See Fig. C.3 for a comparison of the reflection-symmetric conditions to the left and right orthogonality conditions, in terms of the spin expectation values of localized topological states. We plot these results for A_L and A_R representing the two vacua of the Ising chain ($\lambda = 0$, $g = 0.8$) for both zero and nonzero longitudinal field strength h . The tensor B is variationally optimized, as described above, so that the momentum eigenstate $|\phi(A_L, B, A_R, p = 0)\rangle$ approximates the lowest-lying topological excitation. We note that, although the symmetrized states exhibit "smoother" spin expectation values in both cases, they are not perfectly symmetric in the case $h > 0$. The spatial asymmetry in the spin likely reflects the energetic asymmetry of topological states in this case. In both cases, there is certainly an aesthetic improvement to be had by imposing the symmetrization conditions, but it remains to be seen whether the symmetrized states are better representations of localized quasiparticles. To see that they are, we consider how well wavepackets built from them fit into the corresponding quasiparticle subspace.

In Fig. C.5, we plot the portion of a kink wavepacket state (by probability) outside of the targeted kink-quasiparticle subspace for both the orthogonal and reflection-symmetric conditions. We explain how to carry out this kind of projection in App. C.4. We observe that the symmetrized states result in a much more accurate wavepacket than the orthonormal states, by almost two orders of magnitude, confirming that the symmetrized choices are more than just aesthetically pleasing. In the symmetric Ising model ($h = 0$), we can also compare the energy of wavepackets. In Fig. C.4, we see that the kink wavepackets created with the symmetrized states have consistently lower energy, which indicates improved accuracy, since we are targeting the lowest-lying kink quasiparticle.

Two-particle states

To create false-vacuum bubbles, we need to combine two quasiparticles, namely a kink and an antikink. Two-particle states have the form

$$|\phi\phi_{jk}(A_L, B_L, A_C, B_R, A_R)\rangle := \sum_{\vec{s}} |\vec{s}\rangle \times v_L^\dagger \left(\prod_{i=-\infty}^{j-1} A_L^{s_i} \right) B_L^{s_j} \left(\prod_{l=i+1}^{k-1} A_C^{s_l} \right) B_R^{s_k} \left(\prod_{m=l+1}^{\infty} A_R^{s_m} \right) v_R, \quad (\text{C.28})$$

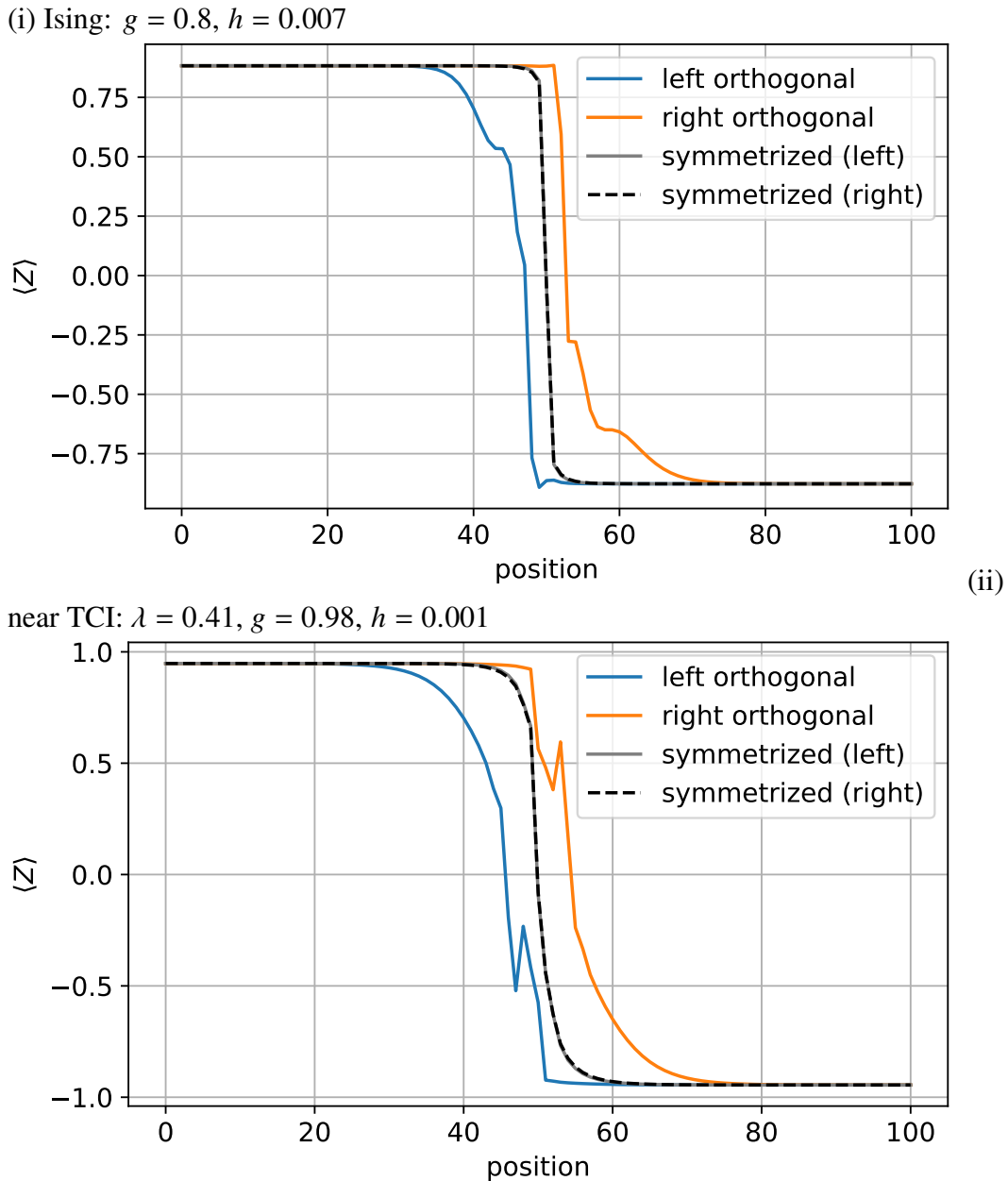


Figure C.3: Spin expectation values of a kink position MPS $|\kappa_j\rangle$ for (i) the Ising model and (ii) close to the Tri-Critical-Ising (TCI) point. The bond dimension is $D = 8$ for the Ising data, and $D = 18$ for the TCI data. We plot the spins for various ways of fixing the momentum-eigenstate freedom: the left and right orthogonal conditions, (C.14) or (C.16), and the reflection-symmetric conditions (C.26), beginning from a B tensor optimized using either the left or right conditions (since this makes a small *physical* difference to the result – see App. C.3).

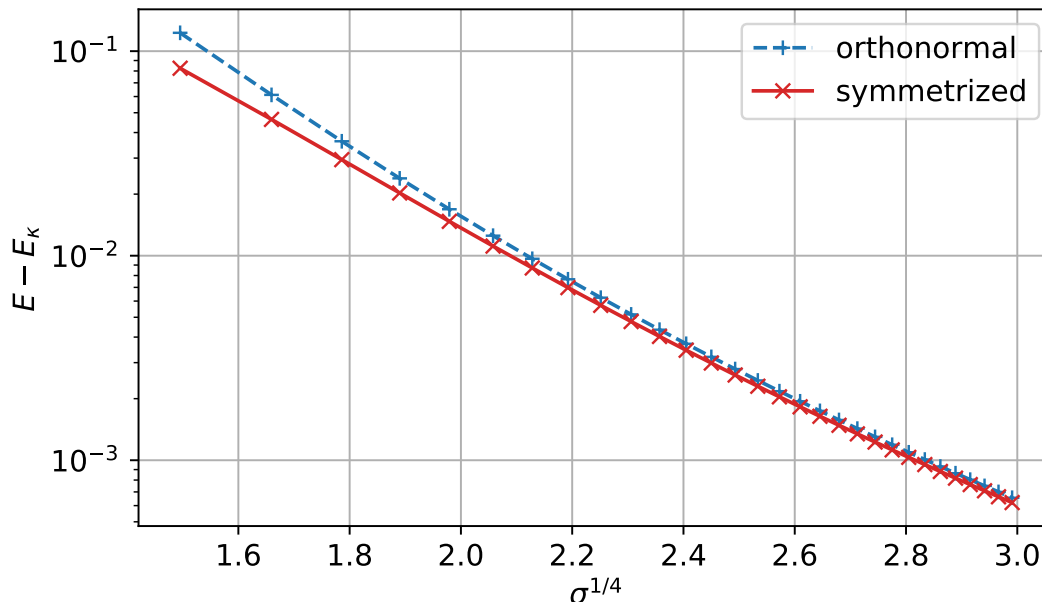


Figure C.4: Single-kink wavepacket energy as a function of the width σ , for the \mathbb{Z}_2 -symmetric Ising model $g = 0.8, \lambda = 0, h = 0$ (in the SSB phase). We plot the energy (relative to the energy of the kink-quasiparticle momentum eigenstate) for two different ways of fixing the momentum-eigenstate freedom on the B tensors used to construct the wavepacket state: an orthogonal choice $\langle \kappa_j | \kappa_k \rangle = \delta_{jk}$ (left and right conditions are equivalent when $h = 0$) and the reflection-symmetrized choice (C.26). In both cases the MPS tensors used to construct the state are tuned to the wavepacket momentum $p = 0$.

where, compared to (C.11), we now have a central (false) vacuum tensor A_C , as well as two excitation tensors, B_L and B_R , instead of one. Analogously to the one-particle states, we use $\phi\phi$ to denote a generic pair of quasiparticles, specifying $\kappa\bar{\kappa}$ or $\mu\mu$ when we are discussing a kink-antikink pair or a meson pair specifically. Such states are illustrated in Fig. 4.4. We will assume that the quasiparticles are sufficiently well separated, so that interactions may be neglected and B_L and B_R can be held constant irrespective of the separation $d := k - j$. A sufficient condition for this to be justified, is that the reduced state for sites i in between the two excitations $j < i < k$ reverts to that of the central vacuum MPS parameterized by A_C for some range of i . If this happens for the reduced state on at least r contiguous sites, where r is the range of interactions in the Hamiltonian (for our model, $r = 2$ when $\lambda = 0$ and $r = 3$ otherwise), this implies that the energy of the two-particle state, as a function of the separation d , is not affected by interaction between the particles at that location (only by differences in the "vacuum" energies). This means there can be no interaction energy.

many times as is necessary to reach site i from the position of B_L . Similarly, for the right environment we define

$$\epsilon_R(i) := \left| \dots \begin{array}{ccc} \boxed{A_C} & \boxed{A_C} & \boxed{B_R} \\ \boxed{A_C^*} & \boxed{A_C^*} & \boxed{B_R^*} \end{array} \begin{array}{c} \text{---} \\ \text{---} \\ \text{---} \\ \text{---} \end{array} \boxed{r_R} - \boxed{r_C} \right|. \quad (\text{C.30})$$

We define the magnitude of interaction effects at separation d to be

$$\epsilon(d) := \min_{j < i < k} (\epsilon_L(i) + \epsilon_R(i)). \quad (\text{C.31})$$

This value is plotted, for the Hamiltonian parameters (ii) of the main text, in Fig. C.7 for a selection of low-energy quasiparticles.

Wavepackets can be constructed from the two-particle position states (C.28) analogously to the single-particle case (C.22):

$$\begin{aligned} |\phi\phi(A_L, B_L, A_C, B_R, A_R, f, g)\rangle := \\ \sum_{j < k} f_j g_k |\phi\phi_{jk}(A_L, B_L, A_C, B_R, A_R)\rangle, \end{aligned} \quad (\text{C.32})$$

where, for our simulations, we choose the packet functions f_j and g_k to be Gaussians centered at x_L and x_R , with momenta p and $-p$, respectively. As in the single-particle case (C.23), these wavepackets can be rewritten as a single MPS with bond dimension $2D$, where D is the bond dimension of the vacua A_L, A_C, A_R . Note that, because position states are not defined for $k \geq j$, the wavepacket functions f and g are effectively truncated, leaving only the terms $j < k$, in this ansatz. Of course, if the wavepacket functions have negligible overlap, the effects of this truncation can themselves be neglected.

C.4 Particle detection via quasiparticle basis states

As discussed in the main text, it is possible to use the optimized quasiparticle states and their two-particle combinations to estimate the particle content of a wavefunction $|\psi(t)\rangle$ as it evolves during simulation. For example, the inner product $\langle \kappa \bar{\kappa}_{jk}^{(a,b)} | \psi(t) \rangle$ is sensitive to the presence of a pair consisting of a type- a kink quasiparticle at position j and a type- b antikink quasiparticle at position k .

The single-particle quasiparticle position states $|\phi_j\rangle$ of (C.11) can be made orthogonal by imposing either the left or right orthogonality conditions, (C.14) or (C.16). For the two-particle states $|\phi\phi_{jk}^{(a,b)}\rangle$ of (C.28) (where $\phi\phi$ is generic notation for either a kink-antikink pair or a meson pair), we can achieve orthogonality by enforcing the left orthogonality conditions on the left excitation tensor, B_L , and the right

orthogonality conditions on right excitation tensor, B_R . With these conditions, the two-particle states are orthogonal for one pair of species a, b

$$\langle \phi\phi_{jk}^{(a,b)} | \phi\phi_{lm}^{(a,b)} \rangle = \delta_{jl}\delta_{km}. \quad (\text{C.33})$$

Furthermore, by limiting the subspace to states with separation $d := k - j$ large enough so that interaction effects are negligible (see App. C.3), we can achieve an approximately orthonormal basis across species as well as positions:

$$\langle \phi\phi_{jk}^{(a,b)} | \phi\phi_{lm}^{(c,d)} \rangle \approx \delta_{jl}\delta_{km}\delta_{ac}\delta_{bd} \quad \forall k \gg j, m \gg l. \quad (\text{C.34})$$

If the left and right bulk vacuum tensors, A_L and A_R of the evolved state $|\psi(t)\rangle$, which in our simulations have the form (C.3), match the left and right bulk tensors A_L and A_R in the two-particle states (C.28), it is then straightforward to (approximately) project $|\psi(t)\rangle$ into the subspace spanned by these states.

However, we must take care when interpreting the overlaps of a wavefunction $|\psi(t)\rangle$ with quasiparticle position states such as $|\phi_j(B)\rangle$, as should be clear from the discussion of excitation tensors and quasiparticle position states above. In particular, the momentum-dependence of the B tensors optimized to represent each quasiparticle, as well as the ambiguity in fixing the degrees of freedom (C.13) in B that are not fixed by the optimization procedure (see App. C.3), make the interpretation of the overlap unclear unless the quasiparticle content of $|\psi(t)\rangle$ consists of broad spatial wavepackets, whose momentum support is focused around the momentum p used to optimize the B tensor. We next discuss two methods for avoiding these issues.

Checking consistency in the projected wavefunction

As described in the main text, one way to avoid issues with momentum-dependence and wavepacket breadth is to choose *some* momentum p , optimize a tensor $B(p)$ at that momentum for the quasiparticle being targeted, then examine the overlaps $\psi_j := \langle \phi_j(B(p)) | \psi(t) \rangle$ (or $\psi_{jk} := \langle \phi\phi_{jk}(B(p), B'(p')) | \psi(t) \rangle$ for a two-particle basis). If the wavepacket width of the projected wavefunction ψ_j is sufficiently large, and the momentum support (computed via Fourier transformation) sufficiently close to the chosen value of p , we know that the error made is small and can trust that the projection is accurately telling us about the quasiparticle content. We can quantify how broad the wavepacket must be, and how close the wavepacket momenta should be to p , via analyses such as those of Fig. C.3 and Fig. C.5.

If the distribution of momenta in the wavepacket indicates a large error due to the choice of p made while constructing the basis, it may be possible to iteratively *tune*

p to achieve a better match. This procedure fails, of course, if the wavepackets in $|\psi(t)\rangle$ are too narrow in position space (and hence too broad in momentum space) for the error to be kept small.

We use this procedure to compute the spin expectations values within each particle "sector" in Fig. 4.8, tuning the basis momenta p_L and p_R for two-particle bases $|\phi\phi_{jk}(B_L(p_L), B_R(p_R))\rangle$ to match the observed momenta.

Fourier analysis

To *fully* account for the momentum-dependence of the quasiparticle states, and to *eliminate* any issues due to the momentum-eigenstate "gauge-freedom" (C.13) on B tensors, we can simply take overlaps with momentum eigenstates instead of with the position states. These states are exactly invariant under (C.13), and the B tensors used to construct them can be optimized for the momentum of the eigenstate to avoid momentum mismatch.

For example, to project onto a single-particle subspace at momentum p , one can compute $\langle\phi(p)|\psi(t)\rangle$, with $|\phi(p)\rangle$ from (C.12). We can expand this overlap in terms of position states:

$$\langle\phi(B(p), p)|\psi(t)\rangle = \sum_j e^{-ipj} \langle\phi_j(B(p))|\psi(t)\rangle, \quad (\text{C.35})$$

where $B(p)$ is an excitation tensor optimized to represent the quasiparticle ϕ at momentum p . This overlap can be computed in practice, despite the infinite sum over j , because the position of excitations in $|\psi(t)\rangle$ is limited to the nonuniform window of (C.3) in which the initial quasiparticles (comprising the bubble) were placed, so that there are only $\sim N$ nonzero position terms in this overlap.

To compute the projection onto the entire quasiparticle subspace, we must evaluate the integral

$$\int_{-\pi}^{\pi} dp \langle\phi(p)|\psi(t)\rangle. \quad (\text{C.36})$$

This can be done approximately by sampling, for example using a numerical integration scheme. In practice, we use the Fast Fourier-Transform (FFT) algorithm to transform the spatial components $\langle\phi_j(B(p))|\psi(t)\rangle$ into a fixed sampling of momentum components at a resolution determined by the number of lattice sites N summed over in (C.35).

We use this method to compute the projected single-kink wavefunction described in Fig. C.5, to compute the kink-antikink scattering outcome probability in Fig. 4.6 of

the main text, and to compute the various scattering outcome probabilities reported in Fig. 4.8.

Efficient computation of the quasiparticle Fourier analysis

The projection of a wavefunction $|\psi(t)\rangle$ onto many momentum modes is relatively computationally intensive, since for each momentum mode we must first compute a tuned excitation tensor $B(p)$, followed by a full set of position overlaps $\langle\phi_j(B(p))|\psi(t)\rangle$. In the case of single-particle states, the cost is $O(NM)$, where M is the number of momentum samples and N is the nonuniform window size of $|\psi(t)\rangle$. For two-particle states, since we must consider cases in which the two particles have different momenta/positions, making the cost $O(M^2N^2)$. If $M \sim N$, and $N \approx 1000$, this may be prohibitive!

To reduce the cost, we can use the observation that the optimized excitation tensor $B(p)$, for a given quasiparticle, usually varies only slowly with the quasiparticle momentum p by introducing a small momentum mismatch in a controlled way: We project the excitation tensors $B(p)$, optimized for each mode of momentum p that we wish to sum over, onto a small basis of excitation tensors that capture the momentum dependence accurately across a wide range of p :

$$B(p) \approx \sum_{\alpha} b_{\alpha}(p)B_{\alpha}, \quad (\text{C.37})$$

for appropriately chosen coefficients $b_{\alpha}(p)$ and suitably chosen basis tensors B_{α} . A suitable basis can be built by orthonormalizing (via a Gram-Schmidt procedure) a set of $B(p_{\alpha})$ obtained at a selection of momenta (say, $p = -2, -1, 0, 1, 2$). We find that < 10 basis tensors is sufficient, for our chosen Hamiltonian parameters, to achieve an accuracy of $\sim 10^{-8}$ in (C.37). Given such a basis, we then compute position-state overlaps only for the basis tensors, from which we can compute the projection of the wavefunction onto an arbitrary momentum mode while making only a small error.

For example, in the case of a two-particle basis, we first compute $\psi_{jk;\alpha\beta} := \langle\phi\phi_{jk}(B_{L,\alpha}, B_{R,\beta})|\psi(t)\rangle$. Then, using the coefficients of (C.37), we approximate the overlap with the momentum-tuned position states as

$$\langle\phi\phi_{jk}(B_L(p), B_R(p'))|\psi(t)\rangle \approx b_{L,\alpha}^*(p)b_{R,\beta}^*(p')\psi_{jk;\alpha\beta}. \quad (\text{C.38})$$

From here, the momentum-mode overlaps are but an FFT away.

Other sources of error

Even for the Fourier analysis, there are at least two sources of inaccuracy beyond the choice of iMPS bond dimensions in the vacua and the quality of the optimization procedures used to find the vacua and the excitations tensors B . First, there is the further ambiguity (see App. C.3) in the case of topological excitations in the symmetry-broken setting ($h > 0$) owing to the dependence of the B -tensor optimization on an arbitrary choice of orthogonality conditions made during optimization. We do not currently know of a way to avoid this source of error. Fortunately, as illustrated in Fig C.2, we have good evidence that it is small.

The other source of error comes from interaction effects, which are not captured properly by the two-particle states. As discussed above, one can choose the minimum separation of the two particles to avoid interaction, by throwing out position states where the "interaction strength" ϵ , defined in (C.31), rises above some threshold. In choosing the threshold, there is a tradeoff between capturing (potentially large) components of the wavefunction that have smaller separation, but likely incur some (possibly small) error due to interaction, and the magnitude of ϵ , which is a conservative estimate of that error and is exponential in the separation. How to make this tradeoff optimally depends on the target wavefunction and the required precision of the projected wavefunction.

For our computations, we examined the dependence of the norm of the projected wavefunctions on the minimum separation d_{\min} allowed in the two-particle basis states. Exemplary results are shown in Figs. C.6 and C.7, which also show the dependence of the norms on the simulation bond-dimension limit. In Fig. C.6, we observe that, for the largest bond-dimension, the norm of the projected wavefunction is essentially constant for $d < 70$, despite the rising magnitude of interaction effects. This suggests that the wavefunction has negligible support at small separations (which we confirm via a Fourier analysis). We also observe that a minimum separation of $d_{\min} = 60$ is sufficient to keep $\epsilon < 10^{-6}$. Noting that the interaction strength is a property of the quasiparticle basis, and hence independent of time, we make the choice $d_{\min} = 60$ to avoid interaction effects when computing the data shown in Fig. 4.6 of the main text.

Fig. C.7 shows similar data for three quasiparticle-pair "sectors" for the Hamiltonian parameters (ii) of the main text. This data was used to estimate the scattering outcome probabilities shown in Fig. 4.8 of the main text. We see that, for this target wavefunction $|\psi(t)\rangle$, interaction effects are not important for the $\kappa\bar{\kappa}^{(0,0)}$ and $\mu\bar{\mu}^{(0,0)}$

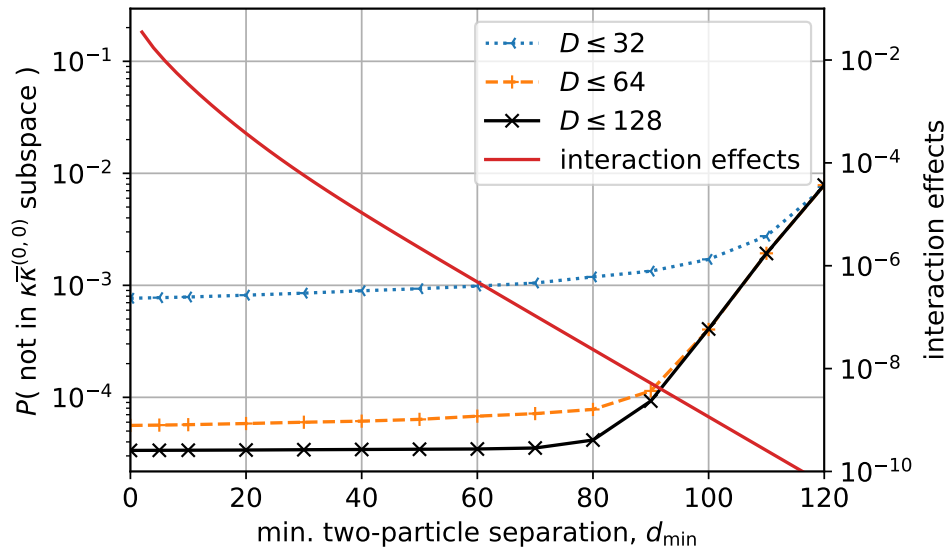


Figure C.6: Portion of the evolved bubble wavefunction outside of the kink-antikink "sector" for simulation (i) of Fig. 4.5 ($\lambda = 0$, $g = 0.8$, $h = 0.007$) at time $t = 150$, as a function of the minimum separation $d_{\min} := \min(k - j)$ permitted in the two-quasiparticles basis states $|\kappa\bar{\kappa}_{j,k}^{(0,0)}\rangle$. Probabilities are computed via a Fourier analysis, taking into account the momentum-dependence of the basis states. The basis error due to interaction effects is estimated using (C.31).

"sectors". However, they may influence the result at the level of ~ 0.01 , possibly more, for $\kappa\bar{\kappa}^{(0,1)}$ (and, by reflection symmetry of the initial bubble state, $\kappa\bar{\kappa}^{(1,0)}$). The $\kappa\bar{\kappa}^{(0,1)}$ and $\kappa\bar{\kappa}^{(1,0)}$ results are likely to be more sensitive to interaction than the $\kappa\bar{\kappa}^{(0,0)}$ result because the former two "sectors" describe bubble states in which one of the walls (the kink or the antikink) is heavier than in the $\kappa\bar{\kappa}^{(0,0)}$ case. These "lopsided" bubbles will be smaller than a $\kappa\bar{\kappa}^{(0,0)}$ bubble at the same energy, leading to larger components of the wavefunction at small separations, where interaction effects are stronger.

C.5 Evolving through time

To evolve an initial bubble iMPS in time, we define a window of N lattice sites surrounding the bubble and allow the MPS tensors belonging to those sites to vary during the evolution, while keeping the rest of the MPS tensors fixed. In other words, we use the nonuniform window ansatz (C.3) with fixed bulk tensors A_L , A_R . To compute the evolved state, we use methods based on the Time-Dependent Variational Principle (TDVP), which is set out for this class of states in [259] and implemented in the *evoMPS* package [262].

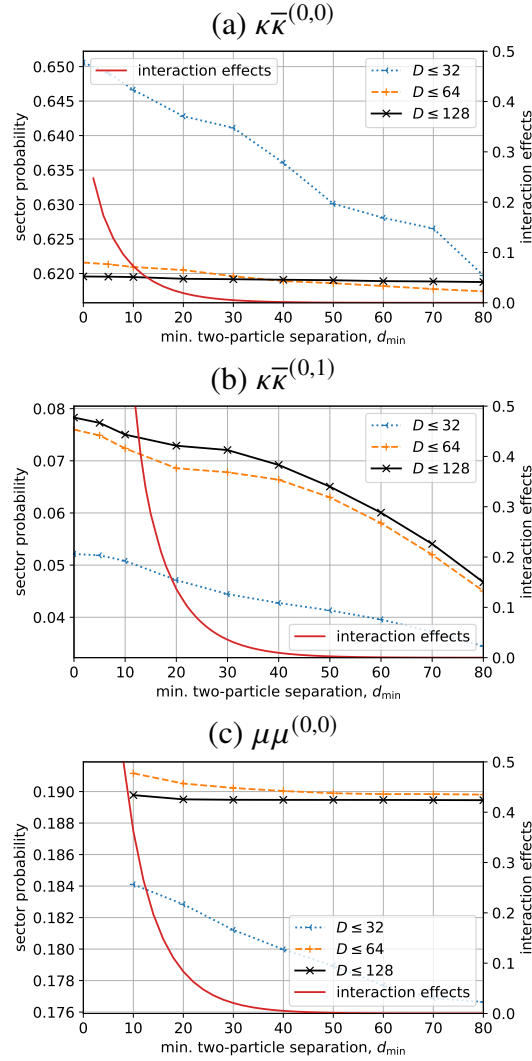


Figure C.7: Quasiparticle "sector" projection probabilities for simulation (ii) of Fig. 4.5 ($\lambda = 0.41$, $g = 0.98$, $h = 0.001$) at time $t = 270$, as a function of the minimum separation $d_{\min} := \min(k - j)$ permitted in the two-quasiparticles basis states $|\cdot \cdot_{j,k}\rangle$. Probabilities are computed via a Fourier analysis, taking into account the momentum-dependence of the basis states. The basis error due to interaction effects is estimated using (C.31).

The TDVP provides flow equations that describe the evolution of the MPS tensors needed to optimally approximate the evolution of the state by the Hamiltonian, given the constraint that the MPS bond dimension must remain *fixed*. Various schemes can be used to integrate the flow equations: we use the popular Runge-Kutta 4/5 (RK4) numerical integrator (to directly integrate the global flow equations) as well as the "projector-splitting" (PS) integrator of [261]. Since we want the MPS bond dimension to grow as needed (up to some maximum) as the entanglement of the state increases, we combine TDVP flow with techniques for increasing the bond dimension. In particular, we use the "dynamical expansion" scheme described in [256] together with the RK4 integrator, as well as the two-site projector-splitting method of [261].

The PS method and the RK4 integrator (with dynamical expansion), despite having similar theoretical error rates for a given time-step size, behave differently in important ways. For a given step size, the PS method has a larger computational overhead per step, but has better numerical stability and precision since, unlike the "traditional" TDVP scheme of [256], it does not require the inversion of matrices with small eigenvalues.

We find that the RK4 scheme with dynamical expansion is too unstable to use reliably during the initial timesteps of our simulations, which begin with an MPS of relatively small bond dimension (at most twice the vacuum bond dimension). However, we find RK4 can be used successfully after performing a small number of initial steps using the two-site PS scheme. During these initial PS steps, the bond dimension increases significantly. Later in the evolution, once the bond dimension has stabilized, we find the much faster RK4 scheme is able to take over without significant impact on the results. During the evolution, we do allow the MPS bond dimension to grow beyond a predefined maximum value.

To better understand the effects of the integration scheme on our simulations, as well as the impact of the bond-dimension limit, we compute two quantities indicative of numerical error: the energy drift and the truncation error. Although the exact evolution of the quantum state conserves the energy, the imperfect integration of the TDVP flow equations, combined with the limited bond dimension, leads to a small energy drift. This drift is an indicator of error incurred more generally during the evolution. We estimate the truncation error – the portion of the state by norm that is lost due to the bond dimension limit – as the maximum value, taken over position, of the *minimum* Schmidt coefficient (the D th-largest) for the left-right bipartition at

that position. Since there are rarely large jumps in the Schmidt spectrum, this value provides a good estimate of the magnitude of the terms that cannot be represented due to the bond-dimension limit.

As shown for simulation (ii) of the main text in Fig. C.8, the energy drift is particularly sensitive to the integration scheme and step size, whereas the truncation error is, unsurprisingly, most sensitive to the bond-dimension limit. We note that the truncation error jumps at the time of the first kink-antikink collision ($t \approx 175$), consistent with the entanglement jump observed in Fig. 4.9 of the main text. Fig. C.9 provides a more detailed picture of the entanglement structure, showing the full entanglement (Schmidt) spectrum (up to truncation) before and after the first collision at the cut with the largest entanglement entropy.

The computational cost of simulating up to some fixed time t scales as $O\left(\frac{D^3}{\delta t}\right)$. We are therefore eventually forced to trade accuracy for computational cost. For this particular simulation, we judge $D \leq 128$ and $\delta t = 0.05$ to provide sufficient accuracy, while keeping the computational requirements manageable, to enable us to study the outcomes of at least the first kink-antikink collision event in detail.

C.6 Comparison with quench approaches

We construct our initial false-vacuum bubble from individual kink and antikink quasiparticles, separated by a region of metastable false vacuum. Similar states can be constructed via a simpler approach: act on the uniform true vacuum $|\Omega\rangle$ with a suitable string operator that, in the case of the Ising-type model we study, flips all the spins over a range of sites:

$$|S_{jk}\rangle := X_j X_{j+1} \dots X_{k-1} X_k |\Omega\rangle \quad (\text{C.39})$$

For small longitudinal field h , we know that flipping *all* the spins gets us from the vacuum to a state *close* to the false vacuum (see App. C.2), so if $d := k - j$ is sufficiently large, the reduced state will be close to that of the false vacuum in the middle of the flipped region and topological excitations will be created at the edges of the string. In general, these excitations will be a combination of many topological quasiparticles of varying energy, hence the walls of a bubble created in this way will be unstable to interactions between these quasiparticles. The walls are also highly localized in position and hence have large momentum uncertainty.

By smearing the edges of the string in space, their momenta can be focused. This

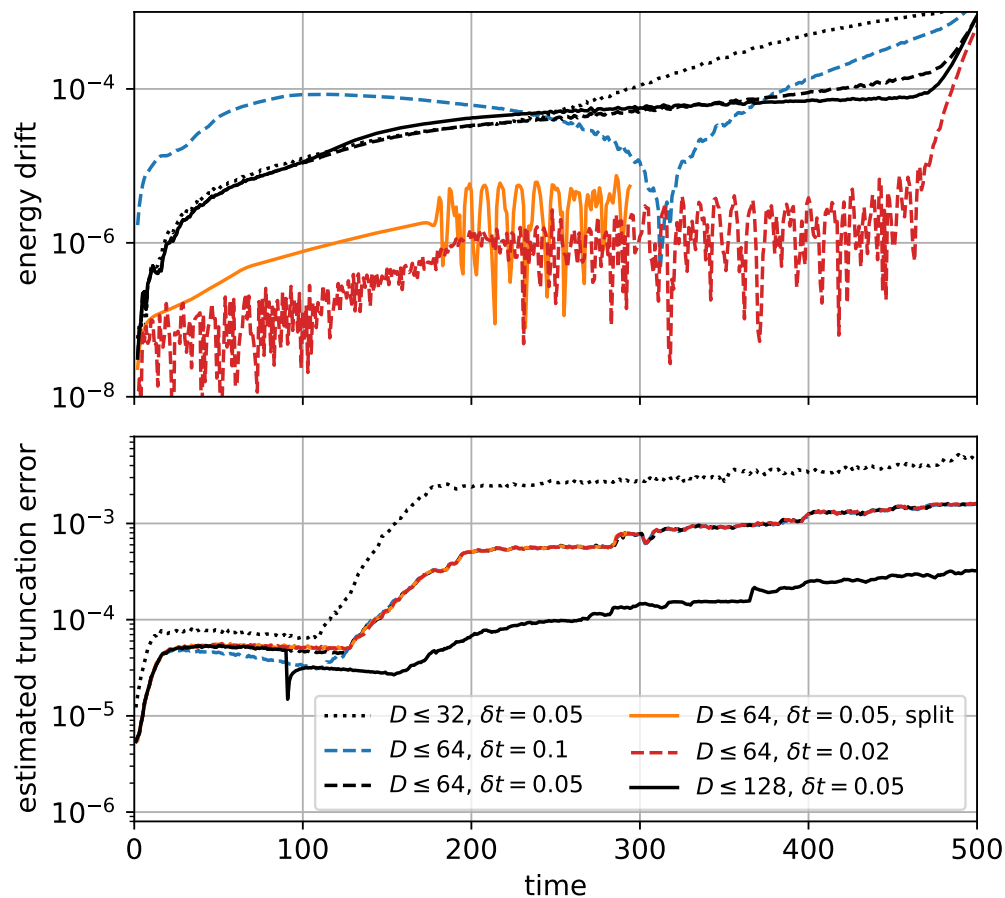


Figure C.8: Evolution of the energy expectation value and MPS truncation error for simulation (ii) of the main text. We compare different maximum bond dimensions D as well as different RK4 time-step sizes δt (for $D \leq 64$), observing that the effects of the time step are most noticeable in the energy drift, whereas the bond-dimension most obviously affects the truncation error at around the time of the first collision ($t \approx 150$). The $D \leq 128$ simulation is initialized from $D \leq 64, \delta t = 0.05$ at $t = 90$. The uptick in the energy drift at $t \approx 480$ is due to unconfined wavepackets hitting the boundaries of the simulation window.

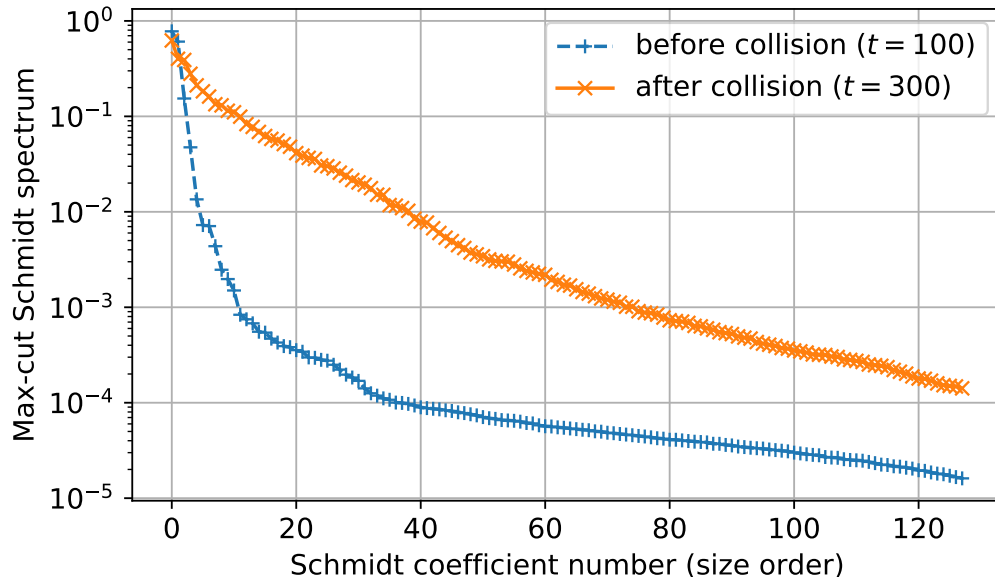


Figure C.9: Schmidt spectra for the maximum-entropy cut before and after the first collision in simulation (ii) of the main text. The bond dimension is 128.

results in states of the form

$$|\Psi\rangle = \sum_{j < k} f_j(x_L, p_L) f_k(x_R, p_R) |S_{jk}\rangle, \quad (\text{C.40})$$

where f_j and f_k are wavepacket functions for the left and right edge, respectively. If we choose these to be Gaussian, as for the wavepackets in the main text, we get a bubble state similar to those used in the main text, except that the walls have undetermined quasiparticle content.

In Fig. C.10, we compare the dynamics of three different initial states for the Hamiltonian parameters (ii) of the main text: (a) the fully localized string of (C.39), (b) the smeared string of (C.40), and (c) the tuned quasiparticle kink-antikink wavepackets used in the main text. We choose the same kink-antikink separation in all cases, and the same wavepacket widths in the latter two. The TDVP step size and the maximum bond dimension were also the same in all three cases. Simulations (a) and (b) both exhibit clear ballistic spread of energy from the initial bubble edges, indicating their instability, whereas simulation (c) only shows ballistic spread after the initial bubble walls have collided, consistent with the walls consisting of individual quasiparticles.

It is noteworthy that the evolution of state (a) encounters catastrophic numerical errors at around $t = 150$, unlike simulations (b) and (c), suggesting that scenario

(a) is much harder to simulate accurately⁴. In Fig. C.11 we show the energy drift and estimated truncation error (smallest retained Schmidt coefficient for the most entangled cut) for the same three simulations. This data clearly indicates that simulation (c) is easiest to simulate, since both the energy drift and the truncation error remain smaller with the same evolution parameters. The large truncation error at early times in cases (a) and (b) is consistent with a large amount of entanglement being generated early on, coming from the multiple excitations created at the ends of the string operator.

C.7 Velocity and Bloch oscillations

Single-kink evolution

In case of explicit symmetry breaking ($h > 0$), an isolated kink wavepacket, with true vacuum on one side and false vacuum on the other, will accelerate toward the false vacuum, absorbing the excess energy density of the latter. On the lattice, however, the kinetic energy cannot increase indefinitely. Instead, as discussed in the main text, the kink begins to undergo *Bloch oscillations*, eventually decelerating and reversing its direction of travel, as shown in Fig C.12 for Ising model parameters. By projecting into the κ basis of single kinks (see App. C.4), we can easily compute the kink position and momentum for such a simulation. As shown in Fig. C.13, the momentum increases linearly with time, making it easy to understand the evolution of the wavepacket position via the group velocity, which is given by $dE(p)/dp$, where $E(p)$ is the quasiparticle dispersion relation. In Fig. C.14 we show the velocity derived from the position of Fig. C.13, compared to the velocity derived from the momentum of Fig. C.13, via the dispersion relation.

Bubble evolution

In the case of a bubble state, the initial kink and antikink behave as their isolated counterparts, accelerating into the false vacuum until they near each other and interact. Their momenta increase linearly until the collision, as shown in lattice units ($-\pi < p \leq \pi$) for the Ising model (parameter set (i) of the main text) in Fig. C.15. It is interesting to note that the momentum *variance* is significantly larger after the collision than it is before, indicative of an (in this case elastic) interaction.

The velocity of the kink and antikink, defined here as the velocity of the point in space at which the (interpolated) spin expectation value crosses zero, evolve as shown

⁴These errors also occur if the PS integrator is used throughout the evolution, rather than switching to RK4 after some entanglement has built up.

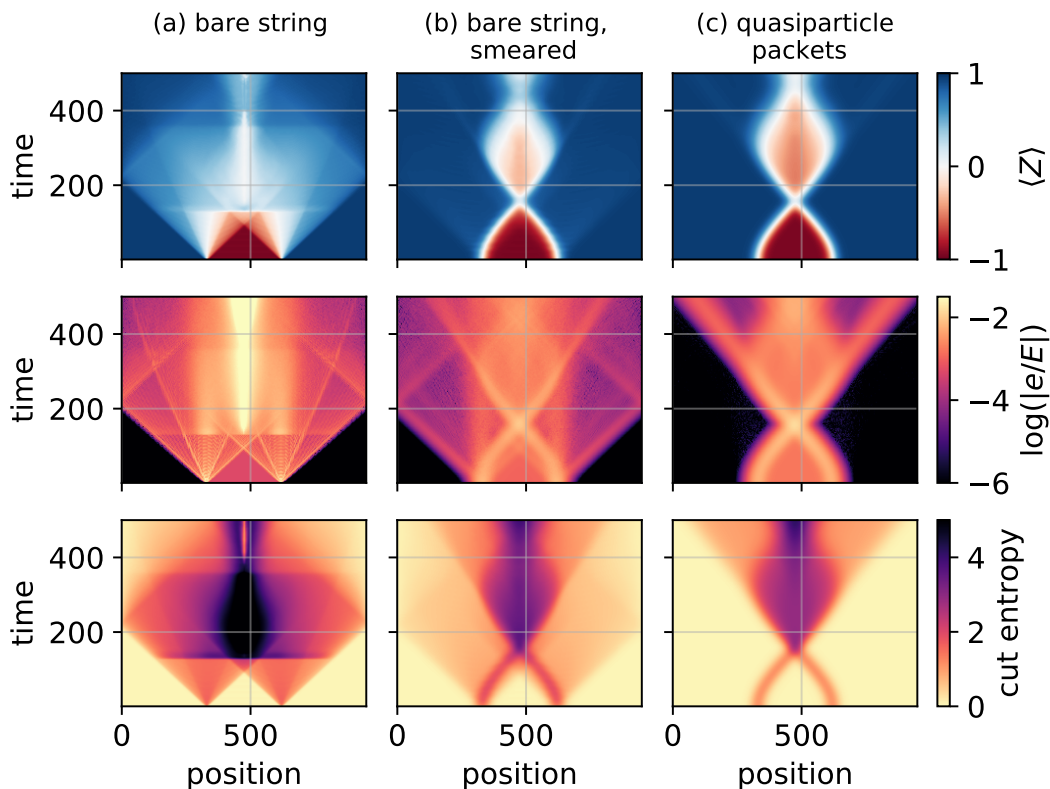


Figure C.10: Evolution of spin and energy density expectation values and the cut entropy for parameter set (ii) of the main text ($\lambda = 0.41$, $g = 0.98$, $h = 0.001$), with three different initial states. State (a) is prepared by acting on the vacuum with a string operator $\prod_{j=x_L}^{x_R-1} X_j$, which flips the spins to form a bubble-like state with energy $E/m_\mu = 8.69$. State (b) is similar to (a), but with the ends of the string smeared out using Gaussian packets of width $\sigma = 40$, reducing the energy to $E/m_\mu = 4.02$. State (c) is the initial state discussed in the main text with $E/m_\mu = 2.62$, using quasiparticle wavepackets for the kinks and the false vacuum for the middle region. The evolution parameters are the same in all cases: The maximum bond dimension is 64 and the RK4 step size is 0.05. In (a), dramatic errors in the simulation occur at $t \approx 150$, indicating the difficulty of simulating these dynamics versus (b) and (c). In both (a) and (b), ballistic energy-spread emanating from the initial kinks indicates that they have complex quasiparticle content, resulting in immediate inelastic scattering. In contrast, the tuned quasiparticle kinks of (c) do not produce appreciable ballistic spread until the bubble walls have collided.

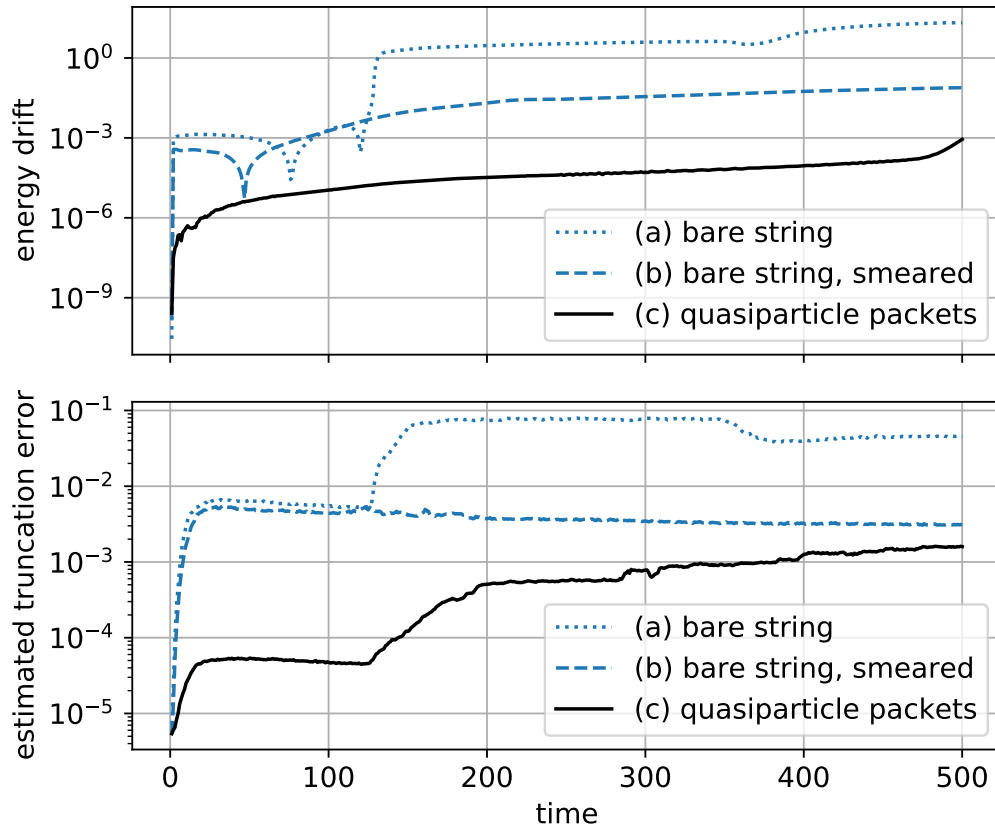


Figure C.11: Evolution of the energy expectation value and MPS truncation error for the simulations of Fig. C.10. Energy drift ($|1 - E(t)/E(0)|$) indicates deviation from unitary evolution and results from restriction to a maximum bond dimension of 64 as well as from numerical integration errors (RK4 step size 0.05). Truncation error (estimated as the maximum over cuts of the smallest Schmidt coefficient) results from the limited bond dimension and increases as entanglement is produced.

in Fig. C.16, in accordance with the dispersion relation of the kink quasiparticle excitation. In this simulation, the kink achieves its maximum velocity well before the collision, and begins to decelerate as part of a Bloch oscillation. The pre-collision velocity can be kept from reaching its maximum by reducing the kink-antikink separation in the initial bubble state, as we have confirmed with other simulations.

In Fig. C.17, we show the kink and antikink velocity evolution for simulation (ii) of the main text. In this case, we have set the initial kink-antikink separation so that the velocity does not reach a maximum prior to collision (indicating that Bloch oscillations have not yet begun).

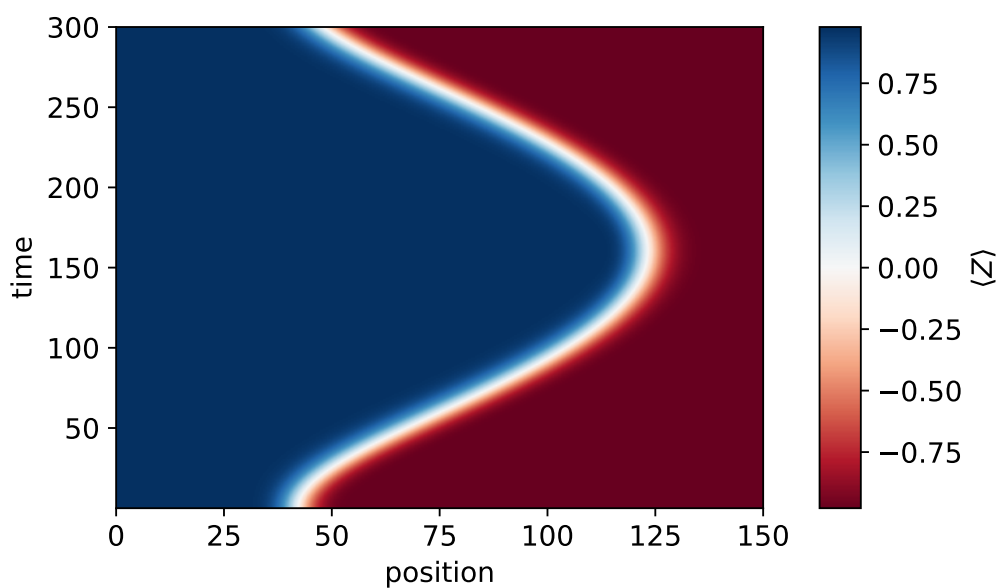


Figure C.12: Evolution of spin expectation values $\langle Z \rangle$ for a single kink in the \mathbb{Z}_2 -broken Ising model, with parameters $\lambda = 0$, $g = 0.4$, $h = 0.01$. The vacuum bond dimension is $D = 6$, allowed to evolve to a maximum $D \leq 32$. The RK4 time-step size was $\delta t = 0.01$.

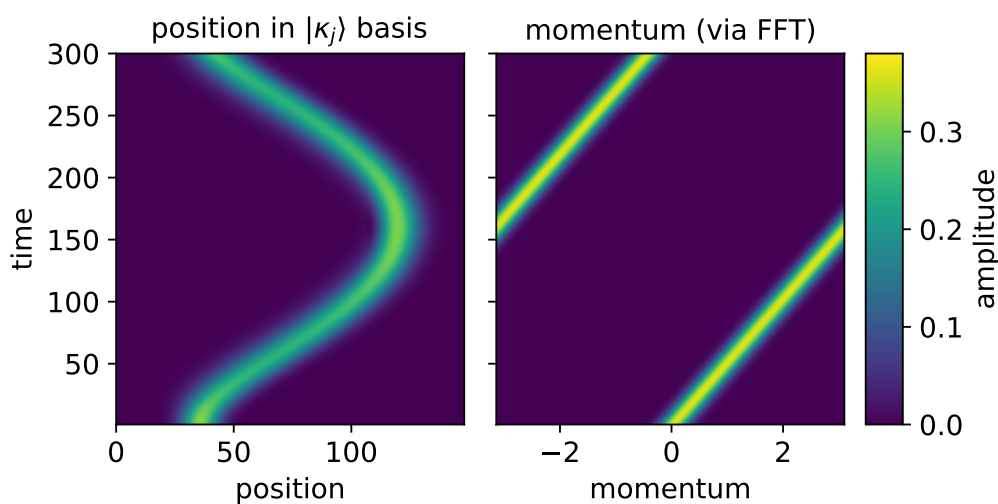


Figure C.13: Evolution of the position and momentum expectation values of the wavefunction of Fig. C.12 after projection onto the single-kink position basis states $|\kappa_j\rangle$. For the Hamiltonian parameters in question (see Fig. C.12), the momentum dependence of the basis states is negligible, and could be ignored for the projection.

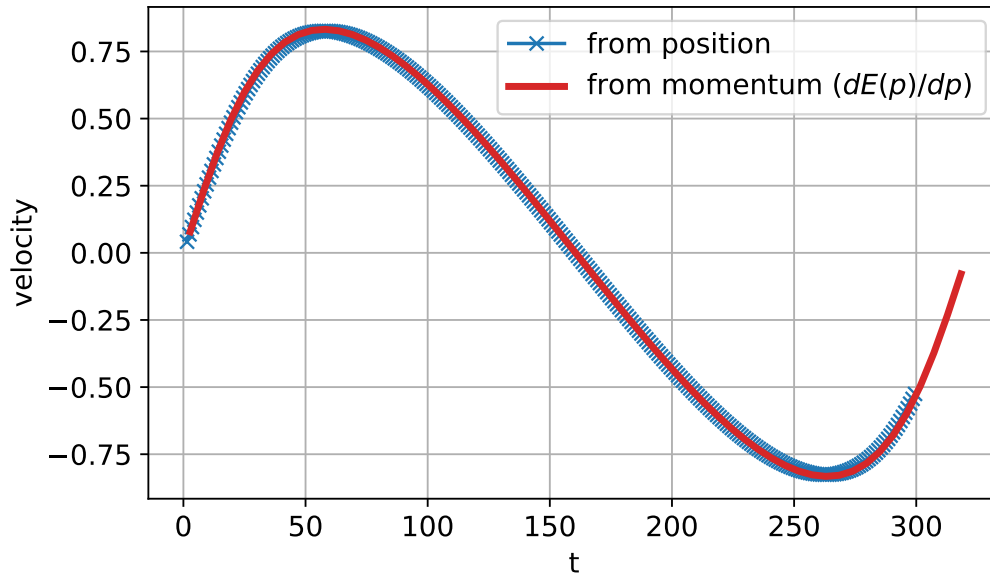


Figure C.14: Evolution of the kink velocity for the single-kink simulation of Fig. C.12. Here, the velocity is computed from the projection of the wavefunction into the $|\kappa_j\rangle$ position basis in two different ways: from finite-differences of the position expectation value and from the momentum expectation value, via the numerical dispersion relation $E(p)$. That there is a good match shows that the kink-quasiparticle ansatz successfully captures the confined quasiparticles present in the \mathbb{Z}_2 -broken Ising model.

C.8 Zero longitudinal field

Here we examine the behavior of "bubbles" (kink-antikink pairs) when we set the longitudinal field $h = 0$. Our model with $\lambda \neq 0$ is not integrable, even if we turn off the longitudinal magnetic field h . Generically, we should therefore expect to observe inelastic kink-antikink collisions.

We prepare bubble states, for the Hamiltonian parameters $g = 0.9$, $\lambda = 0.3$, $h = 0$, in which the kink and antikink have initial momentum p and $-p$, respectively. By varying p , we can choose the total energy to be either above or below the threshold for quasiparticle pair production, which we numerically estimate to be $2m_\mu = 1.88$ (relative to the vacuum energy).

In Fig. C.18, we show the cut entropy as a function of space and time and, separately for clarity, the time-dependence of the cut entropy at the midpoint between the quasiparticle wavepackets. We choose three different initial momenta: $p = \frac{4\pi}{32}$, $p = \frac{5\pi}{32}$, and $p = \frac{6\pi}{32}$, corresponding to bubble energies of $E = 1.65$, $E = 1.92$, and $E = 2.20$, respectively. We observe that the post-collision mid-chain entropy returns

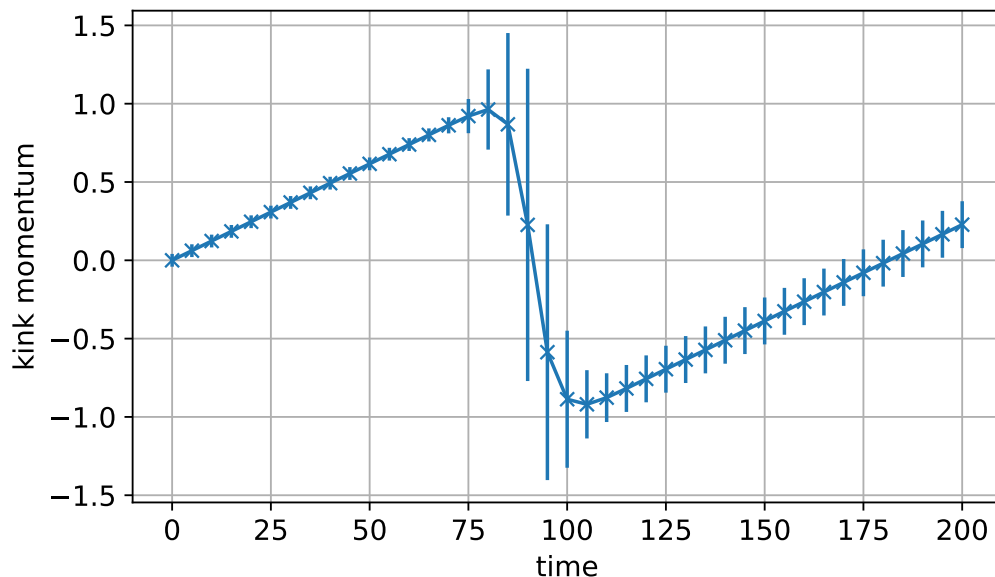


Figure C.15: Momentum of the kink in simulation (i) of the main text (Ising), computed from the projected wavefunction in the $\kappa\bar{\kappa}^{(0,0)}$ basis. The bond dimension is 128. Since the $\kappa\bar{\kappa}^{(0,0)}$ basis does not accurately capture the state when the kink is very close to the antikink, this data is not complete during the collision ($t \approx 90$). The error bars indicate the standard deviation of the momentum distribution.

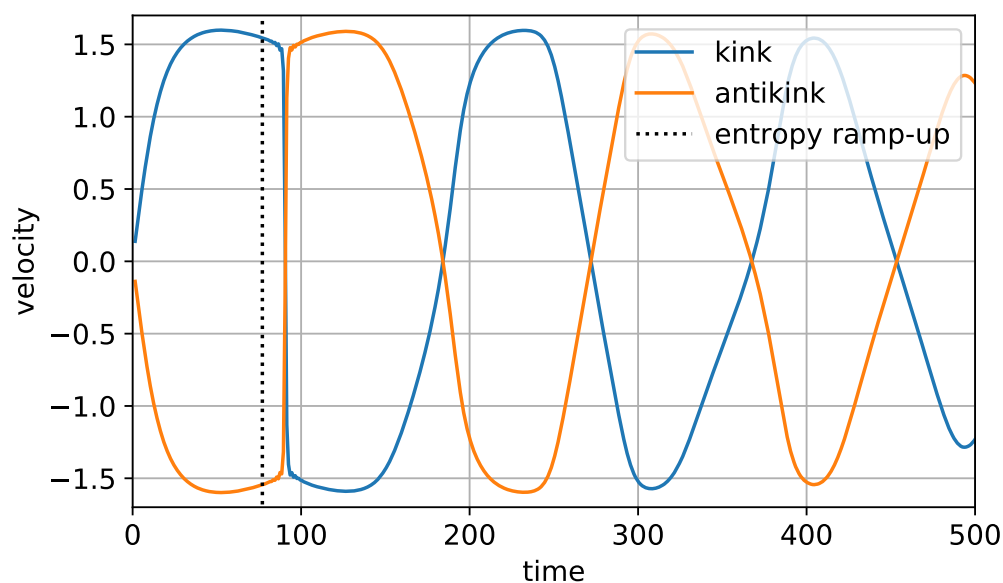


Figure C.16: Kink and antikink wavepacket velocity for the Ising model, simulation (i) of the main text, computed as the finite difference of the interpolated position of the 0-intercept of $\langle Z_j \rangle$. The bond dimension is 128. Note that the data is only likely to be accurate up to $t \approx 500$, as suggested by Fig. 4.9. The onset of the first collision is indicated by the dotted line, which is the time at which the maximum cut entropy begins to grow rapidly.

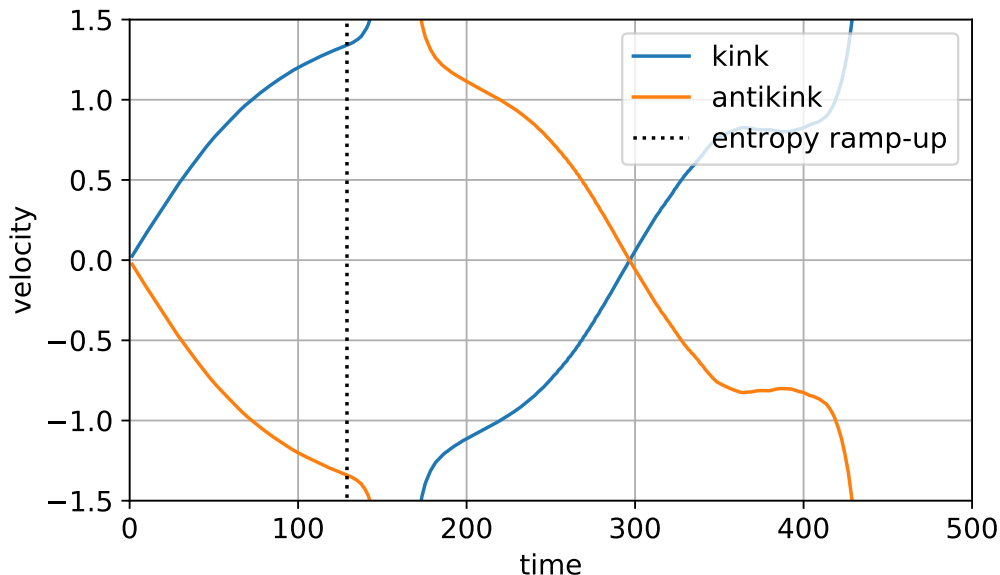


Figure C.17: Kink and antikink wavepacket velocity for simulation (ii), computed as the finite difference of the interpolated position of the 0-intercept of $\langle Z_j \rangle$. The bond dimension is 128. The interpretation of the 0-intercept as the position breaks down both during and, to some extent, after the collision: During the collision, the zero intercept disappears altogether as the kink and antikink merge and all spin expectation values are > 0 . After the collision, there are in this case (see Fig. 4.8) at least two different bubble "branches" of the wavefunction, both contributing to the spin expectation values. The onset of the first collision is indicated by the dotted line, which is the time at which the maximum cut entropy begins to grow rapidly.

to its vacuum value for $p = \frac{4\pi}{32}$, suggesting a *trivial* scattering event (see App. C.9). For $p = \frac{5\pi}{32}$ and $p = \frac{6\pi}{32}$, we observe a residual entropy surplus after the collision, suggesting *nontrivial* scattering. Since the onset of this extra entropy contribution coincides with the energy crossing the two-meson threshold $2m_\mu$, it is likely due to an increasing probability of meson pair production.

It is interesting to note that, if we set $h > 0$ while keeping the other Hamiltonian parameters the same, we observe *nontrivial*, albeit elastic, scattering of kink-antikink pairs when the energy is below the two-meson threshold. Turning off the longitudinal field appears to turn off this nontrivial elastic contribution, so that kinks and antikinks scatter trivially.

C.9 Entanglement generated by an elastic collision

Here we consider how two single-particle wavepackets become entangled when they scatter elastically in one spatial dimension. The entanglement arises from the

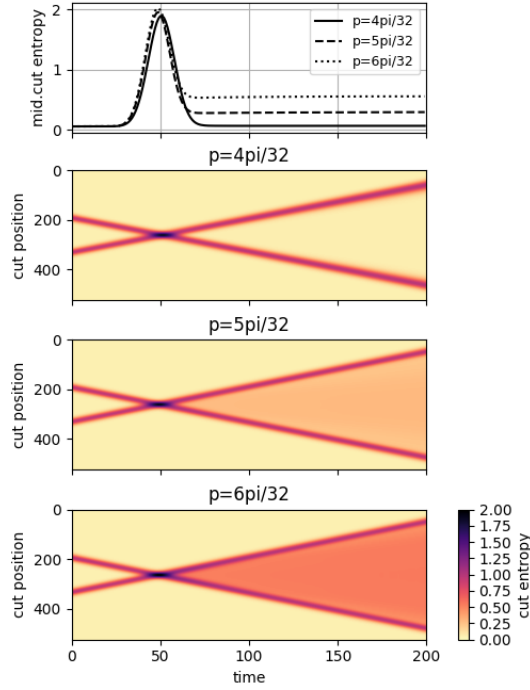


Figure C.18: Cut entropy for kink-antikink collisions, in the absence of a longitudinal field, with initial kink momentum p and antikink momentum $-p$, for three different values of p . The Hamiltonian parameters are $g = 0.9$, $\lambda = 0.3$, $h = 0$, and the wavepacket width is $\sigma = 19.0$. The vacuum bond dimension is $D = 14$, with a limit $D \leq 64$ imposed during evolution. The integration time-step size was $\delta t = 0.05$.

momentum dependence of the scattering phase shift.

For this analysis we ignore lattice effects and consider two distinguishable particles A and B propagating in the continuum. A pure state expanded in the momentum basis has the form

$$|\psi\rangle = \int dpdq \psi(p, q) |p\rangle_A |q\rangle_B, \quad (\text{C.41})$$

with the normalization

$$\int dpdq |\psi(p, q)|^2 = 1. \quad (\text{C.42})$$

We assume the initial state factorizes as the product $\psi(p, q) = \psi_A(p)\psi_B(q)$ of two widely separated wavepackets, but after elastic scattering, the wave packets becomes correlated due to the momentum dependent phase shift $\phi(p, q)$:

$$\psi(p, q) = \psi_A(p)\psi_B(q)e^{i\phi(p, q)}. \quad (\text{C.43})$$

Tracing out particle B , we obtain the reduced density matrix for particle A

$$\begin{aligned}\rho_A &= \int dp_1 dp_2 |p_1\rangle \rho_A(p_1, p_2) \langle p_2| , \\ \rho_A(p_1, p_2) &= \int dq \psi(p_1, q) \psi^*(p_2, q) ,\end{aligned}\quad (\text{C.44})$$

where $*$ denotes complex conjugation.

To quantify the entanglement of particles A and B , we compute the Rényi entropies of ρ_A ,

$$S_n = \frac{1}{1-n} \log_2 \rho_A^n , \quad (\text{C.45})$$

where

$$\begin{aligned}\text{tr} \rho_A^n &= \int dp_1 dp_2 \dots dp_n dq_1 dq_2 \dots dq_n \\ &|\psi_A(p_1)|^2 |\psi_A(p_2)|^2 \dots |\psi_A(p_n)|^2 |\psi_B(q_1)|^2 |\psi_B(q_2)|^2 \dots |\psi_B(q_n)|^2 \\ &\exp [i(\phi(p_1, q_1) - \phi(p_2, q_1) + \phi(p_2, q_2) - \phi(p_3, q_2) \dots + \phi(p_n, q_n) - \phi(p_1, q_n))] .\end{aligned}\quad (\text{C.46})$$

Now suppose that the wave packets for particles A and B are Gaussian:

$$\begin{aligned}|\psi_A(p)|^2 &= \frac{1}{\sqrt{2\pi}\Delta_A} e^{-(p-\bar{p})^2/2\Delta_A^2} , \\ |\psi_B(q)|^2 &= \frac{1}{\sqrt{2\pi}\Delta_B} e^{-(q-\bar{q})^2/2\Delta_B^2} .\end{aligned}\quad (\text{C.47})$$

If the phase shift were slowly varying over the range in p and q where the wave packets have significant support, we could approximate $\text{tr} \rho_A^n$ by expanding $\phi(p, q)$ to quadratic order about (\bar{p}, \bar{q}) . But in that case the scattered wave packets are only slightly entangled. In order to do an analytic computation, we will assume that $\phi(p, q)$ is exactly quadratic even if the phase shift varies rapidly. Then the only term that matters is the cross term

$$\phi(p, q) = \phi_2 pq + \dots , \quad (\text{C.48})$$

because the exponential of the other terms factorizes into a function of p times a function of q , which does not contribute to the entanglement of particles A and B .

By evaluating a Gaussian integral, we find

$$\begin{aligned}\text{tr} \rho_A^n &= \left[\prod_{k=1}^{n-1} \left(1 + 4\alpha^2 \sin^2 \left(\frac{k\pi}{n} \right) \right) \right]^{-1/2} , \\ S_n &= \frac{1}{2(n-1)} \sum_{k=1}^{n-1} \log_2 \left(1 + 4\alpha^2 \sin^2 \left(\frac{k\pi}{n} \right) \right) ,\end{aligned}\quad (\text{C.49})$$

where

$$\alpha = \phi_2 \Delta_A \Delta_B . \quad (\text{C.50})$$

As we anticipated, for $|\alpha| \gg 1$ the phase shift is rapidly varying and the entanglement is substantial. Using the formula

$$\prod_{k=1}^{n-1} 4 \sin^2 \left(\frac{k\pi}{n} \right) = n^2 \quad (\text{C.51})$$

we find

$$\text{tr} \rho_A^n = \frac{1}{n|\alpha|^{n-1}} \left(1 + O(\alpha^{-2}) \right). \quad (\text{C.52})$$

We can extract the large- α behavior of the von Neumann entropy by taking the limit

$$\begin{aligned} S_1 &= \text{tr} \rho_A \log_2 \rho_A = \lim_{n \rightarrow 1} \frac{1}{1-n} \log_2 \text{tr} \rho_A^n \\ &\approx \lim_{n \rightarrow 1} \frac{(n-1) \log_2 |\alpha| + \log_2 n}{n-1} = \log_2(e|\alpha|). \end{aligned} \quad (\text{C.53})$$

The entanglement entropy of particles A and B , after the elastic scattering event, scales like $\log |\alpha|$; therefore we expect to need a bond dimension scaling like $|\alpha|$ to simulate the scattering process accurately using an MPS approximation.

In fact, by invoking properties of Chebyshev polynomials, the product over k in (C.49) can be evaluated explicitly, yielding [273]

$$S_n = \frac{1}{2(n-1)} \left[1 + 2n \log_2 |\alpha| + \log_2(\cosh(bn) - 1) \right], \quad (\text{C.54})$$

where

$$b \equiv \text{arccosh} \left(1 + \frac{1}{2|\alpha|^2} \right). \quad (\text{C.55})$$

In the limit $n \rightarrow 1$ we find

$$S_1 = \log_2 |\alpha| + \frac{b}{2} \left(1 + 4|\alpha|^2 \right)^{1/2} \log_2 e; \quad (\text{C.56})$$

taking the large- α limit using $\text{arccosh}(1+x) = \sqrt{2x} (1 + O(x))$, we recover (C.53).

Appendix D

OTHER PUBLICATIONS

Other publications during the author's graduate school that are related to this thesis.

- A. J. Buser, H. Gharibyan, M. Hanada, M. Honda, and **J. Liu** (corresponding author, alphabetical order), *Quantum simulation of gauge theory via orbifold lattice*, JHEP **09**, 034, (2021), arxiv:2011.06576 [hep-th].
- H. Gharibyan, M. Hanada, M. Honda, and **J. Liu** (alphabetical order), *Toward simulating Superstring/M-theory on a quantum computer*, JHEP **07**, 140, (2021), arxiv:2011.06573 [hep-th].
- J. Liu** (corresponding author), and Y.Z. Li, *On Quantum Simulation Of Cosmic Inflation*, Phys. Rev. D **104**, 086013, (2021), arXiv:2009.10921 [quant-ph].
- J. Liu**, D. Meltzer, D. Poland, and D. Simmons-Duffin (alphabetical order), *The Lorentzian inversion formula and the spectrum of the 3d O(2) CFT*, JHEP **09**, 115, (2020), arXiv:2007.07914 [hep-th].
- X. Yuan, J. Sun, **J. Liu**, Q. Zhao, and Y. Zhou, *Quantum simulation with hybrid tensor networks*, Phys. Rev. Lett **127**, 040501, (2021), arXiv:2007.00958 [quant-ph].
- J. Liu** (corresponding author), and Y. Xin (alphabetical order), *Quantum simulation of quantum field theories as quantum chemistry*, JHEP **12**, 011, (2020), arXiv:2004.13234 [hep-th].
- J. Liu**, *Scrambling and decoding the charged quantum information*, Phys. Rev. Research **2**, 043164, (2020), arXiv:2003.11425 [quant-ph].
- S. M. Chester, W. Landry, **J. Liu**, D. Poland, D. Simmons-Duffin, N. Su, and A. Vichi (alphabetical order), *Carving out OPE space and precise O(2) model critical exponents*, JHEP **06**, 142, (2020), arXiv:1912.03324 [hep-th].
- A. Lewkowycz, **J. Liu**, E. Silverstein, and G. Torroba (alphabetical order), *$T\bar{T}$ and EE, with implications for (A)dS subregion encodings*, JHEP **04**, 152, (2020), arXiv:1909.13808 [hep-th].
- C. Cheung, **J. Liu**, and G. N. Remmen (alphabetical order), *Entropy Bounds on Effective Field Theory from Rotating Dyonic Black Holes*, Phys. Rev. D **100**, 046003, (2019), arXiv:1903.09156 [hep-th].

- J. Liu** (corresponding author), and Y. Zhou (alphabetical order), *Note on global symmetry and SYK model*, JHEP **05**, 099, (2019), arXiv:1901.05666 [hep-th].
- N. Bao, and **J. Liu** (corresponding author, alphabetical order), *Quantum algorithms for conformal bootstrap*, Nucl. Phys. B **946**, 114702, (2019), arXiv:1811.05675 [hep-th].
- J. Liu** (corresponding author), E. Perlmutter, V. Rosenhaus, and D. Simmons-Duffin (alphabetical order), *d-dimensional SYK, AdS Loops, and 6j Symbols*, JHEP **03**, 052, (2019), arXiv:1808.00612 [hep-th].
- J. Liu**, *Spectral form factors and late time quantum chaos*, Phys. Rev. D **98**, 086026, (2018), arXiv:1806.05316 [hep-th].
- N. Bao, and **J. Liu** (corresponding author), *Quantum complexity and the virial theorem*, JHEP **08**, 144, (2018), arXiv:1804.03242 [hep-th].
- P. Kraus, **J. Liu** (corresponding author), and D. Marolf (alphabetical order), *Cutoff AdS_3 versus the $T\bar{T}$ deformation*, JHEP **07**, 027, (2018), arXiv:1801.02714 [hep-th].
- Y. Zhou, and **J. Liu** (corresponding author), *Note on the Green's function formalism and topological invariants*, J. Stat. Mech. **2003**, 033101, (2020), arXiv:1712.08775 [hep-th]].
- N. Hunter-Jones, and **J. Liu** (alphabetical order), *Chaos and random matrices in supersymmetric SYK*, JHEP **05**, 202, (2018), arXiv:1710.08184 [hep-th].
- N. Hunter-Jones, **J. Liu** (corresponding author), and Y. Zhou (alphabetical order), *On thermalization in the SYK and supersymmetric SYK models*, JHEP **02**, 142, (2018), arXiv:1710.03012 [hep-th].
- J. Liu**, *Artificial Neural Network in Cosmic Landscape*, JHEP **12**, 149, (2017), arXiv:1707.02800 [hep-th].
- J. Cotler, N. Hunter-Jones, **J. Liu**, and B. Yoshida (alphabetical order), *Chaos, Complexity, and Random Matrices*, JHEP **11**, 048, (2017), arXiv:1706.05400 [hep-th].
- T. Li, **J. Liu**, Y. Xin, and Y. Zhou (alphabetical order), *Supersymmetric SYK model and random matrix theory*, JHEP **06**, 111, (2017), arXiv:1702.01738 [hep-th].